

Frequency-Domain Analysis and Design for Reset Feedback Control with Application to Precision Motion Systems

Zhang, X.

DOI

[10.4233/uuid:d0ec0e47-9434-45ce-b53a-57e7091d4a48](https://doi.org/10.4233/uuid:d0ec0e47-9434-45ce-b53a-57e7091d4a48)

Publication date

2025

Document Version

Final published version

Citation (APA)

Zhang, X. (2025). *Frequency-Domain Analysis and Design for Reset Feedback Control: with Application to Precision Motion Systems*. [Dissertation (TU Delft), Delft University of Technology].
<https://doi.org/10.4233/uuid:d0ec0e47-9434-45ce-b53a-57e7091d4a48>

Important note

To cite this publication, please use the final published version (if applicable).
Please check the document version above.

Copyright

Other than for strictly personal use, it is not permitted to download, forward or distribute the text or part of it, without the consent of the author(s) and/or copyright holder(s), unless the work is under an open content license such as Creative Commons.

Takedown policy

Please contact us and provide details if you believe this document breaches copyrights.
We will remove access to the work immediately and investigate your claim.

Frequency-Domain Analysis and Design for Reset Feedback Control

with Application to Precision Motion Systems

Frequency-Domain Analysis and Design for Reset Feedback Control

with Application to Precision Motion Systems

Dissertation

for the purpose of obtaining the degree of doctor
at Delft University of Technology,
by the authority of the Rector Magnificus, prof. dr. ir. T.H.J.J. van der Hagen,
chair of the Board of Doctorates,
to be defended publicly
on Thursday April 24, 2025 at 10:00 o'clock

by

Xinxin ZHANG

This dissertation has been approved by the promotor

promotor: Dr. ir. S.H. Hossein Nia Kani

promotor: Prof. dr. ir. J.L. Herder

Composition of the doctoral committee:

Rector Magnificus,	chairperson
Dr. S.H. Hossein Nia Kani,	Delft University of Technology, promotor
Prof. dr. ir. J.L. Herder,	Delft University of Technology, promotor

Independent members:

Prof. dr. ir. B.H.K. De Schutter,	Delft University of Technology
Prof. dr. ir. C.-M. Ionescu,	Ghent University, Belgium
Dr. ir. M. Jafarian,	Delft University of Technology
Prof. dr. -Ing J. Reger,	Ilmenau University of Technology, Germany
Prof.dr. B.M. Vinagre,	University of Extremadura, Spain
Prof.dr. P.G. Steeneken,	Delft University of Technology, reserve member



Keywords: Reset feedback control, precision motion control, frequency response analysis, higher-order sinusoidal input describing function, steady-state performance, transient-state performance

Printed by: Proefschriftmaken

Cover: Nonlinear signals and their power spectral density plots, generated using Midjourney by X. Zhang.

Copyright ©2025 by X. Zhang

ISBN 978-94-6518-039-7

An electronic version of this dissertation is available at
<http://repository.tudelft.nl/>.

Yet the sun—at every moment it is both sunset and sunrise.

Tiesheng Shi, China

Contents

Summary	xi
Samenvatting	xiii
1 Introduction	1
1.1 Precision Motion Control	3
1.2 Frequency Response Analysis	5
1.3 Limitations of Linear Feedback Control	6
1.3.1 Waterbed Effect	7
1.3.2 Bode Phase-Gain Trade-Off	7
1.4 Reset Feedback Control System: Overcome Linear Limitations	8
1.4.1 Definition of Reset Control Systems	8
1.4.2 Stability and Convergence Conditions for Reset Control Systems.	9
1.4.3 Reset Elements	10
1.5 Motivation and Research Problem Statement	12
1.6 Thesis Outline	13
2 Frequency Response Analysis for Open-Loop Reset Control Systems	19
2.1 Introduction	20
2.2 Method: Frequency Response Analysis for Open-loop Reset Systems.	20
2.2.1 Analysis Model for the Sinusoidal-Input Clegg Integrator	21
2.2.2 Higher-Order Sinusoidal Input Describing Functions (HOSIDFs) for Reset Controllers	22
2.2.3 HOSIDFs for Open-Loop Reset Control Systems	23
2.3 Results: Validation of Open-Loop HOSIDFs	24
2.3.1 Case Study 1	24
2.3.2 Case Study 2	25
2.4 Conclusion	27
Appendix	30
2.A Proof of Lemma 1	30
2.B Proof of Theorem 1	31
2.C Proof of Theorem 2	36
2.D Proof of Theorem 3	37
3 Identifying the Reliability of Closed-Loop SIDF Analysis	39
3.1 Introduction	40
3.2 Problem Statement via Illustrative Examples	40
3.3 Method for Identifying the Reliability of SIDF Analysis.	42
3.3.1 Piecewise Expressions for Sinusoidal-Input Reset Systems	42
3.3.2 Identifying Two-Reset Conditions in SIDF Analysis	43

3.4	Results: Validation of Two-Reset Conditions	44
3.5	Conclusion	46
	Appendix	47
3.A	Proof of Lemma 2	47
3.B	Proof of Theorem 4	51
4	Frequency Response Analysis for Closed-Loop Reset Control Systems	55
4.1	Introduction	56
4.2	Method: Frequency Response Analysis for Closed-loop Reset Systems	56
4.2.1	Sinusoidal-Input Closed-Loop Reset Systems Analysis Models	56
4.2.2	HOSIDFs for Closed-Loop Reset Systems	60
4.3	Results: Validation of Closed-Loop HOSIDFs	62
4.3.1	Case Study 1	62
4.3.2	Case Study 2	63
4.4	Conclusion and Discussions	65
	Appendix	67
4.A	Proof of Theorem 5	67
4.B	Proof of Theorem 6	70
5	MATLAB App “Reset Far”	73
5.1	Introduction of the MATLAB App “Reset Far”	74
5.2	Case Study: The Application of the MATLAB App “Reset Far”	75
5.3	Conclusion	79
6	Phase-Lead Shaped Reset Control Systems	83
6.1	Introduction	84
6.2	Preliminaries	85
6.2.1	Reset Elements	86
6.2.2	HOSIDF for Generalized FORE	87
6.2.3	Frequency-Domain Design Objective for Generalized FORE	87
6.3	Frequency-Domain Analysis and Design of the Shaped Reset Systems	87
6.3.1	Phase Lead Benefits of Shaped Generalized FROE	88
6.3.2	Design Procedure for Shaped Generalized FROE	92
6.4	Illustrative Case Studies	95
6.4.1	Case Study 1: Phase Lead Benefit of Shaped Reset Control	95
6.4.2	Case Study 2: Gain Benefit of Shaped Reset Control	99
6.5	Conclusion	104
	Appendix	109
6.A	Proof of Lemma 3	109
6.B	Proof of Lemma 4	110
6.C	Proof of Theorem 7	110
6.D	Proof of Theorem 8	111
7	PID-Shaped Reset Control Systems	113
7.1	Introduction	114
7.2	Problem Statement via Illustrative Example	114
7.3	Analysis and Design of Shaped Reset Control Systems	115

7.4	Case Study: Design of PID-Shaping Filter in CI-Based Reset Systems	117
7.4.1	Design Procedure for the PID Shaping Filter	118
7.4.2	Limit Cycles Elimination of the PID Shaping Filter	121
7.5	Results: Improved Performance of the PID-Shaped Reset Control System	122
7.5.1	Simulation Results: Enhanced Steady-State Performance	123
7.5.2	Experimental Results: Improved Tracking Precision	124
7.5.3	Experimental Results: Enhanced Disturbance and Noise Rejection	125
7.5.4	Experimental Results: Eliminated Limit Cycles	127
7.6	Conclusion and Discussions	129
	Appendix	131
7.A	Proof of Lemma 5	131
7.B	Proof of Theorem 9	133
8	A Fixed-Phase Reset Control System	135
8.1	Introduction	136
8.2	New Reset Element: Fixed-Phase Reset Control (FPRC).	137
8.2.1	The Definition of the Fixed-Phase Reset Control	137
8.2.2	Fixed-Phase Reset Control Elements	137
8.3	The Frequency-domain Analysis of the FPRC.	138
8.3.1	The Open-loop HOSIDF for FPRC systems	138
8.4	Results	142
8.4.1	Validation of the Accuracy of the HOSIDF	142
8.4.2	Frequency-domain Properties of the FPRC	144
8.5	Conclusion	146
9	Conclusions and Recommendations	149
9.1	Conclusions	150
9.2	Concluding Remarks	151
9.3	Discussions and Future Recommendations	153
	Acknowledgments	155
	Curriculum Vitæ	157
	List of Publications	159

Summary

This dissertation focuses on the frequency response analysis and design of Linear Time-Invariant systems (LTI) reset feedback control systems for precision motion applications. In the precision motion industry, there is a growing demand for control systems that deliver higher positioning resolution, faster response, and enhanced stability. However, inherent limitations in linear controllers, such as the “waterbed effect” and the Bode phase-gain trade-off, limit their performance, posing challenges in meeting these evolving requirements.

Reset feedback control has emerged as an effective solution to address the limitations of linear control systems in precision motion applications. The practical implementation of control strategies relies on reliable analysis methods. Among these, frequency response analysis stands out as an effective and widely utilized method across industries. However, existing frequency response analysis methods for both open-loop and closed-loop reset control systems face challenges, including accuracy limitations and restrictions to specific control system structures. The first category of contributions in this dissertation addresses these challenges by introducing frequency response analysis methods for open-loop and closed-loop Single-Input and Single-Output (SISO) LTI reset control systems within a generalized control system structure. Moreover, to further realize the potential of reset control, the second category of contributions focuses on proposing novel reset control designs to enhance system performance. The content is organized into nine chapters.

The first topic of this dissertation centers on the development of frequency response analysis methods for both open-loop and closed-loop SISO LTI reset control systems. First, in Chapter 2, the Higher-Order Sinusoidal Input Describing Function (HOSIDF) for open-loop reset systems within a generalized control system structure, is developed. Simulation results validate the accuracy of the proposed HOSIDF. The HOSIDF offers an analytical decomposition of the system’s response into linear and nonlinear components, forming a critical foundation for subsequent closed-loop analysis.

Before conducting frequency response analysis for closed-loop systems, Chapter 3 introduces a two-reset condition. This condition identifies scenarios under which the Sinusoidal-Input Describing Function (SIDF) provides reliable analysis for closed-loop systems. Simulation and experimental results validate the effectiveness of the proposed approach. Additionally, the method demonstrates measurable time-saving benefits compared to time-domain simulations.

Building on this foundation, Chapter 4 develops HOSIDFs for SISO closed-loop reset systems operating under the two-reset condition. Simulation and experimental results on a precision motion stage confirm the accuracy of the closed-loop HOSIDFs. Together, the open-loop and closed-loop HOSIDF analyses presented in Chapters 2 through 4 address the lack of frequency response analysis methods for generalized reset control structures. Moreover, the proposed HOSIDFs establish a frequency-domain connection between open-

loop and closed-loop reset systems, enabling the application of loop-shaping techniques to reset feedback control design.

To provide a practical and user-friendly platform for engineers to design reset control systems effectively, the frequency response analysis methods presented in Chapters 2 to 4 are integrated into a MATLAB application (app), as detailed in Chapter 5. Then, an illustrative case study is presented to demonstrate the application of the app. The case study, conducted on a precision motion stage, achieves a 21.4% reduction in maximum steady-state error and requires 85.6% less maximum actuation force compared to previous reset systems, underscoring the app's effectiveness in designing reset systems with enhanced performance.

The second topic of this dissertation focuses on reset control design aimed at enhancing steady-state and transient performance in precision motion systems. Reset control inherently introduces both first-order and high-order harmonics. The proposed designs optimize these harmonics to improve system performance.

The first design, presented in Chapter 6, utilizes a phase lead element to fine-tune the phase of the reset instants. This approach enhances the phase and gain benefits of first-order harmonics while preserving the properties of high-order harmonics. Case studies are conducted through experiments on a precision motion stage. In a representative case study, zero overshoot is achieved by leveraging phase improvements, compared to 36.0% overshoot with previous reset control and 64.0% overshoot with linear control. In another illustrative case study, with enhancements in gain, a 37.5% improvement in steady-state precision is achieved compared to previous reset control.

The second design, detailed in Chapter 7, incorporates a PID shaping filter to refine the reset action. This approach effectively reduces the detrimental high-order harmonics while preserving the benefits of the first-order harmonics, leading to improved steady-state precision. A representative case study demonstrates a 51.8% improvement in steady-state precision compared to the previous reset control. Additionally, limit cycles in the step response of the reset control system are eliminated.

Current reset controllers typically use the zero-crossings of filtered feedback error signals as reset instants. To broaden the application scope of reset control, Chapter 8 introduces a novel reset element: Fixed-Phase Reset Control (FPRC). The FPRC distributes reset instants based on a predefined signal. HOSIDFs are developed to analyze the frequency properties of the FPRC, and their validity is confirmed through simulations. While the FPRC offers phase lead advantages over previous reset control, it introduces higher-order harmonics. Further research is needed to explore its practical implementation.

Finally, Chapter 9 summarizes the key contributions of this thesis, including the development of frequency response analysis methods for both open-loop and closed-loop SISO reset feedback control systems, along with the proposal of advanced reset control designs that enhance the transient and steady-state performance of precision motion systems. Additionally, the chapter provides general concluding remarks and recommendations for future research, based on the insights and limitations identified throughout this thesis.

Samenvatting

Dit proefschrift richt zich op de frequentieresponsanalyse en het ontwerp van lineaire tijd-invariante reset feedback regelsystemen voor precisiebewegingstoepassingen. In de precisiebewegingsindustrie is er een groeiende vraag naar regelsystemen die een hogere positioneringsresolutie, snellere respons en verbeterde stabiliteit bieden. De inherente beperkingen van lineaire regelingen, zoals het "waterbed-effect" en de Bode fase-amplitude compensatie, beperken echter hun prestaties, wat uitdagingen met zich meebrengt bij het voldoen aan deze veranderende vereisten.

Reset feedbackregeling is naar voren gekomen als een effectieve methode om de beperkingen van lineaire regelsystemen in precisiebewegingstoepassingen aan te pakken. De praktische implementatie van regelstrategieën steunt op betrouwbare analysemethoden. Van deze methoden steekt frequentieresponsanalyse eruit als een effectieve en veelgebruikte techniek in verschillende industrieën. Echter, bestaande frequentieresponsanalysemethoden voor zowel open-lus als gesloten-lus resetregelsystemen kampen met uitdagingen, waaronder nauwkeurigheidsbeperkingen en restricties tot specifieke regelsysteemstructuren. De eerste categorie bijdragen in dit proefschrift behandelt deze uitdagingen door frequentieresponsanalysemethoden in te voeren voor open-lus en gesloten-lus Single-Input en Single-Output (SISO) lineaire tijd-invariante (LTI) resetregelsystemen binnen een gegeneraliseerd regelsysteemstructuur. Bovendien richt de tweede categorie bijdragen zich op het voorstellen van nieuwe resetregelontwerpen om de systeemprestaties verder te verbeteren en het potentieel van resetregeling te benutten. De inhoud is georganiseerd in negen hoofdstukken.

Het eerste onderwerp van dit proefschrift concentreert zich op de ontwikkeling van frequentieresponsanalysemethoden voor zowel open-lus als gesloten-lus SISO LTI resetregelsystemen. Eerst wordt in Hoofdstuk 2 de Higher-Order Sinusoidal Input Describing Function (HOSIDF) voor open-lus resetregelsystemen binnen een gegeneraliseerd regelsysteemstructuur ontwikkeld. Simulatie-resultaten bevestigen de nauwkeurigheid van de voorgestelde HOSIDF. De HOSIDF biedt een analytische dekompositie van de respons van het systeem in lineaire en niet-lineaire componenten, wat een cruciale basis vormt voor de daaropvolgende gesloten-lus analyse.

Voordat frequentieresponsanalyse voor gesloten-lus systemen wordt uitgevoerd, introduceert Hoofdstuk 3 een twee-resetvoorwaarde. Deze voorwaarde identificeert scenario's waarbij de Sinusoidal-Input Describing Function (SIDF) een betrouwbare analyse voor gesloten-lus systemen biedt. Simulatie- en experimentele resultaten bevestigen de effectiviteit van de voorgestelde aanpak. Bovendien toont de methode meetbare tijdsbesparingen aan in vergelijking met tijdsdomeinsimulaties.

Gebouwd op deze basis, ontwikkelt Hoofdstuk 4 HOSIDF's voor SISO gesloten-lus resetregelsystemen die werken onder de twee-resetvoorwaarde. Simulatie- en experimentele resultaten op een precisiebewegingsmechanisme bevestigen de nauwkeurigheid van de gesloten-lus HOSIDF's. Samen adresseren de open-lus en gesloten-lus HOSIDF-

analyses, gepresenteerd in de hoofdstukken 2 tot 4, het gebrek aan frequentierespons analyse hulpmiddelen voor gegeneraliseerde resetregelstructuren. Bovendien leggen de voorgestelde HOSIDF's een frequentiedomeinverbinding vast tussen open-lus en gesloten-lus resetregelsystemen, waardoor de toepassing van loop-shapingtechnieken op resetfeedbackregelontwerpen mogelijk wordt.

Om een praktisch en gebruiksvriendelijk platform te bieden voor ingenieurs om resetregelsystemen effectief te ontwerpen, worden de frequentieresponsanalysehulpmiddelen gepresenteerd in Hoofdstukken 2 tot 4 geïntegreerd in een MATLAB-app, zoals gedetailleerd in Hoofdstuk 5. Vervolgens wordt een illustratieve casestudy gepresenteerd om de toepassing van de app te demonstreren. De casestudy, uitgevoerd op een precisiebewegingsmechanisme, realiseert een vermindering van 21,4% in de maximale stationaire fout en vereist 85,6% minder maximale actuatiekracht in vergelijking met eerdere resetsystemen. Dit onderstreept de effectiviteit van de app bij het ontwerpen van resetsystemen met verbeterde prestaties.

Het tweede onderwerp van dit proefschrift richt zich op het ontwerp van resetregeling met als doel de steady-state en transiënte prestaties in precisiebewegingssystemen te verbeteren. Resetregeling introduceert inherent zowel eerste-orde als hogere-orde harmonischen. De voorgestelde ontwerpen optimaliseren deze harmonischen om de systeemprestaties te verbeteren.

Het eerste ontwerp, gepresenteerd in Hoofdstuk 6, maakt gebruik van een fase voor-sprong element om de fase van de resetmomenten fijn af te stemmen. Deze benadering verbetert de fase- en versterkingsvoordelen van eerste-orde harmonischen, terwijl de eigenschappen van hogere-orde harmonischen behouden blijven. Case studies worden uitgevoerd door middel van experimenten op een precisiebewegingsmechanisme. In een representatieve casestudy wordt zero overshoot behaald door gebruik te maken van faseverbeteringen, in vergelijking met 36,0% overshoot bij eerdere resetregeling en 64,0% overshoot bij lineaire regeling. In een andere illustratieve casestudy wordt, door verbeteringen in de amplitude, een verbetering van 37,5% in de steady-state precisie bereikt in vergelijking met eerdere resetregeling.

Het tweede ontwerp, gedetailleerd in Hoofdstuk 7, maakt gebruik van een PID vormgevings filter om de resetactie te verfijnen. Deze aanpak vermindert effectief de schadelijke hogere-orde harmonischen terwijl de voordelen van de eerste-orde harmonischen behouden blijven, wat leidt tot een verbeterde steady-state precisie. Een representatieve casestudy toont een verbetering van 51,8% in de steady-state precisie ten opzichte van de vorige resetregeling. Bovendien worden de limietcycli in de staprespons van het resetregelsysteem geëlimineerd.

Huidige resetregelaars gebruiken doorgaans de nuldoorgangen van gefilterde feedbackfoutsignalen als resetmomenten. Om het toepassingsbereik van resetregeling te verbreden, introduceert Hoofdstuk 8 een nieuw resetelement: Fixed-Phase Reset Control (FPRC). De FPRC verdeelt resetmomenten op basis van een vooraf bepaald signaal. HOSIDF's worden ontwikkeld om de frequentie-eigenschappen van de FPRC te analyseren, en de geldigheid wordt bevestigd door middel van simulaties. Hoewel de FPRC voordelen in faselijn biedt ten opzichte van eerdere resetregeling, introduceert het hogere-orde harmonischen. Verder onderzoek is nodig om de praktische implementatie ervan te verkennen.

Ten slotte vat Hoofdstuk 9 de belangrijkste bijdragen van dit proefschrift samen, waaronder de ontwikkeling van frequentieresponsanalyse-methoden voor zowel open-lus als gesloten-lus SISO resetfeedbackregelsystemen, evenals het voorstel van geavanceerde resetregelontwerpen die de transiënt- en steady-state prestaties van precisiebewegingssystemen verbeteren. Daarnaast biedt het hoofdstuk algemene conclusies en aanbevelingen voor toekomstig onderzoek, gebaseerd op de inzichten en beperkingen die gedurende dit proefschrift zijn geïdentificeerd.

1

Introduction

This chapter begins by introducing precision motion control and highlighting the importance of frequency response analysis as a powerful tool for designing high-performance precision motion control systems. It then discusses the inherent limitations of linear controllers and introduces reset control systems as a nonlinear alternative to overcome these challenges. Next, the chapter identifies the motivation and key research problems addressed in this dissertation, focusing on the lack of reliable frequency response analysis methods for reset control systems. Finally, an overview of the dissertation's structure is provided.

In mechatronics industries such as semiconductor manufacturing, robotics, and optical systems, the demands for higher positioning resolution, speed, and stability are continually increasing [1]. For example, in semiconductor manufacturing industries, accurate positioning is crucial for the precise placement of microchip components, where slight precision errors can result in defective circuitry and impaired device functionality [2].

Feedback control, such as the classical Proportional-Integral-Derivative (PID) feedback control, has proven effective in achieving these goals in industries [1, 3]. A typical closed-loop feedback control system is depicted in Fig. 1.1.

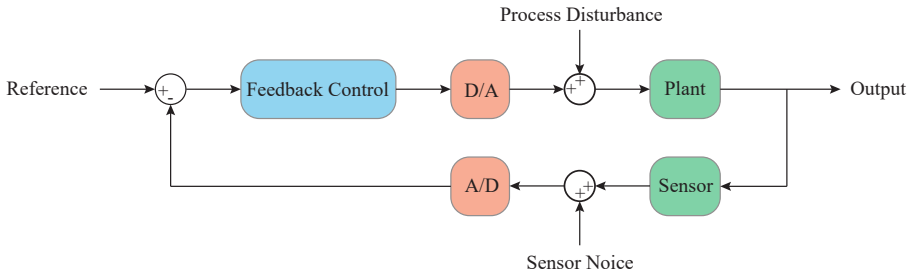


Figure 1.1: Block diagram of a closed-loop feedback control system.

However, inherent limitations of linear controllers, including the Bode gain-phase trade-off and the waterbed effect, limit their ability to meet the growing demands of mechatronics industries. To address these limitations, reset feedback control offers a nonlinear alternative that can break the constraints of linear systems and enhance overall system performance [4–9].

To meet the growing demands for system performance, effective analysis and design methodologies for control systems are essential, with frequency response analysis serving as a powerful tool for this purpose [1, 10]. Frequency response analysis includes both open-loop and closed-loop analyses. By leveraging the connection between these analyses and utilizing the loop-shaping technique [1, 11], control engineers can design control systems in the frequency domain to meet specific time-domain requirements.

Currently, Higher-Order Sinusoidal Input Describing Function (HOSIDF) analysis methods, as developed in [12–15], were employed to analyze open-loop reset feedback control systems. Additionally, a HOSIDF analysis method for closed-loop reset systems was proposed in [13]. However, the applicability of these open-loop and closed-loop HOSIDF analysis methods is constrained to specific reset control structures. To overcome this limitation, this dissertation develops new HOSIDF analysis methods for both open-loop and closed-loop reset feedback control systems within a generalized structure. Additionally, a frequency-domain relationship between open-loop and closed-loop HOSIDFs is established, enabling the application of loop-shaping in reset feedback control systems. Additionally, a MATLAB app has been developed to integrate these HOSIDF analysis methods, enhancing their accessibility for control engineers.

Using frequency-domain analysis methods, this thesis develops strategies to fine-tune the phase and gain characteristics of both first-order and high-order harmonics in reset

control. These advancements improve both transient and steady-state performance in precision motion applications.

1.1 Precision Motion Control

Figure 1.2 shows the experimental setup used in this dissertation, which features a three-degree-of-freedom (3-DoF) precision positioning stage (①). The stage consists of three masses, M_1 , M_2 , and M_3 , each connected to a voice coil actuator labeled A_1 , A_2 , and A_3 . These masses are attached to a central base mass M_c via dual leaf flexures.

The voice coil actuators operate based on electromagnetic principles, where a coil within a magnetic field generates linear motion according to Ampere's Law. These actuators are driven by a linear current source power amplifier (⑤). Position feedback is provided by Mercury M2000 linear encoders (labeled as Enc), which convert linear motion into digital signals with a resolution of 100 nm. To minimize external vibrations from environmental sources, such as machinery or foot traffic, a vibration isolation table (②) is used.

Control systems are implemented on a National Instruments CompactRIO (cRIO) platform (③), a modular embedded system comprising a real-time processor, an FPGA, and interchangeable I/O modules. The real-time processor executes control algorithms and facilitates communication with external devices, while the FPGA enables high-speed parallel processing for real-time signal manipulation and timing-critical operations at a sampling frequency of 10 kHz. The I/O modules handle interfaces for analog and digital signals, ensuring precise control and data acquisition.

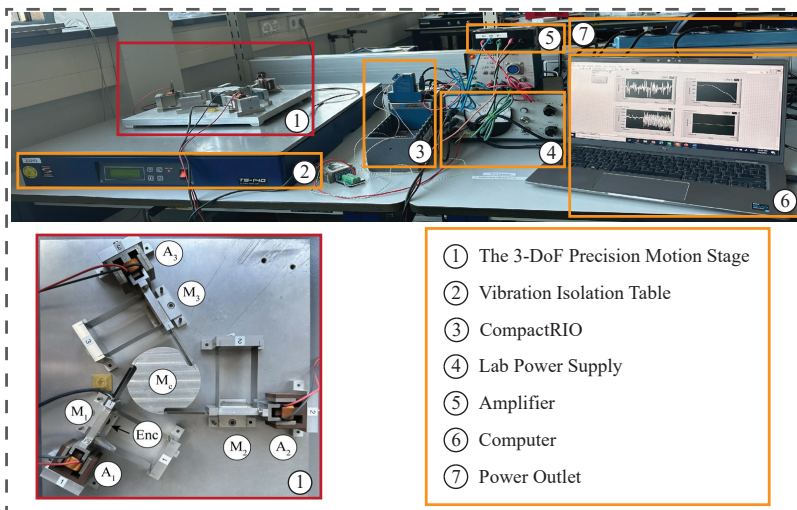


Figure 1.2: Planar precision positioning setup.

In this thesis, the actuator A_1 is used to drive the mass rigidly connected to it. Figure 1.3 shows the measured Frequency Response Function (FRF) of the stage, which exhibits a response characteristic similar to that of a collocated double mass-spring-damper system,

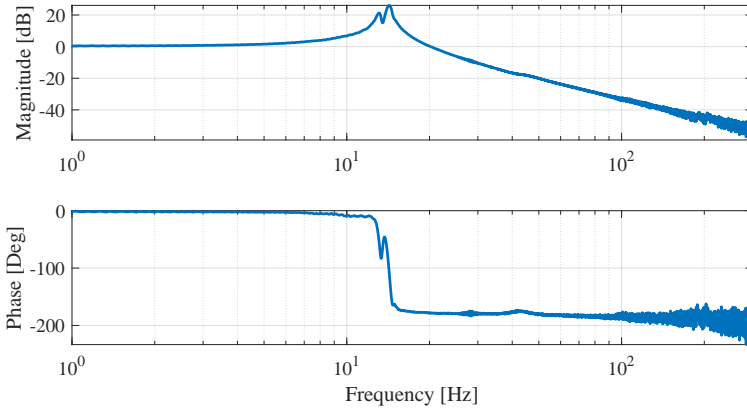


Figure 1.3: The FRF data from actuator A_1 to attached mass M_1 .

along with additional high-frequency parasitic dynamics. Using MATLAB's system identification tools, the system dynamics are modeled as a Linear Time-Invariant (LTI) system, denoted as $\mathcal{P}(s)$, given by

$$\mathcal{P}(s) = \frac{6.615 \times 10^5}{83.57s^2 + 279.4s + 5.837 \times 10^5}. \quad (1.1)$$

This model captures the core behavior of the actuator-mass system and is used to validate the effectiveness of the proposed frequency response analysis methods and the designed reset control systems in this thesis.

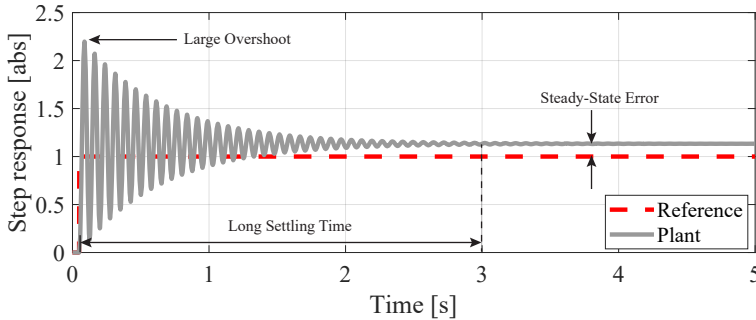


Figure 1.4: Step response of the plant $\mathcal{P}(s)$ (1.1).

The step response of the precision motion stage $\mathcal{P}(s)$ in (1.1) is shown in Fig. 1.4, highlighting two issues: (1) the pronounced oscillations during the transient phase and (2) a steady-state error between the output and the reference signal. The goal of precision motion control is to design controllers that address these issues, including reducing overshoot, shortening response time during transients, and minimizing steady-state errors, while ensuring system stability and robustness. In practice, these challenges are typically

first addressed through feedforward control, which manages predictable inputs and disturbances, and then feedback control is used to correct unanticipated residual errors and deviations [16]. This thesis specifically focuses on feedback control to enhance overall system performance.

1.2 Frequency Response Analysis

To achieve the desired precision motion control performance, effective analysis and design tools for control systems are essential. Frequency response analysis is one of the most widely adopted methods in industrial applications for this purpose [17]. It provides phase and magnitude information of linear time-invariant (LTI) systems by assessing the system's steady-state response to sinusoidal inputs across operating frequencies. Additionally, frequency response analysis allows engineers to predict closed-loop behavior without requiring precise parametric models of the plant. This characteristic is particularly beneficial when obtaining an accurate plant model is challenging or impractical.

The frequency response analysis includes both open-loop and closed-loop analysis, connected through loop-shaping techniques [18]. Based on the loop-shaping connection, control engineers can design controllers in the open loop to ensure control systems meet desired closed-loop performance criteria, such as minimizing steady-state errors and enhancing transient response [19]. By doing so, in precision motion control, maintaining high gain for open-loop control systems at low frequencies ensures steady-state precision, including accurate reference tracking and effective disturbance rejection [20]. Conversely, reducing gain at high frequencies helps enhance robustness against sensor noise and interference [1]. Additionally, ensuring a proper phase margin near the system's bandwidth is essential for stability and transient response [21]. In closed-loop analysis, the modulus margin, or sensitivity margin, indicates robustness, with a higher margin implying greater tolerance to gain variations. The following example uses a linear PID control system to demonstrate the application of open-loop and closed-loop frequency response analysis, along with the loop-shaping technique, in precision motion systems.

Figure 1.5 presents the Bode plot of the plant $\mathcal{P}(s)$ from (1.1) (in gray). A PID controller $\mathcal{C}(s)$ is designed for this plant, structured as follows:

$$\text{PID} = k_p \cdot \left(1 + \frac{\omega_i}{s}\right) \cdot \left(\frac{s/\omega_d + 1}{s/\omega_t + 1}\right). \quad (1.2)$$

Then, the sensitivity function of the closed-loop PID control system is given by:

$$\mathcal{S}(s) = \frac{1}{1 + \mathcal{C}(s)\mathcal{P}(s)}. \quad (1.3)$$

The Bode plots of the open-loop transfer function $\mathcal{C}(s)\mathcal{P}(s)$ (in blue) and the closed-loop sensitivity function $\mathcal{S}(s)$ (in black) are shown in Fig. 1.5. The open-loop transfer function is designed with a phase margin of 50 degrees and a crossover frequency of 100 Hz. The phase margin ensures system stability and contributes to improved transient response. The high gain below 100 Hz enhances precise reference tracking and disturbance rejection, while the low gain above 100 Hz effectively mitigates noise, improving noise rejection. Additionally, the maximum sensitivity gain in the closed-loop Bode plot indicates

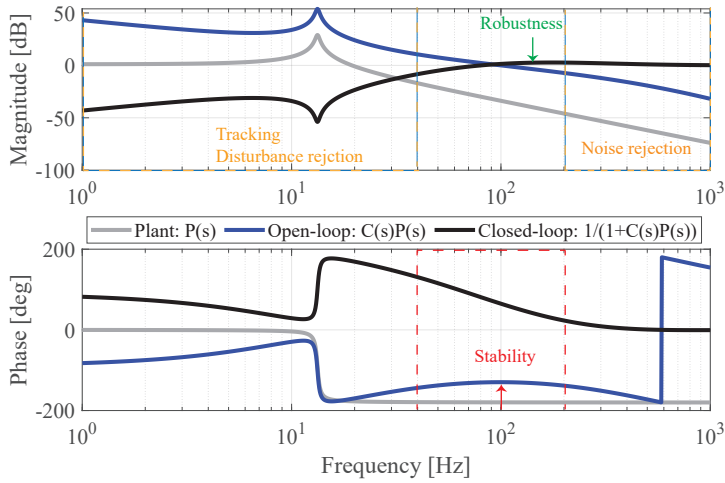


Figure 1.5: Bode plots of the plant $\mathcal{P}(s)$, the open-loop control system $C(s)\mathcal{P}(s)$, and closed-loop system $1/(1+C(s)\mathcal{P}(s))$.

the system's robustness, highlighting its ability to handle disturbances and noise while maintaining stability and performance across a wide frequency range.

Figure 1.6 compares the step responses of the plant $\mathcal{P}(s)$ and the closed-loop system. The designed PID controller effectively reduces overshoot, settling time, and steady-state error, improving upon the plant's open-loop response, as shown in Figure 1.4. This example demonstrates that designing control systems to meet frequency-domain requirements can effectively ensure the desired time-domain steady-state and transient responses.

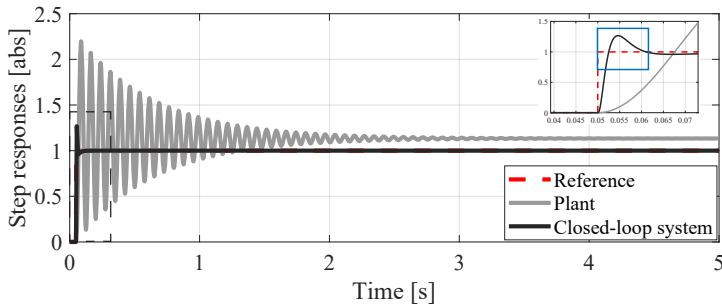


Figure 1.6: Step responses of the plant and the closed-loop control system.

1.3 Limitations of Linear Feedback Control

In spite of the widely recognized effectiveness of linear feedback control, its performance is constrained by two fundamental limitations: the waterbed effect and the Bode gain-phase relationship, as illustrated below.

1.3.1 Waterbed Effect

For a Linear Time-Invariant systems (LTI) that has at least two more poles than zeros and no poles in the right half-plane (i.e., it is stable), the integral of the sensitivity function of the closed-loop control system meets the following condition:

$$\int_0^{\infty} \ln(|\mathcal{S}(j\omega)|) d\omega = 0. \quad (1.4)$$

Equation (1.4) implies that any reduction in sensitivity (improvement in performance) over some frequency range must be compensated by an increase in sensitivity over another frequency range. This is the well-known waterbed effect phenomenon [22].

1.3.2 Bode Phase-Gain Trade-Off

Moreover, minimum-phase linear systems are subject to the Bode phase-gain trade-off, as illustrated below using the Proportional-Integrator (PI) and Derivative (D) elements, with transfer functions defined as follows:

$$\text{PI} = 1 + \frac{\omega_i}{s}, \quad \text{D} = \frac{s/\omega_d + 1}{s/\omega_t + 1}, \quad (1.5)$$

where $\omega_i = k_i \cdot \omega_c$, $\omega_d = \omega_c/a$, $\omega_t = \omega_c \cdot a$, $k_i \in \mathbb{R}$, $a \in \mathbb{R}^+$, $\omega_c \in \mathbb{R}^+$. In the example, we choose $\omega_c = 20\pi$ [rad/s].

The PI element is used to achieve high gain at low frequencies, thereby reducing steady-state errors. As shown in Fig. 1.7(a), increasing the k_i value enhances the integrator's low-frequency gain but reduces the phase margin. In the time domain, while this improves steady-state precision, it can adversely affect system stability and transient performance.

The D control element is used to introduce phase lead, thereby improving transient response and ensuring stability. As shown in Fig. 1.7(b), increasing the a value in (1.5) enhances the phase lead but reduces low-frequency gain. In the time domain, while this improves system stability and transient response, it limits the system's ability to track low-frequency references and reject low-frequency disturbances.

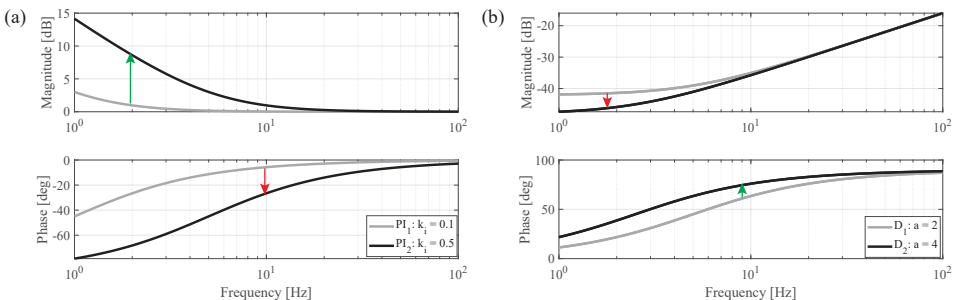


Figure 1.7: (a) Bode plots of PI controllers with different k_i values. (b) Bode plots of D controllers with different a values.

To summarize, both the waterbed effect and the Bode phase-gain trade-off highlight the inherent performance limitations of linear control systems: enhancing performance

in one frequency band often compromises it in others, limiting the controller's ability to optimize performance across the entire frequency spectrum. Specifically, improving steady-state performance by increasing integral action introduces phase lag, which can result in slower rise times and higher overshoot in the transient response. Conversely, increasing transient performance can degrade steady-state performance.

Therefore, while linear controllers, such as the PID, achieve notable improvements in system performance, as demonstrated in Fig. 1.6, they encounter fundamental trade-offs that constrain their ability to satisfy the growing demands for faster and more precise control in high-precision mechatronic applications. Consequently, nonlinear control strategies that surpass the performance limitations of linear controllers are required.

1.4 Reset Feedback Control System: Overcome Linear Limitations

Nonlinear control strategies, such as reset controllers, variable-gain control, split-path nonlinear integrals, and hybrid integrator-gain control, have shown promise in addressing the limitations of linear systems, offering improved performance across diverse industries including chemical process control, teleoperation, and mechatronic systems [5, 7, 23–33]. This thesis focuses on applying reset feedback control in high-precision mechatronic systems. The following subsection provides an overview of reset control, covering its definition, stability and convergence conditions, and commonly used reset elements.

1.4.1 Definition of Reset Control Systems

Figure 1.8 illustrates the block diagram of a generalized reset control system. In this configuration, the signals $r(t)$, $e(t)$, $u(t)$, $d(t)$, $n(t)$, and $y(t)$ correspond to the reference, error, control input, disturbance, noise, and output signals, respectively. The reset controller C_r processes the input signal $z(t)$ to generate the output signal $m(t)$. The reset-triggered signal $z_s(t)$ is obtained by passing $z(t)$ through the LTI shaping filter C_s . Systems C_1 , C_2 , and C_3 are LTI controllers integrated into the feed-through loop that leads to the output signal $y(t)$. The LTI controller C_4 is positioned within the feedback loop, and the plant is denoted by \mathcal{P} .

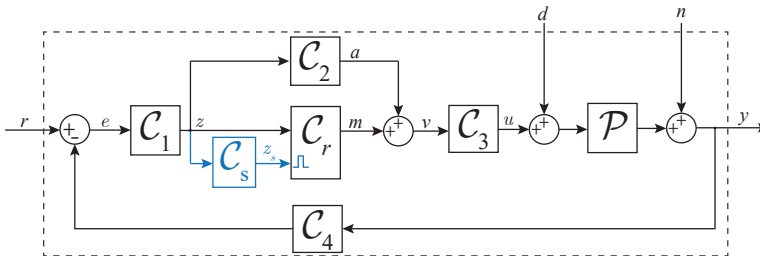


Figure 1.8: Block diagram of the generalized reset control system, with the resetting action denoted by blue lines.

The reset controller C_r is a hybrid system that combines a linear controller with a reset mechanism [33, 34]. The state-space representation of a reset controller, with state

$x_c(t) \in \mathbb{R}^{n_c \times 1}$, input $z(t)$, and output $m(t)$, is given by:

$$\mathcal{C}_r = \begin{cases} \dot{x}_c(t) = A_R x_c(t) + B_R z(t), & t \notin J, \\ x_c(t^+) = A_\rho x_c(t), & t \in J, \\ m(t) = C_R x_c(t) + D_R z(t), \end{cases} \quad (1.6)$$

where matrices $A_R \in \mathbb{R}^{n_c \times n_c}$, $B_R \in \mathbb{R}^{n_c \times 1}$, $C_R \in \mathbb{R}^{1 \times n_c}$, and $D_R \in \mathbb{R}^{1 \times 1}$ define the flow dynamics of the reset controller \mathcal{C}_r , referred to as its Base-Linear Controller (BLC) \mathcal{C}_l , whose transfer function is given by:

$$C_l(\omega) = C_R(j\omega I - A_R)^{-1} B_R + D_R, \quad (1.7)$$

where $\omega \in \mathbb{R}^+$ represents the angular frequency. By replacing \mathcal{C}_r with \mathcal{C}_l (1.7), the system in Fig. 1.8 is termed its Base-Linear System (BLS).

The reset controller \mathcal{C}_r (1.6) in this thesis employs the zero-crossing resetting law as its reset mechanism [33], where the state $x_c(t)$ is reset to $x_c(t^+)$ at the zero-crossings of the reset trigger signal $z_s(t)$. The signal $z_s(t)$ is obtained by filtering the reset control input signal $z(t)$ through the LTI system $\mathcal{C}_s(s)$, expressed as

$$\begin{cases} \dot{x}_s(t) = A_s x_s(t) + B_s z(t), \\ z_s(t) = C_s x_s(t) + D_s z(t), \end{cases}$$

where state-space matrices A_s , B_s , C_s , and D_s describe the LTI system $\mathcal{C}_s(s)$ and $x_s(t)$ represents the state vector of $\mathcal{C}_s(s)$. The set of reset instants is defined as $J = \{t_i \mid z_s(t_i) = 0, i \in \mathbb{N}\}$. At each reset instant $t_i \in J$, the jump dynamics of \mathcal{C}_r are determined by the reset matrix A_ρ , given by

$$A_\rho = \begin{bmatrix} \gamma & \\ & I_{n_c-1} \end{bmatrix} \in \mathbb{R}^{n_c \times n_c}, \quad \gamma \in (-1, 1]. \quad (1.8)$$

The matrix A_ρ in (1.8) defines on reset controllers with a single reset state. Common examples of such controllers include the CI, First-Order Reset Element (FORE), and Second-Order Single State Reset Element (SOSRE) [35]. When $\gamma = 1$ and thus $A_\rho = I_{n_c}$ in (1.8), the reset controller \mathcal{C}_r is identical to \mathcal{C}_l in (1.7).

1.4.2 Stability and Convergence Conditions for Reset Control Systems

Although stability and convergence conditions are not the primary focus of this dissertation, they are needed for frequency response analysis [36, 37]. Following established literature [24, 33, 38–40], we adopt Assumptions 1 and 2 to ensure the stability and convergence conditions for open-loop and closed-loop reset systems, respectively.

The literature [24] demonstrates that the reset controller defined in (1.6), when subjected to an input $z(t) = |Z| \sin(\omega t + \angle Z)$, where $|Z|$ and $\angle Z$ denote the magnitude and phase of the signal $z(t)$ respectively, exhibits a globally asymptotically stable $2\pi/\omega$ -periodic solution and converges globally if and only if:

$$|\lambda(A_\rho e^{A_R \delta})| < 1, \quad \forall \delta \in \mathbb{R}^+, \quad (1.9)$$

where $\lambda(\cdot)$ represents the eigenvalues of the matrix.

To ensure the HOSIDF analysis for open-loop reset control systems, the following assumption is introduced:

Assumption 1. The reset controller C_r (1.6), with an input $z(t) = |Z| \sin(\omega t + \angle Z)$, is assumed to satisfy the condition in (1.9). The LTI systems C_1, C_2, C_3, C_4 , and C_s are Hurwitz.

For a closed-loop reset control system, to ensure that the frequency response is well-defined, the following assumption is made:

Assumption 2. The closed-loop reset control system is asymptotically stable in the absence of inputs, bounded-input bounded-output (BIBO) stable, and exponentially convergent. The reset controller C_r in (1.6) has zero initial conditions, i.e., $x_c(0) = 0$. Furthermore, there exist infinitely many reset instants t_i such that $\lim_{i \rightarrow \infty} t_i = \infty$, and the system does not exhibit Zeno behavior.

The stability and convergence conditions required to satisfy Assumption 2 have been extensively studied in the literature, including the H_β condition discussed in [38, 41] and other criteria presented in [40]. Additionally, this assumption can be ensured through appropriate design considerations, as detailed in [13, 33, 42].

For a closed-loop reset control system subjected to a sinusoidal input signal with frequency ω , satisfying Assumption 2, the system exhibits a periodic steady-state response. This response can be expressed as $x(t) = \mathcal{S}(\sin(\omega t), \cos(\omega t), \omega)$ for some function $\mathcal{S} : \mathbb{R}^3 \rightarrow \mathbb{R}^{n_{cl}}$ [40], where n_{cl} denotes the number of states in the closed-loop reset system.

Hybrid systems may encounter the Zeno phenomenon, where infinitely many actions occur within a finite time span [43]. According to research [44], the outputs of a reset system are Zeno-free (non-Zeno) if the reset time interval $\sigma_i = t_{i+1} - t_i$, $i \in \mathbb{Z}^+$ between any two consecutive reset instants (t_i, t_{i+1}) is lower bounded:

$$\sigma_i > \sigma_{\min}, \quad \sigma_{\min} \in \mathbb{R}^+, \quad (1.10)$$

at least in some working domain Ω [44].

1.4.3 Reset Elements

Reset control originates from the Clegg Integrator (CI). The CI builds upon a linear integrator by incorporating a reset mechanism, introduced by Clegg in 1958 [45]. A linear integrator accumulates system errors over time and contributes to the control signal to minimize steady-state error. However, this cumulative action creates a memory effect, where even if the current error becomes zero or small, the integrator may still output a non-zero value due to past accumulated errors. This behavior can lead to overshoot and stability issues. The CI addresses this challenge by implementing the zero-crossing resetting law [33], which resets the integrator's output to zero whenever the input signal crosses zero.

The CI

The matrices for the generalized CI are given by:

$$A_R = 0, B_R = 1, C_R = 1, D_R = 0, A_\rho = \gamma \in (-1, 1), \quad (1.11)$$

Sinusoidal-Input Describing Function (SIDF) analysis [24] reveals that the first-order harmonic of the CI with $\gamma = 0$ introduces a phase lead of 51.9° , while maintaining the gain characteristics of a linear integrator, as shown in Fig. 1.9. The phase-gain characteristic of

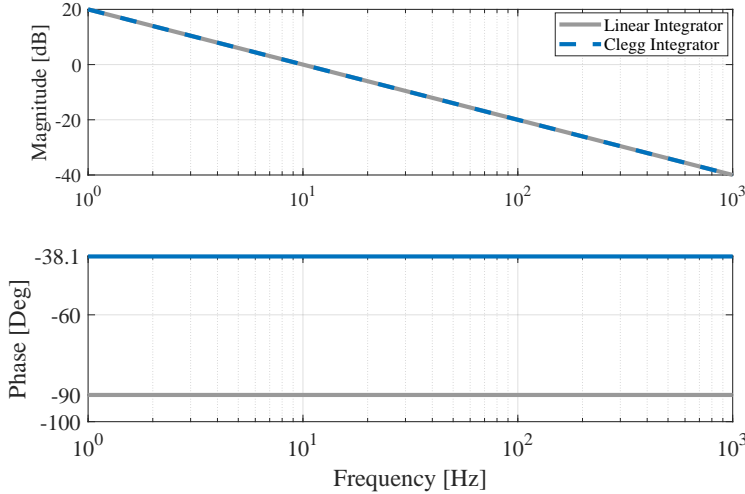


Figure 1.9: Bode plots of the the linear integrator and the first-order harmonic of the CI.

CI illustrates the ability of reset control to surpass the Bode gain-phase limitation inherent in linear controllers [22].

The FORE and SORE

Since then, flourish reset elements have been developed, including the First-order Reset Element (FORE) and the Second-order Reset Element (SORE).

The state-space matrices of the FORE [46, 47] are defined as

$$A_R = -\omega_r, B_R = \omega_r, C_R = 1, D_R = 0, A_\rho = \gamma. \quad (1.12)$$

The state-space matrices of the SORE [48] are defined as

$$A_R = \begin{bmatrix} -2\beta\omega_r & -\omega_r^2 \\ 1 & 0 \end{bmatrix}, B_R = \begin{bmatrix} 1 \\ 0 \end{bmatrix}, C_R = \begin{bmatrix} 0 & \omega_r^2 \end{bmatrix}, D_R = 0, A_\rho = \begin{bmatrix} \gamma & 0 \\ 0 & 1 \end{bmatrix}. \quad (1.13)$$

Other reset elements also add flexibility to control design, including partial reset techniques [38], Proportional-Integral (PI) + CI [49], reset control systems with reset bands [50], Fractional-order Reset Element (FrORE) [51–53], and Constant in gain Lead in phase (CgLp) [25].

Compared to linear control systems, reset control systems can be designed to exhibit phase lead while preserving gain characteristics, or maintain phase margin while improving gain properties. By leveraging the gain-phase advantages, reset elements have shown improvements in both steady-state and transient performance in mechatronics applications, including enhanced disturbance rejection, improved tracking, and reduced overshoot [5, 7, 25, 32, 54–57].

1.5 Motivation and Research Problem Statement

Reset elements have demonstrated potential in enhancing system performance compared to linear systems. To fully realize this potential, as discussed in Section 1.2, effective frequency response analysis tools are essential. However, three main challenges exist in the frequency response analysis of reset control systems.

1. In frequency response analysis of open-loop reset feedback control systems, the Higher-Order Sinusoidal Input Describing Function (HOSIDF) analysis methods, as introduced in [12–14], are utilized. The HOSIDF analysis aligns with the SIDF analysis when higher-order harmonics (beyond the first-order) are negligible [24]. However, the applicability of existing HOSIDF methods is restricted to specific configurations. For instance, no precise analysis tools are available for systems like the one depicted in Fig. 1.8 when the reset-triggering signal $z_s(t)$ differs from the input signal $z(t)$ to the reset controller. Therefore, an accurate open-loop HOSIDF analysis method for the generalized reset control systems presented in Fig. 1.8, as introduced in this thesis, is necessary.
2. In addition to open-loop analysis, closed-loop frequency response analysis is crucial for designing reset control systems and applying loop-shaping techniques. In linear systems, the sensitivity function $\mathcal{S}(s)$ in (1.3) connects the open-loop and closed-loop systems. Furthermore, the sensitivity function evaluates steady-state errors and the modulus margin, which indicates the system's robustness to variations in gain within the control loop [1]. However, this loop connection is not valid in reset control due to the cross-effects between first-order and high-order harmonics within the closed-loop. In [13], a HOSIDF method was introduced for closed-loop reset systems, establishing a connection between open-loop and closed-loop analyses. However, this approach neglected the effects of reset actions on high-order harmonics within the feedback loop, leading to inaccuracies. Additionally, no established frequency response analysis methods currently exist for the generalized closed-loop reset control systems as depicted in Fig. 1.8. Therefore, a reliable closed-loop HOSIDF method is required for this system, coupled with frequency-domain connections to the open-loop HOSIDF. This combination will facilitate the application of loop-shaping techniques, enabling more effective design and optimization of reset control systems.
3. Additionally, in the sinusoidal-input frequency response analysis of closed-loop systems, two scenarios can arise: two-reset control systems, where the system experiences two resets per steady-state cycle, and multiple-reset control systems, where more than two resets occur per cycle. Current closed-loop SIDF analysis methods for reset control systems typically assume the system operates with two resets per cycle [13, 15]. This assumption will lead to deviations in SIDF analysis for multiple-reset systems. Moreover, multiple-reset actions introduce high-order harmonics, which, when excessive, can degrade system performance and should be avoided [58]. Thus, before performing closed-loop SIDF analysis, it is necessary to develop a method to identify whether the system is a two-reset or multiple-reset system. Ensuring a two-reset system guarantees the reliability of the closed-loop SIDF analysis.

Motivated by the limitations in open-loop and closed-loop frequency response analysis for reset feedback control systems, this dissertation aims to address the following research problems:

- First, to develop an accurate open-loop HOSIDF analysis method for the reset control systems in Fig. 1.8.
- Second, to propose a method to identify the two-reset condition for sinusoidal-input reset control systems. By applying this method, the reliability of the closed-loop SIDF analysis for reset control systems can be ensured.
- Third, to develop closed-loop HOSIDF for the reset control systems in Fig. 1.8, including the formulation of sensitivity functions, complementary sensitivity functions, and control sensitivity functions for each harmonic in closed-loop reset control systems. Moreover, to establish a frequency-domain link between open-loop and closed-loop HOSIDFs.

Furthermore, motivated by the performance improvements of reset control in precision motion systems compared to linear control, this dissertation explores methods to further enhance reset control performance by improving the gain and phase properties of both first-order and high-order harmonics. Enhancing the gain of first-order harmonics and mitigating the negative impact of high-order harmonics improves steady-state performance, such as tracking precision and noise and disturbance rejection. Additionally, improving the phase margin results in better transient performance, including reduced overshoot and shorter settling times.

1.6 Thesis Outline

This dissertation contributes to two main areas of reset feedback control systems with applications to precision motion systems, as outlined below.

1. Development of Frequency Response Analysis Tools for Reset feedback Control Systems:

- Chapter 2: Developing frequency response analysis method for open-loop reset feedback control systems.
- Chapter 3: Proposing two-reset conditions for ensuring the reliability of sinusoidal-input Describing Function analysis of closed-loop reset feedback control systems.
- Chapter 4: Developing a frequency response analysis method for closed-loop reset control systems and establishing a connection with open-loop analysis.
- Chapter 5: Developing a MATLAB app that consolidates the analysis methods presented in Chapters 2 to 4, providing an intuitive interface for control engineers to utilize these methods effectively.

2. Design Reset Control Systems for Improved Performance on Precision Motion Stage Using Frequency Response Analysis Methods:

- Chapter 6: The development of a phase lead element-shaped reset control to provide phase lead or enhanced gain performance of the first-order harmonic, while maintaining high-order harmonics, compared to previous reset control. The phase lead benefit improves the system's transient performance, while the gain enhancement improves steady-state performance.
- Chapter 7: The development of a PID-shaped reset control aimed at improving steady-state precision by reducing high-order harmonics, while maintaining the first-order harmonic in reset control systems. Additionally, this method addresses the limit cycle issues in the step responses of reset systems.

The reset elements discussed in Chapters 2 to 6 use filtered feedback error signals as their reset-triggered signals. In contrast, Chapter 8 introduces a predefined reset-triggered signal that distributes different reset instances within one period. This proposed reset element is referred to as Fixed-Phase Reset Control (FPRC). Additionally, the chapter develops frequency response analysis methods for the FPRC element. The FPRC shows phase lead benefits but introduces higher-order harmonics compared to previous reset control. The further application of the FPRC requires future exploration.

An overview of the main contributions from Chapter 2 to Chapter 8 in this dissertation is provided in Fig. 1.10. Finally, the conclusions of this thesis and future recommendations are presented in Chapter 9.

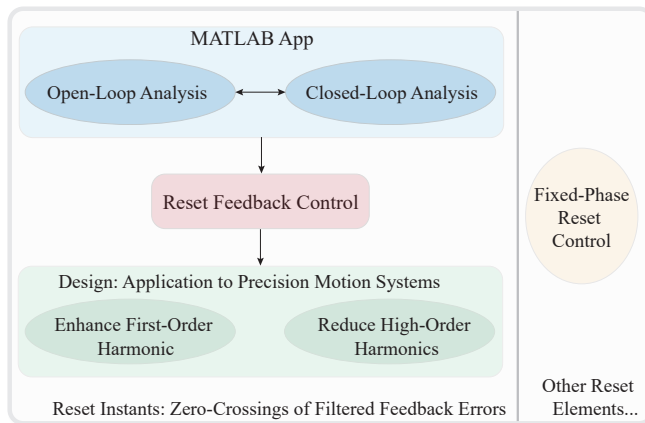


Figure 1.10: Overview of the main contributions in this dissertation.

Bibliography

- [1] R. M. Schmidt, G. Schitter, and A. Rankers. *The design of high performance mechatronics: high-Tech functionality by multidisciplinary system integration*. Ios Press, 2020.
- [2] J. Wu, G. Chen, and F. Chen. “Positioning accuracy control of dual-axis dicing saw for machining semiconductor chip”. In: *The International Journal of Advanced Manufacturing Technology* 109.7 (2020), pp. 2299–2310.
- [3] M. A. Johnson and M. H. Moradi. *PID control*. Springer, 2005.
- [4] Y. Zheng, Y. Chait, C. Hollot, M. Steinbuch, and M. Norg. “Experimental demonstration of reset control design”. In: *Control Engineering Practice* 8.2 (2000), pp. 113–120.
- [5] M. Heertjes, K. Gruntjens, S. Van Loon, N. Van de Wouw, and W. Heemels. “Experimental evaluation of reset control for improved stage performance”. In: *IFAC-PapersOnLine* 49.13 (2016), pp. 93–98.
- [6] L. Chen, N. Saikumar, and S. H. HosseinNia. “Development of robust fractional-order reset control”. In: *IEEE Transactions on Control Systems Technology* 28.4 (2019), pp. 1404–1417.
- [7] G. Zhao, D. Nešić, Y. Tan, and C. Hua. “Overcoming overshoot performance limitations of linear systems with reset control”. In: *Automatica* 101 (2019), pp. 27–35.
- [8] R. Beerens, A. Bisoffi, L. Zaccarian, W. Heemels, H. Nijmeijer, and N. van de Wouw. “Reset integral control for improved settling of PID-based motion systems with friction”. In: *Automatica* 107 (2019), pp. 483–492.
- [9] A. Bisoffi, R. Beerens, W. Heemels, H. Nijmeijer, N. van de Wouw, and L. Zaccarian. “To stick or to slip: A reset PID control perspective on positioning systems with friction”. In: *Annual Reviews in Control* 49 (2020), pp. 37–63.
- [10] S. Skogestad and I. Postlethwaite. *Multivariable feedback control: analysis and design*. John Wiley & sons, 2005.
- [11] J. M. Diaz, R. Costa-Castello, and S. Dormido. “Closed-loop shaping linear control system design: an interactive teaching/learning approach [focus on education]”. In: *IEEE Control Systems Magazine* 39.5 (2019), pp. 58–74.
- [12] P. Nuij, O. Bosgra, and M. Steinbuch. “Higher-order sinusoidal input describing functions for the analysis of non-linear systems with harmonic responses”. In: *Mechanical Systems and Signal Processing* 20.8 (2006), pp. 1883–1904.
- [13] N. Saikumar, K. Heinen, and S. H. HosseinNia. “Loop-shaping for reset control systems: A higher-order sinusoidal-input describing functions approach”. In: *Control Engineering Practice* 111 (2021), p. 104808.

- [14] N. Karbasizadeh, A. A. Dastjerdi, N. Saikumar, and S. H. HosseinNia. “Band-passing nonlinearity in reset elements”. In: *IEEE Transactions on Control Systems Technology* 31.1 (2022), pp. 333–343.
- [15] L. F. van Eijk, D. Kostić, M. Khosravi, and S. H. HosseinNia. “Higher-Order Sinusoidal-Input Describing Function Analysis for a Class of Multiple-Input Multiple-Output Convergent Systems”. In: *IEEE Transactions on Automatic Control* (2024).
- [16] I. Saunders and S. Vijayakumar. “The role of feed-forward and feedback processes for closed-loop prosthesis control”. In: *Journal of neuroengineering and rehabilitation* 8 (2011), pp. 1–12.
- [17] J. H. Lumkes Jr. *Control strategies for dynamic systems: design and implementation*. CRC Press, 2001.
- [18] E. Grassi, K. S. Tsakalis, S. Dash, S. V. Gaikwad, W. MacArthur, and G. Stein. “Integrated system identification and PID controller tuning by frequency loop-shaping”. In: *IEEE Transactions on Control Systems Technology* 9.2 (2001), pp. 285–294.
- [19] H. Richter. *Advanced control of turbofan engines*. Springer Science & Business Media, 2011.
- [20] A. Fuller. “Feedback control systems with low-frequency stochastic disturbances”. In: *International Journal of Control* 24.2 (1976), pp. 165–207.
- [21] C.-H. Chang and K.-W. Han. “Gain margins and phase margins for control systems with adjustable parameters”. In: *Journal of guidance, control, and dynamics* 13.3 (1990), pp. 404–408.
- [22] L. Chen, N. Saikumar, S. Baldi, and S. H. HosseinNia. “Beyond the waterbed effect: Development of fractional order crone control with non-linear reset”. In: *2018 annual american control conference (ACC)*. IEEE. 2018, pp. 545–552.
- [23] N. van de Wouw, H. Pastink, M. F. Heertjes, A. V. Pavlov, and H. Nijmeijer. “Performance of convergence-based variable-gain control of optical storage drives”. In: *Automatica* 44.1 (2008), pp. 15–27.
- [24] Y. Guo, Y. Wang, and L. Xie. “Frequency-domain properties of reset systems with application in hard-disk-drive systems”. In: *IEEE Transactions on Control Systems Technology* 17.6 (2009), pp. 1446–1453.
- [25] N. Saikumar, R. K. Sinha, and S. H. HosseinNia. “Constant in Gain Lead in Phase Element—Application in Precision Motion Control”. In: *IEEE/ASME Transactions on Mechatronics* 24.3 (2019), pp. 1176–1185.
- [26] A. Banos and A. Vidal. “Design of PI+ CI Reset Compensators for second order plants”. In: *2007 IEEE International Symposium on Industrial Electronics*. IEEE. 2007, pp. 118–123.
- [27] A. F. Villaverde, A. B. Blas, J. Carrasco, and A. B. Torrico. “Reset control for passive bilateral teleoperation”. In: *IEEE Transactions on Industrial Electronics* 58.7 (2010), pp. 3037–3045.
- [28] Y. Guo, Y. Wang, L. Xie, H. Li, and W. Gui. “Optimal reset law design and its application to transient response improvement of HDD systems”. In: *IEEE transactions on control systems technology* 19.5 (2010), pp. 1160–1167.

- [29] S. Van Loon, B. Hunnekens, W. M. H. Heemels, N. van de Wouw, and H. Nijmeijer. “Split-path nonlinear integral control for transient performance improvement”. In: *Automatica* 66 (2016), pp. 262–270.
- [30] B. Hunnekens, S. Kamps, and N. Van De Wouw. “Variable-gain control for respiratory systems”. In: *IEEE Transactions on Control Systems Technology* 28.1 (2018), pp. 163–171.
- [31] D. Van Dinther, B. Sharif, S. Van den Eijnden, H. Nijmeijer, M. F. Heertjes, and W. Heemels. “Overcoming performance limitations of linear control with hybrid integrator-gain systems”. In: *IFAC-PapersOnLine* 54.5 (2021), pp. 289–294.
- [32] N. Karbasizadeh and S. H. HosseinNia. “Continuous reset element: Transient and steady-state analysis for precision motion systems”. In: *Control Engineering Practice* 126 (2022), p. 105232.
- [33] A. Banos and A. Barreiro. *Reset control systems*. Springer, 2012.
- [34] Y. Guo and Y. Chen. “Stability analysis of delayed reset systems with distributed state resetting”. In: *Nonlinear Analysis: Hybrid Systems* 31 (2019), pp. 265–274.
- [35] N. Karbasizadeh, N. Saikumar, and S. H. HosseinNia. “Fractional-order single state reset element”. In: *Nonlinear Dynamics* 104 (2021), pp. 413–427.
- [36] A. Pavlov, N. Van De Wouw, and H. Nijmeijer. *Uniform output regulation of nonlinear systems: a convergent dynamics approach*. Vol. 205. Springer, 2006.
- [37] A. Pavlov, N. van de Wouw, and H. Nijmeijer. “Frequency response functions for nonlinear convergent systems”. In: *IEEE Transactions on Automatic Control* 52.6 (2007), pp. 1159–1165.
- [38] O. Beker, C. Hollot, Y. Chait, and H. Han. “Fundamental properties of reset control systems”. In: *Automatica* 40.6 (2004), pp. 905–915.
- [39] D. Nešić, L. Zaccarian, and A. R. Teel. “Stability properties of reset systems”. In: *Automatica* 44.8 (2008), pp. 2019–2026.
- [40] A. A. Dastjerdi, A. Astolfi, N. Saikumar, N. Karbasizadeh, D. Valerio, and S. H. HosseinNia. “Closed-loop frequency analysis of reset control systems”. In: *IEEE Transactions on Automatic Control* 68.2 (2022), pp. 1146–1153.
- [41] Y. Guo, L. Xie, Y. Wang, et al. *Analysis and design of reset control systems*. Vol. 11. IET, 2015.
- [42] T. Samad, S. Mastellone, P. Goupil, A. van Delft, A. Serbezov, and K. Brooks. “Ifac industry committee update, initiative to increase industrial participation in the control community”. In: *Newsletters April 2019*. IFAC (2019).
- [43] T. Wang, J. Sun, X. Wang, Y. Liu, Y. Si, J. S. Dong, X. Yang, and X. Li. “A systematic study on explicit-state non-Zenoness checking for timed automata”. In: *IEEE Transactions on Software Engineering* 41.1 (2014), pp. 3–18.
- [44] A. Barreiro, A. Baños, S. Dormido, and J. A. González-Prieto. “Reset control systems with reset band: Well-posedness, limit cycles and stability analysis”. In: *Systems & Control Letters* 63 (2014), pp. 1–11.

- [45] J. C. Clegg. “A nonlinear integrator for servomechanisms”. In: *Transactions of the American Institute of Electrical Engineers, Part II: Applications and Industry* 77.1 (1958), pp. 41–42.
- [46] K. Krishnan and I. Horowitz. “Synthesis of a non-linear feedback system with significant plant-ignorance for prescribed system tolerances”. In: *International Journal of Control* 19.4 (1974), pp. 689–706.
- [47] I. Horowitz and P. Rosenbaum. “Non-linear design for cost of feedback reduction in systems with large parameter uncertainty”. In: *International Journal of Control* 21.6 (1975), pp. 977–1001.
- [48] L. Hazeleger, M. Heertjes, and H. Nijmeijer. “Second-order reset elements for stage control design”. In: *2016 American Control Conference (ACC)*. IEEE. 2016, pp. 2643–2648.
- [49] A. Baños and A. Vidal. “Definition and tuning of a PI+ CI reset controller”. In: *2007 european control conference (ECC)*. IEEE. 2007, pp. 4792–4798.
- [50] A. Baños, S. Dormido, and A. Barreiro. “Limit cycles analysis of reset control systems with reset band”. In: *Nonlinear analysis: hybrid systems* 5.2 (2011), pp. 163–173.
- [51] N. Saikumar and H. HosseinNia. “Generalized fractional order reset element (GFrORE)”. In: *9th European Nonlinear Dynamics Conference (ENOC)*. EUROMECH. 2017.
- [52] C. Weise, K. Wulff, and J. Reger. “Fractional-order memory reset control for integer-order LTI systems”. In: *2019 IEEE 58th conference on decision and control (CDC)*. IEEE. 2019, pp. 5710–5715.
- [53] C. Weise, K. Wulff, and J. Reger. “Extended fractional-order memory reset control for integer-order LTI systems and experimental demonstration”. In: *IFAC-PapersOnLine* 53.2 (2020), pp. 7683–7690.
- [54] G. Zhao and J. Wang. “Existence and design of non-overshoot reset controllers for minimum-phase linear single-input single-output systems”. In: *IET Control Theory & Applications* 9.17 (2015), pp. 2514–2521.
- [55] G. Zhao and J. Wang. “On L2 gain performance improvement of linear systems with Lyapunov-based reset control”. In: *Nonlinear Analysis: Hybrid Systems* 21 (2016), pp. 105–117.
- [56] G. Zhao, C. Hua, and X. Guan. “Reset observer-based zeno-free dynamic event-triggered control approach to consensus of multiagent systems with disturbances”. In: *IEEE Transactions on Cybernetics* 52.4 (2020), pp. 2329–2339.
- [57] D. A. Deenen, B. Sharif, S. van den Eijnden, H. Nijmeijer, M. Heemels, and M. Heertjes. “Projection-based integrators for improved motion control: Formalization, well-posedness and stability of hybrid integrator-gain systems”. In: *Automatica* 133 (2021), p. 109830.
- [58] X. Zhang, M. B. Kaczmarek, and S. H. HosseinNia. “Frequency response analysis for reset control systems: Application to predict precision of motion systems”. In: *Control Engineering Practice* 152 (2024), p. 106063. ISSN: 0967-0661.

2

Frequency Response Analysis for Open-Loop Reset Control Systems

Frequency response analysis is an effective tool in control system design, offering critical gain and phase information that helps characterize system behavior. Establishing a connection between open-loop and closed-loop frequency responses is crucial for designing open-loop controllers that meet specific closed-loop performance specifications. A critical prerequisite for this process is an accurate method for analyzing open-loop frequency responses. However, no precise analysis methods are available for the generalized reset systems studied in this work. To address this gap, this chapter introduces Higher-Order Sinusoidal Input Describing Functions (HOSIDFs) for open-loop generalized reset systems. The accuracy of the proposed HOSIDFs is validated through simulation results. Moreover, the HOSIDFs decompose the frequency response of open-loop reset control systems into two components: a base-linear element and a filtered-pulse nonlinear term. This decomposition not only enhances understanding of reset system dynamics but also provides a foundation for subsequent closed-loop frequency response analysis.

 This chapter is based on the paper:

Zhang, Xinxin, Marcin B. Kaczmarek, and S. Hassan HosseinNia. "Frequency response analysis for reset control systems: Application to predict precision of motion systems." *Control Engineering Practice* 152 (2024): 106063.

2.1 Introduction

Reset control elements have shown superior performance over linear controllers in both steady-state and transient response characteristics, exhibiting better disturbance rejection, tracking accuracy, and reduced overshoot, as evidenced by [1–8]. To facilitate the practical implementation of reset control systems in the mechatronics industry, effective analysis tools are essential. Frequency response analysis is among the most commonly and effectively used techniques for this purpose in industrial applications [9]. It evaluates a system's steady-state response to sinusoidal inputs across varying frequencies, offering insights into phase and magnitude characteristics of linear time-invariant (LTI) systems. Frequency response analysis covers both open-loop and closed-loop analysis. By leveraging the connection between the open-loop and closed-loop analysis through loop-shaping techniques [10], control engineers can design controllers in the open loop, ensuring that the system meets specified closed-loop performance requirements, such as reducing steady-state errors and improving transient response [11]. Additionally, frequency response analysis allows engineers to predict closed-loop behavior without requiring precise parametric models of the plant. This characteristic is particularly beneficial when obtaining an accurate plant model is impractical.

For open-loop frequency response analysis of reset feedback control systems, Higher-Order Sinusoidal Input Describing Function (HOSIDF) methods have been introduced in [12–15]. The HOSIDF methods converge with the SIDF analysis [16] when the impact of high-order harmonics beyond the first order is negligible. However, the accuracy of these existing HOSIDF methods for open-loop reset control systems is limited to specific configurations. For instance, these methods cannot be directly applied to the generalized reset feedback structure depicted in Fig. 1.8 when the reset controller's input signal differs from its reset-triggering signal.

Motivated by the constraints of current frequency response analysis approaches for open-loop reset control systems, this chapter introduces accurate frequency-domain analysis methods for such systems. The presented method analytically separates the frequency response of open-loop reset control systems into a base-linear component and nonlinear elements, facilitating the derivation of closed-loop frequency response analysis methods for reset control systems.

The remainder of this chapter is organized as follows: Section 2.2 presents the frequency response analysis for the open-loop reset control system. It begins with the development of an analytical model for the CI, followed by an extension of this model to the reset controller, and concludes with the formulation of the HOSIDFs for reset controller and open-loop reset systems. Section 2.3 applies two case studies to validate the accuracy of the proposed open-loop HOSIDFs. Finally, Section 2.4 offers concluding remarks.

2.2 Method: Frequency Response Analysis for Open-loop Reset Systems

Figure 2.1 illustrates the block diagram of the open-loop reset control system. This section develops the Higher-Order Sinusoidal Input Describing Functions (HOSIDFs)

for the reset controller C_r as defined in (1.6), and for the open-loop reset control system. These HOSIDFs characterize the steady-state behavior of each harmonic in nonlinear systems subjected to sinusoidal inputs [12].

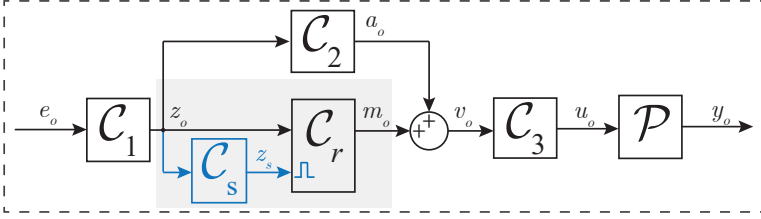


Figure 2.1 The block diagram of the open-loop reset system.

Given that the reset controller C_r in (1.6) is built upon the primitive Clegg Integrator (CI) [17], this section begins by presenting an analytical model of the CI. The model illustrates that the output of a sinusoidal-input CI consists of two components: the output of its base-linear controller (which is a linear integrator), and a square wave.

This model is then extended to a general reset controller C_r , where the output of a sinusoidal-input reset controller is decomposed into its base-linear output and a filtered pulse signal. The “filtered pulse signal” refers to a signal generated by passing a normalized pulse through a finite-dimensional LTI transfer function. Next, using this analytical framework, the HOSIDFs for both the reset controller and the open-loop reset control systems are developed.

2.2.1 Analysis Model for the Sinusoidal-Input Clegg Integrator

The Generalized Clegg Integrator (GCI) is defined as the reset controller C_r described by (1.6), with the following parameter settings: $A_R = 0$, $B_R = 1$, $C_R = 1$, $D_R = 0$, and $A_\rho = \gamma \in \mathbb{R}$ where $\gamma \in (-1, 1)$.

Lemma 1 shows that the output of the sinusoidal-input GCI consists of two components: the base-linear output and a square wave component.

Lemma 1. Consider a Generalized Clegg Integrator (GCI) subjected to a sinusoidal input signal $e(t) = |E_1| \sin(\omega t)$, which satisfies the condition in (1.9). The steady-state output signal $u_{ci}(t)$ of the GCI consists of two components: the output of the base-linear integrator $1/s$ denoted as $u_i(t)$, and a square wave component $q_i(t)$, expressed as:

$$u_{ci}(t) = u_i(t) + q_i(t), \quad (2.1)$$

where

$$\begin{aligned} u_i(t) &= -|E_1| [\cos(\omega t) - 1] / \omega, \\ q_i(t) &= \begin{cases} -2|E_1| \gamma (\gamma + 1)^{-1} / \omega, & \text{for } t \in [2k, 2k + 1) \cdot \pi / \omega, \quad k \in \mathbb{N}, \\ -2|E_1| (\gamma + 1)^{-1} / \omega, & \text{for } t \in [2k + 1, 2k + 2) \cdot \pi / \omega, \end{cases} \end{aligned} \quad (2.2)$$

Proof. The proof can be found in Appendix 2.A. □

Figure 2.2 displays the simulated steady-state output $u_{ci}(t)$ of the GCI with the input signal $e(t) = \sin(\omega t)$ ($\omega = \pi$ rad/s and $\gamma = 0$), the base-linear output $u_i(t)$ and the square wave $q_i(t)$. In this case, $q_i(t)$ is a square wave with a period of 2 seconds and amplitudes of 0 and 0.64, as calculated by (2.2).

2

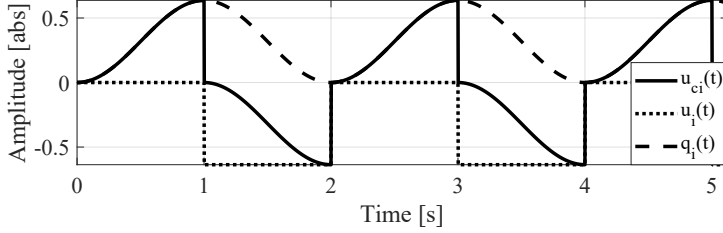


Figure 2.2: The steady-state outputs $u_{ci}(t)$ (solid line), $u_i(t)$ (dotted line), and $q_i(t)$ (dashed line) of the GCI with the input signal $e(t) = \sin(\omega t)$.

2.2.2 Higher-Order Sinusoidal Input Describing Functions (HOSIDEs) for Reset Controllers

Building upon the analysis model for the GCI in Lemma 1, Theorem 1 develops the analysis model for the reset controller \mathcal{C}_r as defined in (1.6).

Theorem 1. Consider a reset controller \mathcal{C}_r described by (1.6), which is subjected to a sinusoidal input signal $z_n(t) = |Z_n| \sin(n\omega t + \angle Z_n)$ and a reset trigger signal $z_s(t) = |Z_s| \sin(\omega t + \angle Z_s)$, generating an output signal $m_n(t)$, where $\angle Z_n, \angle Z_s \in (-\pi, \pi]$ and $n = 2k + 1$, $k \in \mathbb{N}$. Assuming that the condition in (1.9) is satisfied, the Fourier transform of $m_n(t)$, denoted as $M_n(\omega)$, is given by:

$$M_n(\omega) = M_l^n(\omega) + \sum_{\eta=1}^{\infty} M_p^\eta(\omega), \quad \eta = 2k + 1, \quad k \in \mathbb{N} \quad (2.3)$$

where

$$\begin{aligned} M_l^n(\omega) &= C_l(n\omega) \cdot Z_n(\omega), \\ \Delta_l(n\omega) &= (jn\omega I - A_R)^{-1} B_R, \\ \Delta_x(\eta\omega) &= C_R(j\eta\omega I - A_R)^{-1} j\eta\omega, \\ \Delta_c^n(\omega) &= |\Delta_l(n\omega)| \sin(\angle \Delta_l(n\omega) + \angle Z_n - n\angle Z_s), \\ M_p^\eta(\omega) &= \frac{2|Z_n| \Delta_x(\eta\omega) \Delta_q^n(\omega)}{\eta\pi} \cdot \mathcal{F}[\sin(\eta\omega t + \eta\angle Z_s)], \\ \Delta_q^n(\omega) &= (I + e^{A_R\pi/\omega})(A_p e^{A_R\pi/\omega} + I)^{-1} (A_p - I) \Delta_c^n(\omega). \end{aligned} \quad (2.4)$$

and the function $C_l(n\omega)$ is defined in (1.7).

Proof. The proof is provided in Appendix 2.B. □

Corollary 1. From Theorem 1, the output signal $m_n(t)$ of the reset controller \mathcal{C}_r , described by (1.6), subjected to a sinusoidal input signal $z_n(t) = |Z_n| \sin(n\omega t + \angle Z_n)$ and

a reset trigger signal $z_s(t) = |Z_s| \sin(\omega t + \angle Z_s)$ is expressed as:

$$m_n(t) = m_1^n(t) + \sum_{\eta=1}^{\infty} m_\rho^\eta(t), \quad (2.5)$$

where

$$\begin{aligned} m_\rho^\eta(t) &= \mathcal{F}^{-1}[M_\rho^\eta(\omega)], \\ m_1^n(t) &= |Z_n \cdot C_I(n\omega)| \sin(n\omega t + \angle Z_n + \angle C_I(n\omega)). \end{aligned} \quad (2.6)$$

Building on Theorem 1, Theorem 2 introduces the HOSIDF for the reset controller C_r , as defined in (1.6), where the input signal $z_o(t)$ and the reset trigger signal $z_s(t)$ share the same period $2\pi/\omega$, as shown in Fig. 2.1.

Theorem 2. Consider a reset controller C_r described in (1.6), with an input signal $z_o(t) = |Z_o| \sin(\omega t + \angle Z_o)$ and a reset-triggered signal $z_s(t) = |Z_o C_s(\omega)| \sin(\omega t + \angle Z_o + \angle C_s(\omega))$, generating the output signal $m_o(t)$, satisfying the condition in (1.9). Utilizing the ‘‘Virtual Harmonic Generator’’ approach [12], the input signal $z_o(t)$ generates harmonics $z_o^n(t) = |Z_o| \sin(n\omega t + n\angle Z_o)$, with Fourier transforms represented as $Z_o^n(\omega)$. The output $m_o(t)$ comprises n harmonics, denoted by $m_o^n(t)$, with corresponding Fourier transforms $M_o^n(\omega)$. The Higher-Order Sinusoidal Input Describing Function (HOSIDF) of C_r describes the transfer function from $Z_o^n(\omega)$ to $M_o^n(\omega)$, given by:

$$C_r^n(\omega) = \frac{M_o^n(\omega)}{Z_o^n(\omega)} = \begin{cases} C_I(\omega) + C_\rho^1(\omega), & \text{for } n = 1, \\ C_\rho^n(\omega), & \text{for odd } n > 1, \\ 0, & \text{for even } n \geq 2, \end{cases} \quad (2.7)$$

where

$$\begin{aligned} \Delta_I(\omega) &= (j\omega I - A_R)^{-1} B_R, \\ \Delta_x(n\omega) &= C_R(jn\omega I - A_R)^{-1} jn\omega I, \\ \Delta_c^1(\omega) &= |\Delta_I(\omega)| \sin(\angle \Delta_I(\omega) - \angle C_s(\omega)), \\ C_\rho^n(\omega) &= 2\Delta_x(n\omega) \Delta_q(\omega) e^{jn\angle C_s(\omega)/(n\pi)}, \\ \Delta_q(\omega) &= (I + e^{A_R\pi/\omega})(A_\rho e^{A_R\pi/\omega} + I)^{-1}(A_\rho - I) \Delta_c^1(\omega). \end{aligned} \quad (2.8)$$

Proof. The proof is provided in Appendix. 2.C. □

2.2.3 HOSIDFs for Open-Loop Reset Control Systems

By integrating the HOSIDF analysis for the reset controller C_r into the open-loop reset control systems, as shown in Fig. 2.1, Theorem 3 presents the HOSIDF analysis for the open-loop reset control system in Fig. 2.1.

Theorem 3. Consider an open-loop reset control system illustrated in Fig. 2.1 under Assumption 1, subject to an input signal $e_o(t) = |E| \sin(\omega t + \angle E)$, generating an output signal $y_o(t)$, under Assumption 1. Using the concept of the ‘‘Virtual Harmonic Generator’’ [13], the input signal $e_o(t)$ generates harmonics expressed as $e_o^n(t) = |E| \sin(n\omega t + n\angle E)$, with the corresponding Fourier transform denoted as $E_o^n(\omega)$. The output signal $y_o(t)$ consists of n harmonics, represented as $y_o^n(t)$, which have

Fourier transforms $Y_o^n(\omega)$. The HOSIDF of the open-loop reset control system, describing the transfer function from $E_o^n(\omega)$ to $Y_o^n(\omega)$, is given as follows:

$$\mathcal{L}_n(\omega) = \frac{Y_o^n(\omega)}{E_o^n(\omega)} = \begin{cases} \mathcal{C}_1(\omega)[\mathcal{C}_l(\omega) + \mathcal{C}_\rho^1(\omega) + \mathcal{C}_2(\omega)]\mathcal{C}_3(\omega)\mathcal{P}(\omega), & \text{for } n = 1 \\ \mathcal{C}_1(\omega)\mathcal{C}_\rho^n(\omega)\mathcal{C}_3(n\omega)\mathcal{P}(n\omega)e^{j(n-1)\angle\mathcal{C}_1(\omega)}, & \text{for odd } n > 1, \\ 0, & \text{for even } n \geq 2, \end{cases} \quad (2.9)$$

where $\mathcal{C}_l(\omega)$ is given in (1.7) and $\mathcal{C}_\rho^n(\omega)$ is given in (2.8).

Proof. The proof is provided in Appendix. 2.D. \square

Based on Theorem 3, Fig. 2.3 presents the block diagram of the open-loop reset control system for the HOSIDF analysis. Subsequently, Remark 1 provides the calculation for the output $y_o(t)$ of the sinusoidal-input open-loop reset control system.

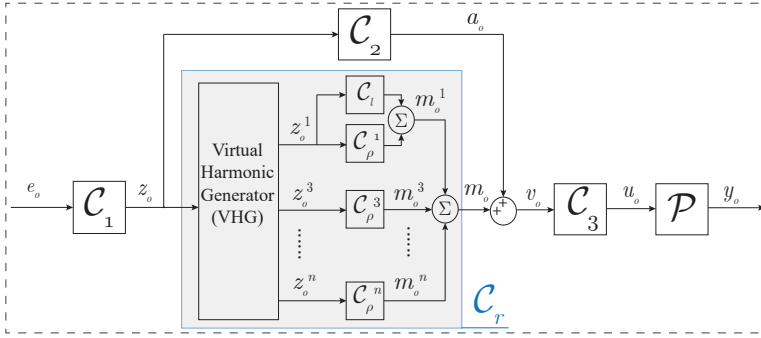


Figure 2.3: The new block diagram of the open-loop reset control system.

Remark 1. Consider an open-loop reset control system with the input signal $e_o(t) = |E|\sin(\omega t + \angle E)$, under Assumption 1. The steady-state output signal $y_o(t)$ is given by

$$y_o(t) = \sum_{n=1}^{\infty} y_o^n(t) = \sum_{n=1}^{\infty} |E\mathcal{L}_n(\omega)| \sin(n\omega t + n\angle E + \angle\mathcal{L}_n(\omega)), \quad n = 2k + 1 (k \in \mathbb{N}). \quad (2.10)$$

2.3 Results: Validation of Open-Loop HOSIDFs

This section validates the accuracy of HOSIDFs for the reset controller \mathcal{C}_r in Theorem 2 and for the open-loop reset control system in Theorem 3.

2.3.1 Case Study 1

This section validates the accuracy of HOSIDFs for the reset controller \mathcal{C}_r using an illustrative reset controller \mathcal{C}_r characterized by the following design parameters: the BLC $\mathcal{C}_l = \left(\frac{30\pi}{s} + 1\right)$ with a reset value of $\gamma = 0$, and the shaping filter defined as $\mathcal{C}_s = \frac{s/(30\pi) + 1}{s/(6000\pi) + 1}$.

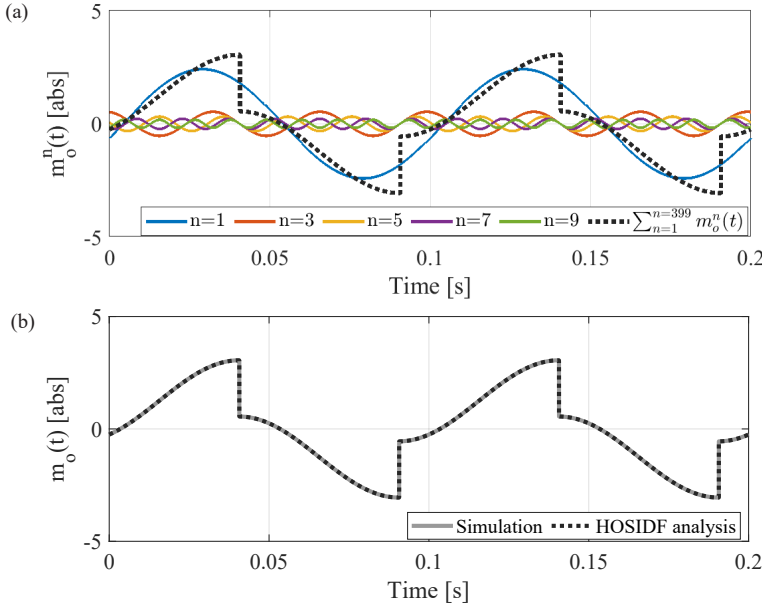


Figure 2.4 (a) The output signal $m_o(t) = \sum_{n=1}^{399} m_o^n(t)$ and its first five harmonics $m_o^n(t)$ (for $n = 1, 3, 5, 7, 9$) for the illustrative open-loop reset controller under a sinusoidal input $z_o(t) = \sin(20\pi t)$, obtained based on Theorem 2. (b) The output signal $m_o(t)$, obtained from simulation, the previous prediction [14], and the new prediction based on Theorem 2 for the reset controller.

Figure 2.4(a) displays the output signal $m_o(t) = \sum_{n=1}^{399} m_o^n(t)$ and its first five harmonics $m_o^n(t)$ (for $n = 1, 3, 5, 7, 9$), obtained using Theorem 2. Additionally, Fig. 2.4(b) compares the reset output $m_o(t)$ obtained through simulation with predictions from Theorem 2. The results confirm the accuracy of the HOSIDF for C_r .

2.3.2 Case Study 2

To validate the accuracy of Theorem 3, this section uses an illustrative system to verify the accuracy of the open-loop HOSIDF, $\mathcal{L}_n(\omega)$, derived in (2.9). The illustrative system is based on the structure shown in Fig. 2.1, with the following design parameters: the reset controller C_r is based on a BLC $C_l = 30\pi/s$ with a reset value $\gamma = 0$, $C_1 = (s/(150\pi))/(s/(3000\pi) + 1)$, $C_2 = C_4 = 1$, $C_s = 1/(s/5 + 1)$, and $C_3 = 1/(s/(150\pi) + 1)$. The plant \mathcal{P} is given in (1.1).

The input to the system is a sinusoidal signal $e_o(t) = \sin(8\pi t)$. Figure 2.5(a) illustrates the output signal $y_o(t) = \sum_{n=1}^{399} y_o^n(t)$ along with its first five harmonic components $y_o^n(t)$ ($n = 1, 3, 5, 7, 9$), computed using Theorem 3 and Remark 1. Moreover, Figure 2.5(b) compares the output signal $y_o(t)$ obtained from simulation with the prediction generated by the HOSIDFs analysis method. The close agreement between the simulated and predicted results demonstrates the accuracy of the proposed HOSIDF analysis method for predicting the behavior of open-loop reset control systems.

The accuracy of the HOSIDFs analysis method in Theorem 3 depends on the number

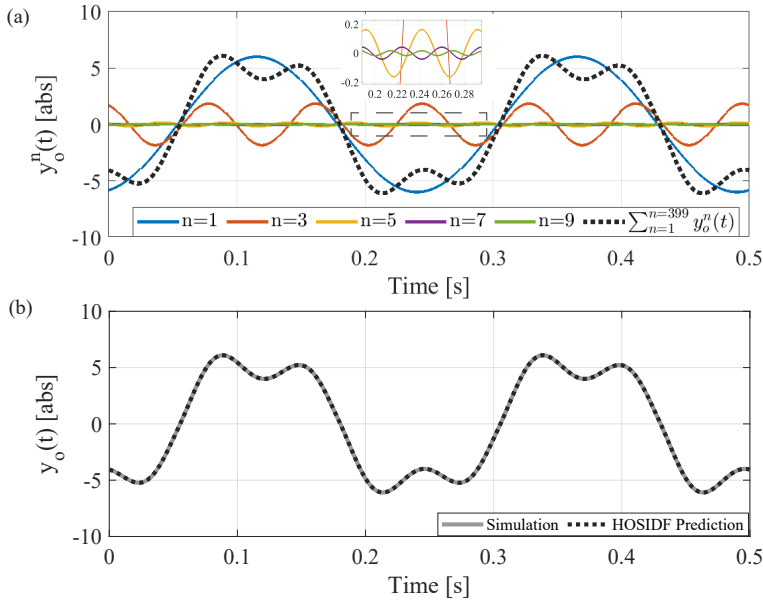


Figure 2.5 (a) The output signal $y_o(t) = \sum_{n=1}^{399} y_o^n(t)$ and its first five harmonics $y_o^n(t)$ (for $n = 1, 3, 5, 7, 9$) for the illustrative open-loop reset control system under a sinusoidal input $e_o(t) = \sin(8\pi t)$, obtained based on Theorem 3. (b) Simulated, previous prediction [14], and Theorem 3-predicted output signal $y_o(t)$.

of harmonics denoted as N_h included in the analysis. Define the prediction error as the difference between the prediction provided by Theorem 3 and the simulation results. Figure 2.6 illustrates the relationship between the prediction error and the number of harmonics N_h . The results demonstrate that incorporating a higher number of harmonics in the calculations enhances prediction accuracy. Given that the true nonlinear output signal $y_o(t)$ of the reset control system contains an infinite number of harmonics, ideally, as the number of harmonics approaches infinity, the prediction error converges to zero.

After validating the accuracy of the open-loop analysis method, Theorem 3 is utilized to perform a frequency-domain analysis of the open-loop reset control systems depicted in Fig. 2.1. Figure 2.7 displays the Bode plot of the open-loop HOSIDF $\mathcal{L}_n(\omega)$ for the illustrative open-loop reset control system. This HOSIDF provides critical magnitude and phase information for each harmonic, which is vital for effective system design.

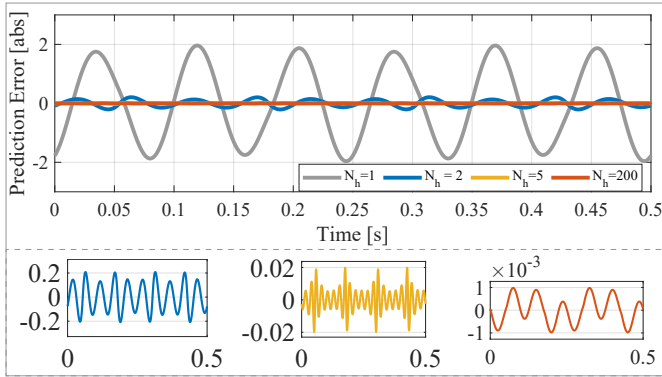


Figure 2.6 The relationship between the prediction error and the number of harmonics N_h considered in the calculation, with values $N_h = 1, 2, 10,$ and 200 .

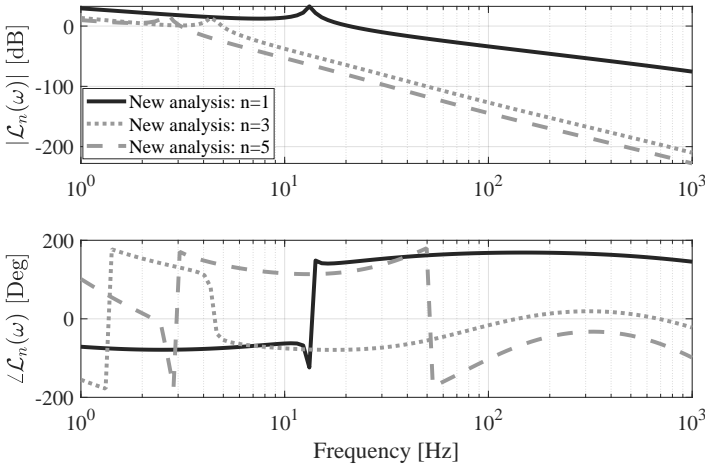


Figure 2.7 The HOSIDF $\mathcal{L}_n(\omega)$ of the open-loop reset system with the first ($n = 1$), third ($n = 3$), and fifth ($n = 5$) order harmonics.

2.4 Conclusion

To summarize this chapter, Theorem 2 and Theorem 3 present HOSIDFs for reset controllers and open-loop reset control systems. More importantly, the methods analytically decompose the HOSIDF of the reset controller into its linear and nonlinear components. This decomposition serves as the foundation for the development of the closed-loop HOSIDF analysis, which will be elaborated upon in Chapter 4.

Bibliography

- [1] G. Zhao and J. Wang. “Existence and design of non-overshoot reset controllers for minimum-phase linear single-input single-output systems”. In: *IET Control Theory & Applications* 9.17 (2015), pp. 2514–2521.
- [2] G. Zhao and J. Wang. “On L2 gain performance improvement of linear systems with Lyapunov-based reset control”. In: *Nonlinear Analysis: Hybrid Systems* 21 (2016), pp. 105–117.
- [3] M. Heertjes, K. Gruntjens, S. Van Loon, N. Van de Wouw, and W. Heemels. “Experimental evaluation of reset control for improved stage performance”. In: *IFAC-PapersOnLine* 49.13 (2016), pp. 93–98.
- [4] N. Saikumar, R. K. Sinha, and S. H. HosseinNia. “Constant in Gain Lead in Phase Element—Application in Precision Motion Control”. In: *IEEE/ASME Transactions on Mechatronics* 24.3 (2019), pp. 1176–1185.
- [5] G. Zhao, D. Nešić, Y. Tan, and C. Hua. “Overcoming overshoot performance limitations of linear systems with reset control”. In: *Automatica* 101 (2019), pp. 27–35.
- [6] G. Zhao, C. Hua, and X. Guan. “Reset observer-based zeno-free dynamic event-triggered control approach to consensus of multiagent systems with disturbances”. In: *IEEE Transactions on Cybernetics* 52.4 (2020), pp. 2329–2339.
- [7] D. A. Deenen, B. Sharif, S. van den Eijnden, H. Nijmeijer, M. Heemels, and M. Heertjes. “Projection-based integrators for improved motion control: Formalization, well-posedness and stability of hybrid integrator-gain systems”. In: *Automatica* 133 (2021), p. 109830.
- [8] N. Karbasizadeh and S. H. HosseinNia. “Continuous reset element: Transient and steady-state analysis for precision motion systems”. In: *Control Engineering Practice* 126 (2022), p. 105232.
- [9] J. H. Lumkes Jr. *Control strategies for dynamic systems: design and implementation*. CRC Press, 2001.
- [10] E. Grassi, K. S. Tsakalis, S. Dash, S. V. Gaikwad, W. MacArthur, and G. Stein. “Integrated system identification and PID controller tuning by frequency loop-shaping”. In: *IEEE Transactions on Control Systems Technology* 9.2 (2001), pp. 285–294.
- [11] H. Richter. *Advanced control of turbofan engines*. Springer Science & Business Media, 2011.
- [12] P. Nuij, O. Bosgra, and M. Steinbuch. “Higher-order sinusoidal input describing functions for the analysis of non-linear systems with harmonic responses”. In: *Mechanical Systems and Signal Processing* 20.8 (2006), pp. 1883–1904.

- [13] N. Saikumar, K. Heinen, and S. H. HosseinNia. “Loop-shaping for reset control systems: A higher-order sinusoidal-input describing functions approach”. In: *Control Engineering Practice* 111 (2021), p. 104808.
- [14] N. Karbasizadeh, A. A. Dastjerdi, N. Saikumar, and S. H. HosseinNia. “Band-passing nonlinearity in reset elements”. In: *IEEE Transactions on Control Systems Technology* 31.1 (2022), pp. 333–343.
- [15] L. F. van Eijk, D. Kostić, M. Khosravi, and S. H. HosseinNia. “Higher-Order Sinusoidal-Input Describing Function Analysis for a Class of Multiple-Input Multiple-Output Convergent Systems”. In: *IEEE Transactions on Automatic Control* (2024).
- [16] Y. Guo, Y. Wang, and L. Xie. “Frequency-domain properties of reset systems with application in hard-disk-drive systems”. In: *IEEE Transactions on Control Systems Technology* 17.6 (2009), pp. 1446–1453.
- [17] A. Banos and A. Barreiro. *Reset control systems*. Springer, 2012.

Appendix

2.A Proof of Lemma 1

Proof. Consider a Generalized Clegg Integrator (GCI) defined as the reset controller C_r in (1.6) with the following parameters: $A_R = 0$, $B_R = 1$, $C_R = 1$, $D_R = 0$, and $A_\rho = \gamma \in (-1, 1)$. This controller is subjected to a sinusoidal input signal $e(t) = |E_1| \sin(\omega t)$ at steady state, under the condition in (1.9).

From (1.6), the output signal $u_{ci}(t)$ of the GCI is given by

$$\begin{cases} \dot{u}_{ci}(t) = e(t), & e(t) \neq 0, \\ u_{ci}(t^+) = \gamma u_{ci}(t), & e(t) = 0. \end{cases} \quad (2.11)$$

For its BLS (which is an integrator), we have

$$\dot{u}_i(t) = e(t). \quad (2.12)$$

Define $q_i(t) = u_{ci}(t) - u_i(t)$. From (2.11) and (2.12), we have

$$\begin{cases} \dot{q}_i(t) = \dot{u}_{ci}(t) - \dot{u}_i(t) = 0, & e(t) \neq 0, \\ q_i(t^+) = \gamma q_i(t) + (\gamma - 1)u_i(t), & e(t) = 0. \end{cases} \quad (2.13)$$

The reset instants of the GCI with a sinusoidal input signal $e(t) = |E_1| \sin(\omega t)$ are given by $t_i = i \cdot \pi / \omega$, where $i \in \mathbb{Z}^+$ and $e(t_i) = 0$. Utilizing (2.13), the signal $q_i(t)$ between two consecutive reset instants $[t_i^+, t_{i+1}]$ (where t_i^+ denotes the after-reset instant) is expressed as follows:

$$q_i(t) = q_i(t_i^+) + \int_{t_i^+}^t \dot{q}_i(\tau) d\tau = q_i(t_i^+), \quad t \in [t_i^+, t_{i+1}]. \quad (2.14)$$

From (1.6), the output signal $u_i(t_i)$ at the reset instant $t_i = i \cdot \pi/\omega$ of the base-linear integrator with the input signal $e(t) = |E_1| \sin(\omega t)$, is given by:

$$u_i(t_i) = \begin{cases} 0, & \text{for even } i, \\ 2|E_1|/\omega, & \text{for odd } i. \end{cases} \quad (2.15)$$

Combining (2.13), (2.14), and (2.15), $q_i(t_i^+)$ is given by

$$\begin{aligned} q_i(t_i^+) &= \gamma q_i(t_{i-1}^+) + (\gamma - 1)u_i(t_i) \\ &= \begin{cases} \gamma q_i(t_{i-1}^+), & \text{for even } i, \\ \gamma q_i(t_{i-1}^+) + 2|E_1|(\gamma - 1)/\omega, & \text{for odd } i. \end{cases} \end{aligned} \quad (2.16)$$

Based on (2.16), for an odd i , $q_i(t_i^+)$ is given by

$$\begin{aligned} q_i(t_i^+) &= q_i(t_{i+2}^+) \\ &= \gamma q_i(t_{i+1}^+) + 2|E_1|(\gamma - 1)/\omega \\ &= \gamma^2 q_i(t_i^+) + 2|E_1|(\gamma - 1)/\omega. \end{aligned} \quad (2.17)$$

Equations (2.16) and (2.17) can be concluded that

$$q_i(t_i^+) = \begin{cases} -2|E_1|\gamma(\gamma + 1)^{-1}/\omega, & \text{for even } i, \\ -2|E_1|(\gamma + 1)^{-1}/\omega, & \text{for odd } i. \end{cases} \quad (2.18)$$

Combining (2.14) and (2.18), $q_i(t)$ in the time domain is obtained as follows:

$$q_i(t) = \begin{cases} -2|E_1|\gamma(\gamma + 1)^{-1}/\omega, & \text{for } t \in [2k, 2k + 1) \cdot \pi/\omega, \\ -2|E_1|(\gamma + 1)^{-1}/\omega, & \text{for } t \in [2k + 1, 2k + 2) \cdot \pi/\omega. \end{cases} \quad (2.19)$$

Here, we conclude the proof. \square

2.B Proof of Theorem 1

Proof. Consider a reset controller C_r (1.6) with an $2\pi/(n\omega)$ -periodic input signal of $z_n(t) = |Z_n| \sin(n\omega t + \angle Z_n)$, where $n = 2k + 1$, $k \in \mathbb{N}$, and a $2\pi/\omega$ -periodic reset trigger signal $z_s(t) = |Z_s| \sin(\omega t + \angle Z_s)$, where $\angle Z_n, \angle Z_s \in (-\pi, \pi]$, generating output signal $m_n(t)$. This proof derives the Fourier transform of $m_n(t)$, denoted as $M_n(\omega)$.

Let $x_c(t)$ and $x_{bl}(t)$ denote the state of the reset controller C_r and its BLC C_l , respectively. Define

$$x_{nl}(t) = x_c(t) - x_{bl}(t) \quad (\in \mathbb{R}^{n_c \times 1}), \quad (2.20)$$

where n_c is the number of states of the reset controller C_r .

From (1.6), the base-linear state $x_{bl}(t)$ is given by

$$x_{bl}(t) = |Z_n \Delta_l(n\omega)| \sin(n\omega t + \angle Z_n + \angle \Delta_l(n\omega)), \quad (2.21)$$

where

$$\Delta_l(n\omega) = (jn\omega I - A_R)^{-1} B_R \quad (\in \mathbb{R}^{n_c \times 1}). \quad (2.22)$$

Based on (1.6) and (2.20), we have:

$$\begin{cases} \dot{x}_{nl}(t) = A_R x_{nl}(t), & z_s(t) \neq 0, \\ x_{nl}(t^+) = A_\rho x_{nl}(t) + (A_\rho - I)x_{bl}(t), & z_s(t) = 0. \end{cases} \quad (2.23)$$

For the reset controller \mathcal{C}_r with a reset-triggered signal $z_s(t) = |Z_s| \sin(\omega t + \angle Z_s)$, the set of reset instants is denoted by $J_o := \{t_i \mid t_i = (i\pi - \angle Z_s)/\omega, i \in \mathbb{Z}^+\}$. Therefore, the reset interval is given by $\sigma_i = t_{i+1} - t_i = \pi/\omega$. According to (2.23), between two consecutive reset instants $[t_i^+, t_{i+1}]$ where $z_s(t) \neq 0$, the expression for $x_{nl}(t)$ is defined as

$$x_{nl}(t) = e^{A_R(t-t_i)} \Delta_n^i(\omega), \quad \text{for } t \in [t_i^+, t_{i+1}], \quad (2.24)$$

where $\Delta_n^i(\omega) \in \mathbb{R}^{n \times 1}$ represents a constant matrix independent of time t , which will be derived in the following content.

From the expression in (2.24), we have:

$$x_{nl}(t_{i+1}) = e^{A_R \pi/\omega} \Delta_n^i(\omega). \quad (2.25)$$

Under Assumption 1, the state of the reset controller with a $2\pi/\omega$ -periodic input signal is a $2\pi/\omega$ -periodic signal, denoted as $x_c(t) = x_c(t + 2\pi/\omega)$. From (2.21), it follows that $x_{bl}(t)$ is also a $2\pi/\omega$ -periodic signal. Consequently, from (2.20), the nonlinear component $x_{nl}(t) = x_c(t) - x_{bl}(t)$ must also be a $2\pi/\omega$ -periodic signal. Since the reset instants satisfy $t_{i+1} - t_{i-1} = 2\pi/\omega$, it implies $x_{nl}(t_{i-1}) = x_{nl}(t_{i+1})$. From (2.25), we have:

$$\Delta_n^{i-1}(\omega) = \Delta_n^{i+1}(\omega). \quad (2.26)$$

Based on (2.24), at the reset instant $t_{i+1} \in J_o$, $x_{nl}(t_{i+1})$ is given by

$$x_{nl}(t_{i+1}) = e^{A_R(t_{i+1}-t_i)} \Delta_n^i(\omega) = e^{A_R \pi/\omega} \Delta_n^i(\omega). \quad (2.27)$$

From (2.23) and (2.24), $x_{nl}(t_{i+1}^+)$ is given by

$$x_{nl}(t_{i+1}^+) = A_\rho x_{nl}(t_{i+1}) + (A_\rho - I)x_{bl}(t_{i+1}). \quad (2.28)$$

Substituting $x_{nl}(t_{i+1})$ from (2.27) into (2.28), $x_{nl}(t_{i+1}^+)$ is obtained as

$$x_{nl}(t_{i+1}^+) = A_\rho e^{A_R \pi/\omega} \Delta_n^i(\omega) + (A_\rho - I)x_{bl}(t_{i+1}). \quad (2.29)$$

From (2.24), $x_{nl}(t_{i+1}^+) \in [t_{i+1}^+, t_{i+2}]$ can be expressed as

$$x_{nl}(t_{i+1}^+) = \Delta_n^{i+1}(\omega). \quad (2.30)$$

Let (2.29) and (2.30) be equal to each other, we have

$$\Delta_n^{i+1}(\omega) = A_\rho e^{A_R \pi/\omega} \Delta_n^i(\omega) + (A_\rho - I)x_{bl}(t_{i+1}). \quad (2.31)$$

From (2.31), we can obtain

$$\Delta_n^i(\omega) = A_\rho e^{A_R \pi/\omega} \Delta_n^{i-1}(\omega) + (A_\rho - I)x_{bl}(t_i). \quad (2.32)$$

From (2.26) and (2.31), we have

$$\Delta_n^{i-1}(\omega) = A_\rho e^{A_R \pi / \omega} \Delta_n^i(\omega) + (A_\rho - I)x_{bl}(t_{i+1}). \quad (2.33)$$

From (2.21) and for an odd number n , at the reset instant $t_i = (i\pi - \angle Z_s)/\omega$, the base-linear state is given by:

$$x_{bl}(t_i) = \begin{cases} |Z_n| \Delta_c^n(\omega), & \text{for even } i, \\ -|Z_n| \Delta_c^n(\omega), & \text{for odd } i, \end{cases} \quad (2.34)$$

where

$$\Delta_c^n(\omega) = |\Delta_l(n\omega)| \sin(\angle \Delta_l(n\omega) + \angle Z_n - n\angle Z_s) \in \mathbb{R}^{n_c \times 1}. \quad (2.35)$$

From (2.34), we have the relation: $x_{bl}(t_{i+1}) = -x_{bl}(t_i)$. Substituting this relation into (2.33), we get:

$$\Delta_n^{i-1}(\omega) = A_\rho e^{A_R \pi / \omega} \Delta_n^i(\omega) - (A_\rho - I)x_{bl}(t_i). \quad (2.36)$$

From (2.32) and (2.36), we obtain

$$\Delta_n^i(\omega) = (A_\rho e^{A_R \pi / \omega} + I)^{-1} (A_\rho - I)x_{bl}(t_i). \quad (2.37)$$

From (2.34) and (2.37), we obtain

$$\Delta_n^i(\omega) = \begin{cases} |Z_n| \Delta_v^n(\omega), & \text{for even } i, \\ -|Z_n| \Delta_v^n(\omega), & \text{for odd } i, \end{cases} \quad (2.38)$$

where

$$\Delta_v^n(\omega) = (A_\rho e^{A_R \pi / \omega} + I)^{-1} (A_\rho - I) \Delta_c^n(\omega) \in \mathbb{R}^{n_c \times 1}. \quad (2.39)$$

From (2.25) and (2.38), $x_{nl}(t_i)$ is given by

$$x_{nl}(t_i) = \begin{cases} -|Z_n| e^{A_R \pi / \omega} \Delta_v^n(\omega), & \text{for even } i, \\ |Z_n| e^{A_R \pi / \omega} \Delta_v^n(\omega), & \text{for odd } i, \end{cases} \quad (2.40)$$

From (2.24) and (2.38), at the time instant t_i^+ , $x_{nl}(t_i^+)$ is given by

$$x_{nl}(t_i^+) = \begin{cases} |Z_n| \Delta_v^n(\omega), & \text{for even } i, \\ -|Z_n| \Delta_v^n(\omega), & \text{for odd } i. \end{cases} \quad (2.41)$$

From the time instant t_i to t_i^+ , $x_{nl}(t_i)$ jumps to $x_{nl}(t_i^+)$. From (2.40) and (2.41), this jump is given by

$$x_{nl}(t_i^+) - x_{nl}(t_i) = \begin{cases} |Z_n| (I + e^{A_R \pi / \omega}) \Delta_v^n(\omega), & \text{for even } i, \\ -|Z_n| (I + e^{A_R \pi / \omega}) \Delta_v^n(\omega), & \text{for odd } i. \end{cases} \quad (2.42)$$

Substituting $\Delta_v^n(\omega)$ from (2.39) into (2.42), the jump at the time instant t_i^+ is expressed as

$$x_{nl}(t_i^+) - x_{nl}(t_i) = \begin{cases} |Z_n| \Delta_q^n(\omega), & \text{for even } i, \\ -|Z_n| \Delta_q^n(\omega), & \text{for odd } i. \end{cases} \quad (2.43)$$

where

$$\Delta_q^n(\omega) = (I + e^{A_R \pi / \omega})(A_p e^{A_R \pi / \omega} + I)^{-1}(A_p - I)\Delta_c^n(\omega) \quad (\in \mathbb{R}^{n_c \times 1}), \quad (2.44)$$

where Δ_c^n is given by (2.35).

Let the state and output of the reset controller during the time interval $[t_i^+, t_{i+1}]$ be denoted as $x_{i+1}(t)$ and $u_{i+1}(t)$, respectively. The jump in (2.43) indicates that a step signal $h_i(t)$ is introduced to the state $x_{i+1}(t)$ during $[t_i^+, t_{i+1}]$, given by:

$$h_i(t) = [x_{ni}(t_i^+) - x_{ni}(t_i)]h(t - t_i) = \begin{cases} |Z_n|\Delta_q^n(\omega)h(t - t_i), & \text{for even } i, \\ -|Z_n|\Delta_q^n(\omega)h(t - t_i), & \text{for odd } i, \end{cases} \quad (2.45)$$

where $h(t) := [t \geq 0]$ is a Heaviside step function.

From (1.6) and (2.45), Fig. 2.8 shows the state-space block diagram of the reset controller \mathcal{C}_r during the time interval $[t_i^+, t_{i+1}]$.

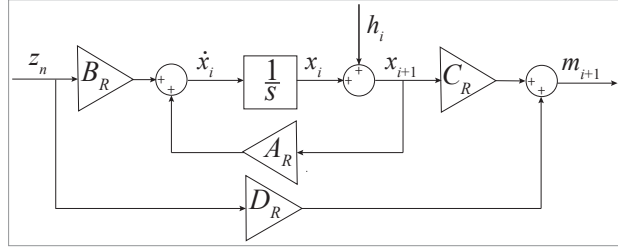


Figure 2.8: State-space block diagram of the reset controller \mathcal{C}_r during the time interval $[t_i^+, t_{i+1}]$.

The reset instant is given by $t_i = (i\pi - \angle Z_s)/\omega$, where $i \in \mathbb{Z}^+$. Within a single $2\pi/\omega$ -steady-state period, there are two reset instants: $t_i = (i\pi - \angle Z_s)/\omega$ and $t_{i+1} = ((i+1)\pi - \angle Z_s)/\omega$, separated by a reset interval of π/ω . From (2.45), at t_i , a step signal $h_i(t) = |Z_n|\Delta_q^n(\omega)h(t - t_i)$ is introduced. At the subsequent instant t_{i+1} , a step signal $h_{i+1}(t) = -h_i(t)$ is introduced. Consequently, over one steady-state period, a square wave is generated, denoted as:

$$q_n(t) = \frac{|Z_n|\Delta_q^n(\omega)}{2} q_0(t), \quad (2.46)$$

where $q_0(t)$ represents a normalized square wave shown in Fig. 2.9 and expressed as

$$q_0(t) = \frac{4}{\pi} \sum_{\eta=1}^{\infty} \left(\frac{1}{\eta} \cdot \sin(\eta\omega t + \eta\angle Z_s) \right), \quad \eta = 2k+1 (k \in \mathbb{N}), \quad (2.47)$$

Thus, the reset controller \mathcal{C}_r with a single sinusoidal input signal $z_n(t) = |Z_n|\sin(n\omega t + \angle Z_n)$ at steady states, behaves equivalently to its base-linear controller \mathcal{C}_l (given in (1.7)) with two inputs: the sinusoidal input $z_n(t)$ and the square wave $q_n(t)$ defined in (2.46), as illustrated in Fig. 2.10. The contributions from $z_n(t)$ and $q_n(t)$ to $m_o(t)$ are denoted as $m_o^z(t)$ and $m_o^q(t)$, respectively. This model serves as the foundation for deriving the HOSIDF of \mathcal{C}_r through the following steps.

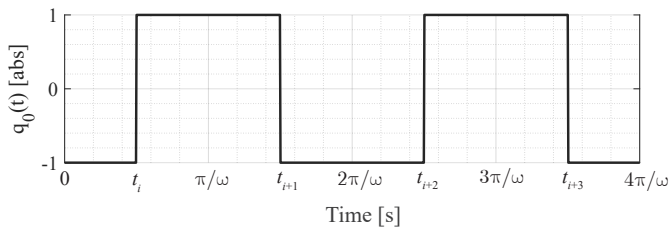


Figure 2.9: Plot of $q_0(t)$ in (2.47) over two periods.

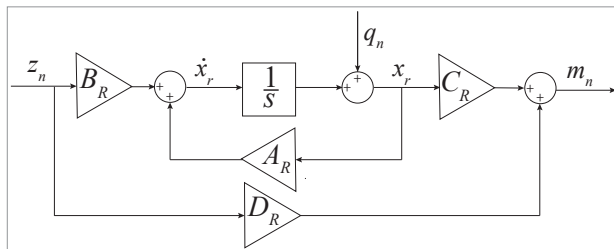


Figure 2.10: State-space block diagram of the reset controller C_r at steady states.

Under Assumption 2, the system is guaranteed to be convergent, ensuring that the trajectories of the system are integrable. This integrability implies that the system's time-domain signals have well-defined Fourier transforms. Let $Z_n(\omega)$, $Q_n(\omega)$, $M_n(\omega)$, $M_o^z(\omega)$, and $M_o^q(\omega)$ represent the Fourier transforms of the signals $z_n(t)$, $q_n(t)$, $m_o(t)$, $m_o^z(t)$, and $m_o^q(t)$, respectively.

Based on the model in Fig 2.10, $M_n(\omega)$ is given by

$$\begin{aligned} M_n(\omega) &= M_o^z(\omega) + M_o^q(\omega) \\ &= \frac{M_o^z(\omega)}{Z_n(\omega)} \cdot Z_n(\omega) + \frac{M_o^q(\omega)}{Q_n(\omega)} \cdot Q_n(\omega). \end{aligned} \quad (2.48)$$

From Fig. 2.10, when $q_n(t) = 0$, the transfer function $\frac{M_o^z(\omega)}{Z_n(\omega)}$ is given by

$$\frac{M_o^z(\omega)}{Z_n(\omega)} = C_l(\omega), \quad (2.49)$$

and when $z_n(t) = 0$, it follows that

$$\frac{M_o^q(\omega)}{Q_n(\omega)} = \Delta_x(\omega) = C_R(j\omega I - A_R)^{-1} j\omega \quad (\in \mathbb{R}^{1 \times n_c}), \quad (2.50)$$

Then, substituting (2.49) and (2.50) into (2.48), $M_n(\omega)$ is given by

$$M_n(\omega) = C_l(\omega) \cdot Z_n(\omega) + \Delta_x(\omega) \cdot Q_n(\omega). \quad (2.51)$$

From the definition of $z_n(t)$, the function $Z_n(\omega)$ is given by

$$Z_n(\omega) = |Z_n| \sum_{\eta=1}^{\infty} \mathcal{F}[\sin(n\omega t + \angle Z_n)]. \quad (2.52)$$

From (2.46) and (2.47), the function $Q_n(\omega)$ is given by

$$Q_n(\omega) = \frac{2|Z_n|\Delta_q^n(\omega)}{\pi} \sum_{\eta=1}^{\infty} \left(\frac{1}{\eta} \mathcal{F}[\sin(\eta\omega t + \eta\angle Z_s)] \right). \quad (2.53)$$

By substituting (2.52) and (2.53) into (2.51), $M_n(\omega)$ is given by

$$M_n(\omega) = M_l^n(\omega) + \sum_{\eta=1}^{\infty} M_\rho^\eta(\omega), \quad (2.54)$$

where

$$\begin{aligned} M_l^n(\omega) &= C_l(n\omega) \cdot Z_n(\omega), \\ M_\rho^\eta(\omega) &= \frac{2|Z_n|\Delta_x(\eta\omega)\Delta_q^\eta(\omega)}{\eta\pi} \cdot \mathcal{F}[\sin(\eta\omega t + \eta\angle Z_s)]. \end{aligned} \quad (2.55)$$

Here, we concludes the proof. \square

2.C Proof of Theorem 2

Proof. Consider a reset controller C_r described by the state-space equation (1.6). The controller processes an input signal $z_o(t)$ and a reset-triggered signal $z_s(t)$, given by

$$\begin{aligned} z_o(t) &= |Z_o| \sin(\omega t + \angle Z_o), \\ z_s(t) &= |Z_o| |C_s(\omega)| \sin(\omega t + \angle Z_o + \angle C_s(\omega)). \end{aligned} \quad (2.56)$$

The reset controller C_r generates the output signal $m_o(t)$, which includes n -order harmonics, expressed as $m_o(t) = \sum_{n=1}^{\infty} m_o^n(t)$. To derive the Higher-Order Sinusoidal Input Describing Function (HOSIDF) for the reset controller C_r , the ‘‘Virtual Harmonics Generator’’ approach is first employed to allow the input signal $z_o(t)$ to produce n harmonics, given by:

$$z_o^n(t) = |Z_o| \sin(n\omega t + n\angle Z_o). \quad (2.57)$$

From Theorem 1, the Fourier transform of the output signal $m_o(t)$ denoted as $M_o(\omega)$ is given by

$$M_o(\omega) = M_l(\omega) + \sum_{n=1}^{\infty} M_\rho^n(\omega), \quad n = 2k + 1, k \in \mathbb{N}, \quad (2.58)$$

where

$$\begin{aligned} M_l(\omega) &= C_l(\omega)Z_o(\omega), \\ M_\rho^n(\omega) &= \Delta_x(n\omega)Q^n(\omega), \\ \Delta_l(\omega) &= (j\omega I - A_R)^{-1}B_R, \\ \Delta_x(n\omega) &= C_R(jn\omega I - A_R)^{-1}jn\omega I, \\ Z_o^n(\omega) &= |Z_o| \mathcal{F}[\sin(n\omega t + n\angle Z_o)], \\ Q^n(\omega) &= 2Z_o^n(\omega)\Delta_q(\omega)e^{jn\angle C_s(\omega)}/(n\pi), \\ \Delta_c^1(\omega) &= |\Delta_l(\omega)| \sin(\angle \Delta_l(\omega) - \angle C_s(\omega)), \\ \Delta_q(\omega) &= (I + e^{A_R\pi/\omega})(A_\rho e^{A_R\pi/\omega} + I)^{-1}(A_\rho - I)\Delta_c^1(\omega). \end{aligned} \quad (2.59)$$

Note that in (2.58), η in Theorem 1 is replaced with the notation n . Both notations represent odd numbers, and this change does not affect the results. The notation n is used specifically for consistency with the closed-loop analysis presented in the following chapters.

From (2.58), $M_o(\omega)$ can be written as the format of the sum of its harmonics, expressed as:

$$M_o(\omega) = \sum_{n=1}^{\infty} M_o^n(\omega), \quad (2.60)$$

where

$$M_o^n(\omega) = \begin{cases} M_l(\omega) + M_\rho^1(\omega), & \text{for } n = 1, \\ M_\rho^n(\omega), & \text{for odd } n > 1, \\ 0, & \text{for even } n \geq 2. \end{cases} \quad (2.61)$$

The n -th HOSIDF for the reset controller C_r is defined as $C_r^n(\omega)$ to describe the transfer function from the input harmonics $z_o^n(t)$ to the output signal $m_o^n(t)$. From (2.58) and (2.61), $C_r^n(\omega)$ is given by

$$C_r^n(\omega) = \frac{M_o^n(\omega)}{Z_o^n(\omega)} = \begin{cases} C_l(\omega) + C_\rho^1(\omega), & \text{for } n = 1 \\ C_\rho^n(\omega), & \text{for odd } n > 1, \\ 0, & \text{for even } n \geq 2, \end{cases} \quad (2.62)$$

where

$$C_\rho^n(\omega) = 2\Delta_x(n\omega)\Delta_q(\omega)e^{jn\angle C_s(\omega)}/(n\pi). \quad (2.63)$$

Thus, the proof is concluded. \square

2.D Proof of Theorem 3

Proof. Consider an open-loop reset control system with an input $e_o(t) = |E|\sin(\omega t + \angle E)$ and output $y_o(t)$ as depicted in Fig. 2.1, satisfying Assumption 1. This proof derives the HOSIDFs for the open-loop system. The derivation process proceeds sequentially from the input signal $e_o(t)$ on the left to the output signal $y_o(t)$ on the right.

First, the block C_1 receives the input $e_o(t)$ and generates the output signal $z_o(t)$. Define $e_o(t)$ with its Fourier transform $E_o(\omega)$. Then, the output signal $z_o(t)$ and its Fourier transform $Z_o(\omega)$ are given by:

$$\begin{aligned} z_o(t) &= |EC_1(\omega)|\sin(\omega t + \angle E + \angle C_1(\omega)), \\ Z_o(\omega) &= E_o(\omega)C_1(\omega). \end{aligned} \quad (2.64)$$

From (2.57) and (2.64), $Z_o^n(\omega)$ is given by

$$Z_o^n(\omega) = E_o(\omega)C_1(\omega)e^{j(n-1)(\angle C_1(\omega) + \angle E)}. \quad (2.65)$$

Next, the signal $z_o(t)$ in (2.64) is filtered by the block C_2 , producing the output signal $a_o(t)$. The signal $a_o(t)$ and its Fourier transform $A_o(\omega)$ are given by the following equations:

$$\begin{aligned} a_o(t) &= |EC_1(\omega)C_2(\omega)|\sin(\omega t + \angle E + \angle C_1(\omega) + \angle C_2(\omega)), \\ A_o(\omega) &= Z_o^1(\omega)C_2(\omega) = E_o(\omega)C_1(\omega)C_2(\omega). \end{aligned} \quad (2.66)$$

From Fig. 2.1, the signal $v_o(t)$ and its Fourier transform denoted as $V_o(\omega)$ are given by

$$\begin{aligned} v_o(t) &= a_o(t) + m_o(t), \\ V_o(\omega) &= A_o(\omega) + M_o(\omega). \end{aligned} \quad (2.67)$$

From (2.65) and (2.67), $V_o(\omega)$ is given by

$$V_o(\omega) = E_o(\omega)\mathcal{C}_1(\omega)\mathcal{C}_2(\omega) + \sum_{n=1}^{\infty} E_o(\omega)\mathcal{C}_1(\omega)e^{j(n-1)(\angle\mathcal{C}_1(\omega)+\angle E)}\mathcal{C}_r^n(\omega). \quad (2.68)$$

From (2.68), $V_o(\omega)$ can be written as the sum of its harmonics, denoted by $V_o^n(\omega)$, expressed as:

$$V_o(\omega) = \sum_{n=1}^{\infty} V_o^n(\omega), \quad (2.69)$$

where

$$V_o^n(\omega) = \begin{cases} E_o(\omega)\mathcal{C}_1(\omega)[\mathcal{C}_2(\omega) + \mathcal{C}_r^1(\omega)], & \text{for } n = 1, \\ E_o(\omega)\mathcal{C}_1(\omega)e^{j(n-1)(\angle\mathcal{C}_1(\omega)+\angle E)}\mathcal{C}_r^n(\omega), & \text{for odd } n > 1, \\ 0, & \text{for even } n \geq 2. \end{cases} \quad (2.70)$$

The output signal $y_o(t)$ of the open-loop system shown in Fig. 2.1 exhibits nonlinear behavior and comprises n harmonic components, defined as $y_o(t) = \sum_{n=1}^{\infty} y_o^n(t)$. Let $Y_o(\omega)$ and $Y_o^n(\omega)$ denote the Fourier transforms of $y_o(t)$ and $y_o^n(t)$, respectively. Based on Fig. 2.1, $Y_o(\omega)$ and $Y_o^n(\omega)$ are given by

$$\begin{aligned} Y_o(\omega) &= \sum_{n=1}^{\infty} Y_o^n(\omega), \\ Y_o^n(\omega) &= V_o^n(\omega)\mathcal{C}_3(n\omega)\mathcal{P}(n\omega). \end{aligned} \quad (2.71)$$

By employing the ‘‘Virtual Harmonics Generator (VHG)’’ [12], the input signal $e_o(t) = |E|\sin(\omega t + \angle E)$ generates n harmonics, given by

$$e_o^n(t) = |E|\sin(n\omega t + n\angle E). \quad (2.72)$$

Let $E_o(\omega)$ and $E_o^n(\omega)$ denote the Fourier transforms of $e_o(t)$ and $e_o^n(t)$, respectively. From (2.72), $E_o^n(\omega)$ is given by

$$E_o^n(\omega) = E_o(\omega)e^{j(n-1)\angle E}. \quad (2.73)$$

Thus, from (2.70), (2.71), and (2.73), the n -th transfer function $\mathcal{L}_n(\omega)$ for the open-loop reset system is given by

$$\mathcal{L}_n(\omega) = \frac{Y_o^n(\omega)}{E_o^n(\omega)} = \begin{cases} \mathcal{C}_1(\omega)[\mathcal{C}_r^1(\omega) + \mathcal{C}_2(\omega)]\mathcal{C}_3(\omega)\mathcal{P}(\omega), & \text{for } n = 1, \\ \mathcal{C}_1(\omega)e^{j(n-1)\angle\mathcal{C}_1(\omega)}\mathcal{C}_r^n(\omega)\mathcal{C}_3(n\omega)\mathcal{P}(n\omega), & \text{for odd } n > 1, \\ 0, & \text{for even } n \geq 2. \end{cases} \quad (2.74)$$

Thus, the proof is concluded. \square

3

Identifying the Reliability of Closed-Loop SIDF Analysis

The Sinusoidal Input Describing Function (SIDF) is an effective tool for control system analysis and design, with its accuracy directly influencing the performance of the resulting control systems. Current SIDF analysis methods are based on the assumption of two reset actions per steady-state cycle in sinusoidal-input closed-loop reset control systems. However, when applied to systems that exhibit multiple (more than two) reset actions per cycle, these SIDF methods will yield inaccurate results. To address this challenge, this chapter presents a method for distinguishing between two-reset and multiple-reset systems. This identification method is used for determining the reliability of SIDF analysis in closed-loop reset systems. The effectiveness and time-saving benefits of this method are demonstrated through simulations and experiments on a precision motion stage, validated across six case studies.

 This chapter is based on the paper:
Zhang, Xinxin, and S. Hassan HosseinNia. "Enhancing the Reliability of Closed-Loop Describing Function Analysis for Reset Control Applied to Precision Motion Systems." arXiv preprint arXiv:2412.00502 (2024).

3.1 Introduction

While reset control enhances gain-phase margins for the first-order harmonic, it also introduces high-order (beyond the first order) harmonics. To evaluate these harmonics in closed-loop reset systems, Higher-Order Sinusoidal Input Describing Function (HOSIDF) analysis is effectively used [1–3]. The HOSIDF analysis quantifies the magnitude and phase of the harmonics in reset systems by measuring the systems' steady-state responses to sinusoidal inputs over a frequency range [1]. When only the first-order harmonic is considered and high-order harmonics are neglected, this is referred as the First-Order Sinusoidal Input Describing Function (FOSIDF) [4]. In this chapter, both HOSIDF and FOSIDF are collectively termed SIDF analysis methods.

Current SIDF analysis methods for closed-loop reset systems [2–4] assume that only two reset actions per steady-state cycle in sinusoidal-input reset systems. However, sinusoidal-input closed-loop reset systems can exhibit either two reset actions or multiple (more than two) reset actions per steady-state cycle, referred to as two-reset systems and multiple-reset systems, respectively. The two-reset assumption in SIDF analysis introduces inaccuracies when applied to multiple-reset systems, as demonstrated in Section 3.2. In such cases, the validity of the SIDF analysis is compromised, and thus the reliability of the reset control system design based on this analysis is not guaranteed.

To improve the reliability of SIDF analysis in closed-loop reset systems, this chapter introduces a method to identify frequency ranges where the validity of SIDF analysis is compromised due to multiple resets. To do so, we begin by deriving piecewise expressions for the steady-state trajectories of sinusoidal-input closed-loop reset control systems. These expressions are then used to evaluate whether the two-reset assumption in SIDF analysis holds for closed-loop systems. Unlike previous methods, which required extensive time-domain simulations across the entire frequency spectrum—making the process computationally intensive—the proposed approach simplifies the evaluation. Experimental results from six case studies demonstrate the efficiency and time-saving advantages of the new method.

The remainder of this chapter is organized as follows: Section 3.2 outlines the research problem through illustrative examples. Section 3.3 presents a method to differentiate between two-reset and multiple-reset actions in sinusoidal-input closed-loop reset systems, establishing conditions for applying SIDF analysis to two-reset systems. Section 3.4 validates the proposed method through simulations and experimental results. Finally, Section 3.5 provides concluding remarks.

3.2 Problem Statement via Illustrative Examples

This section uses an example to illustrate the research problem. PID controllers are commonly employed in mechatronics applications, and when the integrator in the PID controller is replaced with the generalized Clegg Integrator (CI), the system becomes a reset PID control system. The generalized CI is defined by (1.6), with the matrices $A_\rho = \gamma \in (-1, 1)$ and $(A_R, B_R, C_R, D_R) = (0, 1, 1, 0)$. In this example, a reset PID control system is employed to demonstrate the research problems addressed in this chapter.

The block diagram of the reset PID control system used in this chapter is depicted

in Fig. 3.1. The parameter ζ denotes the number of integrators in the system, with this chapter utilizes cases where $\zeta = 0$ and $\zeta = 1$, referred to as Proportional-Clegg Integrator-Derivative (PCID) and PCI-PID control systems, respectively. More discussion on employing multiple integrators ($\zeta > 1$) is beyond the scope of this work and can be found in [5].

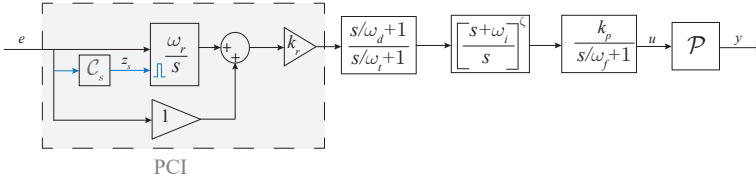


Figure 3.1: Block diagram of the reset PID control system.

A PCID control system is designed as the illustrative example with the following parameters: $k_p = 17.8$, $\omega_c = 300\pi$ [rad/s], $\omega_r = 0.1\omega_c$, $k_r = 0.85$, $\gamma = 0$, $\omega_d = \omega_c/3.8$, $\omega_t = 3.8\omega_c$, $\omega_f = 10\omega_c$, $\zeta = 0$, and $C_s = 1$. A PID controller is also designed for comparison with the following parameters: $k_p = 17.8$, $\omega_c = 300\pi$ [rad/s], $\omega_i = 0.084\omega_c$, $\omega_d = \omega_c/3.8$, $\omega_t = 3.8\omega_c$, and $\omega_f = 10\omega_c$. In this chapter, the bandwidth frequency refers to the crossover frequency of the first-order harmonic of the control system.

The Bode plots for the PID and the first-order harmonic of the PCID control systems are presented in Fig. 3.2. To ensure a fair comparison, both the PID and PCID controllers are designed to maintain the same bandwidth of 100 Hz and a phase margin of 50° with the plant $\mathcal{P}(s)$ in (1.1). However, the PCID controller exhibits a higher gain at frequencies below 100 Hz and a reduced gain at frequencies above 100 Hz. This design aims to enhance low-frequency tracking and disturbance rejection, and high-frequency noise suppression.

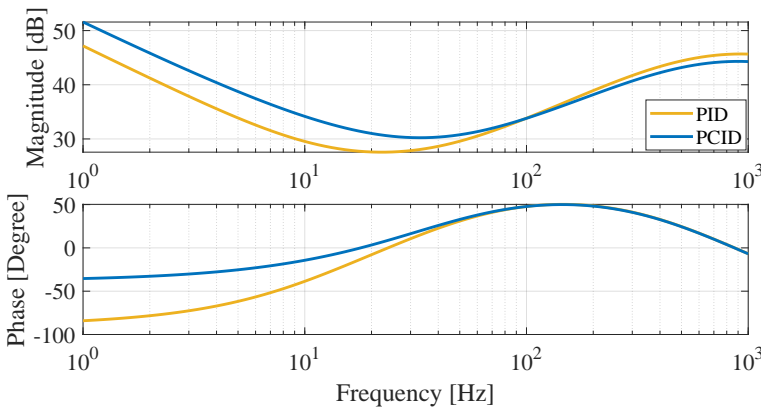


Figure 3.2: Bode plots of the PID and the first-order harmonic of the PCID control systems.

To evaluate the performance of closed-loop reset control systems, SIDF analysis is commonly used. Consider a closed-loop reset system with a sinusoidal input

$r(t) = |R|\sin(\omega t)$, which satisfies Assumption 2. The magnitude of the closed-loop sensitivity function $|\mathcal{S}(\omega)|$ for the PCID control system, analyzed using SIDF analysis [4], is presented in Fig. 3.3. This analytical result is validated by comparing it with the simulated values of $|\mathcal{S}(\omega)|$, obtained by computing $\|e\|_\infty/\|r\|_\infty$ at each frequency ω . Here, $e(t)$ represents the steady-state error, and $r(t)$ denotes the input signal.

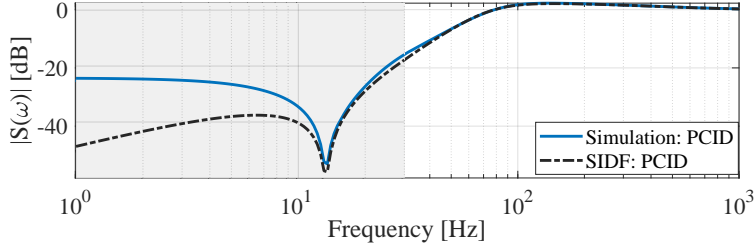


Figure 3.3: The value of $|\mathcal{S}(\omega)|$ in the PCID control system, obtained from simulation and the SIDF analysis. Multiple-reset and two-reset systems are shaded in gray and white, respectively.

In closed-loop reset systems with a sinusoidal input $r(t) = |R|\sin(\omega t)$, a two-reset system is defined by exactly two reset events within each $2\pi/\omega$ steady-state cycle, whereas a multiple-reset system has more than two reset events per cycle. In Fig. 3.3, the region associated with multiple-reset systems is shaded in gray, where notable discrepancies between SIDF analysis and simulation results are observed. These differences arise because the two-reset assumption in the SIDF analysis, does not hold in systems exhibiting multiple-reset actions.

Hence, to ensure the reliability of the SIDF analysis for closed-loop reset systems, it is crucial to establish a two-reset condition. This chapter addresses this issue by the following contribution: Consider a closed-loop reset system subjected to a sinusoidal input signal defined by $r(t) = |R|\sin(\omega t)$, where $|R|$ represents the amplitude and ω denotes the frequency. As ω sweeps through the operational frequency range, the proposed method identifies the frequency ranges where multiple reset actions lead to deviations in the SIDF analysis, as illustrated by the gray area in Fig. 3.3.

3.3 Method for Identifying the Reliability of SIDF Analysis

This section introduces two main contributions. First, Lemma 2 provides the piecewise expressions for the steady-state trajectories of sinusoidal-input closed-loop reset systems. Building on these expressions, Theorem 4 presents a method for identifying the frequency ranges corresponding to multiple-reset and two-reset actions in sinusoidal-input closed-loop reset systems.

3.3.1 Piecewise Expressions for Sinusoidal-Input Reset Systems

Consider a closed-loop reset system with a sinusoidal input $r(t) = |R|\sin(\omega t)$ and satisfying Assumption 2. In order to conduct steady-state analysis, to establish a

reference point for one steady-state cycle is needed. This reference point $t_0 = 0$ is defined at the time instant where $r(t_0) = 0$ and $\dot{r}(t_0) > 0$.

Lemma 2 provides a piecewise expression of steady-state trajectories in sinusoidal-input closed-loop reset systems.

Lemma 2. Consider a closed-loop reset control system as shown in Fig. 1.8, with a sinusoidal reference input $r(t) = |R|\sin(\omega t)$, and satisfying Assumptions 2. Within one steady-state period $(0, 2\pi/\omega]$, the reset instant t_i , at which $z_s(t_i) = 0$, divides the system trajectories into piecewise functions. Let $x_i(t)$, $z_i(t)$, and $z_s^i(t)$ denote the state, reset input, and reset-triggered signal, within the intervals $(t_{i-1}, t_i]$, where $i \in \mathbb{Z}^+$, respectively. They are expressed as follows:

$$\begin{aligned} x_{i+1}(t) &= x_i(t) - h_s(t - t_i)x_i(t_i), \\ z_{i+1}(t) &= z_i(t) - h_\alpha(t - t_i)x_i(t_i), \\ z_s^{i+1}(t) &= z_s^i(t) - h_\beta(t - t_i)x_i(t_i), \end{aligned} \quad (3.1)$$

where

$$\begin{aligned} h_s(t) &= \mathcal{F}^{-1}[\mathcal{T}_s(\omega)], \\ h_\alpha(t) &= \mathcal{F}^{-1}[\mathcal{T}_\alpha(\omega)], \\ \mathcal{T}_\alpha(\omega) &= \mathcal{C}_\sigma(\omega)\mathcal{C}_R\mathcal{T}_s(\omega), \\ \mathcal{S}_l(\omega) &= 1/(1 + \mathcal{L}_l(\omega)), \\ h_\beta(t) &= \mathcal{F}^{-1}[\mathcal{C}_s(\omega)\mathcal{T}_\alpha(\omega)], \\ \mathcal{C}_\sigma(\omega) &= \mathcal{C}_3(\omega)\mathcal{P}(\omega)\mathcal{C}_4(\omega)\mathcal{C}_1(\omega), \\ \mathcal{T}_s(\omega) &= \mathcal{S}_l(\omega)(j\omega I - A_R)^{-1}(A_p - I), \\ \mathcal{L}_l(\omega) &= \mathcal{C}_1(\omega)(\mathcal{C}_l(\omega) + \mathcal{C}_2(\omega))\mathcal{C}_3(\omega)\mathcal{P}(\omega)\mathcal{C}_4(\omega). \end{aligned} \quad (3.2)$$

Proof. The proof is provided in Appendix 3.A. □

3.3.2 Identifying Two-Reset Conditions in SIDF Analysis

Consider a closed-loop reset system with a sinusoidal input $r(t) = |R|\sin(\omega t)$ that satisfies Assumption 2. Let t_1 denote the first reset instant within a single steady-state cycle. Before reaching steady-state responses, the system experiences transient responses. Although transient responses do not influence the steady-state trajectories in linear systems, they do affect the steady-state trajectories of reset systems. The zero-crossings of the steady-state trajectory during the steady-state interval $(0, t_1)$ affect the multiple-reset identification results. To streamline the analysis and obviate the need for transient response calculations, the following assumption is introduced to consider the transient effects during the steady-state time interval $(0, t_1)$ as negligible, by assuming that during this time interval, the reset system dynamics are identical to its BLS.

Assumption 3. The closed-loop reset control system depicted in Fig. 1.8, under the sinusoidal reference input $r(t) = |R|\sin(\omega t)$ and satisfying Assumption 2, follows the same steady-state trajectory as its BLS during the time interval $(0, t_1)$, where t_1 represents the first reset instant of this system within one steady-state cycle.

Assumption 3 may introduce deviations in multiple-reset system identification due to transient effects. In practical reset system designs, these transient effects are often mitigated using techniques such as feedforward control and high-bandwidth feedback loops. Moreover, these deviations will be assessed through case studies in Section 3.4.

Define

$$\begin{aligned} \text{sign}(x) &= \begin{cases} 0, & \text{if } x > 0, \\ 1, & \text{if } x \leq 0, \end{cases} \\ \mathcal{S}_{I_s}(\omega) &= \mathcal{C}_s(\omega)\mathcal{C}_1(\omega)\mathcal{S}_{bl}(\omega), \\ \Theta_{bl}(\omega) &= (j\omega I - A_R)^{-1}B_R\mathcal{C}_1(\omega)\mathcal{S}_{bl}(\omega), \\ t_m &= \angle\mathcal{S}_{I_s}(\omega)/\omega + \pi/\omega \cdot \text{sign}(\mathcal{S}_{I_s}(\omega)), \\ \Theta_s(\omega) &= |\Theta_{bl}(\omega)|\sin(\angle\mathcal{S}_{I_s}(\omega) - \angle\Theta_{bl}(\omega)). \end{aligned} \quad (3.3)$$

Under Assumption 3, Theorem 4 and Remark 2 delineate the condition for ensuring the two-reset condition in the SIDF analysis methods for closed-loop reset control systems [2-4].

Theorem 4. Consider a closed-loop reset control system illustrated in Fig. 1.8 with a sinusoidal reference input $r(t) = |R|\sin(\omega t)$, satisfying Assumption 2 and 3. The system is a multiple-reset system if there exists at least one time instant $t_\delta \in (0, t_m)$, such that:

$$\Delta(t_\delta) = |\mathcal{S}_{I_s}(\omega)|\sin(\omega t_\delta) + h_\beta(t_\delta)\Theta_s(\omega) = 0, \quad (3.4)$$

where $\mathcal{S}_{I_s}(\omega)$ and $\Theta_s(\omega)$ are given in (3.3), and $h_\beta(t)$ is given in (3.2).

Proof. The proof is provided in Appendix 3.B. □

Theorem 4 is applicable to model-based reset control. To use it, first, the FRF data of the plant $\mathcal{P}(s)$, is measured, and system identification methods are employed to derive the system model. Then, Theorem 4 is applied to identify the multiple-reset frequency range in sinusoidal-input closed-loop reset systems. However, if the system identification is inaccurate, the accuracy of Theorem 4 may also be compromised. Additionally, deviations may arise from Assumption 3 if the transient response exhibits large impact on the steady-state behavior. These deviations will be discussed and validated through case studies in Section 3.4.

Based on Theorem 4, Remark 2 establishes the two-reset condition for the SIDF analysis of closed-loop reset systems.

Remark 2. The SIDF analysis for closed-loop reset systems assumes a two-reset condition. This condition holds if, for all frequencies ω within the SIDF analysis frequency range, the criteria outlined in Theorem 4 is not met.

3.4 Results: Validation of Two-Reset Conditions

In this section, simulations and experiments are conducted to validate the effectiveness of the approach introduced in Theorem 4. Specifically, six CI-based reset control systems are designed and implemented on the precision motion system $\mathcal{P}(s)$, as defined in (1.1), serving as case studies.

CI-based reset control systems are selected for this validation due to their straightforward implementation within the classical PID control framework, underscoring their potential for practical applications. However, these systems often experience multiple-reset actions in SIDF analysis [2], which complicates reliable analysis and hinders their broader practical adoption. The systems are configured with the following parameters:

1. Case₁: a PCID control system, using the same design parameters outlined in Section 3.2.
2. Case₂: C_r is built on a BLC $C_l(s) = 125.7/s$ with $\gamma = 0$, $C_1(s) = C_2(s) = C_s(s) = C_4(s) = 1$, $C_3(s) = 40.0 \cdot (s/711.1 + 1)/(s/(8.8 \times 10^3) + 1) \cdot 1/(s/(2.5 \times 10^4) + 1)$.
3. Case₃: C_r is built on a BLC $C_l(s) = 125.7/s$ with $\gamma = 0$, $C_1(s) = C_2(s) = C_s(s) = C_4(s) = 1$, $C_3(s) = 25.0 \cdot (s/327.7 + 1)/(s/(4.8 \times 10^3) + 1) \cdot 1/(s/(1.3 \times 10^4) + 1)$.
4. Case₄: C_r is built on a BLC $C_l(s) = 47.1/s$ with $\gamma = 0$, $C_1(s) = C_2(s) = C_s(s) = C_4(s) = 1$, $C_3(s) = 24.0 \cdot (s/216.6 + 1)/(s/(4.1 \times 10^3) + 1) \cdot (1 + 94.2/s) \cdot 1/(s/(9.4 \times 10^3) + 1)$.
5. Case₅: C_r is built on a BLC $C_l(s) = 94.2/s$ with $\gamma = 0.3$, $C_1(s) = C_2(s) = C_s(s) = C_4(s) = 1$, $C_3(s) = 20.5 \cdot (s/196.1 + 1)/(s/(4.5 \times 10^3) + 1) \cdot (1 + 94.2/s) \cdot 1/(s/(9.4 \times 10^3) + 1)$.
6. Case₆: reset controller has a BLC $C_l = (30\pi)/s$ with the reset value $\gamma = 0$, $C_1(s) = 1/(s/(150\pi) + 1)$, $C_s(s) = (s+1)/(s+2)$, $C_2(s) = 1$, $C_3(s) = 20.5 \cdot (s/(150\pi) + 1)/(s/(3000\pi) + 1) \cdot (s/(62.5\pi) + 1)/(s/(1440\pi) + 1) \cdot (1 + 15\pi/s) \cdot 1/(s/(3000\pi) + 1)$.

All systems have been verified to be stable and convergent.

In these six case studies, multiple-reset actions are observed at low frequencies. Let f_b represent the boundary frequency distinguishing two-reset and multiple-reset systems, as determined by Theorem 4, and f'_b denote the boundary frequency identified through simulations. The deviations between these values, expressed as $|f_b - f'_b|$, are summarized in Table 3.1. Both prediction and simulation methods sweep the frequency range from 1 Hz to 50 Hz with a step of 1 Hz. At each frequency, the sampling rate is set to 10^4 . The analysis reveals discrepancies between 1 and 4 Hz across the cases, mainly due to the exclusion of transient response effects, as outlined in Assumption 3. In practice, the reset system should be designed to minimize transient response effects, for instance, by ensuring an appropriate bandwidth.

Despite deviations of 1–4 Hz between the simulation results and the predictions from Theorem 4, the prediction method offers substantial time-saving benefits. Identifying multiple-reset occurrences through simulation or using the numerical method in [6] requires calculating the time response at each frequency across the entire operational frequency range via a for loop in MATLAB, followed by counting the reset instants per steady-state cycle. In contrast, Theorem 4 streamlines this process. Table 3.1 presents a comparison of computation times for the prediction and simulation methods. Results show that Theorem 4 achieves a reduction in computation time by around 300-fold compared to the simulation approach.

If extreme precise identification of multiple-reset actions is needed, Theorem 4 can be utilized for initial estimation. Subsequent simulations can then focus on

Table 3.1: The Theorem 4-predicted and simulated boundary frequencies f_b and f'_b that separate the two-reset and multiple-reset systems, as well the computation time in Case₁ to Case₆.

Systems	f_b [Hz]	f'_b [Hz]	$ f_b - f'_b $ [Hz]	Prediction Time [s]	Simulation Time [s]
Case ₁	30	32	2	1.38	356.63
Case ₂	39	40	1	1.00	422.51
Case ₃	37	41	4	1.32	386.97
Case ₄	34	32	2	1.56	413.28
Case ₅	37	33	4	1.28	502.76
Case ₆	38	42	4	0.96	370.60

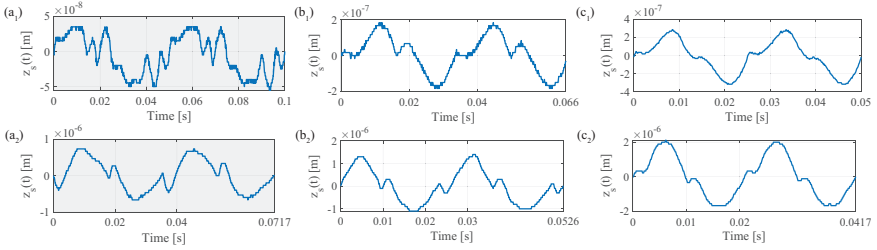


Figure 3.4: Experimental measured reset triggered signal $z_s(t)$ for reset control systems: Case₁ with the input frequencies at (a₁) 20 Hz, (b₁) $f_b = 30$ Hz, and (c₁) 40 Hz. Steady-state reset triggered signal $z_s(t)$ for Case₆ with the input frequencies at (a₂) 28 Hz, (b₂) $f_b = 38$ Hz, and (c₂) 48 Hz. The regions corresponding to multiple-reset systems are shaded in gray.

the predicted frequency range, ensuring both accuracy and efficiency in pinpointing multiple-reset occurrences.

To further validate Theorem 4, Figure 3.4 presents experimentally measured reset-triggered signals $z_s(t)$ for systems Case₁ and Case₆ in response to a reference input of $r(t) = 1 \times 10^{-6} \sin(2\pi ft)$ [m]. Testing was conducted at the predicted threshold frequency $f = f_b$ Hz, as well as at $f = f_b \pm 10$ Hz, over two steady-state cycles. The results show that at $(f_b - 10)$ Hz, the systems exhibit multiple-reset behavior, while at $(f_b + 10)$ Hz, they display two reset instants per cycle, characteristic of a two-reset system. At the predicted threshold frequency f_b , the systems demonstrate 3–4 reset instants per cycle, indicating a transitional behavior between two-reset and multiple-reset categories. These observations confirm that f_b serves as a boundary frequency for distinguishing two-reset from multiple-reset actions, thereby validating Theorem 4 within a 10 Hz tolerance.

3.5 Conclusion

In conclusion, this chapter introduces a method for identifying multiple-reset and two-reset regions in sinusoidal-input closed-loop reset systems, providing engineers with a practical tool to evaluate the reliability of Sinusoidal Input Describing Function (SIDF) analysis. The effectiveness and time-saving advantages of this method have been validated through simulations and experimental results across six case studies.

Bibliography

- [1] P. Nuij, O. Bosgra, and M. Steinbuch. “Higher-order sinusoidal input describing functions for the analysis of non-linear systems with harmonic responses”. In: *Mechanical Systems and Signal Processing* 20.8 (2006), pp. 1883–1904.
- [2] N. Saikumar, K. Heinen, and S. H. HosseinNia. “Loop-shaping for reset control systems: A higher-order sinusoidal-input describing functions approach”. In: *Control Engineering Practice* 111 (2021), p. 104808.
- [3] X. Zhang, M. B. Kaczmarek, and S. H. HosseinNia. “Frequency response analysis for reset control systems: Application to predict precision of motion systems”. In: *Control Engineering Practice* 152 (2024), p. 106063. ISSN: 0967-0661.
- [4] Y. Guo, Y. Wang, and L. Xie. “Frequency-domain properties of reset systems with application in hard-disk-drive systems”. In: *IEEE Transactions on Control Systems Technology* 17.6 (2009), pp. 1446–1453.
- [5] N. Karbasizadeh and S. H. HosseinNia. “Stacking Integrators Without Sacrificing the Overshoot in Reset Control Systems”. In: *2022 American Control Conference (ACC)*. IEEE. 2022, pp. 893–899.
- [6] A. A. Dastjerdi, A. Astolfi, N. Saikumar, N. Karbasizadeh, D. Valerio, and S. H. HosseinNia. “Closed-loop frequency analysis of reset control systems”. In: *IEEE Transactions on Automatic Control* 68.2 (2022), pp. 1146–1153.
- [7] A. Pavlov, N. Van De Wouw, and H. Nijmeijer. *Uniform output regulation of nonlinear systems: a convergent dynamics approach*. Vol. 205. Springer, 2006.

Appendix

3.A Proof of Lemma 2

Proof. Consider a closed-loop reset control system in Fig. 1.8 under a sinusoidal reference input $r(t) = |R|\sin(\omega t)$, and satisfying Assumption 2.

Within each steady-state period $(0, 2\pi/\omega]$, the reset instant t_i is defined as the time at which the reset-triggered signal $z_s(t_i)$ reaches zero. Let $x_i(t)$, $m_i(t)$, $z_i(t)$, and $z_s^i(t)$ represent the state of the reset controller \mathcal{C}_r , the reset output, the reset input, and the reset-triggered signal, during the intervals $(t_{i-1}, t_i]$, where $i \in \mathbb{Z}^+$, respectively. This proof presents the piecewise expressions for the steady-state trajectories of the system, following the three steps outlined below.

Step 1: Derive the Piecewise Expression for $x_i(t)$.

From (1.6), the system operates without any reset actions during the time interval $(t_{i-1}, t_i]$. At the reset instant $t_i \in J$, the state $x_i(t_i)$ undergoes a reset (or jump) to a new

state $x_i(t_i^+)$, given by

$$x_i(t_i^+) = A_\rho x_i(t_i). \quad (3.5)$$

The jump in (3.5) introduces a step input signal $h_i(t)$ into the system, impacting the trajectories during the subsequent time interval $(t_i, t_{i+1}]$ [3]. The signal $h_i(t)$ is given by

$$h_i(t) = [x_i(t_i^+) - x_i(t_i)]h(t - t_i) = (A_\rho - I)x_i(t_i)h(t - t_i), \quad (3.6)$$

where $h(t)$ is a unit step signal given by

$$h(t) = \begin{cases} 1, & t > 0 \\ 0, & t \leq 0 \end{cases}, \quad (3.7)$$

with the Fourier transform $H(\omega) = \mathcal{F}[h(t)] = (j\omega)^{-1}$.

Based on (1.6) and (3.6), the block diagram of the controller \mathcal{C} for the time interval $(t_i, t_{i+1}]$ is illustrated in Fig. 3.5.

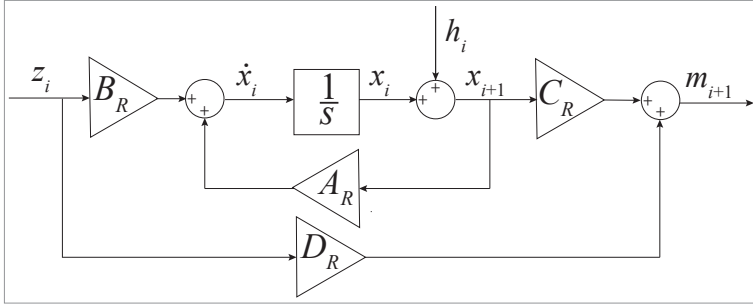


Figure 3.5: State-space block diagram of \mathcal{C}_r during the time interval $(t_i, t_{i+1}]$.

From Fig. 3.5, the signal $x_{i+1}(t)$ is derived from two inputs: $z_i(t)$ and $h_i(t)$. The respective contributions to $x_{i+1}(t)$ from $z_i(t)$ and $h_i(t)$ are labeled as $x_{i+1}^z(t)$ and $x_{i+1}^h(t)$, respectively.

Under Assumption 2, the system's steady-state trajectories are guaranteed to have well-defined Fourier transforms. This integrability implies that the system's time-domain signals have well-defined Fourier transforms. Let $Z_i(\omega)$, $H_i(\omega)$, $X_i(\omega)$, $X_{i+1}^z(\omega)$, and $X_{i+1}^h(\omega)$ represent the Fourier transforms of the signals $z_i(t)$, $h_i(t)$, $x_i(t)$, $x_{i+1}^z(t)$, and $x_{i+1}^h(t)$, respectively.

Since no reset actions occur during the time interval $(t_i, t_{i+1}]$, the superposition law holds. Therefore, $X_{i+1}(\omega)$ is express as

$$\begin{aligned} X_{i+1}(\omega) &= X_{i+1}^z(\omega) + X_{i+1}^h(\omega) \\ &= \frac{X_{i+1}^z(\omega)}{Z_i(\omega)} \cdot Z_i(\omega) + \frac{X_{i+1}^h(\omega)}{H_i(\omega)} \cdot H_i(\omega). \end{aligned} \quad (3.8)$$

Based on Figs. 1.8 and 3.5, within the closed-loop reset system, when $h_i(t) = 0$, we have

$$\frac{X_{i+1}^z(\omega)}{Z_i(\omega)} = (j\omega I - A_R)^{-1} B_R, \quad (3.9)$$

and when $z_i(t) = 0$, it follows that

$$\frac{X_{i+1}^h(\omega)}{H_i(\omega)} = \mathcal{S}_l(\omega)(j\omega I - A_R)^{-1}j\omega, \quad (3.10)$$

By combining (3.8), (3.9), and (3.10), we derive

$$X_{i+1}(\omega) = (j\omega I - A_R)^{-1}B_R Z_i(\omega) + \mathcal{S}_l(\omega)(j\omega I - A_R)^{-1}j\omega H_i(\omega). \quad (3.11)$$

According to (1.6), during the reset interval $(t_i, t_{i+1}]$, we obtain $X_i(\omega) = (j\omega I - A_R)^{-1}B_R Z_i(\omega)$. Substituting this $X_i(\omega)$ into (3.11) yields

$$X_{i+1}(\omega) = X_i(\omega) + \mathcal{S}_l(\omega)(j\omega I - A_R)^{-1}j\omega H_i(\omega). \quad (3.12)$$

From (3.6), the Fourier transform of $h_i(t)$ is given by

$$H_i(\omega) = \mathcal{F}[h_i(t)] = (A_p - I)(j\omega)^{-1}e^{-j\omega t_i}x_i(t_i). \quad (3.13)$$

Substituting (3.13) into (3.12), we obtain

$$X_{i+1}(\omega) = X_i(\omega) + \mathcal{T}_s(\omega)e^{-j\omega t_i}x_i(t_i), \quad (3.14)$$

where

$$\mathcal{T}_s(\omega) = \mathcal{S}_l(\omega)(j\omega I - A_R)^{-1}(A_p - I). \quad (3.15)$$

Conducting the Fourier transforms of equation (3.14), we obtain:

$$x_{i+1}(t) = x_i(t) + h_s(t - t_i)x_i(t_i), \text{ where } h_s(t) = \mathcal{F}^{-1}[\mathcal{T}_s(\omega)]. \quad (3.16)$$

Till here, the state of the reset controller during the time interval $(t_i, t_{i+1}]$ denoted as $x_{i+1}(t)$ is derived.

Step 2: Derive the Piecewise Expression for $z_i(t)$.

Similarly to Step 1, from Fig. 3.5, the signal $m_{i+1}(t)$ is derived from two inputs: $z_i(t)$ and $h_i(t)$. The contributions to the output $m_{i+1}(t)$ from $z_i(t)$ and $h_i(t)$ are denoted as $m_{i+1}^z(t)$ and $m_{i+1}^h(t)$, respectively. Let $M_i(\omega)$, $M_{i+1}^z(\omega)$, and $M_{i+1}^h(\omega)$ represent the Fourier transforms of the signals $m_i(t)$, $m_{i+1}^z(t)$, and $m_{i+1}^h(t)$, respectively. Using the same calculation process as in Step 1, $M_{i+1}(\omega)$ is expressed as:

$$M_{i+1}(\omega) = \frac{M_{i+1}^z(\omega)}{Z_i(\omega)} \cdot Z_i(\omega) + \frac{M_{i+1}^h(\omega)}{H_i(\omega)} \cdot H_i(\omega), \quad (3.17)$$

where

$$\begin{aligned} \frac{M_{i+1}^z(\omega)}{Z_i(\omega)} &= C_R(j\omega I - A_R)^{-1}B_R + D_R = \mathcal{C}_l(\omega), \\ \frac{M_{i+1}^h(\omega)}{H_i(\omega)} &= \mathcal{S}_l(\omega)C_R(j\omega I - A_R)^{-1}j\omega. \end{aligned} \quad (3.18)$$

Substituting (3.18) into (3.17), $M_{i+1}(\omega)$ is simplified to

$$M_{i+1}(\omega) = \mathcal{C}_l(\omega)Z_i(\omega) + \mathcal{S}_l(\omega)C_R(j\omega I - A_R)^{-1}j\omega H_i(\omega). \quad (3.19)$$

From (1.6), during the reset interval $(t_i, t_{i+1}]$, we have

$$M_i(\omega) = C_i(\omega)Z_i(\omega). \quad (3.20)$$

Substituting (3.13) and (3.20) into (3.19), $M_{i+1}(\omega)$ is given by

$$M_{i+1}(\omega) = M_i(\omega) + C_R \mathcal{T}_s(\omega) e^{-j\omega t_i} x_i(t_i). \quad (3.21)$$

From Fig. 1.8, in the closed-loop reset system, the following relation holds:

$$\begin{aligned} Z_i(\omega) &= R(\omega) - (A(\omega) + M_i(\omega))\mathcal{C}_\sigma(\omega), \\ Z_{i+1}(\omega) &= R(\omega) - (A(\omega) + M_{i+1}(\omega))\mathcal{C}_\sigma(\omega), \end{aligned} \quad (3.22)$$

where $A(\omega) = \mathcal{F}[a(t)]$ and

$$\mathcal{C}_\sigma(\omega) = \mathcal{C}_3(\omega)\mathcal{P}(\omega)\mathcal{C}_4(\omega)\mathcal{C}_1(\omega). \quad (3.23)$$

From (3.22), the following equations are derived

$$\begin{aligned} M_i(\omega) &= [R(\omega) - Z_i(\omega)] \cdot \mathcal{C}_\sigma(\omega)^{-1} - A(\omega), \\ M_{i+1}(\omega) &= [R(\omega) - Z_{i+1}(\omega)] \cdot \mathcal{C}_\sigma(\omega)^{-1} - A(\omega). \end{aligned} \quad (3.24)$$

Substituting $M_{i+1}(\omega)$ and $M_i(\omega)$ from (3.24) into (3.21), $Z_{i+1}(\omega)$ is obtained as

$$Z_{i+1}(\omega) = Z_i(\omega) - \mathcal{T}_\alpha(\omega) e^{-j\omega t_i} x_i(t_i), \quad (3.25)$$

where

$$\mathcal{T}_\alpha(\omega) = \mathcal{C}_\sigma(\omega)C_R\mathcal{T}_s(\omega). \quad (3.26)$$

Conducting the Fourier transforms of equation (3.25), we obtain:

$$z_{i+1}(t) = z_i(t) - h_\alpha(t - t_i)x_i(t_i), \text{ where } h_\alpha(t) = \mathcal{F}^{-1}[\mathcal{T}_\alpha(\omega)]. \quad (3.27)$$

Up to this point, the input of the reset controller during the time interval $(t_i, t_{i+1}]$ denoted as $z_{i+1}(t)$ is derived.

Step 3: Derive the Piecewise Expression for $z_s^i(t)$.

During the reset intervals $(t_{i-1}, t_i]$ and $(t_i, t_{i+1}]$, no reset action takes place. Let $Z_s^i(\omega)$ denotes the Fourier transforms of $z_s^i(t)$. Therefore, the following relationship holds:

$$Z_s^i(\omega) = C_s(\omega)Z_i(\omega), \text{ and } Z_s^{i+1}(\omega) = C_s(\omega)Z_{i+1}(\omega). \quad (3.28)$$

Substituting (3.28) into (3.25), we obtain

$$Z_s^{i+1}(\omega) = Z_s^i(\omega) - C_s(\omega)\mathcal{T}_\alpha(\omega) e^{-j\omega t_i} x_i(t_i). \quad (3.29)$$

Conducting the Fourier transforms of equation (3.29), we obtain:

$$z_s^{i+1}(t) = z_s^i(t) - h_\beta(t - t_i)x_i(t_i), \quad (3.30)$$

where

$$h_\beta(t) = \mathcal{F}^{-1}[C_s(\omega)\mathcal{T}_\alpha(\omega)]. \quad (3.31)$$

Till here, the expression of the reset triggered signal during the time interval $(t_i, t_{i+1}]$ denoted as $z_s^{i+1}(t)$ is derived. We conclude the proof. \square

3.B Proof of Theorem 4

Proof. Consider the reset control system shown in Fig. 1.8 with a sinusoidal reference input $r(t) = |R|\sin(\omega t)$ and satisfies Assumptions 2 and 3. This proof derives the multiple-reset conditions in the sinusoidal-input reset system. It is organized into four steps as follows.

Step 1: Derive the First Reset Instant t_1 Within One Steady-State Cycle.

Under Assumption 3, the state and reset-triggered signal of the reset system during the interval $(0, t_1]$, denoted as $x_1(t)$ and $z_s^1(t)$, are equivalent to those of its BLS, denoted as $x_{bl}(t)$ and $z_{bl}(t)$, respectively, as expressed by:

$$\begin{aligned} x_1(t) &= x_{bl}(t) = |R\Theta_{bl}(\omega)|\sin(\omega t + \angle\Theta_{bl}(\omega)), \\ z_s^1(t) &= z_{bl}(t) = |R\mathcal{S}_{ls}(\omega)|\sin(\omega t + \angle\mathcal{S}_{ls}(\omega)), \end{aligned} \quad (3.32)$$

where $\angle\Theta_{bl}(\omega) \in (-\pi, \pi]$ and $\angle\mathcal{S}_{ls}(\omega) \in (-\pi, \pi]$. Functions $\Theta_{bl}(\omega)$ and $\mathcal{S}_{ls}(\omega)$ are given in (3.3).

From Assumption 3 and (3.32), the first reset instant denoted as t_1 within one steady-state cycle, which corresponds to the first zero-crossing point of the reset-triggered signal $z_s^1(t)$, is expressed as:

$$t_1 = \begin{cases} (\pi - \angle\mathcal{S}_{ls}(\omega))/\omega, & \text{if } \angle\mathcal{S}_{ls}(\omega) \in (0, \pi], \\ (-\angle\mathcal{S}_{ls}(\omega))/\omega, & \text{if } \angle\mathcal{S}_{ls}(\omega) \in (-\pi, 0]. \end{cases} \quad (3.33)$$

From (3.33), we have $t_1 \leq \pi/\omega$.

Step 2: Draw the Conclusion that Reset Instants Occurring π/ω -Periodically.

Under Assumption 2, the reset-triggered signal $z_s(t)$ in the sinusoidal-input reset system can be represented as an infinite series of harmonics [7], denoted by $z_{sn}(t)$, and is given by

$$z_s(t) = \sum_{n=1}^{\infty} z_{sn}(t) = \sum_{n=1}^{\infty} |Z_{sn}|\sin(n\omega t + \angle Z_{sn}), \quad (3.34)$$

where $|Z_{sn}|$ denotes the magnitude and $\angle Z_{sn}$ represents the phase of each harmonic component $z_{sn}(t)$.

From (8.9), we obtain

$$z_s(t_i) = -z_s(t_i \pm \pi/\omega) = 0. \quad (3.35)$$

From (3.35), the reset instant t_i , where $z_s(t_i) = 0$, occurs periodically with a period of π/ω .

Step 3: Establish the Condition for Multiple-Reset Systems: The Reset Triggered Signal $z_s^2(t)$ Must Exhibit at Least One Zero-Crossing Within the Interval $(t_1, \pi/\omega)$.

From (3.35), within a steady-state period $(0, 2\pi/\omega]$, we obtain two conclusions:

1. At the time instant t_1 and $t_1 + \pi/\omega$, we have $z_s(t_1) = z_s(t_1 + \pi/\omega) = 0$.
2. Since t_1 represents the first reset instant within a steady-state cycle $(0, 2\pi/\omega]$, there is no zero-crossings of $z_s(t)$ in the both the time intervals $(0, t_1)$ and $(\pi/\omega, t_1 + \pi/\omega)$.

By defining $t = t_\delta + t_1$ and substituting $x_1(t_1)$ from (3.37) into (3.36), along with $z_s^1(t)$ defined from (3.32), we obtain:

$$z_s^2(t_\delta + t_1) = \begin{cases} -|R|\Delta(t_\delta), & \text{if } \angle \mathcal{S}_{I_s}(\omega) \in (0, \pi], \\ |R|\Delta(t_\delta), & \text{if } \angle \mathcal{S}_{I_s}(\omega) \in (-\pi, 0], \end{cases} \quad (3.39)$$

where

$$\Delta(t_\delta) = |\mathcal{S}_{I_s}(\omega)| \sin(\omega t_\delta) + h_\beta(t_\delta) \Theta_s(\omega). \quad (3.40)$$

The multiple-reset condition requires that $z_s^2(t)$ has at least one zero-crossing within the time interval $(t_1, \pi/\omega)$. Using the relation $t = t_\delta + t_1$ and from (3.39), this condition is transformed to: there exists a time interval $t_\delta \in (0, \pi/\omega - t_1)$ such that $z_s^2(t_\delta + t_1)$ has at least one zero-crossing.

From (3.33), the value of $\pi/\omega - t_1$ is given by

$$\pi/\omega - t_1 = \begin{cases} (\angle \mathcal{S}_{I_s}(\omega))/\omega, & \text{if } \angle \mathcal{S}_{I_s}(\omega) \in (0, \pi], \\ (\pi + \angle \mathcal{S}_{I_s}(\omega))/\omega, & \text{if } \angle \mathcal{S}_{I_s}(\omega) \in (-\pi, 0]. \end{cases} \quad (3.41)$$

From (3.41), $\pi/\omega - t_1$ can be expressed as

$$t_m = \pi/\omega - t_1 = \angle \mathcal{S}_{I_s}(\omega)/\omega + \pi/\omega \cdot \text{sign}(\mathcal{S}_{I_s}(\omega)), \quad (3.42)$$

where

$$\text{sign}(x) = \begin{cases} 0, & \text{if } x > 0, \\ 1, & \text{if } x \leq 0. \end{cases} \quad (3.43)$$

Since a zero-crossing is independent of amplitude, the multiple-reset condition is simplified to verifying the existence of a time interval $t_\delta \in (0, t_m)$ such that $\Delta(t_\delta) = 0$. This completes the proof. \square

4

Frequency Response Analysis for Closed-Loop Reset Control Systems

4

Building on the open-loop Higher-Order Sinusoidal Input Describing Functions (HOSIDFs) presented in Chapter 2 and the two-reset conditions provided in Chapter 3, this chapter develops HOSIDFs for closed-loop two-reset control systems. The closed-loop HOSIDFs correct the inaccuracies in previous analysis methods and establish a connection with open-loop HOSIDFs analysis. The accuracy and effectiveness of the proposed methods are successfully validated through simulations and experiments conducted on a precision motion system.

 This chapter is based on the paper:

Zhang, Xinxin, and S. Hassan HosseinNia. "Higher-Order Sinusoidal Input Describing Functions for Open-Loop and Closed-Loop Reset Control with Application to Mechatronics Systems." arXiv preprint arXiv:2412.13086 (2024).

4.1 Introduction

For frequency response analyses of reset control systems, both open-loop and closed-loop analyses are crucial. Based on their connection, controllers are designed in open-loop to shape and optimize closed-loop system performance [1, 2]. Chapter 2 introduced accurate Higher-Order Sinusoidal Input Describing Functions (HOSIDFs) for open-loop reset control systems. However, performing frequency response analysis for closed-loop reset feedback control systems is challenging, as high-order harmonics introduce additional harmonics through the feedback loop, disrupting the superposition principle and complicating system dynamics. The study in [3] introduced HOSIDFs analysis for such systems and established open-loop and closed-loop HOSIDFs connection. However, it failed to account for the effects of reset actions on high-order harmonics within the feedback loop, leading to inaccuracies. Furthermore, no HOSIDFs currently exist for analyzing the closed-loop generalized reset control systems in Fig. 1.8.

Motivated by the limitations in closed-loop frequency response analysis, this chapter develops new HOSIDFs for closed-loop generalized reset control systems, addressing the inaccuracies found in previous research. Additionally, it establishes a connection between open-loop and closed-loop HOSIDFs in the frequency domain. The chapter is structured as follows: Section 4.2 introduces the analysis model for closed-loop reset systems and formulates the HOSIDF analysis method. Section 4.3 presents simulations and experimental validations on a precision motion stage to demonstrate the effectiveness of the proposed approach. Finally, Section 4.4 summarizes the findings and conclusions.

4.2 Method: Frequency Response Analysis for Closed-loop Reset Systems

4.2.1 Sinusoidal-Input Closed-Loop Reset Systems Analysis Models

Consider a closed-loop reset control system depicted in Fig. 1.8, operating under the conditions specified in Assumption 2 and subjected to a sinusoidal input signal of frequency ω . Under these conditions, the system's trajectories—namely $e(t)$ (error), $z(t)$ (input to the reset controller), $z_s(t)$ (reset-triggered signal), $u(t)$ (control input), and $y(t)$ (output)—become periodic and share the same fundamental frequency as the input signal ω [4, 5]. These signals can be expressed as:

$$\begin{aligned}
 e(t) &= \sum_{n=1}^{\infty} e_n(t) = \sum_{n=1}^{\infty} |E_n| \sin(n\omega t + \angle E_n), \\
 z(t) &= \sum_{n=1}^{\infty} z_n(t) = \sum_{n=1}^{\infty} |Z_n| \sin(n\omega t + \angle Z_n), \\
 z_s(t) &= \sum_{n=1}^{\infty} z_s^n(t) = \sum_{n=1}^{\infty} |Z_s^n| \sin(n\omega t + \angle Z_s^n), \\
 &= \sum_{n=1}^{\infty} |Z_n \mathcal{C}_s(n\omega)| \sin(n\omega t + \angle Z_n + \angle \mathcal{C}_s(n\omega)), \\
 u(t) &= \sum_{n=1}^{\infty} u_n(t) = \sum_{n=1}^{\infty} |U_n| \sin(n\omega t + \angle U_n), \\
 y(t) &= \sum_{n=1}^{\infty} y_n(t) = \sum_{n=1}^{\infty} |Y_n| \sin(n\omega t + \angle Y_n),
 \end{aligned} \tag{4.1}$$

where the phase for each signal, such as the $\angle E_n$, is defined within the range of $(-\pi, \pi]$. The Fourier transforms of the signals and their n th harmonic are denoted as $E(\omega)$ ($E_n(\omega)$), $Z(\omega)$ ($Z_n(\omega)$), $Z_s(\omega)$ ($Z_s^n(\omega)$), $U(\omega)$ ($U_n(\omega)$), and $Y(\omega)$ ($Y_n(\omega)$).

During the design phase of reset control systems, we utilize the method outlined in Chapter 3 to ensure that the system exhibits two reset instances per steady-state period. This configuration indicates that the first-order harmonic $z_s^1(t)$ is predominant in the reset-triggered signal $z_s(t)$ in (4.1), while the contributions of higher-order harmonics $z_s^n(t)$ for $n > 1$ are minimal. Consequently, we introduce the following assumption:

Assumption 4. In the closed-loop reset control system with a sinusoidal input signal $\sin(\omega t)$, the reset-triggered signal is given by $z_s(t) = z_s^1(t)$.

While this assumption may introduce some deviation in the closed-loop analysis, such deviations are expected to be minor, as will be demonstrated in the forthcoming examples.

Under Assumption 4, the set of reset instants of the closed-loop reset control system is given by $J := \{t_c = (c \cdot \pi - \angle Z_s^1)/\omega | \eta \in \mathbb{Z}^+\}$. Since the reset interval $\sigma_i = t_{i+1} - t_i = \pi/\omega > \delta_{\min}$ [6], the trajectories for the reset control system are Zeno-free.

Consider a closed-loop reset control system, as illustrated in Fig. 1.8, subjected to a sinusoidal input signal $r(t) = |R|\sin(\omega t)$. The system operates under the conditions specified in Assumptions 2 and 4. This subsections presents two analysis models for this system. The following content outlines the process of deriving the first analytical model for this system, as depicted in Fig. 4.1.

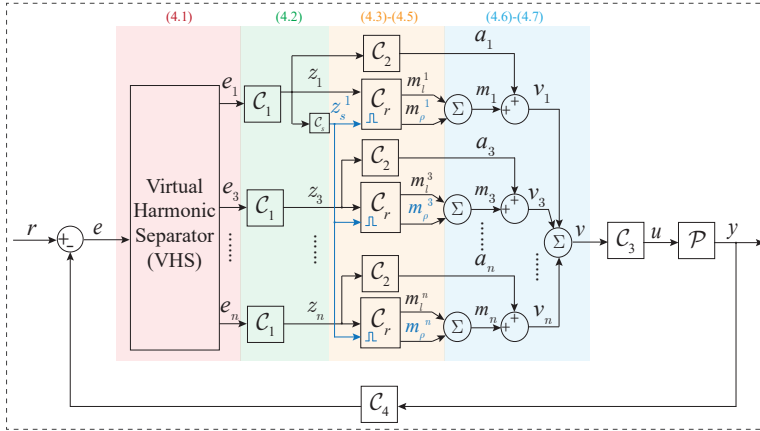


Figure 4.1: Block diagram of the closed-loop reset control system, showing the decomposition of $v(t)$ into its n -th harmonic components, expressed as $v(t) = \sum_{n=1}^{\infty} v_n(t)$. The colored blocks correspond to the equations with matching colors.

First, using the concept of the “Virtual Harmonic Separator” [7], the error signal $e(t)$, is decomposed into its harmonic components, denoted by $e_n(t)$, where $n = 2k + 1$ and $k \in \mathbb{N}$, as defined in (4.1). Next, each harmonic $e_n(t)$ filtered by the LTI system C_1 ,

generates the output signal $z_n(t)$ given by

$$\begin{aligned} z_n(t) &= |Z_n| \sin(n\omega t + \angle Z_n), \\ |Z_n| &= |E_n C_1(n\omega)|, \\ \angle Z_n &= \angle E_n + \angle C_1(n\omega). \end{aligned} \quad (4.2)$$

Signals $z_n(t)$, processed through the blocks C_r and C_2 , produce outputs $m_n(t)$ and $a_n(t)$, respectively. We first derive the expression for $m_n(t)$.

The reset trigger signal $z_s^1(t)$ is given by

$$\begin{aligned} z_s^1(t) &= |Z_s^1| \sin(\omega t + \angle Z_s^1), \\ |Z_s^1| &= |Z_1(\omega)| \cdot |C_s(\omega)| = |E_1 C_1(\omega) C_s(\omega)|, \\ \angle Z_s^1 &= \angle Z_1 + \angle C_s(\omega) = \angle E_1 + \angle C_1(\omega) + \angle C_s(\omega). \end{aligned} \quad (4.3)$$

Based on Corollary 1, the reset controller C_r under a sinusoidal input signal $z_n(t)$ in (4.2) and a reset triggered signal $z_s^1(t)$ in (4.3) generates the output $m_n(t)$, given by

$$m_n(t) = m_l^n(t) + m_p^n(t), \quad (4.4)$$

where $m_l^n(t)$ is the linear component, given by

$$\begin{aligned} m_l^n(t) &= |M_l^n| \sin(n\omega t + \angle M_l^n), \\ |M_l^n| &= |Z_n C_l(n\omega)| = |E_n C_1(n\omega) C_l(n\omega)|, \\ \angle M_l^n &= \angle Z_n + \angle C_l(n\omega) = \angle E_n + \angle C_1(n\omega) + \angle C_l(n\omega), \end{aligned} \quad (4.5)$$

and $m_p^n(t)$ is the nonlinear component given in (2.6).

Meanwhile, the LTI system C_2 processes the input signal $z_n(t)$ in (4.2) and produces the output $a_n(t)$, given by

$$\begin{aligned} a_n(t) &= |A_n| \sin(n\omega t + \angle A_n), \\ |A_n| &= |Z_n| \cdot |C_2(n\omega)| = |E_n C_1(n\omega) C_2(n\omega)|, \\ \angle A_n &= \angle Z_n + \angle C_2(n\omega) = \angle E_n + \angle C_1(n\omega) + \angle C_2(n\omega). \end{aligned} \quad (4.6)$$

Finally, by summing $m_n(t)$ from (4.4) and $a_n(t)$ from (4.6), the signal $v(t)$ in Fig. 4.1, is obtained as follows:

$$\begin{aligned} v(t) &= \sum_{n=1}^{\infty} v_n(t), \\ v_n(t) &= m_n(t) + a_n(t). \end{aligned} \quad (4.7)$$

Here, the block diagram in Fig. 4.1 is constructed.

Then, building upon Fig. 4.1, Theorem 5 concludes the development of the second analysis model for the closed-loop reset control system, visually in Fig. 4.2.

Theorem 5. Consider a closed-loop reset control system in Fig. 1.8 with the reset controller C_r (1.6), under a sinusoidal reference input signal $r(t) = |R| \sin(\omega t)$ and

satisfying Assumptions 2 and 4. The steady-state signal $v(t)$ in Fig. 4.1 is given by:

$$\begin{aligned}
 v(t) &= v_l(t) + v_\rho(t), \\
 v_\rho(t) &= \Gamma(\omega) m_\rho^1(t), \\
 v_l(t) &= \sum_{n=1}^{\infty} v_l^n(t), \\
 v_l^n(t) &= \mathcal{F}^{-1}[\mathcal{C}_\lambda^n(n\omega) Z_n(\omega)], \\
 m_\rho^1(t) &= \sum_{n=1}^{\infty} \mathcal{F}^{-1}[|\mathcal{C}_\rho^n(\omega)| \sin(n\omega t + n\angle Z_1 + \angle \mathcal{C}_\rho^n(\omega))].
 \end{aligned} \tag{4.8}$$

where

$$\begin{aligned}
 \Psi_n(\omega) &= |\mathcal{L}_\rho(n\omega)| / |1 + \mathcal{L}_l(n\omega)|, \\
 \Delta_c^1(\omega) &= |\Delta_l(\omega)| \sin(\angle \Delta_l(\omega) - \angle \mathcal{C}_s(\omega)), \\
 \Gamma(\omega) &= 1 / (1 - \sum_{n=3}^{\infty} \Psi_n(\omega) \Delta_c^n(\omega) / \Delta_c^1(\omega)), \\
 \mathcal{L}_\rho(n\omega) &= \mathcal{C}_1(n\omega) \mathcal{C}_\rho^n(\omega) \mathcal{C}_3(n\omega) \mathcal{P}(n\omega) \mathcal{C}_4(n\omega), \\
 \Delta_c^n(\omega) &= -|\Delta_l(n\omega)| \sin(\angle \Delta_l(n\omega) + \angle \mathcal{L}_\rho(n\omega) - \angle(1 + \mathcal{L}_l(n\omega)) - n\angle \mathcal{C}_s(\omega)), \text{ for } n > 1.
 \end{aligned} \tag{4.9}$$

Function $\mathcal{C}_l(\omega)$ is given in (1.7), $\mathcal{C}_\rho^n(\omega)$ and $\Delta_l(n\omega)$ can be found in (2.8), $\mathcal{L}_l(n\omega)$ is defined in (3.2).

Proof. The proof is provided in Appendix 4.A. □

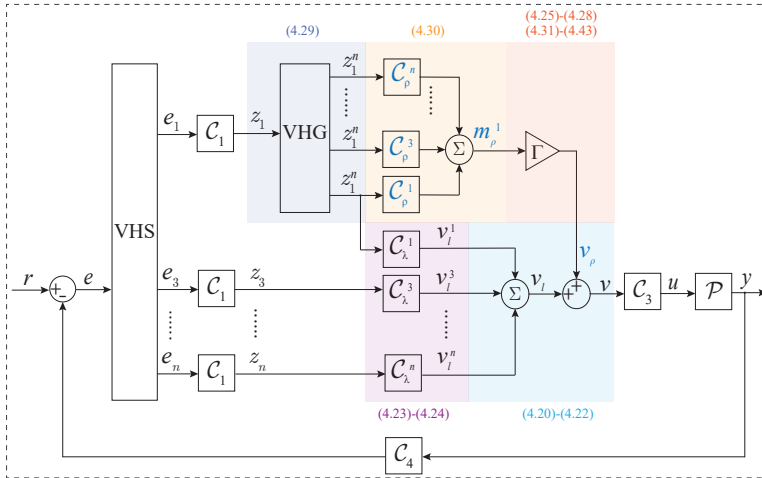


Figure 4.2: Block diagram of the closed-loop reset control system, showing the decomposition of $v(t)$ into its linear component $v_l(t)$ and nonlinear component $v_\rho(t)$. The colored blocks correspond to the equations with the same colors referenced in the proof in Appendix 4.A.

4.2.2 HOSIDFs for Closed-Loop Reset Systems

From the analysis model for the closed-loop reset control system as shown in Fig. 4.2 and Theorem 5, the HOSIDFs for closed-loop reset control systems are derived in Theorem 6.

Theorem 6. Consider a closed-loop two-reset control system in Fig. 1.8, with the input signal defined as $r(t) = |R|\sin(\omega t)$, under Assumptions 2 and 4. Utilizing the “Virtual Harmonic Generator” approach [7], the input signal $r(t)$ generates harmonics $r_n(t) = |R|\sin(n\omega t)$ with Fourier transforms of $R_n(\omega) = |R|\mathcal{F}[\sin(n\omega t)]$. The n th Higher-Order Sinusoidal Input Sensitivity Function (HOSISF) $\mathcal{S}_n(\omega)$, Higher-Order Sinusoidal Input Complementary Sensitivity Function $\mathcal{T}_n(\omega)$, and the Higher-Order Sinusoidal Input Control Sensitivity Function $\mathcal{CS}_n(\omega)$ are given as follows:

$$\mathcal{S}_n(\omega) = \frac{E_n(\omega)}{R_n(\omega)} = \begin{cases} 1/(1 + \mathcal{L}_o(\omega)), & \text{for } n = 1, \\ -\mathcal{S}_l(n\omega) \cdot |\mathcal{S}_1(\omega)| e^{jn\angle\mathcal{S}_1(\omega)} \cdot \Gamma(\omega) \mathcal{L}_n(\omega) \mathcal{C}_4(n\omega), & \text{for odd } n > 1, \\ 0, & \text{for even } n \geq 2, \end{cases} \quad (4.10)$$

$$\mathcal{T}_n(\omega) = \frac{Y_n(\omega)}{R_n(\omega)} = \begin{cases} \mathcal{L}_o(\omega)/[\mathcal{C}_4(\omega) \cdot (1 + \mathcal{L}_o(\omega))], & \text{for } n = 1, \\ \mathcal{S}_l(n\omega) \cdot |\mathcal{S}_1(\omega)| e^{jn\angle\mathcal{S}_1(\omega)} \cdot \Gamma(\omega) \mathcal{L}_n(\omega), & \text{for odd } n > 1, \\ 0, & \text{for even } n \geq 2, \end{cases} \quad (4.11)$$

$$\mathcal{CS}_n(\omega) = \frac{U_n(\omega)}{R_n(\omega)} = \begin{cases} \mathcal{L}_o(\omega)/[\mathcal{C}_4(\omega) \cdot \mathcal{P}(\omega) \cdot (1 + \mathcal{L}_o(\omega))], & \text{for } n = 1, \\ \mathcal{S}_l(n\omega) \cdot |\mathcal{S}_1(\omega)| e^{jn\angle\mathcal{S}_1(\omega)} \cdot \Gamma(\omega) \mathcal{L}_n(\omega)/\mathcal{P}(n\omega), & \text{for odd } n > 1, \\ 0, & \text{for even } n \geq 2, \end{cases} \quad (4.12)$$

Where

$$\mathcal{L}_o(n\omega) = \mathcal{L}_n(\omega) + (\Gamma(\omega) - 1)\mathcal{L}_\rho(n\omega). \quad (4.13)$$

and the function $\mathcal{S}_l(n\omega)$ represents the base-linear sensitivity function defined in (3.2). The functions $\Gamma(\omega)$ and $\mathcal{L}_\rho(n\omega)$ are specified in (4.9), while $\mathcal{L}_l(n\omega)$ is defined in (3.2).

Proof. The proof is provided in Appendix 4.B. \square

Following the derivation process outlined in Theorem 6 and its proof in Appendix 4.B, Corollary 2 presents the Higher-Order Sinusoidal Input Process Sensitivity Function $\mathcal{PS}_n(\omega)$ for closed-loop reset control systems.

Corollary 2. Consider a closed-loop two-reset control system in Fig. 1.8, with the disturbance input signal $d(t) = |D|\sin(\omega t)$, under Assumptions 2 and 4. Utilizing the “Virtual Harmonic Generator” [7], the input signal $d(t)$ generates harmonics $d_n(t) = |D|\sin(n\omega t)$ with Fourier transforms of $D_n(\omega) = |D|\mathcal{F}[\sin(n\omega t)]$. The n th Higher-Order Sinusoidal Input Process Sensitivity Function $\mathcal{PS}_n(\omega)$ is given as follows:

$$\mathcal{PS}_n(\omega) = \frac{E_n(\omega)}{D_n(\omega)} = \begin{cases} -\mathcal{P}(\omega)\mathcal{C}_4(\omega)/(1 + \mathcal{L}_o(\omega)), & \text{for } n = 1, \\ -\mathcal{S}_l(n\omega) \cdot |\mathcal{PS}_1(\omega)| e^{jn\angle\mathcal{PS}_1(\omega)} \cdot \Gamma(\omega) \mathcal{L}_n(\omega) \mathcal{C}_4(n\omega), & \text{for odd } n > 1, \\ 0, & \text{for even } n \geq 2. \end{cases} \quad (4.14)$$

Theorem 6 and Corollary 2 establish the relationship between the HOSIDFs for open-loop and closed-loop control systems. The following remark illustrates this connection for the sensitivity functions $\mathcal{S}_n(\omega)$.

Remark 3. The sensitivity functions $\mathcal{S}_n(\omega)$ in (4.10) for the closed-loop reset feedback control system in Fig. 1.8 are related to the open-loop transfer function $\mathcal{L}_n(\omega)$ in (2.9) and the base-linear sensitivity function $\mathcal{S}_l(\omega)$ in (3.2) as follows:

1. For the first-order harmonic ($n = 1$), the sensitivity function is given by:

$$\mathcal{S}_1(\omega) = \frac{\mathcal{S}_{\text{DF}}(\omega)}{1 + \Gamma_\rho(\omega)\mathcal{S}_{\text{DF}}(\omega)}, \quad (4.15)$$

where

$$\begin{aligned} \mathcal{S}_{\text{DF}}(\omega) &= \frac{1}{1 + \mathcal{L}_1(\omega)}, \\ \Gamma_\rho(\omega) &= (\Gamma(\omega) - 1)\mathcal{L}_\rho(\omega). \end{aligned} \quad (4.16)$$

Here, $\mathcal{S}_{\text{DF}}(\omega)$ represents the sensitivity function derived using the SIDF analysis. From (4.15) and (4.16), when $\Gamma(\omega) = 1$, it follows that $\mathcal{S}_1(\omega) = \mathcal{S}_{\text{DF}}(\omega)$. This indicates that the first-order harmonic $\mathcal{S}_1(\omega)$ is directly related to the first-order harmonic of the open-loop transfer function $\mathcal{L}_1(\omega)$, enabling the application of linear loop-shaping techniques for the design of reset control systems [8]. Conversely, as $\Gamma(\omega)$ deviates further from 1, i.e., when $|\Gamma(\omega) - 1|$ becomes larger, $\mathcal{S}_1(\omega)$ diverges from the predictions of DF analysis, indicating an increased influence of high-order harmonics.

2. For higher-order harmonics where $n > 1$, the magnitude ratio to the first-order harmonic is expressed as:

$$\frac{|\mathcal{S}_n(\omega)|}{|\mathcal{S}_1(\omega)|} = \left| \mathcal{S}_l(n\omega) \cdot \Gamma(\omega)\mathcal{L}_n(\omega)\mathcal{C}_4(n\omega) \right|. \quad (4.17)$$

From (4.17), for a reset control system with a settled base-linear sensitivity function $\mathcal{S}_l(n\omega)$, reducing $|\Gamma(\omega)\mathcal{L}_n(\omega)\mathcal{C}_4(n\omega)|$ in the open loop can decrease $|\mathcal{S}_n(\omega)|/|\mathcal{S}_1(\omega)|$ in the closed loop.

Based on Theorem 6, Remark 4 provides a method for calculating the steady-state trajectories of sinusoidal reference input in closed-loop reset control systems.

Remark 4. Under Assumptions 2 and 4, in a closed-loop reset control system in Fig. 1.8 with a sinusoidal reference signal $r(t) = |R|\sin(\omega t)$, the steady-state error signal $e_r(t)$, output signal $y_r(t)$, and control input signal $u_r(t)$ are given by

$$\begin{aligned} e_r(t) &= \sum_{n=1}^{\infty} |R| \cdot |\mathcal{S}_n(\omega)| \sin(n\omega t + \angle \mathcal{S}_n(\omega)), \\ y_r(t) &= \sum_{n=1}^{\infty} |R| \cdot |\mathcal{T}_n(\omega)| \sin(n\omega t + \angle \mathcal{T}_n(\omega)), \\ u_r(t) &= \sum_{n=1}^{\infty} |R| \cdot |\mathcal{C}\mathcal{S}_n(\omega)| \sin(n\omega t + \angle \mathcal{C}\mathcal{S}_n(\omega)). \end{aligned} \quad (4.18)$$

Based on Corollary 2, Remark 5 provides a method for calculating the steady-state error in a closed-loop reset control system when subjected to a sinusoidal disturbance input.

Remark 5. Under Assumptions 2 and 4, the steady-state error signal $e_d(t)$ of a closed-loop reset control system in Fig. 1.8, with a sinusoidal disturbance input $d(t) = |D|\sin(\omega t)$, is given by:

$$e_d(t) = \sum_{n=1}^{\infty} |D| \cdot |\mathcal{PS}_n(\omega)| \sin(n\omega t + \angle \mathcal{PS}_n(\omega)). \quad (4.19)$$

4.3 Results: Validation of Closed-Loop HOSIDFs

4.3.1 Case Study 1

This subsection uses illustrative examples and conducts simulations and experiments to validate the accuracy of Theorem 6 and Corollary 2.

The parameters of the illustrative system are as follows: $C_1(s) = \frac{s/(150\pi)+1}{s/(3000\pi)+1}$, $C_s(s) = 1/(s/100+1)$, reset controller is built with a BLS system $C_l = 1/(s/(300\pi)+1)$ with a reset value $\gamma = 0$, $C_2(s) = C_4(s) = 1$, $C_3(s) = 45 \cdot (s/(300\pi)+1)/(s/(30000\pi)+1) \cdot (s+30\pi)/s \cdot (s/(130\pi)+1)/(s/(699\pi)+1) \cdot 1/(s/(3000\pi)+1)$, and the plant $\mathcal{P}(s)$ is the precision motion stage given in (1.1). The two-reset condition discussed in Chapter 3 is applied to ensure that this reset control system, when subjected to sinusoidal inputs, exhibits two reset instants per steady-state cycle across the entire operating frequency range.

To validate the accuracy of Theorem 6, let $\|e_r\|_{\infty}/\|r\|_{\infty}$ and $\|u_r\|_{\infty}/\|r\|_{\infty}$ denote the ratios of the \mathcal{L}_{∞} norms of the steady-state error e_r and control input u_r to the sinusoidal reference input $r = \sin(\omega t)$, respectively. Figures 4.3(a) and (b) compare the values derived from simulations with those predicted by Theorem 6. The results confirm that Theorem 6 accurately predicts system dynamics across the frequency range [1,1000] Hz. Similar to the open-loop HOSIDF analysis in Fig. 2.6, prediction accuracy improves with the number of harmonics N_h considered in the computation. In this chapter, $N_h = 100$ is used to ensure reliable predictions.

Next, experimental validation of Theorem 6 is conducted. Figures 4.3(c) and (d) compare the steady-state error $e_r(t)$ and control input $u_r(t)$ of the system under a reference input $r(t) = 6 \times 10^{-7} \sin(400\pi t)$ [m], obtained from simulations, experimental measurements, and predictions based on Theorem 6. The results demonstrate good agreement between the predictions and simulation data. Minor discrepancies between the experimental and simulation results can be attributed to approximations in system identification and noise in the measurements.

Similarly, the accuracy of Corollary 2 is validated. Figure 4.4(a) compares the $\|e_d\|_{\infty}/\|d\|_{\infty}$ values derived from predictions and simulations. Figure 4.4(b) compares the steady-state error $e_d(t)$ of the system under a disturbance input $d(t) = 1 \times 10^{-4} \sin(40\pi t)$ [m], obtained from predictions, simulations, and experiments. The results confirm that Corollary 2 accurately predicts the system's response to sinusoidal disturbances.

After validating the accuracy, Theorem 6 and Corollary 2 can be reliably employed to predict the behavior of closed-loop two-reset control systems. For illustration, Fig. 4.5 presents the Bode plots of the sensitivity functions and the process sensitivity

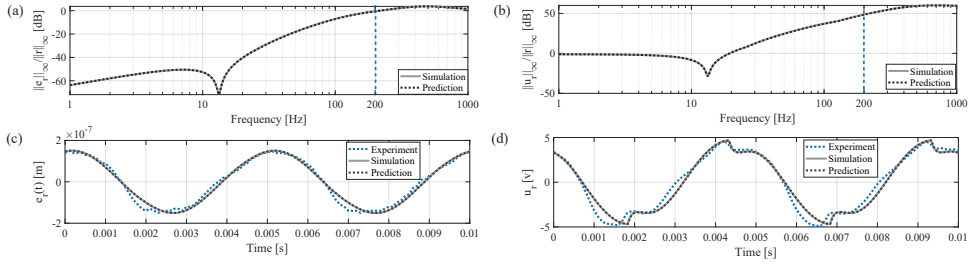


Figure 4.3: Theorem 6-predicted and simulated values for (a) $\|e_r\|_\infty/\|r\|_\infty$ and (b) $\|u_r\|_\infty/\|r\|_\infty$ of the reset control system across the frequency range [1,1000] Hz. Comparison of Theorem 6-predicted, simulated, and experimentally measured closed-loop (c) steady-state error signal $e_r(t)$ and (d) control input signal $u_r(t)$ under the reference input signal $r(t) = 6 \times 10^{-7} \sin(400\pi t)$ [m].

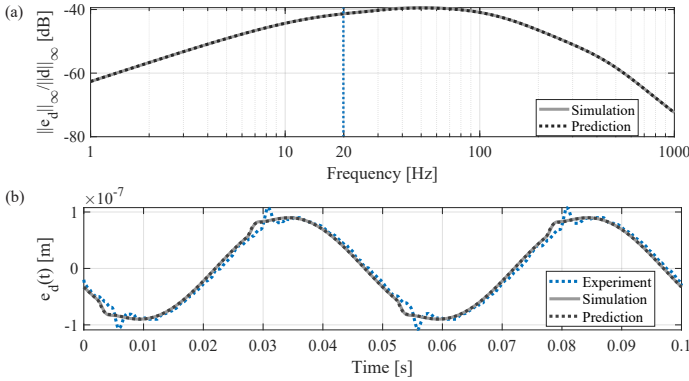


Figure 4.4: (a) Corollary 2-predicted and simulated $\|e_d\|_\infty/\|d\|_\infty$ values of the reset control system across the frequency range [1,1000] Hz. (b) Comparison of Theorem 6-predicted, simulated, and experimentally measured closed-loop steady-state error signal $e_d(t)$ under the reference input signal $d(t) = 1 \times 10^{-4} \sin(40\pi t)$ [m].

function for the closed-loop reset control system. The magnitude and phase information for each harmonic of the closed-loop reset control systems serve as the foundation for system dynamic analysis.

4.3.2 Case Study 2

Though Theorem 6 effectively predicts the system dynamics in Case Study 1, it has limitations, as demonstrated in Case Study 2. The design parameters for this case are as follows: $C_1(s) = C_2(s) = C_4(s) = C_5(s) = 1$, reset controller $C_I = 30\pi/s$ with a reset value $\gamma = 0$, $C_3(s) = 20.5 \cdot (s/(62.5\pi) + 1)/(s/(1440\pi) + 1) \cdot (1 + 30\pi/s) \cdot 1/(s/(3000\pi) + 1)$, $\gamma = 0$, and the plant $\mathcal{P}(s)$ is the precision motion stage given in (1.1).

Figure 4.6(a) compares the $\|e_r\|_\infty/\|r\|_\infty$ values of this system, obtained from simulations, with those predicted by Theorem 6. Figures 4.6(b) and 4.6(c) compare the steady-state errors $e_r(t)$ derived from simulations, experiments, and predictions for an input signal of $r(t) = 10^7 \sin(2\pi ft)$ [m] at input frequencies of 10 Hz and 100 Hz,

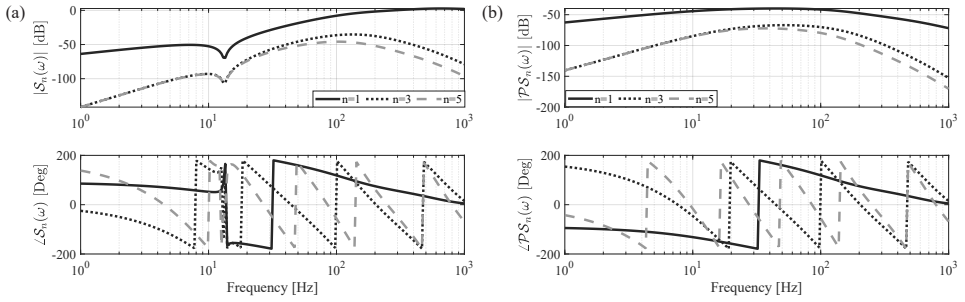


Figure 4.5: (a) The sensitivity function $S_n(\omega)$ and (b) the process sensitivity function $\mathcal{P}S_n(\omega)$ of a closed-loop reset control system with $n = 1, 3, 5$.

4

respectively.

Using the method from Theorem 4, the range of multiple-reset system behavior is identified as (0, 33) Hz, shaded in gray. The results indicate that Theorem 6 accurately predicts system behavior in two-reset control systems, such as for an input frequency of 100 Hz, shown in Fig. 4.6(c). However, in multiple-reset control systems, such as for an input frequency of 10 Hz, shown in Fig. 4.6(b), the theorem exhibits deviations.

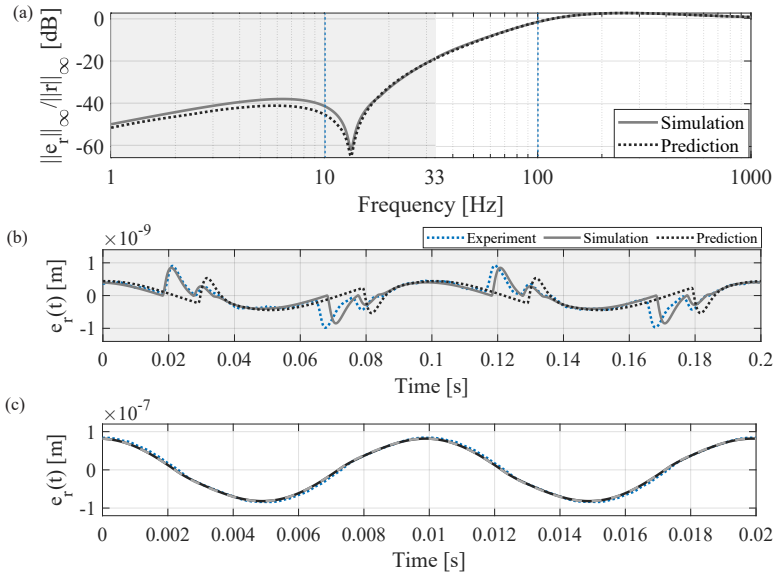


Figure 4.6: (a) Theorem 6-predicted and simulated $\|e_r\|_\infty / \|r\|_\infty$ value. The steady-state errors under input signal of $r(t) = 10^7 \sin(2\pi ft)$ [m] at input frequencies of (b) 10 Hz and (c) 100 Hz, obtained from prediction, simulation, and the experiments.

Thus, to ensure the accuracy of Theorem 6, it is essential to apply Theorem 4 to guarantee that the system operates within the two-reset range across the working

frequency domain.

4.4 Conclusion and Discussions

In conclusion, this chapter introduces the HOSIDFs for closed-loop reset systems with two reset instants per steady-state cycle. The accuracy and effectiveness of the proposed methods are validated through simulations and experiments conducted on a precision motion stage. The frequency response analysis methods in Theorems 3 to 6, developed for the generalized reset feedback control structure shown in Fig. 1.8, enable the tuning of linear elements in parallel, in series before and after the reset controller, and within the shaping filter to refine reset actions. This flexibility broadens the potential for designing reset feedback control systems with enhanced performance characteristics.

In linear systems, the analytical connection between open-loop and closed-loop frequency-domain analysis in (1.3) serves as a powerful tool for system design and performance prediction. However, in reset systems, this relationship does not hold for either the first-order harmonic ($n = 1$) or higher-order harmonics ($n > 1$). Theorem 6 reveals that the interactions between open-loop and closed-loop harmonics are mediated by the parameter $\Gamma(\omega)$, which captures the cross effects of first- and higher-order harmonics. Previous SIDF analysis [9] and HOSIDF analysis [3] assume $\Gamma(\omega) = 1$ for all ω , implying no reset actions on high-order harmonics ($n > 1$), resulting in inaccuracies. Theorem 6 addresses this limitation by introducing $\Gamma(\omega)$ in (4.9).

Moreover, as discussed in Remark 3, achieving $\Gamma(\omega) \rightarrow 1$ allows the closed-loop sensitivity function to be approximated using classical linear SIDF and loop-shaping methods. Furthermore, ensuring $|\mathcal{S}_n(\omega)|/|\mathcal{S}_1(\omega)| \rightarrow 0$ suppresses higher-order harmonics to negligible levels, maintaining the benefits of first-order harmonics. Striking this balance supports the application of the superposition principle in closed-loop, multiple-input reset control systems, enhancing both design flexibility and system performance.

Bibliography

- [1] K. Ogata. *Modern Control Engineering*. Upper Saddle River, NJ: Prentice Hall, 2010.
- [2] S. Van Loon, K. Gruntjens, M. F. Heertjes, N. van de Wouw, and W. Heemels. “Frequency-domain tools for stability analysis of reset control systems”. In: *Automatica* 82 (2017), pp. 101–108.
- [3] N. Saikumar, K. Heinen, and S. H. HosseinNia. “Loop-shaping for reset control systems: A higher-order sinusoidal-input describing functions approach”. In: *Control Engineering Practice* 111 (2021), p. 104808.
- [4] A. A. Dastjerdi, A. Astolfi, N. Saikumar, N. Karbasizadeh, D. Valerio, and S. H. HosseinNia. “Closed-loop frequency analysis of reset control systems”. In: *IEEE Transactions on Automatic Control* 68.2 (2022), pp. 1146–1153.
- [5] A. Pavlov, N. van de Wouw, and H. Nijmeijer. “Convergent piecewise affine systems: analysis and design part i: continuous case”. In: *Proceedings of the 44th IEEE Conference on Decision and Control*. IEEE, 2005, pp. 5391–5396.
- [6] A. Barreiro, A. Baños, S. Dormido, and J. A. González-Prieto. “Reset control systems with reset band: Well-posedness, limit cycles and stability analysis”. In: *Systems & Control Letters* 63 (2014), pp. 1–11.
- [7] P. Nuij, O. Bosgra, and M. Steinbuch. “Higher-order sinusoidal input describing functions for the analysis of non-linear systems with harmonic responses”. In: *Mechanical Systems and Signal Processing* 20.8 (2006), pp. 1883–1904.
- [8] R. M. Schmidt, G. Schitter, and A. Rankers. *The design of high performance mechatronics-: high-Tech functionality by multidisciplinary system integration*. Ios Press, 2020.
- [9] Y. Guo, Y. Wang, and L. Xie. “Frequency-domain properties of reset systems with application in hard-disk-drive systems”. In: *IEEE Transactions on Control Systems Technology* 17.6 (2009), pp. 1446–1453.

Appendix

4.A Proof of Theorem 5

Proof. Consider a closed-loop reset control system depicted in Fig. 1.8, with a sinusoidal reference input signal $r(t) = |R|\sin(\omega t)$, satisfying Assumptions 2 and 4.

From (4.4) and (4.7), $v_n(t)$ is given by

$$v_n(t) = m_l^n(t) + m_p^n(t) + a_n(t). \quad (4.20)$$

From (4.7) and (4.20), the signal $v(t)$ can be expressed as

$$v(t) = v_l(t) + v_\rho(t), \quad (4.21)$$

where

$$\begin{aligned} v_\rho(t) &= \sum_{n=1}^{\infty} m_\rho^n(t), \\ v_l(t) &= \sum_{n=1}^{\infty} v_l^n(t), \\ v_l^n(t) &= m_l^n(t) + a_n(t). \end{aligned} \quad (4.22)$$

Define $Z_n(\omega)$, $V(\omega)$, $V_n(\omega)$, $V_l(\omega)$, $V_\rho(\omega)$, $M_\rho^n(\omega)$, $M_l^n(\omega)$, and $A_n(\omega)$ as the Fourier transforms of $z_n(t)$, $v(t)$, $v_n(t)$, $v_l(t)$, $v_\rho(t)$, $m_\rho^n(t)$, $m_l^n(t)$, and $a_n(t)$, respectively.

From (4.5), (4.6), and (4.22), $V_l(\omega)$ is expressed as

$$V_l(\omega) = \sum_{n=1}^{\infty} V_l^n(\omega), \quad (4.23)$$

where

$$\begin{aligned} V_l^n(\omega) &= C_\lambda^n(\omega) Z_n(\omega), \\ C_\lambda^n(\omega) &= C_l(n\omega) + C_2(n\omega). \end{aligned} \quad (4.24)$$

From (4.21), we have $V(\omega) = V_l(\omega) + V_\rho(\omega)$. The function $V_l(\omega)$ is derived in (4.24). The following content derives $V_\rho(\omega)$.

According to Theorem 1 and Corollary 1, the reset controller \mathcal{C}_r processes distinct input signals $z_n(t)$ while relying on the same reset-triggered signal $z_s^1(t)$ generates two components: $m_l^n(t)$ as given in (4.5) and the nonlinear output signal $m_\rho^n(t)$, whose Fourier transform is given by:

$$M_\rho^n(\omega) = \sum_{\eta=1}^{\infty} \frac{2|Z_n|\Delta_x(\eta\omega)\Delta_q^n(\omega)}{\eta\pi} \cdot \mathcal{F}[\sin(\eta\omega t + \eta\angle Z_s)], \text{ where } \eta = 2k + 1, k \in \mathbb{N}. \quad (4.25)$$

where $\Delta_x(\eta\omega)$ and $Q_\eta(\omega)$ are given in (2.4).

We then define $V_\rho(\omega) = \sum_{n=1}^{\infty} M_\rho^n(\omega)$, and introduce a factor $\Gamma(\omega)$ to represent the ratio of $V_\rho(\omega)$ to $M_\rho^1(\omega)$, defined as:

$$\Gamma(\omega) = \frac{V_\rho(\omega)}{M_\rho^1(\omega)} = \frac{\sum_{n=1}^{\infty} M_\rho^n(\omega)}{M_\rho^1(\omega)}, \text{ where } n = 2k + 1, k \in \mathbb{N}. \quad (4.26)$$

From (4.25), the nonlinear components $M_\rho^n(\omega)$ for different n share identical phase and period. Therefore, $\Gamma(\omega)$ is a real number.

From (2.4), (4.25), and (4.26), $\Gamma(\omega)$ is expressed as

$$\Gamma(\omega) = \frac{\sum_{n=1}^{\infty} |Z_n|\Delta_c^n(\omega)}{|Z_1|\Delta_c^1(\omega)}, \quad (4.27)$$

where $\Delta_c^n(\omega)$ is given by

$$\begin{aligned} \Delta_l(\omega) &= (j\omega I - A_R)^{-1} B_R, \\ \Delta_c^n(\omega) &= |\Delta_l(n\omega)| \sin(\angle \Delta_l(n\omega) + \angle Z_n - n\angle Z_s^1). \end{aligned} \quad (4.28)$$

However, in (4.27) and (4.28), the ratio $|Z_n|/|Z_1|$ and the value of $(\angle Z_n - n\angle Z_1^1)$ remain undetermined. Therefore, the subsequent analysis addresses these unknown parameters by leveraging the underlying system dynamics and harmonic relationships, enabling the determination of $\Gamma(\omega)$.

Consider the reset controller \mathcal{C}_r in Fig. 4.1 with the input signal $z_1(t) = |Z_1| \sin(\omega t + \angle Z_1)$ and the reset triggered signal $z_s^1(t) = |Z_1 \mathcal{C}_s(\omega)| \sin(\omega t + \angle Z_1 + \angle \mathcal{C}_s(\omega))$. Using the ‘‘Virtual Harmonics Generator’’, the input signal $z_1(t)$ generates n harmonics, defined as

$$z_1^n(t) = |Z_1| \sin(n\omega t + n\angle Z_1), \quad (4.29)$$

whose Fourier transform is $Z_1^n(\omega) = \mathcal{F}[z_1^n(t)]$.

According to Theorem 2, the reset controller \mathcal{C}_r with an input of $z_1^n(t)$ generates two components: $m_1^1(t)$ calculated by (4.5) and the nonlinear output signal $m_\rho^1(t)$, whose Fourier transform is given by:

$$M_\rho^1(\omega) = \sum_{n=1}^{\infty} Z_1^n(\omega) \mathcal{C}_\rho^n(n\omega). \quad (4.30)$$

From (4.30) and (4.26), $V_\rho(\omega)$ can be expressed as

$$V_\rho(\omega) = \sum_{n=1}^{\infty} \Gamma(\omega) \mathcal{C}_\rho^n(\omega) Z_1^n(\omega). \quad (4.31)$$

Let the n th harmonic component in $V_\rho(\omega)$ from (4.25) and (4.31) be equal to each other. Then, $M_\rho^n(\omega)$ is determined as

$$M_\rho^n(\omega) = \Gamma(\omega) \mathcal{C}_\rho^n(\omega) Z_1^n(\omega). \quad (4.32)$$

From (4.21), (4.24), and (4.32), $V_n(\omega)$ is given by

$$V_n(\omega) = \mathcal{C}_\lambda^n(\omega) Z_n(\omega) + \Gamma(\omega) \mathcal{C}_\rho^n(\omega) Z_1^n(\omega). \quad (4.33)$$

In the closed-loop system in Fig. 4.1, $Z_n(\omega)$ is given by

$$Z_n(\omega) = -\mathcal{C}_1(n\omega) \mathcal{C}_4(n\omega) \mathcal{P}(n\omega) \mathcal{C}_3(n\omega) V_n(\omega). \quad (4.34)$$

Substituting (4.33) into (4.34), we have

$$Z_n(\omega) = -\mathcal{L}_1(n\omega) Z_n(\omega) - \Gamma(\omega) \mathcal{L}_\rho(n\omega) Z_1^n(\omega), \quad (4.35)$$

where

$$\begin{aligned} \mathcal{L}_1(n\omega) &= \mathcal{C}_\lambda^n(\omega) \mathcal{C}_3(n\omega) \mathcal{P}(n\omega) \mathcal{C}_4(n\omega) \mathcal{C}_1(n\omega), \\ \mathcal{L}_\rho(n\omega) &= \mathcal{C}_\rho^n(\omega) \mathcal{C}_3(n\omega) \mathcal{P}(n\omega) \mathcal{C}_4(n\omega) \mathcal{C}_1(n\omega). \end{aligned} \quad (4.36)$$

From (4.2), (4.29), the relation between $Z_1^n(\omega)$ and $Z_n(\omega)$ is given by

$$Z_1^n(\omega) = \frac{|Z_1(\omega)| e^{j(n\angle Z_1(\omega) - \angle Z_n(\omega))}}{|Z_n(\omega)|} Z_n(\omega). \quad (4.37)$$

From (4.35) and (4.37), the following equations can be deduced:

$$\begin{cases} |Z_n| = \Gamma(\omega)\Psi_n(\omega)|Z_1|, & \text{for } n > 1 \\ \angle Z_n = n\pi + n\angle Z_1 + \angle \mathcal{L}_\rho(n\omega) - \angle(1 + \mathcal{L}_I(n\omega)), & \text{for } n > 1, \end{cases} \quad (4.38)$$

where

$$\Psi_n(\omega) = |\mathcal{L}_\rho(n\omega)|/|1 + \mathcal{L}_I(n\omega)|. \quad (4.39)$$

By substituting the phase relationship between $\angle Z_1$ and $\angle Z_n$ ($n > 1$) from (4.38) and $\angle Z_s^1 = \angle Z_1 + \angle \mathcal{C}_s(\omega)$ from (4.3) into (4.28), we derive:

1. For $n = 1$,

$$\Delta_c^1(\omega) = |\Delta_I(\omega)| \sin(\angle \Delta_I(\omega) - \angle \mathcal{C}_s(\omega)). \quad (4.40)$$

2. For $n = 2k + 1 > 1$,

$$\begin{aligned} \Delta_c^n(\omega) &= |\Delta_I(n\omega)| \sin(\angle \Delta_I(\omega) + \angle Z_n - \angle Z_s^1) \\ &= -|\Delta_I(n\omega)| \sin(\angle \Delta_I(n\omega) + \angle \mathcal{L}_\rho(n\omega) - \angle(1 + \mathcal{L}_I(n\omega)) - n\angle \mathcal{C}_s(\omega)). \end{aligned} \quad (4.41)$$

Substituting $\Delta_c^n(\omega)$ from (4.40) and (4.41) into (4.27), we have

$$\Gamma(\omega) = 1 + \frac{\sum_{n=3}^{\infty} |Z_n| \Delta_c^n(\omega)}{|Z_1| \Delta_c^1(\omega)}, \quad n = 2k + 1, k \in \mathbb{N}. \quad (4.42)$$

Then, by substituting $|Z_n| = \Gamma(\omega)\Psi_n(\omega)|Z_1|$ from (4.38) into (4.42), $\Gamma(\omega)$ is derived as

$$\Gamma(\omega) = 1 / \left(1 - \sum_{n=3}^{\infty} \Psi_n(\omega) \Delta_c^n(\omega) / \Delta_c^1(\omega) \right). \quad (4.43)$$

Up to this point, $\Gamma(\omega)$ is derived and the block diagram of the closed-loop reset control system in Fig. 4.2 is constructed. We conclude the proof. \square

4.B Proof of Theorem 6

Proof. Consider a closed-loop reset system in Fig. 1.8 with a sinusoidal reference input signal $r(t) = |R| \sin(\omega t)$, under Assumption 2 and 4. This proof derives the HOSIDFs for the closed-loop system.

By applying the ‘‘Virtual Harmonics Generator’’, the input signal $r(t) = |R| \sin(\omega t)$ generates n harmonics, defined as

$$r_n(t) = |R| \sin(n\omega t), \quad (4.44)$$

whose Fourier transform is denoted as $R_n(\omega)$.

The output signal $y(t)$ of the closed-loop reset control system includes infinite many harmonics $y_n(t)$, as defined in (4.1). Define $Y_n(\omega) = \mathcal{F}[y_n(t)]$. From the block diagram in Fig. 4.2, we have

$$Y_1(\omega) = [\mathcal{L}_I(\omega) + \Gamma(\omega)\mathcal{L}_\rho(\omega)]/\mathcal{C}_4(\omega)E_1(\omega). \quad (4.45)$$

In the closed loop, the following relation holds:

$$E^1(\omega) = R_1(\omega) - C_4(\omega)Y^1(\omega). \quad (4.46)$$

Combining (4.45) and (4.46), the first-order sensitivity function $S_1(\omega)$ for the closed-loop reset control system is defined as

$$S_1(\omega) = \frac{E_1(\omega)}{R_1(\omega)} = \frac{1}{1 + \mathcal{L}_o(\omega)}, \quad (4.47)$$

where

$$\mathcal{L}_o(n\omega) = \mathcal{L}_l(n\omega) + \Gamma(\omega)\mathcal{L}_\rho(n\omega) = \mathcal{L}_n(\omega) + (\Gamma(\omega) - 1)\mathcal{L}_\rho(n\omega). \quad (4.48)$$

The subsequent content focuses on deriving the high-order sensitivity function $S_n(\omega)$ for $n > 1$ for the closed-loop reset control system.

From (4.29), $Z_1^n(\omega) = \mathcal{F}[z_1^n(t)]$ is expressed as

$$Z_1^n(\omega) = |C_1(\omega)S_1(\omega)|e^{jn(\angle C_1(\omega) + \angle S_1(\omega))}R_n(\omega). \quad (4.49)$$

From the block diagram in Fig. 4.2, the n th order harmonic $Z_n(\omega)$ is given by

$$Z_n(\omega) = -\mathcal{L}_l(n\omega)Z_n(\omega) - \Gamma(\omega)\mathcal{L}_\rho(n\omega)Z_1^n(\omega). \quad (4.50)$$

Substituting $Z_1^n(\omega)$ from (4.49) into (4.50), we have

$$Z_n(\omega) = -\mathcal{L}_l(n\omega)Z_n(\omega) - \Gamma(\omega)|C_1(\omega)S_1(\omega)|e^{jn(\angle C_1(\omega) + \angle S_1(\omega))}\mathcal{L}_\rho(n\omega)R_n(\omega). \quad (4.51)$$

From (4.51), we obtain:

$$\frac{Z_n(\omega)}{R_n(\omega)} = -S_l(n\omega) \cdot \Gamma(\omega)|C_1(\omega)S_1(\omega)|e^{jn(\angle C_1(\omega) + \angle S_1(\omega))}\mathcal{L}_\rho(n\omega), \quad (4.52)$$

where $S_l(n\omega)$ denotes the sensitivity function of the BLS, given by

$$S_l(n\omega) = \frac{1}{1 + \mathcal{L}_l(n\omega)}. \quad (4.53)$$

From (4.2), $Z_n(\omega)$ and $E^n(\omega)$ has the relationship of

$$Z_n(\omega) = C_1(n\omega)E^n(\omega). \quad (4.54)$$

Thus, from (2.9), (4.36), (4.52), and (4.54), the n th order (for $n > 1$) harmonic in the sensitivity function for the closed-loop reset control system is given by

$$S_n(\omega) = \frac{E^n(\omega)}{R_n(\omega)} = \frac{Z_n(\omega)}{R_n(\omega)C_1(n\omega)} = -S_l(n\omega) \cdot |S_1(\omega)|e^{jn\angle S_1(\omega)} \cdot \Gamma(\omega)\mathcal{L}_n(\omega)C_4(n\omega). \quad (4.55)$$

The n th order complementary sensitivity function $\mathcal{T}_n(\omega)$ and the control sensitivity function $\mathcal{CS}_n(\omega)$ can be derived through a same procedure as $S_n(\omega)$ from (4.45) to (4.55). Here, we concludes the proof. \square

5

MATLAB App “Reset Far”

5

In this chapter, we develop a MATLAB app called “Reset Far,” which integrates both open-loop and closed-loop HOSIDFs for reset control systems. This app offers control engineers a practical, user-friendly tool for analyzing and designing reset control systems. A link to the app and a detailed description of its functionalities are provided. Then, the utility of the app is demonstrated through a case study that analyzes and compares the performance of three controllers: a linear PID controller, a reset controller, and a shaped reset controller. Both analytical and experimental results on a precision motion stage show that the proposed shaped reset controller offers superior tracking precision while reducing actuation forces, outperforming both the reset and PID controllers. These findings underscore the effectiveness of the proposed frequency-domain methods in analyzing and optimizing the performance of reset-controlled mechatronic systems.

 The app is provided via the [link](#) and this chapter is based on the paper: Zhang, Xinxin, and S. Hassan HosseinNia. “Higher-Order Sinusoidal Input Describing Functions for Open-Loop and Closed-Loop Reset Control with Application to Mechatronics Systems.” arXiv preprint arXiv:2412.13086 (2024).



Figure 5.1: GUI of the frequency response analysis app for the generalized reset control system, named “Reset Far”.

5.1 Introduction of the MATLAB App “Reset Far”

The contributions from Chapters 2 to 4 have been consolidated into a MATLAB application called “Reset Far”, accessible via the [link](#). The app’s graphical user interface (GUI) is displayed in Fig. 5.1.

The app contains five panels, each providing specific functions as outlined below:

- Panel ①: Displays the block diagram of the reset feedback control system in Fig. 1.8.
- Panel ②: Allows users to specify system parameters, including the numerators and denominators for systems C_1 , C_2 , C_3 , C_4 , C_s , C_r (entered as the parameters of its base-linear counterpart C_l), along with the reset value γ , and the plant \mathcal{P} . Additionally, the panel includes input fields for defining the frequency range for analysis (logarithmically spaced) and the number of harmonics to be considered.
- Panel ③: Generates HOSIDFs for the reset controller C_r and the open-loop system $\mathcal{L}_n(\omega)$ based on Theorems 2 and 3. Select either “Cr” or “Ln” until the indicator turns green, then click the “Plot” button to display the function. Use

the “Clear” button to clear plots and “Export” to save the HOSIDF data as a “.mat” file to the workspace.

- Panel ④: Identifies the frequency range where the sinusoidal-input closed-loop reset control system exhibits multiple (more than two) reset instants per steady-state cycle. To use, click the “Test” button, which turns green when active, and select the sweeping step size, defaulting to 1 Hz. The output will either indicate “There is No Multiple-Reset Region,” meaning the system operates with only two reset instants per cycle across the tested frequency range, or it will specify “Multiple-Reset Regions: f_α to f_β [Hz],” showing the frequency range(s) where multiple resets occur, with f_α and f_β as the boundaries. If multiple-reset regions are detected, subsequent closed-loop HOSIDF analysis may yield inaccuracies, and adjusting system design parameters is recommended until “There is No Multiple-Reset Region” is achieved.
- Panel ⑤: Generates HOSIDFs for the closed-loop reset control system, including $S_n(\omega)$, $T_n(\omega)$, $CS_n(\omega)$, and $PS_n(\omega)$ based on Theorem 6 and Corollary 2. First, select “Sn”, “Tn”, “CSn”, or “PSn” until the indicator turns green, then click “Plot” to display. The “Clear” button erases the plots, while “Export” saves the HOSIDF data as a “.mat” file to the workspace.

In the provided [link](#), more detailed instructions, along with an illustrative example, are offered to guide users through the process of using the app. Note that the App is specifically designed for closed-loop reset control systems with a single reset state, as defined by (1.6) and (1.8). Extending its capabilities to systems with multiple reset states could be an exciting avenue for future research, leveraging the derivation methods outlined in this study.

Additionally, a key advantage of this App is its computational efficiency. Traditional methods for obtaining the frequency response of open-loop and closed-loop reset control systems, such as point-to-point time-domain simulations or the approach in [1], which relies on time-domain calculations and Fourier transforms, are time-consuming. For instance, in the case studies presented in Section 4.3, using time-domain methods to sweep the same frequency range with a fixed time step can take tens of minutes or even hours. In contrast, the frequency-domain analysis method employed in the App eliminates the need for point-to-point calculations and completes the task in just a few seconds.

5.2 Case Study: The Application of the MATLAB App “Reset Far”

This section presents case studies to demonstrate the effectiveness of the MATLAB app in the frequency-domain analysis of reset control systems, applied to the precision motion stage $\mathcal{P}(s)$ in (1.1).

We design three control systems—PID, CgLp-PID, and shaped CgLp-PID. Note that these systems are primarily used to demonstrate the application of the proposed methods in system analysis, rather than representing optimized designs. The stability and convergence of the illustrative reset control system are verified.

The Constant-in-gain-Lead-in-phase (CgLp) reset element, as proposed in [2], is composed of a First-Order Reset Element (FORE) and a lead element, as illustrated in Fig. 5.2(a). The PID system is defined as

$$\text{PID} = k_p \left(1 + \frac{\omega_i}{s} \right) \left(\frac{s/\omega_d + 1}{s/\omega_t + 1} \right) \left(\frac{1}{s/\omega_f + 1} \right). \quad (5.1)$$

By leveraging the phase lead advantage of reset control, the CgLp-PID element in this

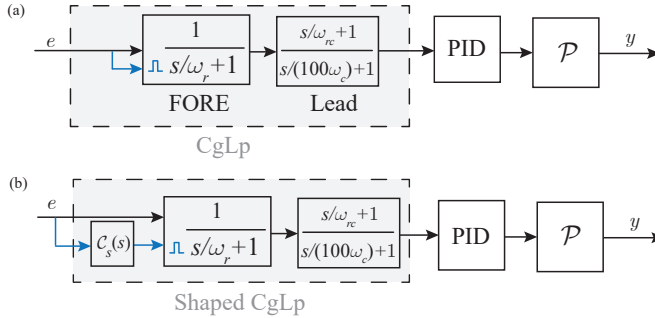


Figure 5.2: Open-loop block diagram of the Shaped CgLp-PID control system.

study is designed to provide phase lead while maintaining similar gain properties to a linear PID controller [2]. The design parameters for the CgLp-PID control system are as follows: $k_p = 35.7$, $\omega_c = 240\pi$ [rad/s], $\omega_r = 244.8\pi$ [rad/s], $\gamma = 0$, $\omega_d = 120\pi$ [rad/s], $\omega_t = 480\pi$ [rad/s], $\omega_{rc} = 216\pi$ [rad/s], $\omega_i = 24\pi$ [rad/s], and $\omega_f = 2400\pi$ [rad/s]. As depicted in the Bode plots in Fig. 5.3, both the CgLp-PID and PID systems achieve a crossover frequency of 120 Hz and maintain the same low-frequency gain. The cross-over frequency of $\mathcal{L}_1(\omega)$ from (2.9), where $|\mathcal{L}_1(\omega)| = 0$ dB, is defined as the bandwidth of the open-loop system. The PID system has a phase margin of 25.7 degrees, while the CgLp-PID system provides a phase margin of 40.7 degrees, offering a 15-degree phase lead.

A shaping filter $C_s(s)$ is designed and integrated into the CgLp-PID control system to form the shaped CgLp-PID control system, as shown in Fig. 5.2(b). Note that in this case study, the shaping filter $C_s(s)$ is specifically designed to reduce high-order harmonics of the CgLp-PID control system at the target frequency 100 Hz. By adjusting the parameters of $C_s(s)$, high-order harmonics at other targeted frequencies can be reduced as well. However, since this example primarily serves as an example to illustrate the application of the proposed frequency response analysis methods, the detailed design and tuning process of the shaping filter will be explored in future research. The transfer function of $C_s(s)$ is given by

$$C_s(s) = \frac{s/(660\pi) + 1}{s/(237.6\pi) + 1}. \quad (5.2)$$

Then, Theorems 3 and 6 are employed to analyze and compare the frequency-domain characteristics of the PID, CgLp-PID, and shaped CgLp-PID control systems.

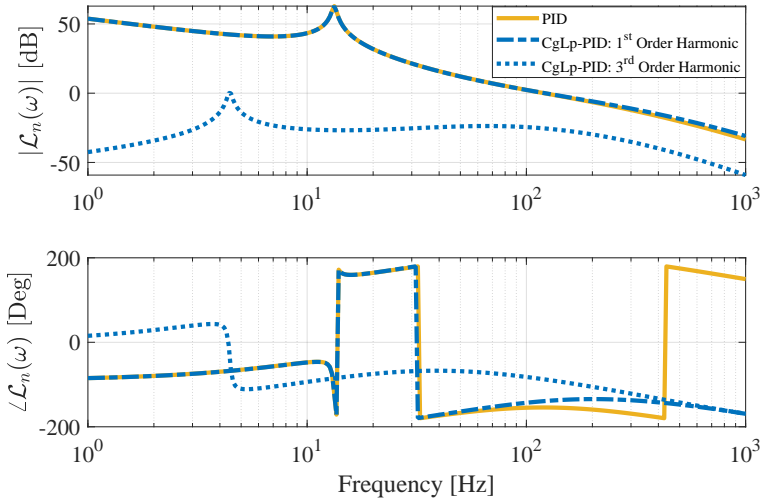


Figure 5.3: The open-loop block diagram of the Shaped CgLp-PID control system.

First, using Theorem 3 (Panel ③ in Fig. 5.1), the parameters of the shaped CgLp-PID system are tuned to $\omega_r = 466.8\pi$ [rad/s] and $\gamma = 0.4$, ensuring the same phase margin as the CgLp-PID system. Figure 5.4 shows the Bode plots of the PID control system along with the open-loop HOSIDF $\mathcal{L}_n(\omega)$ for both the CgLp-PID and shaped CgLp-PID control systems, with $n = 1$ and $n = 3$. For simplicity, higher-order harmonics ($n > 3$) are omitted in the figure, as they have lower magnitudes than the third-order harmonics but can be derived using Theorem 3.

As shown in Fig. 5.4, the shaped CgLp-PID system maintains the same phase margin as the CgLp-PID system while offering a larger bandwidth. Additionally, it effectively reduces high-order harmonics. Specifically, at an input frequency of 100 Hz, the magnitude of the third-order harmonic is decreased from 0.0592 in the CgLp-PID system to 9.14×10^{-5} in the shaped CgLp-PID system, representing a reduction of 99.85%.

Second, the multiple-reset control system identification tool introduced in Chapter 3 in Fig. 5.1) is applied to verify that both the sinusoidal-input CgLp-PID and shaped CgLp-PID control systems operate as two-reset control systems within the working frequency range of [1, 1000] Hz. This verification ensures that the two-reset condition is met for accurate closed-loop HOSIDF analysis.

Third, Theorem 6 (Panel ⑤ in Fig. 5.1) is applied to perform the closed-loop frequency response analysis for these three systems. Figures 5.5(a) and (b) show the sensitivity function \mathcal{S}_n and the control sensitivity function \mathcal{CS}_n for the PID control system with $n = 1$, as well as for CgLp-PID and shaped CgLp-PID control systems, with $n = 1$ and $n = 3$.

From the analysis of the sensitivity function in Fig. 5.5(a), the CgLp-PID and shaped CgLp-PID control systems exhibit similar first-order harmonics. However, in the shaped CgLp-PID system, a reduction in the magnitude of high-order harmonics

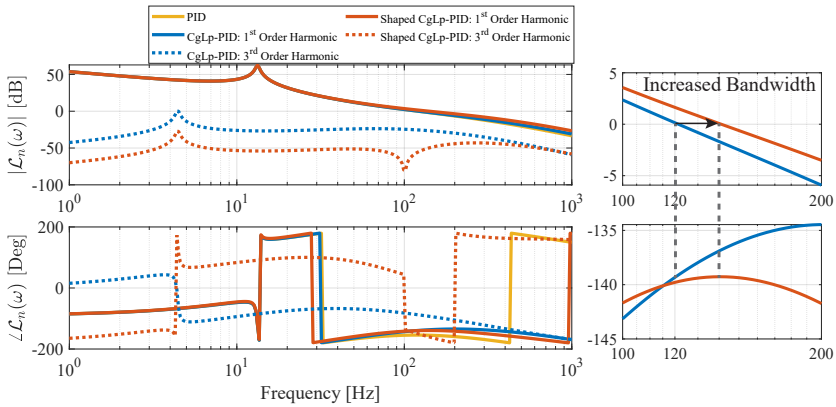


Figure 5.4: Bode plots of open-loop HOSIDF \mathcal{L}_n for the CgLp-PID and shaped CgLp-PID control systems. The harmonics $n = 1$ and $n = 3$ (with dotted lines). The right zoom-in figure shows the first-order harmonics during the frequency range [100, 300] Hz.

5

($n = 3$) is observed. Specifically, at an input frequency of 100 Hz, the value of $|\mathcal{S}_3(\omega)|$ decreases drastically from 0.096 to 1.36×10^{-4} , which corresponds to a 99.86% reduction. This decrease in the sensitivity function will result in a corresponding reduction in steady-state errors, as demonstrated by the subsequent experimental results.

Figures 5.5(c) and (d) present the experimentally measured steady-state error and control input signals for the three control systems when subjected to a sinusoidal input signal $r(t) = 1.2 \times 10^{-7} \sin(200\pi t)$ [m]. For a quantitative analysis, Table 5.1 summarizes the L_∞ and L_2 norms of the steady-state errors and control inputs over one steady-state cycle, denoted as $\|e\|_\infty$ [m], $\|e\|_2$ [m], $\|u\|_\infty$ [V], and $\|u\|_2$ [V], for the three control systems. Additionally, the settling time for each system, defined as the time required for the trajectory to reach steady-state performance, is also provided in Table 5.1. Notably, the shaped CgLp-PID control system achieves a 21.43% reduction in maximum error compared to the CgLp-PID control system at 100 Hz. This improvement in precision is primarily attributed to the reduction in $|\mathcal{S}_n(\omega)|$ at 100 Hz, as shown in Fig. 5.5(a).

The advantages of reducing high-order harmonics in the shaped CgLp-PID system are more pronounced in the control input signal. The control sensitivity function analysis in Fig. 5.5(b) shows that the CgLp-PID system exhibits substantial high-magnitude high-order harmonics at 100 Hz, which are nearly equal to the first-order harmonic. This results in noticeable spikes in the control input signal, as observed in Fig. 5.5(d). In contrast, the shaped CgLp-PID system effectively reduces these high-order harmonics, leading to a smoother, more linear control input signal. As highlighted in Table 5.1, the maximum control input required by the shaped CgLp-PID system is reduced by 85.64% compared to the CgLp-PID system.

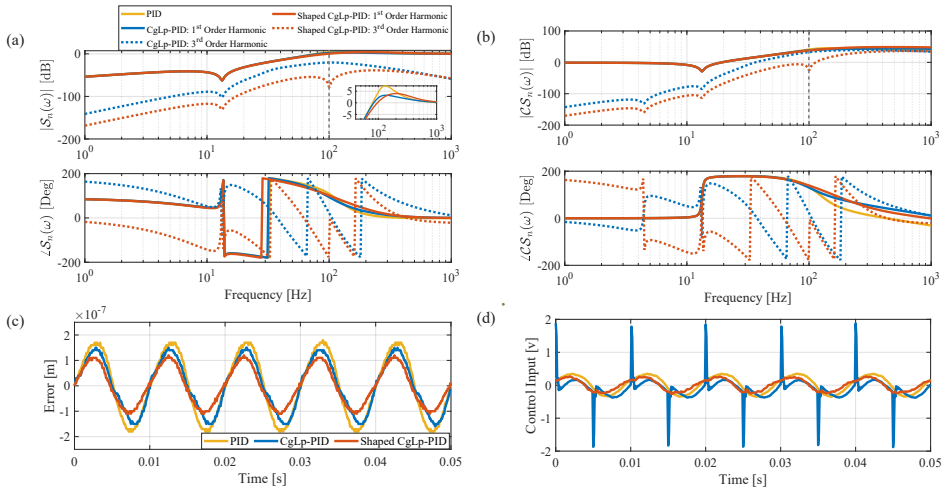


Figure 5.5: (a) The closed-loop Higher-Order Sinusoidal Input Sensitivity Function (HOSISF) \mathcal{S}_n and (b) Control Sensitivity Function $\mathcal{CS}_n(\omega)$ for the CgLp-PID and shaped CgLp-PID systems, where $n = 1, 3$. (c) The experimentally measured steady-state errors and (d) control input signals for these two systems at the input frequency of 100 Hz.

Table 5.1 The L_∞ and L_2 norms of the steady-state errors and control inputs over one steady-state cycle, denoted as $\|e\|_\infty$ [m], $\|e\|_2$ [m], $\|u\|_\infty$ [V], $\|u\|_2$ [V], along with the settling time for the PID, CgLp-PID, and shaped CgLp-PID control systems.

Systems	$\ e\ _\infty$ [m]	$\ e\ _2$ [m]	$\ u\ _\infty$ [v]	$\ u\ _2$ [v]	Settling Time [s]
PID	1.80×10^{-7}	5.51×10^{-7}	0.35	1.09	6.90×10^{-3}
CgLp-PID	1.50×10^{-7}	4.46×10^{-7}	1.88	1.73	7.50×10^{-3}
Shaped CgLp-PID	1.20×10^{-7}	3.34×10^{-7}	0.27	0.76	7.00×10^{-3}

5.3 Conclusion

The MATLAB app provides control engineers with an intuitive platform for designing and analyzing reset control systems in both open-loop and closed-loop configurations within the frequency domain.

Furthermore, in Section 5.2, we proposed a shaped reset control structure that enhances tracking accuracy while reducing actuation demands at the targeted frequency. Industrial mechatronics applications often face tracking challenges due to dominant frequencies or specific disturbances with notable spectral characteristics, such as friction, vibrations, actuator dynamics, and sensor noise [3–5]. The proposed shaped reset control structure is well-suited to address these challenges. However, this chapter primarily focuses on frequency response analysis; future research will explore detailed parameter optimization and tuning for targeted frequencies across different applications.

Bibliography

- [1] A. A. Dastjerdi, A. Astolfi, N. Saikumar, N. Karbasizadeh, D. Valerio, and S. H. HosseinNia. “Closed-loop frequency analysis of reset control systems”. In: *IEEE Transactions on Automatic Control* 68.2 (2022), pp. 1146–1153.
- [2] N. Saikumar, R. K. Sinha, and S. H. HosseinNia. “Constant in Gain Lead in Phase Element–Application in Precision Motion Control”. In: *IEEE/ASME Transactions on Mechatronics* 24.3 (2019), pp. 1176–1185.
- [3] M. Iwasaki, K. Seki, and Y. Maeda. “High-precision motion control techniques: A promising approach to improving motion performance”. In: *IEEE Industrial Electronics Magazine* 6.1 (2012), pp. 32–40.
- [4] H.-W. Chow and N. C. Cheung. “Disturbance and response time improvement of submicrometer precision linear motion system by using modified disturbance compensator and internal model reference control”. In: *IEEE Transactions on Industrial Electronics* 60.1 (2012), pp. 139–150.
- [5] K. Gruntjens, M. F. Heertjes, S. Van Loon, N. Van De Wouw, and W. Heemels. “Hybrid integral reset control with application to a lens motion system”. In: *2019 American Control Conference (ACC)*. IEEE. 2019, pp. 2408–2413.

6

Phase-Lead Shaped Reset Control Systems

This chapter presents a shaped reset feedback control strategy to enhance the performance of precision motion systems. The approach utilizes a phase-lead compensator as a shaping filter to tune the phase of reset instants, thereby shaping the nonlinearity in the first-order reset control. The design achieves either an increased phase margin while maintaining gain properties or improved gain without sacrificing phase margin, compared to reset control without the shaping filter. Then, frequency-domain design procedures are provided for both Clegg Integrator (CI)-based and First-Order Reset Element (FORE)-based reset control systems. Finally, the effectiveness of the proposed strategy is demonstrated through two experimental case studies on a precision motion stage. In the first case, the shaped reset control leverages phase-lead benefits to achieve zero overshoot in the transient response. In the second case, the shaped reset control strategy enhances the gain advantages of the previous reset element, resulting in improved steady-state performance, including better tracking precision and disturbance rejection, while reducing overshoot for an improved transient response.

6

 This chapter is based on the paper: Zhang, Xinxin, and S. Hassan HosseinNia. "Enhancing Reset Control Phase with Lead Shaping Filters: Applications to Precision Motion Systems." arXiv preprint arXiv:2503.15020 (2025).

6.1 Introduction

This chapter focuses on developing reset feedback control strategies to enhance the performance of precision positioning systems. High-precision industries, such as semiconductor manufacturing and robotics, demand systems capable of delivering accurate positioning, effective disturbance and noise rejection, fast response times, stability, and robustness [1]. To address these requirements, effective control strategies are crucial.

Linear feedback control, particularly the classical Proportional-Integral-Derivative (PID) controller, remains widely used due to its simplicity and effectiveness [2]. To meet the demands of industrial precision motion control, the loop-shaping technique is commonly employed in linear control design. This technique focuses on maintaining high gain at low frequencies to ensure effective low-frequency reference tracking and disturbance rejection [3]. At the same time, low gain at high frequencies is maintained to reduce sensitivity to high-frequency sensor noise and external disturbances [1]. Additionally, achieving an appropriate phase margin around the system's bandwidth is crucial for ensuring stability and a desired transient response [4], thereby facilitating reliable and smooth operation.

However, linear controllers face fundamental frequency-domain constraints, such as the waterbed effect and the Bode gain-phase trade-off [5]. These limitations restrict their ability to meet the increasingly stringent performance demands of precision motion systems [6]. Consequently, advanced control strategies are needed to overcome these trade-offs and achieve superior performance, addressing the evolving demands of precision motion systems.

Nonlinear control strategies, specifically reset feedback control, have emerged as a promising alternative [7]. The concept of reset control originated with the Clegg Integrator (CI) in 1958, which resets the integrator's output whenever the input crosses zero. Sinusoidal-Input Describing Function (SIDF) analysis demonstrates that the CI offers a 52° phase lead compared to a linear integrator while maintaining its gain properties [8, 9]. Over time, other reset elements have been introduced to enhance system performance, such as the First-order Reset Element (FORE), Second-order Reset Element (SORE), reset elements with reset bands, and Fractional-order Reset Elements (FrORE), and Constant in Gain Lead in Phase (CgLp) [6, 10–16].

This chapter focuses on first-order reset controllers, including CI- and FORE-based reset elements such as PI+CI control systems [17], reset PID controllers [18, 19], and CgLp controllers. Leveraging their gain and phase advantages, first-order reset controllers have been extensively studied in the literature to enhance transient performance—by reducing overshoot and settling time—and steady-state performance—by improving tracking accuracy and disturbance rejection, particularly in precision motion systems [5, 19–23].

Motivated by the performance of first-order reset controllers, this chapter aims to further enhance their phase and gain characteristics. Reset control introduces both first-order and high-order harmonics in the frequency domain, and by adjusting reset instants, these harmonics' characteristics can be tailored to improve overall system performance. In closed-loop reset feedback systems, the feedback error signal has traditionally been used as the reset-triggered signal that trigger reset actions. Recent

studies have explored alternative reset-triggered signals to tune system performance further. For instance, research in [24, 25] developed strategies to modify reset actions to reduce high-order harmonics. However, these techniques focus on reducing high-order harmonics within specific frequency ranges, at the expense of sacrificing the phase and gain characteristics of both first-order and high-order harmonics in other frequency ranges. These limitations restrict the applicability of these methods. In contrast, this work contributes by optimizing the gain and phase of first-order harmonics while preserving the properties of high-order harmonics, thereby improving system performance. The main contributions are as follows:

- First, a linear time-invariant (LTI) phase lead component is proposed as a shaping filter to tune the phase of reset instants, termed shaped reset control. This approach improves the phase-gain margin of the first-order harmonic performance while maintaining similar high-order harmonic characteristics compared to previous reset control strategies. Leveraging the enhanced phase-gain margin, it improves phase lead, resulting in better transient response, or it can be designed to optimize gain properties, leading to superior steady-state performance.
- Then, frequency-domain analysis and design procedures are provided for shaped CI- and FORE-based reset elements to achieve phase lead and gain improvements over previous reset control systems.
- Finally, two case studies on a precision motion stage experimentally validate the effectiveness of the shaped reset control strategy. In the first case, the shaped reset PID system introduces phase lead while retaining similar gain properties compared to the reset PID system. This phase lead benefit results in zero-overshoot transient performance, outperforming both the linear PID and reset PID systems. In the second case, the shaped CgLp-PID system is designed to preserve phase margin and high-frequency gain while achieving higher gain at low frequencies and increased bandwidth. These gain enhancements improve tracking precision and disturbance suppression compared to the CgLp-PID and linear PID systems.

The remainder of the chapter is organized into four sections. Section 6.2 presents the reset elements employed in this chapter and the frequency-domain design objectives for reset control in precision motion systems. Section 6.3 presents the analysis and design procedure of the shaped reset control, highlighting its frequency-domain benefits in terms of phase lead and gain improvements. Section 6.4 details experimental results conducted on a precision motion stage, validating the effectiveness of the shaped reset control systems compared with linear and reset control systems. Finally, Section 6.5 summarizes the main findings and offers suggestions for future research directions.

6.2 Preliminaries

Figure 6.1 depicts the block diagram of a closed-loop reset feedback control system used in this chapter. This system comprises a reset controller \mathcal{C} defined by (1.6) and (6.3), a LTI controller \mathcal{C}_α , and the plant \mathcal{P} . The LTI system \mathcal{C}_s (where $\angle \mathcal{C}_s(\omega) \in (-\pi, \pi]$) is referred to as the “shaping filter” used to shape the reset actions. Signals r , e , e_s , v ,

u , d , n , and y denote the reference, error, reset triggered, reset output, control input, process disturbance, sensor noise, and system output signals, respectively.

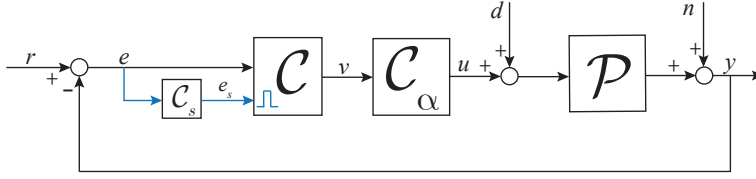


Figure 6.1: Block diagram of the closed-loop reset feedback control system, where the blue lines represent the reset action.

6.2.1 Reset Elements

This chapter focuses on the first-order reset elements, including the CI- and FORE-based reset elements, which are widely applied in the literature and have proven effective for enhancing system performance. The state-space matrices for these reset elements are defined as follows.

6

Generalized Clegg Integrator (CI)

The generalized Clegg Integrator (CI) is characterized by the following matrices:

$$A_R = 0, B_R = 1, C_R = 1, D_R = 0, A_p = \gamma \in (-1, 1). \quad (6.1)$$

When $\gamma = 0$, equation (6.1) characterizes the CI ([8]).

First-Order Reset Element (FORE)

The FORE is designed as a Low-Pass Filter (LPF) with a reset mechanism, whose state-space matrices are defined as:

$$\begin{aligned} A_R &= -\omega_r, B_R = \omega_r, C_R = 1, D_R = 0, \\ A_p &= \gamma \in (-1, 1), \quad \text{where } \omega_r \in \mathbb{R}^+. \end{aligned} \quad (6.2)$$

Generalized FORE

In this chapter, since both the generalized CI in (6.1) and the FORE in (6.2) are first-order reset elements, we define a generalized FORE that collectively describes these elements, with its matrices expressed as:

$$\begin{aligned} A_R &= -\omega_\alpha, B_R = \omega_\beta, C_R = 1, D_R = 0, \\ A_p &= \gamma \in (-1, 1), \text{ where } \omega_\alpha \geq 0 \in \mathbb{R}, \omega_\beta \in \mathbb{R}^+. \end{aligned} \quad (6.3)$$

In (6.3), a system with $\omega_\alpha = 0$ and $\omega_\beta = 1$ corresponds to the generalized CI in (6.1), while a system with $\omega_\alpha = \omega_\beta > 0$ corresponds to the FORE in (6.2).

6.2.2 HOSIDF for Generalized FORE

From (2.7) and (6.3), the HOSIDF for \mathcal{C} , denoted as $\mathcal{C}_n(\omega)$, is given by:

$$\mathcal{C}_n(\omega) = \begin{cases} (\Psi(\omega) + 1) \cdot \omega_\beta / (\omega_\alpha + j\omega), & \text{for } n = 1, \\ \Psi(\omega) \cdot \omega_\beta / (\omega_\alpha + jn\omega) \cdot e^{j(n-1)\angle\mathcal{C}_s(\omega)}, & \text{for odd } n > 1, \\ 0, & \text{for even } n \geq 2, \end{cases} \quad (6.4)$$

where

$$\begin{aligned} \Lambda(\omega) &= \omega^2 + \omega_\alpha^2, \\ \Theta(\omega) &= e^{-\pi\omega_\alpha/\omega}, \\ \Psi(\omega) &= 2j\omega\Omega(\omega)\alpha(\omega)/(\pi\Lambda(\omega)), \\ \Omega(\omega) &= (1 - \gamma) \cdot (1 + \Theta(\omega))/(1 + \gamma\Theta(\omega)), \\ \alpha(\omega) &= e^{j\angle\mathcal{C}_s(\omega)} [\omega \cos(\angle\mathcal{C}_s(\omega)) + \omega_\alpha \sin(\angle\mathcal{C}_s(\omega))]. \end{aligned} \quad (6.5)$$

6.2.3 Frequency-Domain Design Objective for Generalized FORE

From (6.4), the n th transfer function of the open-loop reset system shown in Fig. 6.1, which satisfies Assumption 1, is defined as follows:

$$\mathcal{L}_n(\omega) = \mathcal{C}_n(\omega)\mathcal{C}_\alpha(n\omega)\mathcal{P}(n\omega). \quad (6.6)$$

The bandwidth frequency $\omega_c \in \mathbb{R}^+$ of a reset control system is defined as the frequency at which the magnitude of the first-order harmonic open-loop transfer function $\mathcal{L}_1(\omega)$, as given in (6.6), reaches 0 dB, mathematically expressed as:

$$\mathcal{L}_1(\omega_c) = 0 \text{ dB}. \quad (6.7)$$

In this chapter, the proposed shaped reset control element is designed to enhance the performance of precision motion systems by satisfying the first-order harmonic $\mathcal{L}_1(\omega)$ requirements specified in Remark 6, while preserving similar high-order harmonics $\mathcal{L}_n(\omega)$ for $n > 1$.

Remark 6. Inspired by the loop-shaping technique in linear precision motion control, the design of the first-order harmonic $\mathcal{L}_1(\omega)$ in (6.6) for open-loop reset feedback control systems aims to achieve the following key objectives:

- (i) Ensuring a phase margin of $\angle\mathcal{L}_1(\omega_c) + 180^\circ$ at the bandwidth frequency ω_c defined in (6.7), to guarantee system stability and optimize transient performance.
- (ii) Maintaining a high gain $|\mathcal{L}_1(\omega)|$ at frequencies where $\omega < \omega_c$ to ensure low-frequency reference tracking precision and disturbance rejection.
- (iii) Achieving low gain $|\mathcal{L}_1(\omega)|$ at frequencies where $\omega > \omega_c$ to suppress high-frequency noise and improve robustness.

6.3 Frequency-Domain Analysis and Design of the Shaped Reset Systems

In this section, we first present the phase properties of the generalized FORE derived from its HOSIDF, as detailed in Remark 7 and Remark 8. Subsequently, Lemmas 3 and

4 outline the conditions necessary to enhance the phase margin of the generalized FORE while maintaining similar gain properties. To fulfill these conditions, Theorems 7 and 8 establish the requirements for designing the shaping filter \mathcal{C}_s for CI and FORE elements. Finally, design procedures are provided for the shaped generalized FORE to improve system performance.

6.3.1 Phase Lead Benefits of Shaped Generalized FROE

From the HOSIDF expressions for the generalized FORE in (6.4) and (6.5), two key properties of $\mathcal{C}_n(\omega)$ are identified. First, Remark 7 highlights the impact of the shaping filter $\mathcal{C}_s(\omega)$ on the HOSIDF $\mathcal{C}_n(\omega)$.

Remark 7. The phase of the shaping filter, $\angle\mathcal{C}_s(\omega)$, and the HOSIDF of the generalized FORE, $\mathcal{C}_n(\omega)$, are related by $\mathcal{C}_n(\angle\mathcal{C}_s(\omega)) = \mathcal{C}_n(\angle\mathcal{C}_s(\omega) + k\pi)$, where $k \in \mathbb{Z}$. Furthermore, the magnitude of the shaping filter, $|\mathcal{C}_s(\omega)|$, has no effect on the HOSIDF.

The following Remark 8 derives the phase of the first-order harmonic, $\angle\mathcal{C}_1(\omega)$, at the bandwidth frequency ω_c in the generalized FORE.

Remark 8. From (6.4) and (6.5), the phase of the first-order harmonic $\mathcal{C}_1(\omega)$ at the bandwidth frequency ω_c is expressed as:

$$\angle\mathcal{C}_1(\omega_c) = \begin{cases} \phi_\lambda(\omega_c), & \text{for } \omega_\alpha = 0, \\ \phi_\alpha(\omega_c) - \arctan(\omega_c/\omega_\alpha), & \text{for } \omega_\alpha > 0. \end{cases} \quad (6.8)$$

where

$$\begin{aligned} \kappa_\gamma(\omega_c) &= \omega_c \cdot \Omega(\omega_c) / (\pi \cdot \Lambda(\omega_c)), \\ \phi_\alpha(\omega_c) &= \arctan\left(\frac{1}{(\kappa_\gamma(\omega_c) \cdot \kappa_\gamma(\omega_c))^{-1} - \tan(\angle\mathcal{C}_s(\omega_c))}\right), \\ \phi_\lambda(\omega_c) &= \arctan\left(\frac{\sin(2\angle\mathcal{C}_s(\omega_c)) - \pi(1 + \gamma)/(2(1 - \gamma))}{\cos(2\angle\mathcal{C}_s(\omega_c)) + 1}\right), \\ \kappa_\gamma(\omega_c) &= \omega_c \cdot \cos(2\angle\mathcal{C}_s(\omega_c)) + \omega_\alpha \cdot \sin(2\angle\mathcal{C}_s(\omega_c)) + \omega_c. \end{aligned} \quad (6.9)$$

Functions $\Lambda(\omega)$ and $\Omega(\omega)$ are defined in (6.5).

The performance of the generalized FORE is mainly influenced by three main parameters within the HOSIDF $\mathcal{C}_n(\omega)$ as defined in (6.4), including: (1) the phase of the first-order harmonic at the bandwidth frequency ω_c : $\angle\mathcal{C}_1(\omega_c)$ given in (6.8), (2) the magnitude of the first-order harmonic: $|\mathcal{C}_1(\omega)|$, and (3) the magnitude of the high-order harmonics: $|\mathcal{C}_n(\omega)|$, for $n > 1$.

In this chapter, the design of the shaping filter \mathcal{C}_s aims to provide a phase lead to the first-order harmonic at the bandwidth frequency, $\angle\mathcal{C}_1(\omega_c)$ as defined in (6.8), while preserving similar gain characteristics $|\mathcal{C}_n(\omega)|$ compared to the system without the shaping filter (i.e., $\mathcal{C}_s = 1$). To achieve this, Lemma 3 specifies the necessary conditions for the shaping filter to effectively provide the phase lead advantage.

Lemma 3. The phase of the first-order harmonic in the generalized FORE at the bandwidth frequency ω_c , represented as $\angle\mathcal{C}_1(\omega_c) \in (-\pi, \pi]$, is larger than that of the

system without the shaping filter (i.e., $C_s = 1$) if the phase of the shaping filter satisfies the following conditions:

$$\begin{cases} \angle C_s(\omega_c) \in \left(k\pi, \frac{\pi}{2} - \arctan\left(\frac{\pi(1+\gamma)}{4(1-\gamma)}\right) + k\pi \right), & \text{for } \omega_\alpha = 0, \\ \angle C_s(\omega_c) \in \left(k\pi, \frac{\pi}{2} - \arctan\left(\frac{\omega_c}{\omega_\alpha}\right) + k\pi \right), & \text{for } \omega_\alpha > 0, \end{cases} \quad (6.10)$$

where $k = -1, 0$.

Proof. The proof is provided in Appendix 6.A. \square

The shaping filter can not only provide phase lead as demonstrated in Lemma 3, but for the generalized CI with $\omega_\alpha = 0$, as derived from (6.8), it can also be designed to ensure a phase greater than 0 by satisfying the condition outlined in the following Remark.

Remark 9. The phase of the first-order harmonic in the generalized CI at the bandwidth frequency ω_c exceeds 0, denoted as $\angle C_1(\omega_c) \in (0, \pi]$, provided that the phase of the shaping filter $\angle C_s(\omega_c)$ satisfies the following conditions:

$$\angle C_s(\omega_c) \in \left(k\pi + \theta_p, k\pi + \frac{\pi}{2} - \theta_p \right), \quad (6.11)$$

where $k = -1, 0$, and

$$\theta_p = \frac{\arcsin\left(\frac{\pi(1+\gamma)}{2(1-\gamma)}\right)}{2}. \quad (6.12)$$

Lemma 3 outlines the conditions required for $\angle C_s(\omega_c)$ to achieve a phase lead. However, from (6.4), altering $C_s(\omega)$ modifies the gain properties of $|C_n(\omega)|$. To ensure a fair comparison, it is essential to limit these gain variations, which can be achieved by adhering to the constraints in Lemma 4.

Lemma 4. To limit the gain variation of $|C_n(\omega)|$ in the generalized FORE with a shaping filter $C_s \neq 1$, compared to the system where $C_s = 1$, the following condition must be satisfied:

$$\kappa_\alpha(\omega) \in (1 - \sigma, 1 + \sigma), \text{ for } \omega \neq \omega_c, \quad (6.13)$$

where $\sigma \in (0, 1) \subset \mathbb{R}$, and

$$\kappa_\alpha(\omega) = |\cos(\angle C_s(\omega)) + \sin(\angle C_s(\omega)) \cdot \omega_\alpha / \omega|. \quad (6.14)$$

Proof. The proof is provided in Appendix 6.B. \square

In practice, the value of $\sigma \in (0, 1)$ should be kept small. Specifically, when $\sigma = 0$, the gain properties of the generalized FORE remain unchanged. By adhering to the constraints in Lemma 4 and choosing an appropriate σ , the gain changes can be effectively restricted, ensuring similar gain properties. The selection of σ depends on the system's gain requirements, as demonstrated in the case studies in Section 6.4.

To illustrate the effects of σ , we examine the CI with a shaping filter that satisfies the constraints in Lemmas 3 and 4, referred to as the shaped CI. Figure 6.2 presents the magnitude $|\mathcal{C}_1(\omega)|$ and phase $\angle\mathcal{C}_1(\omega)$ of the first-order harmonic, along with the magnitude $|\mathcal{C}_3(\omega)|$ of the third-order harmonic, for both the CI and the shaped CI with $\gamma = 0$. The analysis considers $\sigma = 0.01, 0.05, 0.1, 0.2$.

For clarity, higher-order harmonics $|\mathcal{C}_n(\omega)|$ for $n > 3$ are omitted, as they exhibit the same trend as $|\mathcal{C}_3(\omega)|$ but with smaller magnitudes and minimal variations. Additionally, the shaping filters used in this example, while selected to satisfy Lemmas 3 and 4, are not the only possible options. The design of \mathcal{C}_s will be further discussed in subsequent sections.

The results in Fig. 6.2 demonstrate a distinct phase lead in $\angle\mathcal{C}_1(\omega)$ with minimal variations in $|\mathcal{C}_n(\omega)|$ for $n = 1, 3$. Specifically, for $\sigma = 0.1$, the phase lead at 100 Hz is 12.6 degrees, while the changes in $|\mathcal{C}_1(\omega)|$ and $|\mathcal{C}_3(\omega)|$ are negligible. The minimal effects of these small changes will be further shown in the case studies presented in Section 6.4.

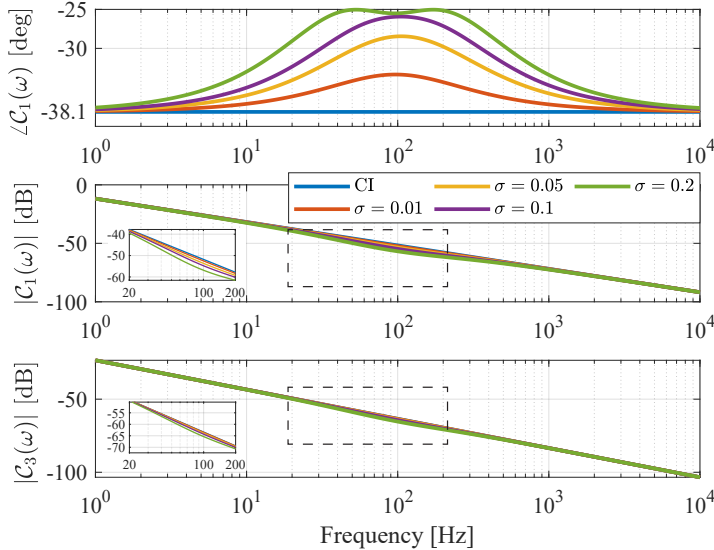


Figure 6.2: The magnitudes $|\mathcal{C}_1(\omega)|$ and phases $\angle\mathcal{C}_1(\omega)$ of the first-order harmonic, along with the magnitude $|\mathcal{C}_3(\omega)|$ of the third-order harmonic, for both the CI and the shaped CI with $\gamma = 0$ considering $\sigma = 0.01, 0.05, 0.1, 0.2$.

To summarize, Lemmas 3 and 4 outline the conditions for enhancing the phase margin of the generalized FORE while preserving similar gain benefits. To simultaneously meet these requirements, Theorems 7 and 8 specify the conditions for $\mathcal{C}_s(\omega)$ in the generalized FORE, as defined in (6.3), for cases where $\omega_\alpha = 0$ (generalized CI) and $\omega_\alpha > 0$ (FORE), respectively.

Theorem 7. In the generalized CI defined in (6.1), to achieve phase lead while maintaining similar gain properties compared to the system with $\mathcal{C}_s = 1$, the shaping

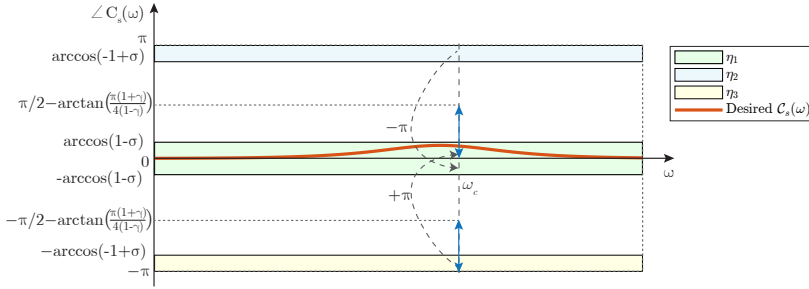


Figure 6.3: The three bounds, η_1 (—), η_2 (—), and η_3 (—), for $\angle C_s(\omega)$ are depicted as shaded regions. The constraint on $\angle C_s(\omega)$ at the bandwidth frequency ω_c is highlighted with blue double arrows (\leftrightarrow). The desired curve of $\angle C_s(\omega)$ for the generalized CI is shown in red, adhering to the constraints.

filter C_s , where $\angle C_s(\omega) \in (-\pi, \pi]$, needs to satisfy the following conditions:

$$\begin{cases} \angle C_s(\omega_c) \in \left(k\pi, \frac{\pi}{2} - \arctan\left(\frac{\pi(1+\gamma)}{4(1-\gamma)}\right) + k\pi \right), & \text{for } \omega = \omega_c, \\ \angle C_s(\omega) \in \{\eta_1 \cup \eta_2 \cup \eta_3\}, & \text{for } \omega \neq \omega_c, \end{cases} \quad (6.15)$$

where $k = -1, 0$, and

$$\begin{aligned} \eta_1 &= (-\arccos(1-\sigma), \arccos(1-\sigma)), \\ \eta_2 &= (\arccos(-1+\sigma), \pi], \\ \eta_3 &= [-\pi, -\arccos(-1+\sigma)), \quad \sigma \in (0, 1) \subset \mathbb{R}. \end{aligned} \quad (6.16)$$

The ranges of η_1 , η_2 , and η_3 are visualized in Fig. 6.3.

Proof. The proof is provided in Appendix 6.C. \square

From (6.16), we have

$$\eta_1 = \{\eta_2 - \pi\} \cup \{\eta_3 + \pi\}. \quad (6.17)$$

Since the effects of the shaping filter $C_s(\omega)$ on the HOSIDF of the generalized FORE are π -periodic, as noted in Remark 7, positioning $\angle C_s(\omega)$ within $\eta_2 \cup \eta_3$ can be effectively achieved by positioning it within η_1 . For reference, we plot a desired curve for $\angle C_s(\omega)$ within η_1 for $\omega \neq \omega_c$, while $\angle C_s(\omega_c)$ satisfies the constraint outlined in Theorem 7. However, the choice of $\angle C_s(\omega)$ is not unique; other curves for $\angle C_s(\omega)$ that remain within the specified bounds can also achieve phase lead and preserve similar gain.

Theorem 8. In the FORE defined in (6.2), to achieve phase lead while maintaining similar gain properties compared to the system with $C_s = 1$, the shaping filter C_s , where $\angle C_s(\omega) \in (-\pi, \pi]$, needs to satisfy the following conditions:

$$\begin{cases} \angle C_s(\omega_c) \in \left(k\pi, \frac{\pi}{2} - \arctan\left(\frac{\omega_c}{\omega_\alpha}\right) + k\pi \right), & \text{for } \omega = \omega_c, \\ \angle C_s(\omega) \in \{\beta_1 \cup \beta_2 \cup \beta_3 \cup \beta_4\}, & \text{for } \omega \neq \omega_c, \end{cases} \quad (6.18)$$

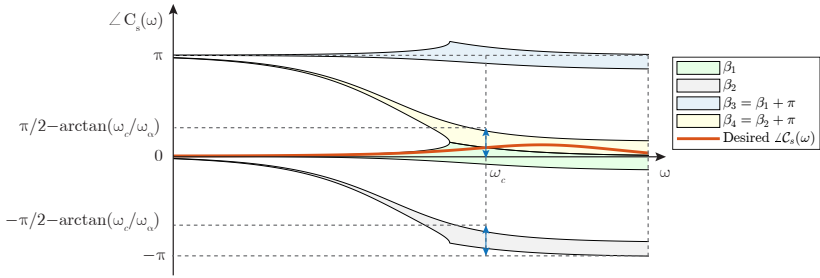


Figure 6.4: The four bounds, β_1 (green), β_2 (grey), β_3 (blue), and β_4 (yellow), for $\angle C_s(\omega)$ are depicted as shaded regions. The constraint on $\angle C_s(\omega)$ at the bandwidth frequency ω_c is highlighted with blue double arrows (\leftrightarrow). The desired curve of $\angle C_s(\omega)$ for the FORE is shown in red, adhering to the constraints.

where $k = -1, 0$, and

$$\begin{aligned}
 \beta_1 &= (\arctan \theta_\alpha - \arccos(\theta_\gamma), \arctan \theta_\alpha - \arccos(\theta_\eta)), \\
 \beta_2 &= (\arctan \theta_\alpha - \arccos(-\theta_\eta), \arctan \theta_\alpha - \arccos(-\theta_\gamma)), \\
 \beta_3 &= \beta_1 + \pi, \\
 \beta_4 &= \beta_2 + \pi, \\
 \theta_\alpha &= \frac{\omega_\alpha}{\omega}, \\
 \theta_\gamma &= \frac{1 - \sigma}{\sqrt{1 + \theta_\alpha^2}}, \quad \theta_\eta = \frac{1 + \sigma}{\sqrt{1 + \theta_\alpha^2}}, \quad \sigma \in (0, 1) \subset \mathbb{R}.
 \end{aligned} \tag{6.19}$$

Note that the value of $\arccos(x)$ is defined within the interval $[0, \pi]$. The ranges of β_1 , β_2 , β_3 , and β_4 are visualized in Fig. 6.4.

Proof. The proof is provided in Appendix 6.D. \square

Similar to Fig. 6.3, a desired curve for $\angle C_s(\omega)$ is plotted within the bounds of $\beta_1 \cup \beta_4$ for $\omega \neq \omega_c$, while $\angle C_s(\omega_c)$ is constrained by the condition outlined in Theorem 8.

6.3.2 Design Procedure for Shaped Generalized FROE

While various shaping filters C_s satisfying the constraints in Theorems 7 and 8 can be selected to achieve phase lead while maintaining similar gain properties, this chapter adopts a derivative element:

$$C_s(s) = \frac{s/\omega_\zeta + 1}{s/\omega_\eta + 1}, \quad \text{where } \omega_\zeta, \omega_\eta \in \mathbb{R}^+, \tag{6.20}$$

which aligns with the desired phase curve shapes of $\angle C_s(\omega)$ illustrated in both Fig. 6.3 for the generalized FORE with $\omega_\alpha = 0$ and Fig. 6.4 for the generalized FORE with $\omega_\alpha > 0$, respectively.

However, implementing a single derivative element between the error signal $e(t)$ and the reset-triggered signal $e_s(t)$ can amplify high-frequency harmonics for

frequencies $\omega > \omega_\eta$ in $e_s(t)$. In practical scenarios, especially when high-frequency noise from sensors or external interference is present, this amplification can increase the system's sensitivity to such noise, potentially compromising its steady-state performance.

To address this issue, a low-pass filter $\frac{1}{s/\omega_\psi+1}$ is needed to filter out high-frequency harmonics in the reset-triggered signal $e_s(t)$. Therefore, the transfer function of the shaping filter $C_s(s)$ is designed as:

$$C_s(s) = \frac{s/\omega_\zeta + 1}{s/\omega_\eta + 1} \cdot \frac{1}{s/\omega_\psi + 1}, \quad (6.21)$$

where $\omega_\zeta, \omega_\eta \in \mathbb{R}^+$, and $\omega_\psi \in \mathbb{R}^+ > \omega_\eta$. To mitigate excessive sensitivity of the shaped reset control to high-frequency noise, particularly at frequencies above the crossover frequency ω_c , the design of ω_ψ ensures that for all $\omega > \omega_c$, the condition $|C_s(\omega)|/|C_s(\omega_c)| < \delta_n$ holds, where $\delta_n \in (1, 5) \subset \mathbb{R}$. The choice of δ_n is based on the noise characteristics and high-order harmonics in the practical shaped reset control systems. Iterative tuning may be required in cases of unmeasured noise. In this study, we set $\delta_n = 2.1$, thereby limiting the shaping filter's amplification of high-frequency noise to a factor below 2.1. This constraint has been validated to ensure robustness in the case studies, both through simulations with white noise of magnitude 1×10^{-5} and experimental validation.

Note that while using a second-order or higher-order phase-lead element as the shaping filter can also provide phase lead, but it may exacerbate the issue of high-frequency noise amplification in the reset-triggered signal $e_s(t)$, making the system less robust to practical noise. The feasibility of using a higher-order lead element is outside the scope of this chapter and requires further investigation.

The reset control system with a shaping filter, defined in (6.21) and satisfying the conditions specified in Theorems 7 and 8, is referred to as the shaped reset control system in this chapter. The phase lead at the bandwidth frequency ω_c , provided by the shaping filter C_s , is calculated as described in Remark 10.

Remark 10. The phase lead of the shaped generalized FORE with the shaping filter $C_s(s) \neq 1$ compared to the generalized FORE where $C_s(s) = 1$ is given by:

$$\phi_{\text{lead}} = \angle C_1(\omega_c) - \angle C_1^0(\omega_c), \quad (6.22)$$

where $\angle C_1(\omega_c)$ represents the phase of the shaped generalized FORE, which can be calculated using (6.8), and $\angle C_1^0(\omega_c)$ represents the phase of the generalized FORE with $C_s = 1$, as given by:

$$\angle C_1^0(\omega_c) = \begin{cases} \arctan\left(\frac{-\pi(1+\gamma)}{4(1-\gamma)}\right), & \text{for } \omega_\alpha = 0, \\ \arctan\left(2\omega_c \kappa_\zeta(\omega_c)\right) - \arctan\left(\frac{\omega_c}{\omega_\alpha}\right), & \text{for } \omega_\alpha > 0, \end{cases} \quad (6.23)$$

where $\kappa_\zeta(\omega_c)$ is given in (6.9).

MATLAB code for calculating the phase lead ϕ_{lead} in (6.22) is available at this [link](#) to facilitate ease of use for readers. Next, Remark 11 presents the maximum phase lead that can be achieved by the shaping filter under the constraints specified in Theorems 7 and 8.

Remark 11. From Lemma 3, the maximum phase of shaping filter $\angle C_s(\omega_c) \in (-\pi, \pi]$ is given by

$$\max \angle C_s(\omega_c) = \begin{cases} \frac{\pi}{2} - \arctan\left(\frac{\pi(1+\gamma)}{4(1-\gamma)}\right), & \text{for } \omega_\alpha = 0, \\ \frac{\pi}{2} - \arctan\left(\frac{\omega_c}{\omega_\alpha}\right), & \text{for } \omega_\alpha > 0. \end{cases} \quad (6.24)$$

By substituting $\max \angle C_s(\omega_c)$ from (6.24) into (6.22) and (6.23), the maximum phase lead, denoted as $\max \phi_{\text{lead}}$, of the shaped generalized FORE (where $C_s \neq 1$) compared to the generalized FORE without the shaping filter (where $C_s = 1$) can be determined.

Finally, summarizing the constraints in Theorems 7 and 8, along with conclusions in Remarks 10 and 11, the design procedure for the shaping filter $\angle C_s(s)$ in the shaped generalized FORE-based reset control system, aimed at achieving a phase lead $\phi_d \in (0, \max \phi_{\text{lead}}]$ compared to the generalized FORE-based reset control system with $C_s = 1$, is outlined as follows:

6

- (i) Design a generalized FORE-based reset control system without the shaping filter (i.e., $C_s = 1$) and set the bandwidth frequency ω_c .
- (ii) Apply a shaping filter C_s as defined in (6.21).
- (iii) Choose $\sigma \in (0, 1)$. Next, tune ω_ζ , ω_η , and ω_ψ in $C_s(\omega)$ to satisfy the conditions specified in Theorem 7 if $\omega_\alpha = 0$, and in Theorem 8 if $\omega_\alpha > 0$.
- (iv) Calculate the phase lead ϕ_{lead} provided by the shaping filter using (6.22). If $\phi_{\text{lead}} < \phi_d$, decrease ω_ζ or increase ω_η , and repeat from step (iii) until $\phi_{\text{lead}} = \phi_d$.

If the system requirements prioritize gain improvement over phase margin enhancement, the design procedure for shaping the filter $C_s(s)$ involves first following the above steps to achieve phase lead, and then transferring this phase lead benefit to gain improvement by relaxing the gain constraint in Lemma 4 for frequencies $\omega \neq \omega_c$. The design procedure to obtain gain benefits while maintaining phase margin compared to a generalized FORE-based reset control system with $C_s = 1$ is outlined as follows:

- (i) Design a shaped generalized FORE-based reset control system to provide a phase lead ϕ_{lead} .
- (ii) Gradually adjust parameters such as ω_α and γ to increase the first-order harmonic gain $|C_1(\omega)|$ at frequencies below ω_c or reducing gain at higher frequencies. As gain benefits increase, the phase lead ϕ_{lead} diminishes; tuning continues until $\phi_{\text{lead}} = 0$, where the shaped generalized FORE maintains phase margin while maximizing gain benefits.

Note that for the generalized FORE with $\omega_\alpha > 0$, both ω_α and γ offer flexibility in tuning; in contrast, systems with $\omega_\alpha = 0$ rely solely on γ . Therefore, the FORE-based control systems with $\omega_\alpha > 0$ are preferable for providing enhanced gain benefits due to their greater tuning flexibility.

In Section 6.4, two case studies are presented to demonstrate the design procedure of shaped generalized FORE control systems, aiming to achieve phase and gain benefits, respectively.

6.4 Illustrative Case Studies

In this section, two case studies are then conducted on this stage to demonstrate the enhanced performance of the shaped generalized FORE-based reset control system:

- Case Study 1 uses a reset PID controller to showcase the phase lead advantages provided by the shaped reset control.
- Case Study 2 employs a CgLp-PID control system to emphasize the gain benefits, particularly achieving enhanced low-frequency gain.

Note that these cases may not represent the optimized designs; and the aim of these cases is to illustrate how the shaped reset control can offer improvements over previous reset control systems under a fair comparison framework. In both cases, the systems are verified for stability and convergence.

6.4.1 Case Study 1: Phase Lead Benefit of Shaped Reset Control

In Case Study 1, a reset PID control system is designed to showcase the phase lead benefit of shaped reset control within the framework of the generalized FORE-based reset control when $\omega_\alpha = 0$. This design is informed by Theorem 7. The following content illustrates the design and comparison process.

By replacing the Proportional Integrator (PI) with the Proportional Clegg Integrator (PCI) in the PID control system, a Proportional Clegg Integrator Derivative (PCID) system is built. However, the closed-loop PCID system tends to exhibit a limit cycle behavior [18]. To mitigate this issue, one approach is to incorporate an additional integrator, resulting in the PCI-PID system, whose block diagram is shown in Fig. 6.5.

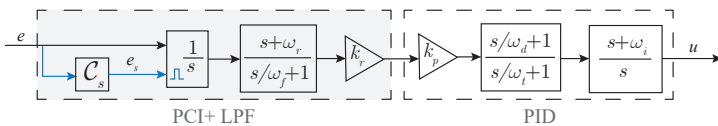


Figure 6.5: Block diagram of the PCI-PID control system.

By designing the PCI reset elements shown within the gray block in Fig. 6.5, the PCI-PID system can leverage gain benefits while maintaining the same phase characteristics as its base linear system, the PI²D system, as given by:

$$PI^2D = k_p \cdot \left(\frac{s + \omega_i}{s} \right)^2 \cdot \frac{s/\omega_d + 1}{s/\omega_t + 1} \cdot \frac{1}{s/\omega_f + 1}. \tag{6.25}$$

The design parameters of the PCI-PID control system are: $\omega_r = 1.6 \times 10^3$ [rad/s], $k_r = 0.12$, $k_p = 13.1$, $\omega_f = 5.0 \times 10^3$ [rad/s], $\omega_d = 213.6$ [rad/s], $\omega_t = 1.2 \times 10^3$ [rad/s], $\omega_i = 50.3$ [rad/s], and $\gamma = -0.3$.

The bode plots of the first-order harmonic for the PCI-PID and PI²D control systems, within the frequency range of [1,1000] Hz, are presented in Fig. 6.6. Compared to the PI²D controller, the PCI-PID controller maintains the same phase margin at the bandwidth frequency of 80 Hz but achieves a higher gain at frequencies lower than 80 Hz and a lower gain at frequencies higher than 80 Hz. By designing

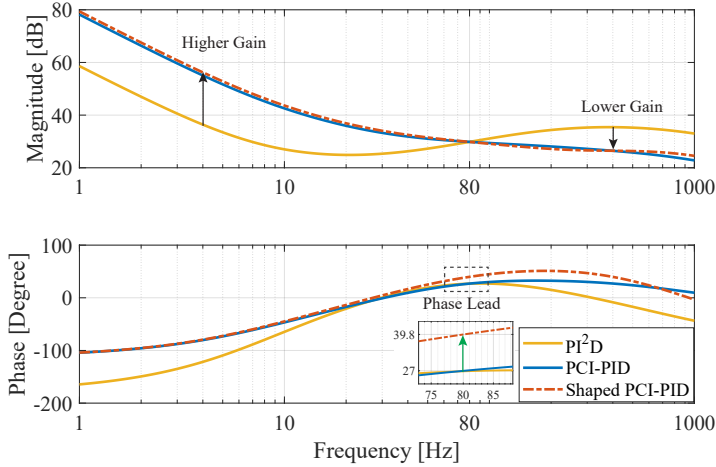


Figure 6.6: Bode plots of the first-order transfer functions $\mathcal{L}_1(\omega)$ of open-loop linear PI²D, PCI-PID, and shaped PCI-PID controllers. From here on, black arrows in this chapter indicate the improvement of reset control over linear control, while green arrows represent the enhancement of shaped reset control compared to reset control.

a shaping filter for the PCI-PID control system, the objective is to achieve phase lead while controlling gain variations. Setting $\sigma = 0.1$ limits the gain variation. According to Theorem 7, the phase bounds for $\angle \mathcal{C}_s(\omega)$ are chosen as follows:

$$\begin{cases} \angle \mathcal{C}_s(\omega_c) \in (0, 67.08^\circ), & \text{for } \omega = \omega_c, \\ \angle \mathcal{C}_s(\omega) \in \eta_1 = (-25.84^\circ, 25.84^\circ), & \text{for } \omega \neq \omega_c, \end{cases} \quad (6.26)$$

The constraint for $\angle \mathcal{C}_s(\omega)$ where $\omega \neq \omega_c$ in (6.26) are depicted by the shaded green region in Fig. 6.7. To achieve the desired phase lead relative to the CI, a shaping filter $\mathcal{C}_s(s)$ is implemented. The transfer function of $\mathcal{C}_s(s)$ is expressed as:

$$\mathcal{C}_s(s) = \frac{s/950 + 1}{s/3000 + 1} \cdot \frac{1}{s/10^4 + 1}. \quad (6.27)$$

As shown in Fig. 6.7, the shaping filter defined in (6.27) introduces a phase of 15.5° at the bandwidth frequency of 80 Hz. Since the PCI-PID control system is built upon the CI, the phase lead introduced by the shaping filter is initially applied to the CI

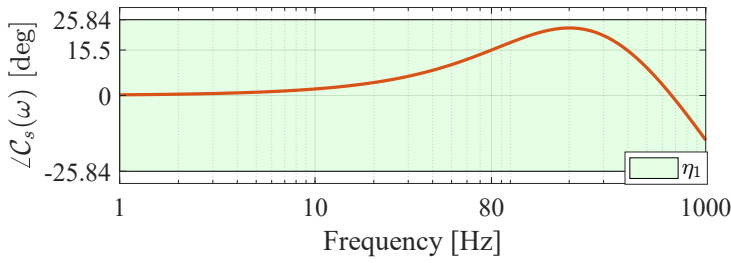


Figure 6.7: Plot of $\angle C_s(\omega)$ and its bound for the shaped PCI-PID control system.

and subsequently influences the entire PCI-PID control system. The Bode plots of the CI and the shaped CI, both with $\gamma = -0.3$, are presented in Fig. 6.8. The shaped CI maintains a gain profile similar to the CI while introducing a phase lead at frequencies below 665 Hz, as indicated by the green-shaded region. Specifically, at the bandwidth frequency of 80 Hz, the shaped CI achieves a phase margin of -10.1° , providing a 12.8° phase lead compared to the -22.9° phase margin of the CI.

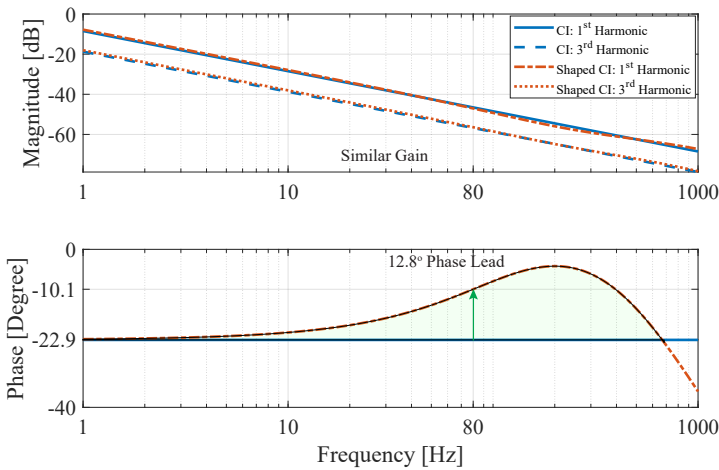


Figure 6.8: Bode plots of the CI and the shaped CI with the shaping filter C_s in (6.27), where $\gamma = -0.3$.

This designed shaped CI in Fig. 6.8 is incorporated into the PCI-PID control system to form the shaped PCI-PID control structure in Fig. 6.5. In this configuration, the parameter $k_r = 0.13$ is adjusted to ensure the same gain as the PCI-PID control system at the 80 Hz bandwidth frequency. As shown in Fig. 6.6, the open-loop Bode plot of the shaped PCI-PID controller closely matches the gain profile of the PCI-PID system but provides a phase lead of 12.8° .

Figure 6.9 displays the Bode plots for the PI^2D , PCI-PID, and shaped PCI-PID control systems, implemented on the stage shown in Fig. 1.2, including both the first- and third-order harmonics. All three systems share the same bandwidth frequency of 80 Hz. Compared to the PI^2D system, the PCI-PID system maintains the same phase

margin of 27.2° but demonstrates higher gain at low frequencies and lower gain at high frequencies. The shaped PCI-PID system behaves even better. It retains similar gain characteristics as the PCI-PID system but achieves a phase margin of 40° , with an increased phase margin of 12.8° in the time domain. This 12.8° phase lead is expected to improve the transient response of the system, a benefit that will be validated through experiments.

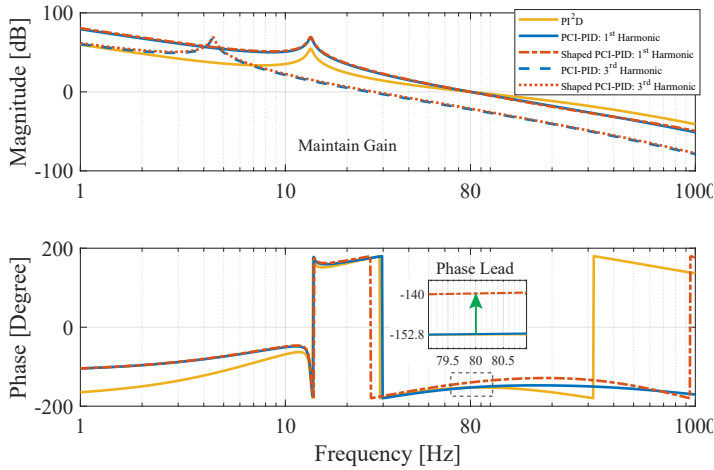


Figure 6.9: Bode plots of PI^2D , PCI-PID, and shaped PCI-PID control systems. The third-order harmonics of PCI-PID and shaped PCI-PID control systems are shown in dashed lines.

Figure 6.10 illustrates the experimentally measured step responses for the PI^2D , PCI-PID, and shaped PCI-PID control systems. The overshoot of the PI^2D and PCI-PID control systems are 64% and 36%, respectively, while the shaped PCI-PID achieve the zero overshoot performance. These results highlight the improved transient performance achieved with the shaped reset control, directly attributed to the enhancement in phase lead.

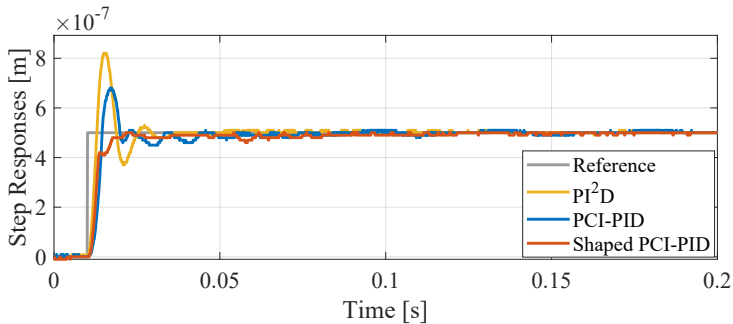


Figure 6.10: Experimentally measured step responses of the PI^2D , PCI-PID, and shaped PCI-PID control systems.

6.4.2 Case Study 2: Gain Benefit of Shaped Reset Control

In Case Study 2, a reset CgLp-PID control system is designed to demonstrate the gain benefits of shaped reset control within the generalized FORE-based reset control when $\omega_\alpha > 0$. The design follows Theorem 8.

The CgLp reset element consists of a FORE combined with a lead element, as shown in Fig. 6.11.

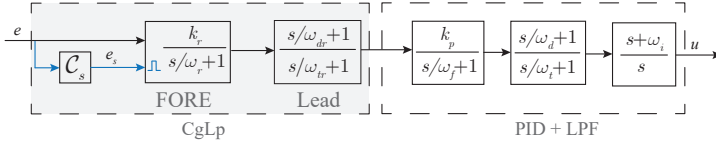


Figure 6.11: Block diagram of the CgLp-PID control system.

Compared to a linear PID controller, the CgLp-PID can maintain the same phase lead while benefiting from improved gain [6], as illustrated below. The design parameters for the CgLp-PID controller are: $\omega_r = 160.2$ [rad/s], $k_r = 1$, $k_p = 6.5$, $\omega_{dr} = 336.8$ [rad/s], $\omega_{tr} = 3.14 \times 10^4$ [rad/s], $\omega_f = 3.1 \times 10^3$ [rad/s], $\omega_d = 143.9$ [rad/s], $\omega_t = 685.6$ [rad/s], $\omega_i = 31.4$ [rad/s], and $\gamma = -0.3$. The design parameters for the PID controller are: $k_p = 3.0$, $\omega_d = 81.9$ [rad/s], $\omega_t = 1.2 \times 10^3$ [rad/s], $\omega_f = 3.1 \times 10^3$ [rad/s], and $\omega_i = 31.4$ [rad/s].

Figure 6.6 shows the Bode plots of the first-order harmonic for these systems within the frequency range of [1,1000] Hz. The CgLp-PID matches the PID in both gain and phase at the bandwidth frequency 50 Hz, while exhibiting higher gain at frequencies lower than 50 Hz and lower gain at frequencies higher than 50 Hz. The following content designs a shaped CgLp-PID controller that maintains the same phase and high-frequency gain properties as the CgLp-PID system while providing improved low-frequency gain and bandwidth benefits.

The CgLp-PID control system is built upon the FORE. To design a shaped FORE with phase lead, according to Theorem 8, by choosing $\sigma = 0.1$, the bound of $\angle C_s(\omega)$ is chosen as

$$\begin{cases} \angle C_s(\omega_c) \in (0, 27.02^\circ), & \text{for } \omega = \omega_c, \\ \angle C_s(\omega) \in \beta_1 \cup \beta_4, & \text{for } \omega \neq \omega_c, \end{cases} \quad (6.28)$$

where

$$\begin{aligned} \beta_1 &= (\arctan \theta_\alpha - \arccos(\theta_\gamma), \arctan \theta_\alpha - \arccos(\theta_\eta)), \\ \beta_4 &= (\arctan \theta_\alpha + \arccos(\theta_\eta), \arctan \theta_\alpha + \arccos(\theta_\gamma)), \\ \theta_\alpha &= \frac{\omega_r}{\omega}, \quad \theta_\gamma = \frac{0.9}{\sqrt{1 + \theta_\alpha^2}}, \quad \theta_\eta = \frac{1.1}{\sqrt{1 + \theta_\alpha^2}}. \end{aligned} \quad (6.29)$$

The bound specified in (6.28) for $\omega \neq \omega_c$ is depicted in Fig. 6.13. A shaping filter $C_s(s)$ that adheres to this bound is designed as follows:

$$C_s(s) = \frac{s/950 + 1}{s/2000 + 1} \cdot \frac{1}{s/10^5 + 1}. \quad (6.30)$$

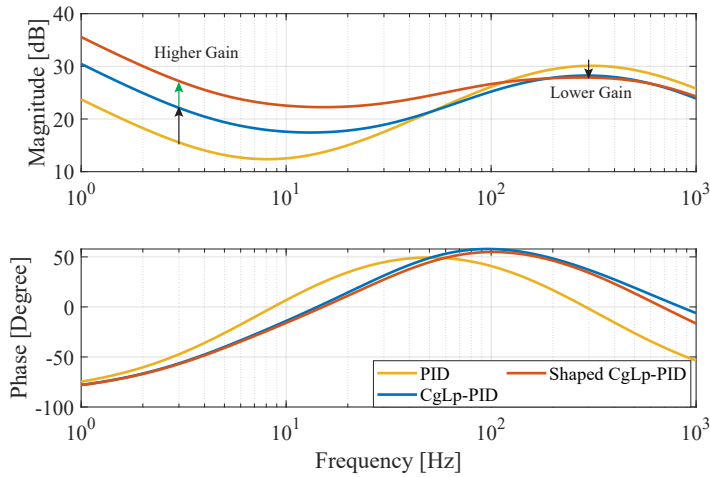


Figure 6.12: Bode plots of the first-order transfer functions $\mathcal{L}_1(\omega)$ for the open-loop linear PID, CgLp-PID, and shaped CgLp-PID controllers.

As shown in Fig. 6.13, the $\angle \mathcal{C}_s(\omega)$ is 10° at the bandwidth frequency of 50 Hz. According to (6.22), the phase of $\angle \mathcal{C}_s(\omega_c) = 9.2^\circ$ results in a $\phi_{lead} = 5.9^\circ$ phase lead in the shaped FORE, compared to the FORE with $\angle \mathcal{C}_s = 1$.

6

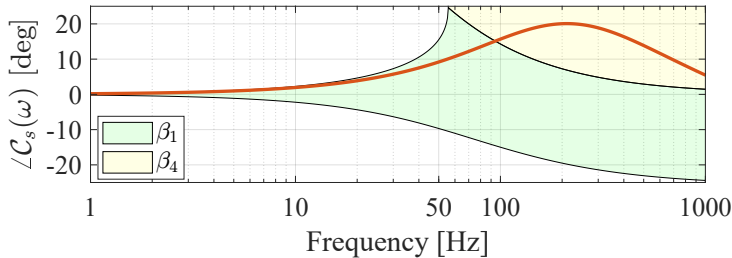


Figure 6.13: Plot of $\angle \mathcal{C}_s(\omega)$ and its bounds for the shaped CgLp-PID control system.

Then, to achieve the desired gain performance while retaining the phase margin, the parameters of the shaped CgLp controller are adjusted to $\omega_r = 145.6$ [rad/s], $k_r = 1.8$, and $\gamma = 0.08$. The Bode plots of the shaped CgLp-PID control system are presented in Fig. 6.12.

Then, applying the PID, CgLp-PID, and shaped CgLp-PID controllers to the plant in (1.1), the resulting open-loop Bode plots are presented in Fig. 6.14. All three systems achieve an identical phase margin of 50° and similar gain at frequencies higher than 50 Hz. However, the shaped CgLp-PID control system exhibits higher gain than the CgLp-PID at frequencies below 50 Hz. Additionally, the shaped CgLp-PID system achieves a wider bandwidth of 61.6 Hz, compared to 50 Hz for the CgLp-PID system. Although higher-order harmonics show a slight increase at frequencies below 50 Hz, their magnitudes remain negligible relative to the first-order harmonics. The higher

gain at low frequencies is expected to enhance precision in that frequency range, which will be further validated through experimental results.

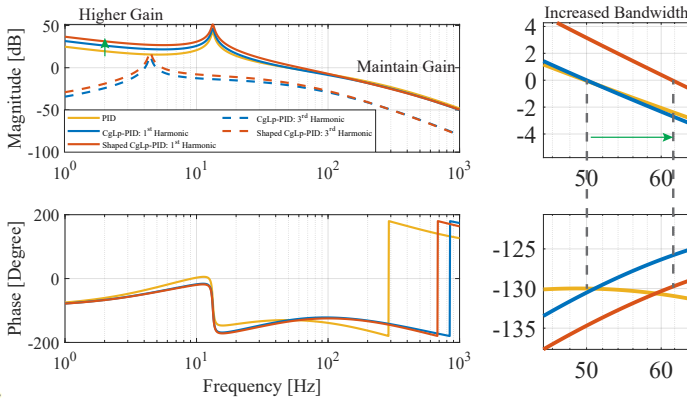


Figure 6.14: Bode plots of PID, CgLp-PID, and shaped CgLp-PID control systems. The third-order harmonics of CgLp-PID and shaped CgLp-PID control systems are shown in dashed lines.

Steady-State Performance: Improved Tracking Precision

As shown in Fig. 6.14, the shaped CgLp-PID system is designed to have higher gain at frequencies lower than 50 Hz while maintaining similar gain at frequencies higher than 50 Hz. Consequently, to compare the tracking precision of the PID, CgLp-PID, and shaped CgLp-PID control systems, the steady-state errors at input frequencies of 3 Hz, 5 Hz, 10 Hz, and 30 Hz are measured. Additionally, to validate the high-frequency performance is retained, the performance at a input frequency of 200 Hz is also tested.

Figure 6.15 presents the measured steady-state errors for the three control systems when tracking a reference signal $r(t) = 1 \times 10^{-5} \sin(2\pi t)$ [m] at frequencies of 3 Hz, 5 Hz, 10 Hz, 30 Hz, and 200 Hz. The maximum errors $\|e\|_{\infty}$ [m] for each system are summarized in Table 6.2. The results show that the shaped CgLp-PID system achieves a steady-state performance improvement of 41.3%, 40.0%, 30.6%, 25.0%, and 0 at frequencies of 3 Hz, 5 Hz, 10 Hz, 30 Hz, and 200 Hz, respectively, compared to the CgLp-PID system.

Table 6.1: Maximum steady-state errors $\|e\|_{\infty}$ [m] for the CgLp-PID and shaped CgLp-PID control systems under reference signals $r(t) = 1 \times 10^{-5} \sin(2\pi t)$ [m], where $f = 3$ Hz, 5 Hz, 10 Hz, 30 Hz, and 200 Hz. The precision improvement achieved by the shaped CgLp-PID compared to the CgLp-PID system are highlighted.

Systems	Frequency [Hz]				
	3	5	10	30	200
PID	1.4×10^{-6}	1.6×10^{-6}	1.2×10^{-6}	6.5×10^{-6}	9.4×10^{-6}
CgLp-PID	8.0×10^{-7}	1.0×10^{-6}	9.8×10^{-7}	8.0×10^{-6}	9.3×10^{-6}
Shaped CgLp-PID	4.7×10^{-7}	6.0×10^{-7}	6.8×10^{-7}	6.0×10^{-6}	9.3×10^{-6}
Precision Improvement	41.3%	40.0%	30.6%	25.0%	0

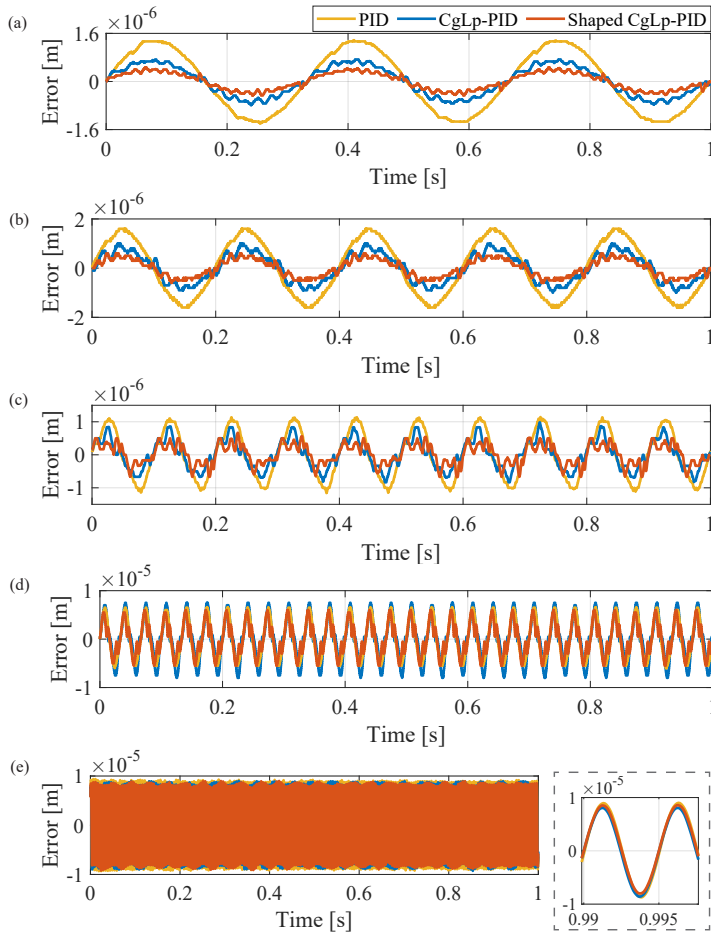


Figure 6.15: Experimentally measured steady-state errors of PID, CgLp-PID, and shaped CgLp-PID control systems under reference signals $r(t) = 1 \times 10^{-5} \sin(2\pi ft)$ [m], where $f =$ (a) 3 Hz, (b) 5 Hz, (c) 10 Hz, (d) 30 Hz, and (e) 200 Hz.

Steady-State Performance: Improved Tracking Precision and Disturbance Rejection

To evaluate the disturbance rejection capability of the shaped CgLp-PID control system, a disturbance signal $d_1(t) = 1 \times 10^{-8} [75.0 \sin(10\pi t) + 7.5 \sin(20\pi t) + 1.5 \sin(40\pi t)]$ [m] is applied to the three control systems. The measured steady-state errors for the PID, CgLp-PID, and shaped CgLp-PID control systems are displayed in Fig. 6.16. The maximum errors for each system are summarized in Table 6.2. The results show that the shaped CgLp-PID system achieves a precision improvement of 40.0% compared to the CgLp-PID system.

Then, to assess both reference tracking and disturbance rejection performance, a reference signal $r_2(t) = 7.5 \times 10^{-7} \sin(10\pi t)$ [m] and a disturbance signal $d_2(t) =$

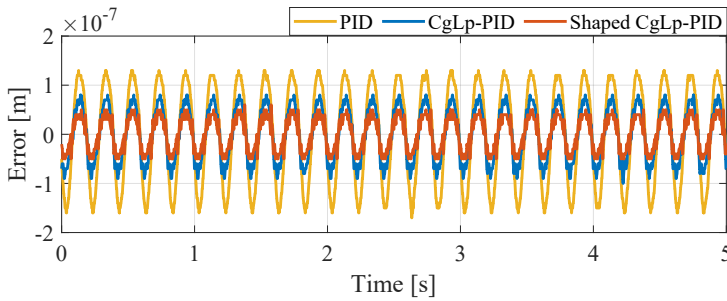


Figure 6.16: Experimentally measured steady-state errors of PID, CgLp-PID, and shaped CgLp-PID control systems under a disturbance signal $d_1(t)$.

Table 6.2: Maximum steady-state errors $\|e\|_\infty$ [m] for the CgLp-PID and shaped CgLp-PID control systems under the disturbance signal $d_1(t)$ and multiple inputs $r_2(t) + d_2(t)$.

Systems	Inputs	
	$d_1(t)$	$r_2(t) + d_2(t)$
PID	1.7×10^{-7}	1.5×10^{-7}
CgLp-PID	1.0×10^{-7}	8.0×10^{-8}
Shaped CgLp-PID	6.0×10^{-8}	5.0×10^{-8}
Precision Improvement	40.0%	37.5%

$1 \times 10^{-8}[19.1 \sin(2\pi t) + 1.8 \sin(4\pi t) + 3.3 \sin(16\pi t)]$ [m] are applied to the three control systems. The measured steady-state errors for the PID, CgLp-PID, and shaped CgLp-PID systems are shown in Fig. 6.17. The maximum errors for each system are summarized in Table 6.2. The results show that the shaped CgLp-PID system achieves a precision improvement of 37.5% compared to the CgLp-PID system.

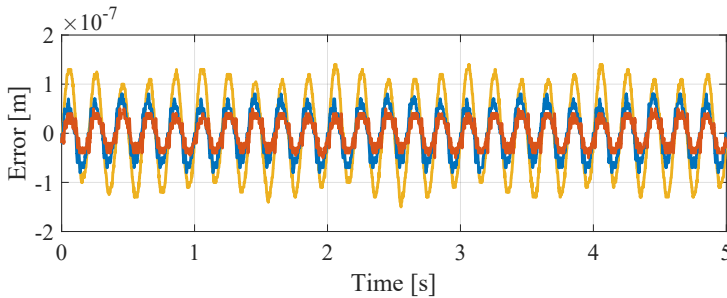


Figure 6.17: Experimentally measured steady-state errors for PID, CgLp-PID, and shaped CgLp-PID control systems under multiple inputs: reference signal $r_2(t)$ and disturbance signal $d_2(t)$.

These results highlight the improved steady-state precision of the shaped CgLp-PID control system, which is attributed to the gain benefits conferred by the shaping filter in the CgLp-PID design, as illustrated in Fig. 6.14.

Transient Performance Improvement: Reduced Overshoot

In addition to enhancing steady-state performance, measurements of the step responses of the three systems, shown in Fig. 6.18, reveal that the shaped CgLp-PID reduces the overshoot observed in the CgLp-PID system, achieving a non-overshoot performance.

This transient performance improvement can be attributed to the introduction of the phase lead element between the error signal $e(t)$ and the reset-triggered signal $e_s(t)$, as discussed in the research [26].

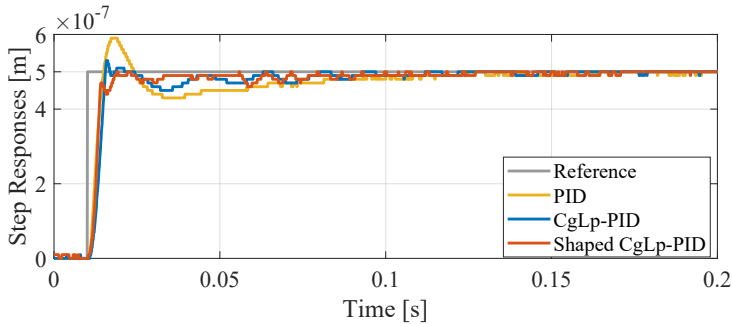


Figure 6.18: Experimentally measured step responses of PID, CgLp-PID, and shaped CgLp-PID control systems.

6

Thus, the phase-lead shaping filter not only contributes to better steady-state performance but also improves the transient response of the CgLp-PID system.

6.5 Conclusion

In conclusion, this chapter introduces a phase-lead shaping filter to improve phase and gain characteristics in CI-based and FORE-based reset control systems, referred to as shaped reset control. Frequency-domain design procedures for both CI-based and FORE-based reset control systems are provided. Experimental validation on two reset control systems implemented on a precision motion stage demonstrated the effectiveness of the proposed approach. In the first case study, the shaped reset control enhances transient performance by achieving zero overshoot, benefiting from the phase lead. In the second case study, the shaped reset control improves steady-state precision in reference tracking and disturbance rejection tasks, due to the gain benefit.

However, the benefits of the phase lead shaping filter in (6.21) are limited by high-frequency noise in practical systems. The phase lead element can amplify high-frequency noise in the reset-triggered signal, making it necessary to integrate a low-pass filter into the shaping filter. While this low-pass filter mitigates noise amplification, it also reduces some of the benefits provided by the phase lead. When system noise is minimized, the low-pass filter in (6.21) can be removed, allowing the advantages of phase lead-shaped reset control to be more pronounced. Future research could explore combining phase lead-shaped reset control with noise reduction techniques, such as the Kalman filter, to further enhance system performance. Investigating the potential of second-order phase lead shaping filters could also provide a promising direction for improvement.

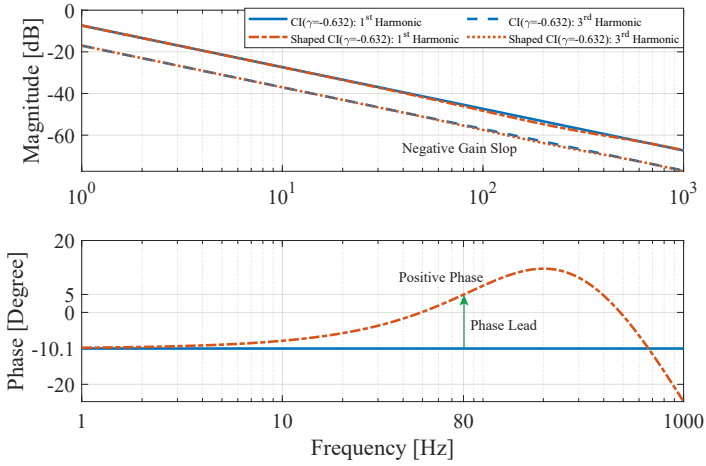


Figure 6.19: Bode plots of the CI and the shaped CI with the shaping filter C_s in (6.27), where $\gamma = -0.632$.

Furthermore, using the results from Remark 9, the shaped CI, designed with the shaping filter from (6.27), achieves a positive phase of 5° at 80 Hz when $\gamma = -0.632$, whereas the conventional CI exhibits a phase of -10.1° , as depicted in Fig. 6.19. Notably, the shaped CI demonstrates the ability to maintain a similar negative gain slope as the integrator while achieving a positive phase through appropriate design. This outcome highlights exciting potential for future applications.

Bibliography

- [1] R. M. Schmidt, G. Schitter, and A. Rankers. *The design of high performance mechatronics-: high-Tech functionality by multidisciplinary system integration*. Ios Press, 2020.
- [2] J. Han. “From PID to active disturbance rejection control”. In: *IEEE transactions on Industrial Electronics* 56.3 (2009), pp. 900–906.
- [3] A. Fuller. “Feedback control systems with low-frequency stochastic disturbances”. In: *International Journal of Control* 24.2 (1976), pp. 165–207.
- [4] C.-H. Chang and K.-W. Han. “Gain margins and phase margins for control systems with adjustable parameters”. In: *Journal of guidance, control, and dynamics* 13.3 (1990), pp. 404–408.
- [5] L. Chen, N. Saikumar, and S. H. HosseinNia. “Development of robust fractional-order reset control”. In: *IEEE Transactions on Control Systems Technology* 28.4 (2019), pp. 1404–1417.
- [6] N. Saikumar, R. K. Sinha, and S. H. HosseinNia. “Constant in Gain Lead in Phase Element–Application in Precision Motion Control”. In: *IEEE/ASME Transactions on Mechatronics* 24.3 (2019), pp. 1176–1185.
- [7] A. Banos and A. Barreiro. *Reset control systems*. Springer, 2012.
- [8] J. C. Clegg. “A nonlinear integrator for servomechanisms”. In: *Transactions of the American Institute of Electrical Engineers, Part II: Applications and Industry* 77.1 (1958), pp. 41–42.
- [9] Y. Guo, Y. Wang, and L. Xie. “Frequency-domain properties of reset systems with application in hard-disk-drive systems”. In: *IEEE Transactions on Control Systems Technology* 17.6 (2009), pp. 1446–1453.
- [10] K. Krishnan and I. Horowitz. “Synthesis of a non-linear feedback system with significant plant-ignorance for prescribed system tolerances”. In: *International Journal of Control* 19.4 (1974), pp. 689–706.
- [11] I. Horowitz and P. Rosenbaum. “Non-linear design for cost of feedback reduction in systems with large parameter uncertainty”. In: *International Journal of Control* 21.6 (1975), pp. 977–1001.
- [12] A. Baños, S. Dormido, and A. Barreiro. “Limit cycles analysis of reset control systems with reset band”. In: *Nonlinear analysis: hybrid systems* 5.2 (2011), pp. 163–173.
- [13] L. Hazeleger, M. Heertjes, and H. Nijmeijer. “Second-order reset elements for stage control design”. In: *2016 American Control Conference (ACC)*. IEEE, 2016, pp. 2643–2648.

- [14] N. Saikumar and H. HosseinNia. “Generalized fractional order reset element (GFrORE)”. In: *9th European Nonlinear Dynamics Conference (ENOC)*. EUROMECH. 2017.
- [15] C. Weise, K. Wulff, and J. Reger. “Fractional-order memory reset control for integer-order LTI systems”. In: *2019 IEEE 58th conference on decision and control (CDC)*. IEEE. 2019, pp. 5710–5715.
- [16] C. Weise, K. Wulff, and J. Reger. “Extended fractional-order memory reset control for integer-order LTI systems and experimental demonstration”. In: *IFAC-PapersOnLine* 53.2 (2020), pp. 7683–7690.
- [17] A. Baños and A. Vidal. “Definition and tuning of a PI+ CI reset controller”. In: *2007 european control conference (ECC)*. IEEE. 2007, pp. 4792–4798.
- [18] S. H. HosseinNia, I. Tejado, and B. M. Vinagre. “Fractional-order reset control: Application to a servomotor”. In: *Mechatronics* 23.7 (2013), pp. 781–788.
- [19] A. Bisoffi, R. Beerens, W. Heemels, H. Nijmeijer, N. van de Wouw, and L. Zaccarian. “To stick or to slip: A reset PID control perspective on positioning systems with friction”. In: *Annual Reviews in Control* 49 (2020), pp. 37–63.
- [20] Y. Zheng, Y. Chait, C. Hollot, M. Steinbuch, and M. Norg. “Experimental demonstration of reset control design”. In: *Control Engineering Practice* 8.2 (2000), pp. 113–120.
- [21] M. Heertjes, K. Gruntjens, S. Van Loon, N. Van de Wouw, and W. Heemels. “Experimental evaluation of reset control for improved stage performance”. In: *IFAC-PapersOnLine* 49.13 (2016), pp. 93–98.
- [22] G. Zhao, D. Nešić, Y. Tan, and C. Hua. “Overcoming overshoot performance limitations of linear systems with reset control”. In: *Automatica* 101 (2019), pp. 27–35.
- [23] R. Beerens, A. Bisoffi, L. Zaccarian, W. Heemels, H. Nijmeijer, and N. van de Wouw. “Reset integral control for improved settling of PID-based motion systems with friction”. In: *Automatica* 107 (2019), pp. 483–492.
- [24] N. Karbasizadeh, A. A. Dastjerdi, N. Saikumar, and S. H. HosseinNia. “Band-passing nonlinearity in reset elements”. In: *IEEE Transactions on Control Systems Technology* 31.1 (2022), pp. 333–343.
- [25] N. Karbasizadeh and S. H. HosseinNia. “Complex-order Reset Control System”. In: *2022 IEEE/ASME International Conference on Advanced Intelligent Mechatronics (AIM)*. IEEE. 2022, pp. 427–433.
- [26] N. Karbasizadeh and S. H. HosseinNia. “Continuous reset element: Transient and steady-state analysis for precision motion systems”. In: *Control Engineering Practice* 126 (2022), p. 105232.

Appendix

6.A Proof of Lemma 3

Proof. This proof derives the condition for the shaping filter \mathcal{C}_s to increase the phase of the first-order harmonic at the bandwidth frequency, denoted as $\angle\mathcal{C}_1(\omega_c)$. The proof is divided into two steps: the first addresses the generalized CI when $\omega_\alpha = 0$, and the second focuses on the FORE when $\omega_\alpha > 0$.

Step 1: Condition for the generalized FORE where $\omega_\alpha = 0$.

To ensure that the generalized FORE with a shaping filter $\mathcal{C}_s \neq 1$ exhibits a phase lead compared to the system with $\mathcal{C}_s = 1$, we need to ensure:

$$\angle\mathcal{C}_1(\omega_c) > \angle\mathcal{C}_1^0(\omega_c), \quad (6.31)$$

where $\angle\mathcal{C}_1(\omega_c)$ is the phase of the shaped generalized FORE with the shaping filter $\mathcal{C}_s(s) \neq 1$, and $\angle\mathcal{C}_1^0(\omega_c)$ is the phase of the generalized FORE with $\mathcal{C}_s(s) = 1$.

In the generalized FORE with $\omega_\alpha = 0$, from (6.8), we have $\angle\mathcal{C}_1(\omega_c) = \phi_\lambda(\omega_c)$. Therefore, to meet the condition in (6.31), $\phi_\lambda(\omega_c)$ needs to be larger than its value when $\mathcal{C}_s(s) = 1$. From (6.9), the following condition needs to be satisfied:

$$\frac{\sin(2\angle\mathcal{C}_s(\omega_c)) - \pi(1+\gamma)/(2(1-\gamma))}{\cos(2\angle\mathcal{C}_s(\omega_c)) + 1} > \frac{-\pi(1+\gamma)}{4(1-\gamma)}, \quad (6.32)$$

where the right-hand side corresponds to the element in $\phi_\lambda(\omega_c)$ when $\mathcal{C}_s(s) = 1$.

Then, solving (6.32), and given the π -period properties of $\angle\mathcal{C}_s(\omega)$ from Remark 7, the first condition for the $\angle\mathcal{C}_s(\omega_c)$ in (6.10) is derived.

Step 2: Condition for the generalized FORE where $\omega_\alpha > 0$.

In the generalized FORE with $\omega_\alpha > 0$, from (6.8), we have

$$\angle\mathcal{C}_1(\omega_c) = \phi_\alpha(\omega_c) - \arctan\left(\frac{\omega_c}{\omega_\alpha}\right),$$

where $\phi_\alpha(\omega_c)$ is an increasing function of $\kappa_\gamma(\omega_c) \cdot \kappa_\zeta(\omega_c)$, and $\tan(\angle\mathcal{C}_s(\omega_c))$.

Given the conditions $\omega > 0$, $\omega_\alpha > 0$, $\omega_\beta > 0$, $\gamma \in (-1, 1)$, and $\omega > 0$, it follows from the definition of $\kappa_\gamma(\omega_c)$ in (6.9) that $\kappa_\zeta(\omega_c) > 0$. To ensure that the generalized FORE with a shaping filter $\mathcal{C}_s \neq 1$ achieves a phase lead, both the values of $\tan(\angle\mathcal{C}_s(\omega_c))$ and $\kappa_\gamma(\omega_c)$ needs to exceed their respective values in the system where $\angle\mathcal{C}_s = 0$. This can be achieved by satisfying the following conditions:

$$\angle\mathcal{C}_s(\omega_c) \in (0, k \cdot \pi/2), \quad k \in \mathbb{N}, \quad (6.33)$$

and

$$\omega_c \cdot \cos(2\angle\mathcal{C}_s(\omega_c)) + \omega_\alpha \cdot \sin(2\angle\mathcal{C}_s(\omega_c)) > \omega_c. \quad (6.34)$$

Solving (6.33) and (6.34), and given the π -period properties of $\angle\mathcal{C}_s(\omega)$ from Remark 7, the second condition for the $\angle\mathcal{C}_s(\omega_c)$ in (6.10) is derived. \square

6.B Proof of Lemma 4

Proof. This proof establishes the condition required to limit gain changes for a system with a shaping filter compared to a system without the shaping filter at frequencies $\omega \neq \omega_c$.

From (6.4) and (6.5), the phase $\angle C_s(\omega)$ determines the function $\alpha(\omega)$, thereby influencing the HOSIDF $C_n(\omega)$. The function $\alpha(\omega)$ for the generalized FORE with and without the shaping filter is given by

$$\alpha(\omega) = \begin{cases} \omega, & \text{for } \angle C_s(\omega) = 0, \\ e^{j\angle C_s(\omega)} [\omega \cos(\angle C_s(\omega)) \\ + \omega_\alpha \sin(\angle C_s(\omega))], & \text{for } \angle C_s(\omega) \neq 0. \end{cases} \quad (6.35)$$

To limit gain changes of the generalized FORE at frequencies $\omega \neq \omega_c$, the change in $\alpha(\omega)$ should be minimized. To evaluate the change in $\alpha(\omega)$, the ratio of $\alpha(\omega)$ for the generalized FORE with and without the shaping filter in (6.35) is defined as:

$$\Delta_\alpha(\omega) = e^{j\angle C_s(\omega)} [\cos(\angle C_s(\omega)) + \omega_\alpha/\omega \sin(\angle C_s(\omega))]. \quad (6.36)$$

When $\Delta_\alpha(\omega) \rightarrow 1$ at frequencies $\omega \neq \omega_c$, the gain properties of the generalized FORE tend to remain unchanged.

From (6.36), $\Delta_\alpha(\omega)$ consists of two components: the phase $\angle \Delta_\alpha(\omega) = \angle C_s(\omega)$ and the magnitude given by

$$\kappa_\alpha(\omega) = |\Delta_\alpha(\omega)| = \left| \cos(\angle C_s(\omega)) + \frac{\omega_\alpha}{\omega} \sin(\angle C_s(\omega)) \right|. \quad (6.37)$$

To ensure that $\Delta_\alpha(\omega)$ approaches 1, two requirements must be met: First, the phase $\angle \Delta_\alpha(\omega) = \angle C_s(\omega)$ should tend to 0. Based on Remark 7, $\angle C_s(\omega)$ affects $C_n(\omega)$ with a period of π , so $\angle C_s(\omega) \rightarrow k \cdot \pi$, where $k \in \mathbb{Z}$ is required. Second, the magnitude $\kappa_\alpha(\omega)$ should tend to 1.

The constraint $\kappa_\alpha(\omega) \in (1 - \sigma, 1 + \sigma)$, where $\sigma \in (0, 1) \subset \mathbb{R}$, ensures that both the phase and gain conditions are satisfied. Additionally, as $\sigma \rightarrow 0$, the change in $|C_n(\omega)|$ tends to 0. This concludes the proof. \square

6.C Proof of Theorem 7

Proof. This proof derives the conditions for $\angle C_s(\omega)$ in the generalized CI where $\omega_\alpha = 0$ to meet the requirements specified in Lemmas 3 and 4.

In the generalized CI with $\omega_\alpha = 0$, from Lemma 3, the restriction on $\angle C_s(\omega) \in (-\pi, \pi]$ at ω_c requires that $\angle C_s(\omega_c)$ lies within the bounds:

$$\angle C_s(\omega_c) \in \left(k\pi, \frac{\pi}{2} - \arctan\left(\frac{\pi(1+\gamma)}{4(1-\gamma)}\right) + k\pi \right), \quad k = -1, 0.$$

From (6.14), the value of $\kappa_\alpha(\omega)$ is given by:

$$\kappa_\alpha(\omega) = |\cos(\angle C_s(\omega))|. \quad (6.38)$$

From Lemma 4 and (6.38), at frequencies where $\omega \neq \omega_c$, the following condition needs to be satisfied:

$$(1 - \sigma) < |\cos(\angle \mathcal{C}_s(\omega))| < (1 + \sigma), \quad \text{for } \omega \neq \omega_c. \quad (6.39)$$

Given the inherent property of $\cos(\angle \mathcal{C}_s(\omega)) \in [-1, 1]$ and $\sigma > 0$, the condition from (6.39) is expressed as:

$$(1 - \sigma) < \cos(\angle \mathcal{C}_s(\omega)) \leq 1, \text{ or} \\ -1 \leq \cos(\angle \mathcal{C}_s(\omega)) \leq -1 + \sigma, \text{ for } \omega \neq \omega_c. \quad (6.40)$$

Solving (6.40), the conditions for $\angle \mathcal{C}_s(\omega) \in (-\pi, \pi]$ are given by

$$\angle \mathcal{C}_s(\omega) \in (-\arccos(1 - \sigma), \arccos(1 - \sigma)) \\ \cup (\arccos(-1 + \sigma), \pi] \\ \cup [-\pi, -\arccos(-1 + \sigma)), \text{ for } \omega \neq \omega_c. \quad (6.41)$$

Defining η_1 , η_2 , and η_3 as in (6.16) and substituting them into (6.41) concludes the proof. \square

6.D Proof of Theorem 8

Proof. This proof derives the conditions for $\angle \mathcal{C}_s(\omega) \in (-\pi, \pi]$ in the FORE where $\omega_\alpha > 0$ to meet the requirements specified in Lemmas 3 and 4.

From Lemma 3, at frequencies where $\omega = \omega_c$, the following condition needs to be satisfied:

$$\angle \mathcal{C}_s(\omega_c) \in \left(k\pi, \frac{\pi}{2} - \arctan\left(\frac{\omega_c}{\omega_\alpha}\right) + k\pi \right), \quad k = -1, 0. \quad (6.42)$$

From (6.14), the function $\kappa_\alpha(\omega)$ can be written as

$$\kappa_\alpha(\omega) = \left| \cos(\angle \mathcal{C}_s(\omega)) + \frac{\omega_\alpha}{\omega} \sin(\angle \mathcal{C}_s(\omega)) \right| \\ = \sqrt{1 + \theta_\alpha^2} \left| \cos(\angle \mathcal{C}_s(\omega) - \arctan \theta_\alpha) \right|, \quad (6.43)$$

where

$$\theta_\alpha = \frac{\omega_\alpha}{\omega}. \quad (6.44)$$

From Lemma 4, at $\omega \neq \omega_c$, the following condition needs to be satisfied:

$$(1 - \sigma) < \kappa_\alpha(\omega) < (1 + \sigma), \text{ for } \omega \neq \omega_c. \quad (6.45)$$

From (6.43) and (6.45), at $\omega \neq \omega_c$, the following condition needs to be satisfied:

$$0 < \frac{(1 - \sigma)}{\sqrt{1 + \theta_\alpha^2}} < \cos(\angle \mathcal{C}_s(\omega) - \arctan \theta_\alpha) < \frac{(1 + \sigma)}{\sqrt{1 + \theta_\alpha^2}}, \text{ or} \\ \frac{(-1 - \sigma)}{\sqrt{1 + \theta_\alpha^2}} < \cos(\angle \mathcal{C}_s(\omega) - \arctan \theta_\alpha) < \frac{(-1 + \sigma)}{\sqrt{1 + \theta_\alpha^2}} < 0, \quad (6.46)$$

Solving (6.46), the resulting conditions for $\angle \mathcal{C}_s(\omega)$ are given in (6.18). Note that $\arccos(x)$ is defined within the interval $[0, \pi]$. This completes the proof. \square

7

PID-Shaped Reset Control Systems

Reset control introduces both first-order and high-order harmonics into the system, where high-order harmonics with dominated magnitudes can degrade system performance. In sinusoidal-input Describing Function (SIDF) analysis, multiple-reset control systems are indicative of high-order harmonics with dominated magnitudes. To reduce these problematic harmonics, the method outlined in Chapter 3 is first employed to identify the frequency range where multiple-reset actions occur. Subsequently, this chapter proposes a shaped reset control strategy that incorporates a shaping filter to refine reset actions and reduce high-order harmonics in the identified range. A frequency-domain design procedure for a PID shaping filter in a reset control system is then presented as a case study. The PID filter effectively suppresses high-order harmonics and addresses limit-cycle issues under step inputs. Finally, simulations and experimental results on a precision motion stage validate the effectiveness of the proposed shaped reset control, demonstrating enhanced SIDF analysis accuracy, improved steady-state precision compared to both linear and reset controllers, and successful elimination of limit cycles under step inputs.

7

 This chapter is based on the paper:

Zhang, Xinxin, and S. Hassan HosseinNia. "Enhancing the Reliability of Closed-Loop Describing Function Analysis for Reset Control Applied to Precision Motion Systems." arXiv preprint arXiv:2412.00502 (2024).

7.1 Introduction

Multiple-reset actions in sinusoidal-input reset systems indicate the presence of high-order harmonics, which, when large, can increase the system's sensitivity to high-frequency noise and potentially lead to instability, thereby compromising overall system performance. Chapter 3 introduces a method to pinpoint the frequency ranges where high-magnitude higher-order harmonics arise.

Then, to address this issue, this chapter introduces a shaped reset control strategy that employs a shaping filter to tune reset actions, effectively reducing high-order harmonics while retaining the advantages of the first-order harmonic. A comprehensive design procedure is presented for a PID-shaped reset control system, specifically aimed at minimizing high-order harmonics in a CI-based reset framework. Furthermore, the PID-shaped reset control resolves limit-cycle issues observed in reset systems under step inputs. Experimental validation on a precision motion stage demonstrates that mitigating the influence of high-order harmonics enhances the reliability of SIDF analysis and improves steady-state precision, including superior reference tracking accuracy, disturbance rejection, and noise suppression. Additionally, the approach successfully eliminates limit-cycle phenomena.

The remainder of this chapter is organized as follows: Section 7.2 outlines the research problem through illustrative examples. Section 7.3 presents the shaped reset control strategy aimed at reducing high-order harmonics. Section 7.4 outlines a design procedure for a PID shaping filter, showcased as a case study to decrease high-order harmonics and eliminate limit cycles. Section 7.5 then provides simulation and experimental results to validate the PID-shaped reset control system's effectiveness on a precision motion stage. Section 7.6 summarizes the main findings and offers recommendations for future research directions.

7

7.2 Problem Statement via Illustrative Example

PID controllers are widely employed in the mechatronics industry due to their simplicity and effectiveness. In this section, the PCID control system designed in Section 3.2 is used to illustrate the high-order harmonics issues in closed-loop reset feedback control systems. To ensure a fair comparison, both the PID and PCID controllers are designed to maintain the same bandwidth of 100 Hz and a phase margin of 50° with the plant $\mathcal{P}(s)$ in (1.1).

The reset system does not only consist of the first-order harmonic but also introduces higher-order harmonics. These large high-order harmonics can adversely affect overall system performance and this detrimental effect is further illustrated in Fig. 7.1.

The steady-state errors of the closed-loop PCID and PID control systems, subjected to sinusoidal reference inputs $r(t) = \sin(20\pi t)$ (10 Hz) and $r(t) = \sin(100\pi t)$ (50 Hz), are illustrated in Fig. 7.1. Additionally, the corresponding Power Spectral Density (PSD) plots are presented. To facilitate a clearer comparison, the magnitude of the first-order harmonic of the steady-state error in the PCID control system is normalized to 1, with the same scaling factor applied to the PID control system for fair comparison.

At an input frequency of 50 Hz, as shown in Fig. 7.1(b₂), the first-order harmonic

component dominates, and the magnitudes of the high-order harmonics are relatively small. In this scenario, as illustrated in Fig. 7.1(a₂), the PCID control system demonstrates two-reset actions and a lower steady-state error compared to the PID control system.

In contrast, at an input frequency of 10 Hz, the error signal exhibits multiple reset instants as shown in Fig. 7.1(a₁), which are associated with the presence of high-magnitude, high-order harmonics in Fig. 7.1(b₁). These high-magnitude high-order harmonics diminish the benefits of the first-order harmonic in the PCID control system, leading to a larger steady-state error compared to the linear PID control system in Fig. 7.1(a₁).

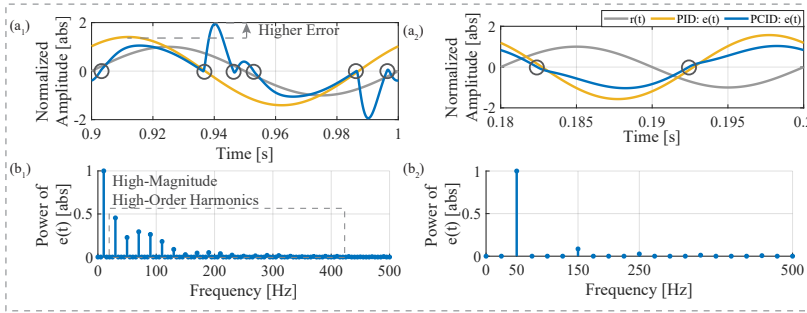


Figure 7.1: Steady-state errors $e(t)$ for the PID and PCID systems under two input signals: (a₁) $r(t) = \sin(20\pi t)$ and (a₂) $r(t) = \sin(100\pi t)$. The gray circles mark the reset instants per cycle. Panels (b₁) and (b₂) display the PSD plots for the errors $e(t)$ in (a₁) and (a₂), respectively.

This chapter addresses this issue. First, the two-reset condition in Chapter 3 is employed to identify the frequency ranges with high-magnitude high-order harmonics. Following this, a shaped reset control is proposed to mitigate these harmonics, thereby preventing system performance degradation, as illustrated in Fig. 7.1(a₁). This shaped reset control approach not only reduces higher-order harmonics but also effectively resolves limit-cycle problems in reset control systems.

Note that though the practical applications extend beyond sinusoidal-input systems, the sinusoidal-input analysis serves as an effective tool for investigating the frequency-domain harmonic characteristics within these reset control systems.

7.3 Analysis and Design of Shaped Reset Control Systems

Multiple-reset actions in sinusoidal-input closed-loop reset systems are indicative of high-order harmonics with dominated magnitudes. To reduce these harmonics, this section introduces a shaped reset control strategy. First, Lemma 5 provides an analytical decomposition of the steady-state reset-triggered signal $z_s(t)$ in such systems into a base-linear trajectory and a nonlinear component. Building on this, Theorem 9 defines a function $\beta_n(\omega)$, which quantifies the presence of high-order harmonics in $z_s(t)$. This function serves as the foundation for designing a shaped reset control approach to reduce high-order harmonics.

Lemma 5. Consider a closed-loop reset control system as shown in Fig. 1.8, with a sinusoidal reference input $r(t) = |R|\sin(\omega t)$ and adhering to Assumptions 2 and 3. Let μ denote the number of reset instants occurring within a half π/ω -cycle. In this system, the steady-state reset-triggered signal $z_s(t)$ is composed of two components: a base-linear element $z_{bl}(t)$ and a nonlinear element $z_{nl}(t)$, expressed as

$$\begin{aligned} z_s(t) &= z_{bl}(t) + z_{nl}(t), \\ z_{bl}(t) &= |R| \cdot |\mathcal{S}_{I_s}(\omega)| \sin(\omega t + \angle \mathcal{S}_{I_s}(\omega)), \\ z_{nl}(t) &= - \sum_{n=1}^{\infty} \mathcal{F}^{-1}[\mathcal{C}_s(n\omega) \mathcal{T}_{\beta}(n\omega) D_s^n(\omega)], \end{aligned} \quad (7.1)$$

where

$$\begin{aligned} \mathcal{T}_{\beta}(n\omega) &= \mathcal{T}_{\alpha}(n\omega) \cdot jn\omega \ (\in \mathbb{R}^{1 \times n_c}), \\ D_s^n(\omega) &= \frac{2(A_{\rho} - I)}{n\pi} \sum_{i=1}^{i=\mu} \mathcal{F}[x_c(t_i) \sin(n\omega(t - t_i))] \ (\in \mathbb{R}^{n_c \times 1}). \end{aligned} \quad (7.2)$$

In (7.1) and (7.2), $\mathcal{T}_{\alpha}(\omega)$ and $\mathcal{S}_{I_s}(\omega)$ are defined as in (3.2) and (3.3), respectively, and $x_c(t_i)$ denotes the state of the reset controller \mathcal{C}_r at the reset instant t_i .

Proof. The proof is provided in Appendix 7.A. \square

In the reset triggered signal $z_s(t)$, the nonlinear component $z_{nl}(t)$ in (7.1) can be represented as the sum of its harmonic components, expressed as:

$$\begin{aligned} z_{nl}(t) &= \sum_{n=1}^{\infty} z_{nl}^n(t), \\ z_{nl}^n(t) &= \sum_{n=1}^{\infty} |Z_{nl}^n| \sin(n\omega t + \angle Z_{nl}^n), \end{aligned} \quad (7.3)$$

where $|Z_{nl}^n|$ and $\angle Z_{nl}^n$ represent the magnitude and the phase of the signal $z_{nl}^n(t)$.

Let $Z_{nl}^n(\omega)$ represent the Fourier transform of the n -th harmonic $z_{nl}^n(t)$ within $z_{nl}(t)$. The following theorem provides the magnitude ratio of the higher-order harmonics ($n > 1$) to the first-order harmonic ($n = 1$) in $z_{nl}(t)$.

Theorem 9. Consider the closed-loop reset control system depicted in Fig. 1.8, with a sinusoidal reference input $r(t) = |R|\sin(\omega t)$, and assume it satisfies Assumptions 2 and 3. At the input frequency ω , the magnitude ratio of the higher-order harmonics (where $n > 1$) to the first-order harmonic (where $n = 1$) in $z_{nl}(t)$ in (7.1) is given by:

$$\beta_n(\omega) = \frac{|Z_{nl}^n(\omega)|}{|Z_{nl}^1(\omega)|} = \frac{|\mathcal{C}_s(n\omega) \mathcal{T}_{\beta}(n\omega)|}{n|\mathcal{C}_s(\omega) \mathcal{T}_{\beta}(\omega)|}, \text{ where } n > 1. \quad (7.4)$$

Proof. The proof is provided in Appendix 7.B. \square

Remark 12. According to (7.4), when $\beta_n(\omega) \rightarrow 0$, $|Z_{nl}^n(\omega)| \ll |Z_{nl}^1(\omega)|$ holds for $n > 1$. In this case, from (7.1), the reset-triggered signal $z_s(t)$ can be approximated as $z_s(t) \approx z_{nl}^1(t) + z_{bl}(t)$, indicating that only the first-order harmonic is present in $z_s(t)$. This ensures the low-pass filtering assumption [**vander1968multiple, khalil2002nonlinear**] to ensure the accuracy of the SIDF analysis. Conversely, the occurrence of multiple reset zero-crossings in $z_s(t)$, which indicates multiple-reset actions within the system, is driven by high-order harmonics $z_{nl}^n(t)$ for $n > 1$.

However, due to the inherent nonlinearity of reset control systems, it is not feasible to completely eliminate high-order harmonics (i.e., achieve $\beta_n(\omega) = 0$).

Although high-order harmonics do not always cause issues, they can lead to multiple-reset actions in sinusoidal-input closed-loop systems, compromising the accuracy of SIDF analysis and reducing the reliability of system design and performance predictions. Additionally, high-order harmonics with dominated magnitude increase the system's sensitivity to high-frequency disturbances and noise. To address this, we identify the multiple-reset frequency ranges as key areas where high-order harmonics should be reduced. Decreasing $\beta_n(\omega)$ in these ranges improves the accuracy of SIDF analysis and decreases the system's sensitivity to high-frequency noise.

According to (7.1) and (7.4), when the base-linear component $z_{bl}(t)$ remains constant, maintaining $\beta_n(\omega)$ within a bound less than 1, i.e., $\beta_n(\omega) \leq \sigma_\beta \in (0, 1)$, ensures that the ratio $|Z_{nl}^n(\omega)|/|Z_{nl}^1(\omega)|$ remains within a controlled range, thereby limiting the impact of high-order harmonics.

Based on (7.4), to guide the design of a shaping filter that achieves $\beta_n(\omega) = \sigma_\beta$, the magnitude condition for \mathcal{C}_s is given as follows:

$$|\mathcal{C}_s(\omega)| = n\sigma_\beta/|\mathcal{T}_\beta(\omega) \cdot \mathbf{1}_{n_c \times 1}|. \quad (7.5)$$

Since the reset action is independent of the magnitude of $\mathcal{C}_s(\omega)$ [1], the value of n does not affect the system performance. By default, $n = 3$ is used in (7.5). Then, the following steps outline the design procedure for shaping filters in reset systems:

- Step 1: Start by designing the reset control system with $\mathcal{C}_s(\omega) = 1$, and use Theorem 4 to identify the frequency range where multiple-reset actions occur.
- Step 2: Then, select a value $\sigma_\beta \in (0, 1)$, and design the shaping filter $|\mathcal{C}_s(\omega)|$ using (7.5) to achieve $\beta_n(\omega) = \sigma_\beta$ within the identified multiple-reset frequency range.
- Step 3: Since the introduction of $\mathcal{C}_s(\omega)$ affects both the magnitude and phase of the first-order harmonics, adjusting other system parameters to compensate for these changes is needed in order to preserve the benefits of the first-order harmonic.

A detailed design procedure of an illustrative example following these steps is presented in Section 7.4.

7.4 Case Study: Design of PID-Shaping Filter in CI-Based Reset Systems

This section details the analysis and design procedure for a shaped reset control systems as an illustrative example. First, Subsection 7.4.1 outlines the design process for a PID shaping filter aimed at reducing high-order harmonics in a CI-based reset control system. Next, Subsection 7.4.2 shows that this PID-shaped reset control system also addresses limit cycle issues in the step responses of reset control systems.

7.4.1 Design Procedure for the PID Shaping Filter

The PCID control system, Case₁, with design parameters outlined in Section 7.2, is chosen as the example due to its high-order harmonic issues, as shown in Fig. 7.1(a₁).

Following the steps outlined in Section 7.3, Theorem 4 is applied to identify the multiple-reset frequency range for the PCID control system, Case₁, as (0, 30) Hz. The value of 30 Hz is determined by sweeping the entire frequency range with a 1 Hz step size. For improved accuracy, smaller step resolutions can be utilized. Within this identified frequency range, reducing high-order harmonics is needed.

Next, by setting $\sigma_\beta = 0.6$ and applying equation (7.5), the resulting magnitude plot of $|C_s(\omega)|$ is shown in Fig. 7.2. The value $\sigma_\beta = 0.6$ is chosen based on experimental evaluations to achieve improved system performance, as demonstrated in Section 7.5. In practice, other values of $\sigma_\beta \in (0, 1)$ may also be selected, depending on the specific requirements for high-order harmonic reduction in the system.

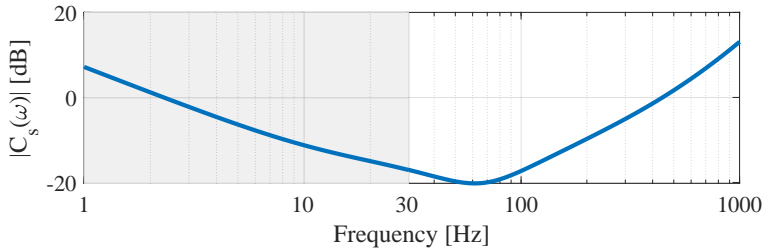


Figure 7.2: The plot of $|C_s(\omega)|$ meeting the condition of $\beta_n(\omega) = 0.6$ based on (7.5).

From Fig. 7.2, the shaping filter can be simplified as the LTI PI shaping filter, given by

$$C_s(s) = 1 + \omega_\alpha/s, \quad (7.6)$$

where $\omega_\alpha = 2\pi \cdot 30 = 60\pi$ [rad/s].

The objective of the shaping filter design is to attenuate high-order harmonics while preserving the benefits of the first-order harmonic. However, as demonstrated in Theorem 2, the integration of the PI shaping filter affects the phase of the HOSIDF in the reset controller. It is crucial to ensure that the shaping filter does not introduce phase lag but instead introduces phase lead, as achieved by the design outlined in Remark 13.

Remark 13. The PID shaping filter $C_s(s)$ reduces $\beta_n(\omega)$ in (7.4) for frequencies $\omega < \omega_\alpha$, while simultaneously introducing a phase lead at the bandwidth frequency of ω_b , compared to the system without the shaping filter (i.e., $C_s = 1$), by the following design:

$$C_s(s) = k_s \cdot \left(1 + \frac{\omega_\alpha}{s}\right) \cdot \frac{s/\omega_\beta + 1}{s/\omega_\eta + 1} \cdot \frac{1}{s/\omega_\psi + 1}, \quad (7.7)$$

with $\angle C_s(\omega_b)$ meets the conditions presented in Lemma 3 and ω_b is the bandwidth frequency.

Since reset actions are amplitude-independent [1], the value of $k_s \neq 0 \in \mathbb{R}$ does not impact system performance. By default, $k_s = 1$. The introduction of the derivative element in (7.7) may amplify high-frequency noise, potentially causing multiple-reset actions. Therefore, the low-pass filter is incorporated to attenuate high-frequency components in $z_s(t)$. The cutoff frequency ω_ψ for the LPF is chosen based on the characteristics of the noise present in practice.

In this chapter, reset systems incorporating the shaping filter from (7.7) are termed PID-shaped reset control systems. CI-based reset systems, including Case₁, are built upon the generalized CI. Therefore, the phase margin introduced by the PID shaping filter in the CI-based reset system is first applied to the shaped CI, and then propagated throughout the entire system. Remark 10 provides the calculation of the phase lead introduced by the shaping filter to the shaped CI in comparison to the CI.

Based on (7.6) and Remark 13, the shaping filter $C_s(s)$ (7.7) for Case₁ is designed with the following parameters: $\omega_\alpha = 60\pi$ rad/s, $\omega_\beta = 1.05 \cdot \omega_b = 659.7$ rad/s, $\omega_\eta = 12 \cdot \omega_b = 7.5 \times 10^3$ rad/s, $\omega_\psi = 75 \cdot \omega_b = 4.7 \times 10^4$ rad/s, and $k_s = 213$. The Bode plot of $C_s(s)$ is shown in Fig. 7.3. At frequencies $\omega < \omega_\alpha$, $C_s(s)$ functions as a PI controller. Noted that, due to the integral property of the shaping filter and the presence of an integral buffer, the output signal of C_s may exhibit an offset and lack zero-crossings within specific frequency ranges. Under these conditions, the system operates linearly. As the primary objective of the PI shaping filter is to attenuate high-order harmonics, the transition to linear behavior does not degrade system performance. Instead, it enhances performance, as linear control outperforms reset control within these frequency ranges. Additionally, its phase at the bandwidth frequency $\omega_b = 200\pi$ rad/s is $\angle C_s(\omega_b) = 21^\circ$.

Without the shaping filter, the CI with $\gamma = 0$ has a phase of $\phi_0 = -38.1^\circ$ at $\omega_b = 200\pi$ rad/s. In contrast, by applying the designed shaping filter $C_s(s)$, the phase of the shaped CI improves to $\phi_s = -27.4^\circ$, resulting in a phase lead of $\phi_{\text{lead}} = 10.7^\circ$ in the PCID control system, as determined using Remark 10. To preserve the phase margin and gain properties of the first-order harmonic, the parameters are set to $\omega_r = 141.4$ rad/s, $\gamma = 0.13$, and $k_r = 1.02$. Under these settings, the phase lead is $\phi_{\text{lead}} = 0^\circ$.

Applying the designed PID shaping filter, the Bode plots for the PID, PCID, and shaped PCID controllers—showing both first- and third-order harmonics—are provided in Fig. 7.4. Then, Fig. 7.5 provides the corresponding Bode plots when these controllers are applied to the plant $\mathcal{P}(s)$ in (1.1). Collectively, these figures demonstrate that the shaped PCID control system reduces high-order harmonics within the frequency range of (0, 30) Hz, while preserving the gain and phase benefits of the first-order harmonic, compared to the PCID control system. Note that the PID shaping filter amplifies high-order harmonics in certain frequency ranges, such as [30, 100] Hz in this case study, as shown in Fig. 7.4. However, this amplification is minimal, and within this range, the first-order harmonics are also amplified. Therefore, this amplification does not lead to system performance degradation, as will be validated by the experimental results in Section 7.5.

Moreover, the plots of $\beta_3(\omega)$ for both the closed-loop PCID and shaped PCID control systems are shown in Fig. 7.6. The shaped PCID control system reduces $\beta_3(\omega)$, ensuring that $\beta_3(\omega) < 0.6$. Note that in this shaped PCID control system, the values

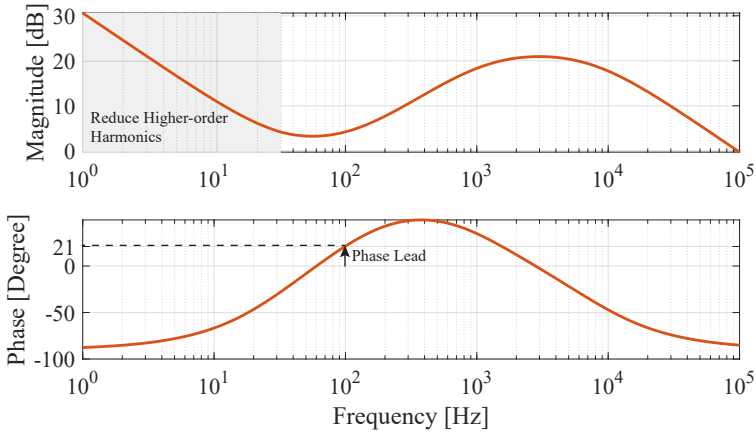


Figure 7.3: Bode plot of the shaping filter $C_s(s)$.

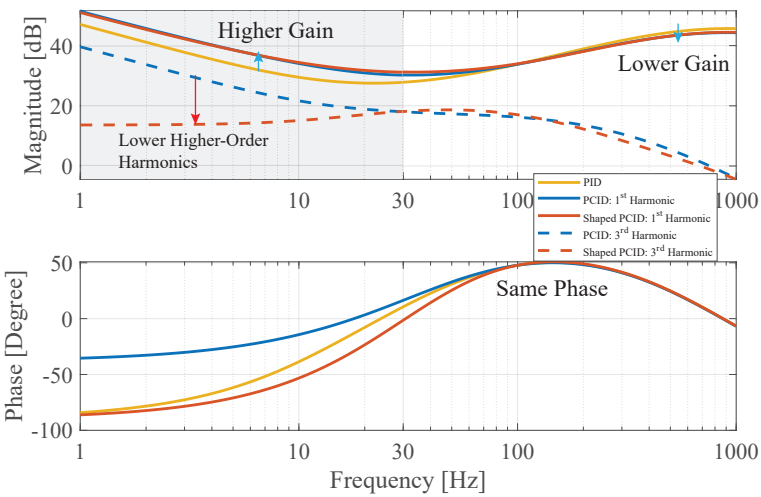


Figure 7.4: Bode plots of the PID controller, the first-order and third-order harmonics in the PCID, and shaped PCID controllers. The multiple-reset region (0,30) Hz identified for the PCID system using Theorem 4 is shaded in gray.

of $\beta_n(\omega)$ for $n > 3$ are smaller than $\beta_3(\omega)$ and, for clarity, are not displayed. However, they can be computed using (7.4).

The results shown in Figures 7.4 to 7.6 indicate that the PID shaping filter designed in this chapter reduces high-order harmonics while maintaining the advantages of the first-order harmonic in the PCID system. These improvements are anticipated to enhance the accuracy of SIDF analysis and improve the steady-state precision of the PCID system. Further validation of these enhancements will be provided through simulations and experimental results in Section 7.5.

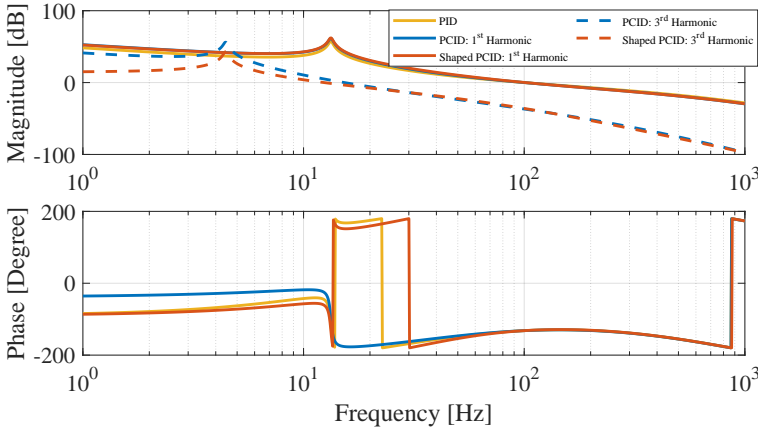


Figure 7.5: Bode plots of the open-loop PID control system and the first- and third-order harmonics in the open-loop PCID and shaped PCID control systems on the precision motion stage $\mathcal{P}(s)$.

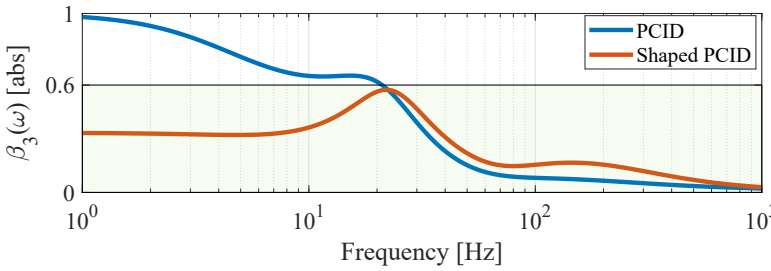


Figure 7.6: The plot of $\beta_3(\omega)$ in the closed-loop PCID and shaped PCID control systems.

7.4.2 Limit Cycles Elimination of the PID Shaping Filter

In addition to reducing high-order harmonics, the PID shaping filter also eliminates the limit cycle issues in the step responses of reset systems.

Consider a closed-loop reset control system in Fig. 6.1 subjected to an unit step input $h(t)$, with the Laplace transform of $h(t)$ given by $H(s) = 1/s$. In this system, the final value of $z_s(t)$ denoted by $\lim_{t \rightarrow \infty} z_s(t)$ is given by

$$\lim_{t \rightarrow \infty} z_s(t) = \lim_{s \rightarrow 0} s \cdot Z_s(s) = \lim_{s \rightarrow 0} s C_s(s) \mathcal{C}_1(s) \mathcal{S}_{bl}(s) \cdot 1/s = \lim_{s \rightarrow 0} C_s(s) \mathcal{S}_\alpha(s), \quad (7.8)$$

where

$$\mathcal{S}_\alpha(s) = C_1(s) \mathcal{S}_{bl}(s). \quad (7.9)$$

In the reset systems with the shaping filter $C_s(s) = 1$, limit cycles occur when the reset-triggered signal continues to trigger the reset actions at steady states, characterized by:

$$\lim_{t \rightarrow \infty} z_s(t) = \lim_{s \rightarrow 0} \mathcal{S}_\alpha(s) = 0, \quad (7.10)$$

while the reset controller's output $m(t)$ does not settle to a steady-state equilibrium at zero; instead, it continues to oscillate persistently around certain non-zero values as $t \rightarrow \infty$, i.e.,

$$\lim_{t \rightarrow \infty} m(t) = \lim_{s \rightarrow 0} sC_1(s)C_I(s)S_{bl}(s)1/s = \text{constant} \neq 0. \quad (7.11)$$

The following content demonstrates that the PID shaping filter, as defined in (7.7), can eliminate limit cycle issues in reset systems.

The PID shaping filter $C_s(s)$ in (7.7) can be expressed as:

$$C_s(s) = F(s)/s, \quad (7.12)$$

where

$$F(s) = k_s \cdot (s + \omega_\alpha) \cdot \frac{s/\omega_\beta + 1}{s/\omega_\eta + 1} \cdot \frac{1}{s/\omega_\psi + 1}. \quad (7.13)$$

With the PID shaping filter in (7.12), $\lim_{t \rightarrow \infty} z_s(t)$ in (7.8) is written as

$$\lim_{t \rightarrow \infty} z_s(t) = \lim_{s \rightarrow 0} F(s) \cdot S_\alpha(s)/s. \quad (7.14)$$

From (7.13), the value of $F(s)$ as $s \rightarrow 0$ is given by

$$\lim_{s \rightarrow 0} F(s) = k_s \cdot \omega_\alpha = \text{constant} \neq 0. \quad (7.15)$$

From (7.10), the transfer function $S_\alpha(s)$ can be expressed in terms of polynomial terms, given by

$$S_\alpha(s) = \frac{n_1 s^n + n_2 s^{n-1} + \dots + n_q s}{m_1 s^m + m_2 s^{m-1} + \dots + m_q}, n_1, \dots, n_q, m_1, \dots, m_q \in \mathbb{R}, m_q \neq 0, n_q \neq 0. \quad (7.16)$$

From (7.16), we find that:

$$\lim_{s \rightarrow 0} \frac{S_\alpha(s)}{s} = \lim_{s \rightarrow 0} \frac{n_1 s^{n-1} + n_2 s^{n-2} + \dots + n_q}{m_1 s^m + m_2 s^{m-1} + \dots + m_q} = n_q/m_q = \text{constant} \neq 0. \quad (7.17)$$

Combining (7.14), (7.15), and (7.17), we derive:

$$\lim_{t \rightarrow \infty} z_s(t) = \lim_{s \rightarrow 0} F(s) \cdot S_\alpha(s)/s = \text{constant} \neq 0. \quad (7.18)$$

Thus, from (7.18), by applying the PID shaping filter $C_s(s)$, as specified in (7.7), the limit-cycle behaviors in reset systems are eliminated.

7.5 Results: Improved Performance of the PID-Shaped Reset Control System

This section presents simulation and experimental results to validate the effectiveness of the PID-shaped reset system designed in Section 7.4 in comparison to both linear and reset systems, as applied to the precision motion stage in Fig. 1.2.

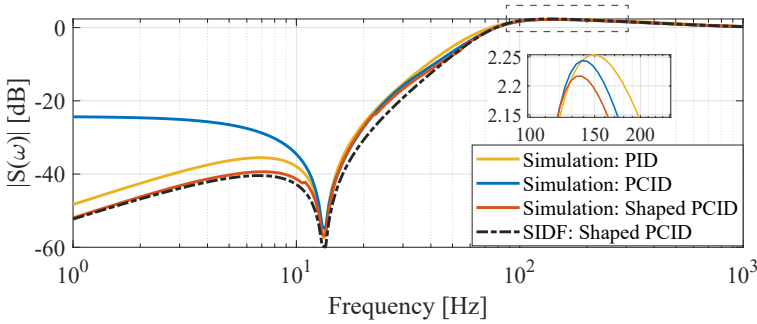


Figure 7.7: Plots of simulated $\|e\|_{\infty}/\|r\|_{\infty}$ for the PID, PCID, and shaped PCID control systems, alongside the SIFD-predicted $\|e\|_{\infty}/\|r\|_{\infty}$ for the shaped PCID control system.

7.5.1 Simulation Results: Enhanced Steady-State Performance

To evaluate the closed-loop performance of the shaped PCID control system, Fig. 7.7 presents the simulated $\|e\|_{\infty}/\|r\|_{\infty}$ for the PID, PCID, and shaped PCID systems. The shaped PCID system demonstrates the lowest $\|e\|_{\infty}/\|r\|_{\infty}$ compared to the other two systems, indicating improved precision. This enhancement is attributed to the shaped PCID control system's superior gain properties in the first-order harmonic compared to the PID control system, while reducing high-order harmonics relative to the PCID control system, as demonstrated in Figures 7.4 and 7.5.

Table 7.1 presents a quantitative comparison of $\|e\|_{\infty}/\|r\|_{\infty}$ for the PID, PCID, and shaped PCID systems at selected frequencies: 5 Hz, 10 Hz, 30 Hz, and 200 Hz. The choice of 5, 10, and 30 Hz validates the improved precision resulting from high-order harmonics reduction in the shaped PCID system within the targeted frequency range of (0,30) Hz. Additionally, the inclusion of 200 Hz ensures that high-frequency precision has also been attained. Across all frequencies, the shaped PCID system consistently exhibits lower steady-state errors, highlighting its effectiveness.

Table 7.1: The $\|e\|_{\infty}/\|r\|_{\infty}$ values for the PCID and shaped PCID systems under sinusoidal inputs at frequencies of 5, 10, 30, and 200 Hz.

Systems	Input Frequencies [Hz]			
	5	10	30	200
PID	1.5×10^{-2}	1.3×10^{-2}	1.7×10^{-1}	1.28
PCID	4.8×10^{-2}	1.9×10^{-2}	1.6×10^{-1}	1.26
Shaped PCID	1.0×10^{-2}	8.9×10^{-3}	1.5×10^{-1}	1.25
Precision Improvement	79.17%	53.16%	6.25%	0.79%

Another notable observation from Fig. 7.7 is that the SIFD analysis provides more accurate predictions for the shaped PCID system compared to the PCID system in Fig. 3.3. Here, $|S(\omega)| = \|e\|_{\infty}/\|r\|_{\infty}$, and the Relative Prediction Error (RPE) of the SIFD analysis is defined as $\text{RPE} = \frac{|\mathcal{S}_{\text{sim}}(\omega)| - |\mathcal{S}_{\text{sifd}}(\omega)|}{|\mathcal{S}_{\text{sifd}}(\omega)|}$, where $|\mathcal{S}_{\text{sim}}(\omega)|$ and $|\mathcal{S}_{\text{sifd}}(\omega)|$ are derived from simulations and the SIFD analysis [2], respectively. Table

7.2 compares the RPE values at six frequencies, reinforcing this observation. The enhanced reliability of SIDF analysis in the shaped PCID system is attributed to the reduction in high-order harmonics. However, discrepancies persist between SIDF predictions and simulation results, as SIDF only accounts for the first-order harmonic. To mitigate this, restricting $\beta_n(\omega) \rightarrow 0$ can help preserve the two-reset condition, and employing HOSIDF methods from [3, 4] can achieve greater accuracy by incorporating higher-order harmonics.

Table 7.2: Relative Prediction Error (RPE) of the SIDF analysis for PCID and shaped PCID control systems at frequencies of 1, 10, 50, 100, 500, and 1000 Hz.

Systems	Input Frequencies [Hz]					
	1	10	50	100	500	1000
PCID	15.51	0.97	0.03	0.02	2.35×10^{-3}	3.21×10^{-3}
Shaped PCID	0.03	0.18	0.02	0.01	8.39×10^{-4}	3.15×10^{-3}

7.5.2 Experimental Results: Improved Tracking Precision

Figure 7.8 illustrates the experimentally measured steady-state errors for the PID, PCID, and shaped PCID systems in response to a normalized sinusoidal input signal defined as $r(t) = 1 \times 10^{-5} \sin(2\pi ft)$ [m], with frequencies $f = 5, 10, 30, 200$ Hz. Note that during practical experiments, the magnitudes of input signals employed for these four frequencies were different; however, for the purposes of comparison, the magnitude of all input signals have been normalized to 1×10^{-5} [m].

Table 7.3 presents the maximum steady-state errors at the three test frequencies for the PID, PCID, and shaped PCID systems. The results demonstrate that the shaped PCID system achieves lowest position errors among the three systems, especially at low frequency range of (0,30) Hz. Notably, at 5 Hz, the shaped PCID system improves precision by 72.56% compared to the PCID system.

Table 7.3: The maximum steady-state errors $\|e\|_{\infty}$ [m] in the reset PID system and shaped PCID systems under single sinusoidal inputs at frequencies of 5, 10, 30, 200 Hz.

Systems	Input Frequency [Hz]			
	5	10	30	200
PID	2.03×10^{-7}	1.41×10^{-7}	1.72×10^{-6}	1.23×10^{-5}
PCID	5.03×10^{-7}	2.16×10^{-7}	1.65×10^{-6}	1.21×10^{-5}
Shaped PCID	1.38×10^{-7}	9.30×10^{-8}	1.56×10^{-6}	1.14×10^{-5}
Precision Improvement	72.56%	56.94%	5.45%	7.00%

Real-world input signals are often more complex than a single sinusoid. In this subsection, the results of the single sinusoidal reference inputs serve to illustrate the steady-state performance of the three systems across varying frequencies. To comprehensively evaluate the positioning performance of the shaped reset control system, multiple inputs—including disturbances and noise—will be applied to the three systems in the next subsection.

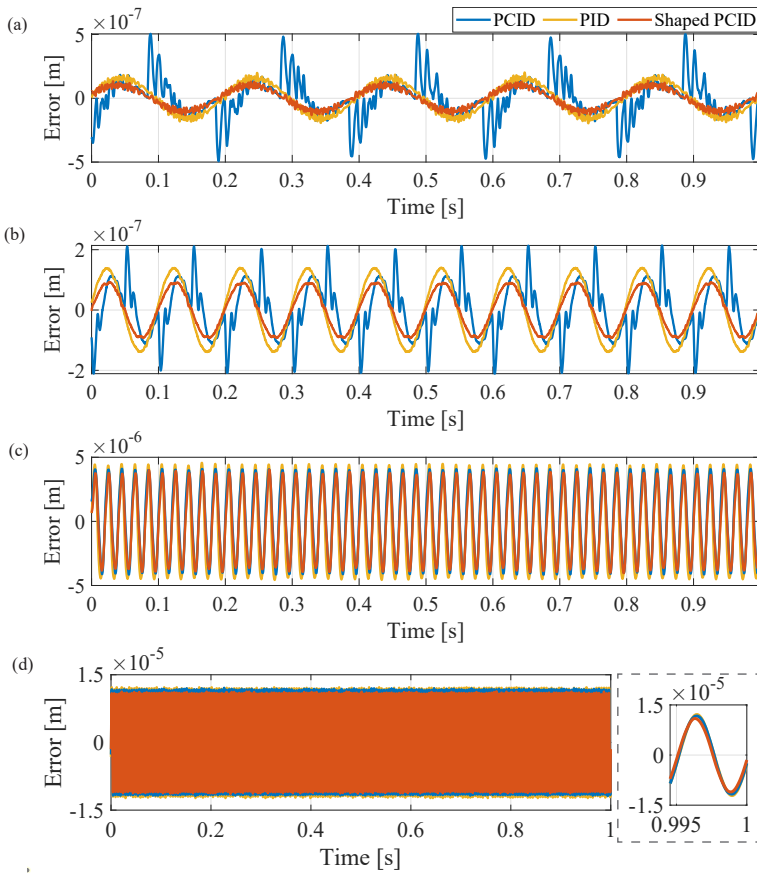


Figure 7.8: Normalized experimental measured steady-state errors of the PID, PCID, and shaped PCID control systems under sinusoidal input $r(t) = 1 \times 10^{-5} \sin(2\pi t)$ [m].

7.5.3 Experimental Results: Enhanced Disturbance and Noise Rejection

This subsection presents the steady-state errors of three systems under multiple input conditions.

Figure 7.9(a) shows the measured steady-state errors of the three systems in response to a disturbance input signal defined as $d_1(t) = 1 \times 10^{-7} [149.3 \sin(4\pi t) + 1.2 \sin(16\pi t) + 11.9 \sin(16\pi t) + 3.0 \sin(40\pi t)]$ [m].

Next, a white noise input $n(t)$ with a power bound of 3×10^{-12} [m] is added to the disturbance input $d_1(t)$. The resulting steady-state errors for the three systems are presented in Fig. 7.9(b). Table 7.4 summarizes the maximum steady-state errors for the PID, PCID, and shaped PCID systems under these inputs. The results show that the shaped PCID system improves precision by 80.07% compared to the PCID system, effectively rejecting both the disturbance and noise.

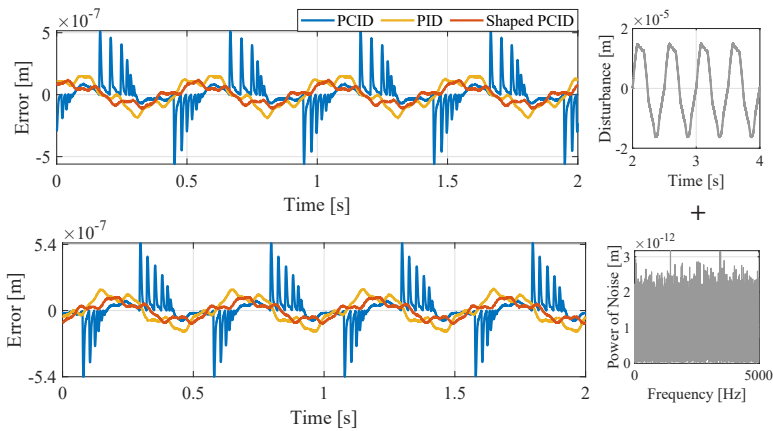


Figure 7.9: Experimental measured steady-state errors of PID, PCID, and shaped PCID control systems under $d_1(t) + n(t)$.

Table 7.4: The maximum steady-state errors $\|e\|_\infty$ [m] in the PID, PCID, and shaped PCID control systems.

Systems	Input Signals		
	$d_1(t) + n(t)$	$r_2(t) + d_2(t) + n(t)$	$r_3(t) + d_3(t) + n(t)$
PID	1.80×10^{-7}	1.22×10^{-7}	1.17×10^{-7}
PCID	5.52×10^{-7}	3.63×10^{-7}	2.00×10^{-7}
Shaped PCID	1.10×10^{-7}	8.80×10^{-8}	9.64×10^{-8}
Precision Improvement	80.07%	75.78%	51.79%

To evaluate both the reference tracking, as well as the disturbance and noise rejection of the closed-loop shaped PCID control system, Figure 7.10 compares the steady-state errors of the PID, PCID, and shaped PCID systems under multiple input signals. In Fig. 7.10(a), the inputs include a reference signal $r_2(t) = 6 \times 10^{-6} \sin(10\pi t)$ [m], alongside the disturbance $d_2(t) = 1 \times 10^{-8} [49.0 \sin(4\pi t) + 5.5 \sin(16\pi t) + 1.1 \sin(40\pi t)]$ [m] and white noise $n(t)$ with a power bound of 3×10^{-12} [m]. In Fig. 7.10(b), the inputs consist of a reference signal $r_3(t) = 6 \times 10^{-6} \sin(20\pi t)$ [m], a disturbance $d_3(t) = 1 \times 10^{-7} [2.7 \sin(10\pi t) + 3.7 \sin(14\pi t) + 3.0 \sin(30\pi t)]$ [m], and the white noise $n(t)$ with a power bound of 3×10^{-12} [m]. The maximum steady-state errors for these two cases are summarized in Table 7.4, indicating that the shaped PCID system improves precision by 73.5% and 53.06% in the two scenarios, respectively.

Moreover, Figure 7.11 illustrates the control inputs for these two cases, demonstrating that the shaped PCID system requires the least control input force while achieving the lowest steady-state error. Together, Figures 7.10 and 7.11 highlight the improved control efficiency of the shaped PCID system, which can be attributed to the reduction of high-order harmonics.

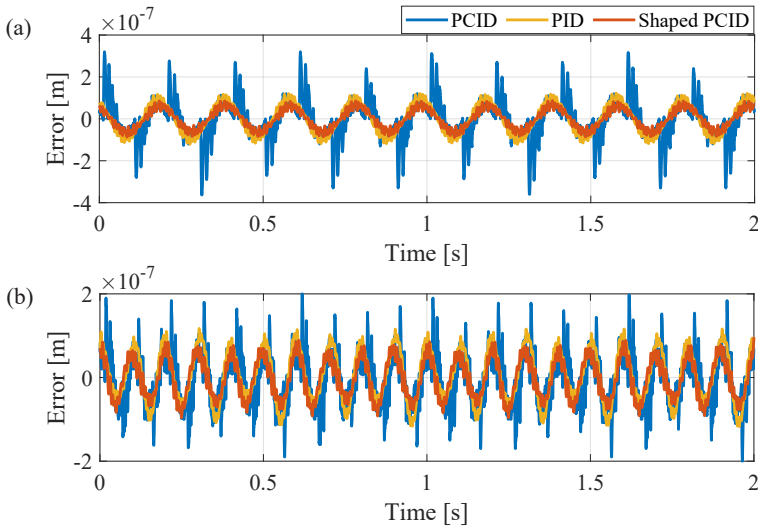


Figure 7.10: Experimental measured steady-state errors of PID, PCID, and shaped PCID control systems under (a) $r_2(t) + d_2(t) + n(t)$ and (b) $r_3(t) + d_3(t) + n(t)$.

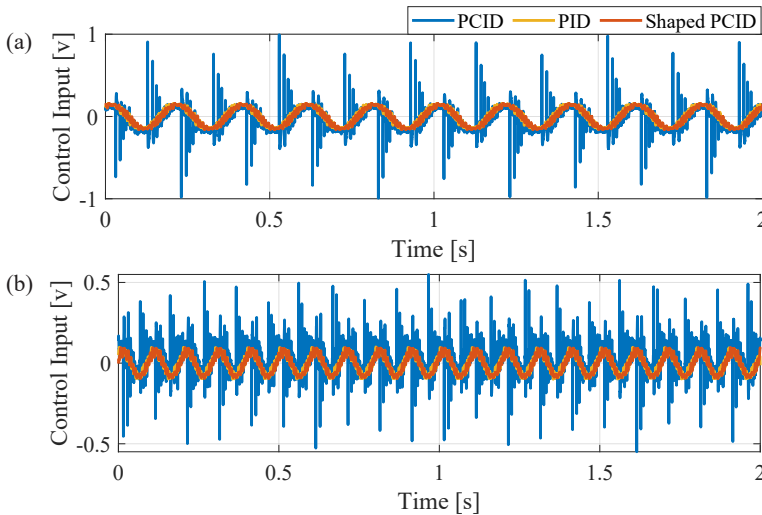


Figure 7.11: Experimental measured control input of PID, PCID, and shaped PCID control systems under (a) $r_2(t) + d_2(t) + n(t)$ and (b) $r_3(t) + d_3(t) + n(t)$.

7.5.4 Experimental Results: Eliminated Limit Cycles

The shaped reset system also eliminates the limit cycle issues in the step responses of reset PID systems. Current solutions for addressing the limit cycle problem include the “PI+CI” structure [5] and the PCI-PID structure in Fig. 3.1. To provide a fair comparison of the effectiveness of five control structures—PID, PCID, shaped PCID,

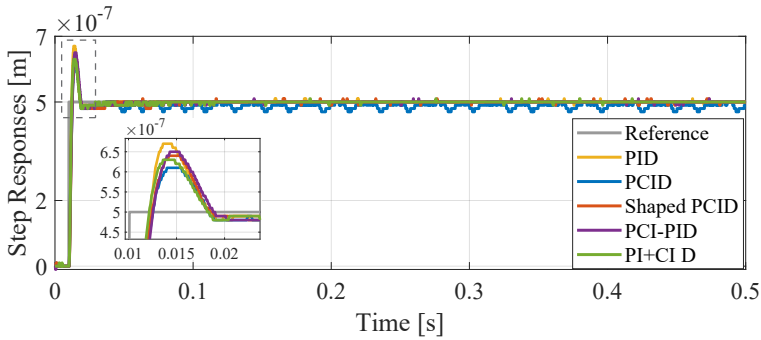


Figure 7.12: Experimental measured step responses of PID, PCID, shaped PCID, PCI-PID, PI+CI D control systems.

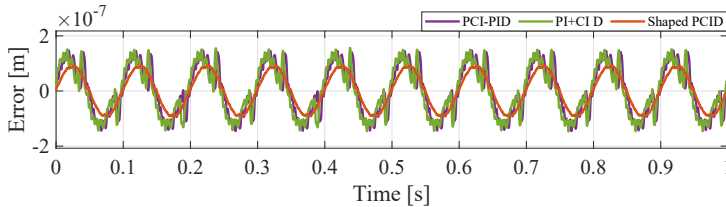


Figure 7.13: Experimental measured steady-state errors of the PCI-PID, PI+CI D, and shaped PCID control systems under sinusoidal input $r(t) = 1 \times 10^{-5} \sin(20\pi t)$ [m].

PI+CI D, and PCI-PID—we designed these systems with the same bandwidth of 100 Hz and phase margin of 50° of the first-order harmonics for fair comparison.

Figure 7.12 presents the step responses of the five systems, highlighting the effectiveness of the shaped PCID, PI+CI D, and PCI-PID systems in mitigating the limit cycle issues observed in the PCID system. These systems also exhibit lower overshoot compared to the PID system. However, the PI+CI D and PCI-PID structures address limit cycle problems at the cost of reduced steady-state performance.

For example, as shown in Fig. 7.13, under a sinusoidal input signal $r(t) = 1 \times 10^{-5} \sin(20\pi t)$ [m], the steady-state errors of the PI+CI D and PCI-PID systems are larger than those of the shaped PCID system. This occurs because the PI+CI D and PCI-PID systems exhibit high-order harmonics with dominated magnitudes at low frequencies, similar to the PCID system. In contrast, the shaped PCID system reduces these high-order harmonics, leading to improved steady-state performance.

In summary, the proposed shaped PCID control system improves positioning accuracy and control efficiency compared to both PID and PCID control systems on the precision motion stage. Additionally, it effectively eliminates limit cycles, leading to enhanced overall system performance.

7.6 Conclusion and Discussions

In conclusion, this chapter introduces a shaped reset control strategy to reduce high-order harmonics. As an illustrative example, the procedure for designing a PID shaping filter in CI-based reset systems is presented. The resulting PID-shaped reset control system reduces high-order harmonics while preserving the benefits of the first-order harmonic compared to the reset control system. Experimental results from precision motion stages highlight three key benefits of the PID-shaped reset system: (1) Improved SIDF analysis accuracy; (2) Enhanced tracking precision, disturbance and noise rejection, and overall control efficiency; and (3) Elimination of limit-cycle issues in the step responses of reset systems.

In Chapter 6, a phase lead element (PD) was introduced to provide phase lead while limiting gain variation, as guided by Lemma 4. Unlike that approach, this chapter incorporates an integrator into the shaping filter, forming a PID structure. Although the integrator introduces phase lag to the system, it enhances gain improvement by relaxing the gain constraints outlined in Lemma 4. Both structures in Chapters 6 and 7 achieve gain or phase improvements based on system requirements by adjusting the phase of the reset instants. Future research could explore applying the shaped reset control system design method from Section 7.3 to other reset control structures, aiming to achieve further performance enhancements.

Bibliography

- [1] A. Banos and A. Barreiro. *Reset control systems*. Springer, 2012.
- [2] Y. Guo, Y. Wang, and L. Xie. “Frequency-domain properties of reset systems with application in hard-disk-drive systems”. In: *IEEE Transactions on Control Systems Technology* 17.6 (2009), pp. 1446–1453.
- [3] N. Saikumar, K. Heinen, and S. H. HosseinNia. “Loop-shaping for reset control systems: A higher-order sinusoidal-input describing functions approach”. In: *Control Engineering Practice* 111 (2021), p. 104808.
- [4] X. Zhang, M. B. Kaczmarek, and S. H. HosseinNia. “Frequency response analysis for reset control systems: Application to predict precision of motion systems”. In: *Control Engineering Practice* 152 (2024), p. 106063. ISSN: 0967-0661.
- [5] A. Baños and A. Vidal. “Definition and tuning of a PI+ CI reset controller”. In: *2007 european control conference (ECC)*. IEEE. 2007, pp. 4792–4798.
- [6] A. Pavlov, N. Van De Wouw, and H. Nijmeijer. *Uniform output regulation of nonlinear systems: a convergent dynamics approach*. Vol. 205. Springer, 2006.

Appendix

7

7.A Proof of Lemma 5

Proof. Consider a closed-loop reset control system as shown in Fig. 1.8, with a sinusoidal reference input $r(t) = |R|\sin(\omega t)$ and satisfying Assumptions 2 and 3. This proof demonstrates that the steady-state reset-triggered signal $z_s(t)$ is composed of a base-linear component $z_{bl}(t)$ and a nonlinear component $z_{nl}(t)$, where $z_{nl}(t)$ is obtained by filtering a stair-step signal $d_s(t)$ through an LTI transfer function. The proof is organized into three steps.

Step 1: Prove that Reset Actions Introduce Square Waves into Systems.

The state $x_c(t)$ of the reset controller C_r is nonlinear and can be represented as the sum of its harmonics [6], expressed as

$$x_c(t) = \sum_{n=1}^{\infty} x_c^n(t) = |X_c^n| \sin(n\omega t + \angle X_c^n), \quad (7.19)$$

where $|X_c^n|$ and $\angle X_c^n$ represent the magnitude and phase of each harmonic $x_c^n(t)$ in $x_c(t)$.

From (7.19), the following relation holds

$$x_c(t_i) = -x_c(t_i \pm \pi/\omega). \quad (7.20)$$

Based on (3.35), the reset instant t_i occurs π/ω -periodically. At each reset instant t_i , according to (3.6), the state $x_c(t_i)$ undergoes a jump to $A_\rho x_c(t_i)$, generating a step input defined by $h_i(t) = (A_\rho - I)x_c(t_i)h(t - t_i)$.

Then, based on (7.20), a step input with an opposite sign $h'_i(t) = -h_i(t) = -(A_\rho - I)x_c(t_i)h(t - t_i \pm \pi/\omega)$ is introduced at the time instant $t_i + \pi/\omega$. Signals $h_i(t)$ and $-h_i(t)$ together produce a square wave signal over each steady-state cycle, beginning at t_i with an amplitude of $(A_\rho - I)x_c(t_i)$ and a period of $2\pi/\omega$, as illustrated in Fig.7.14.

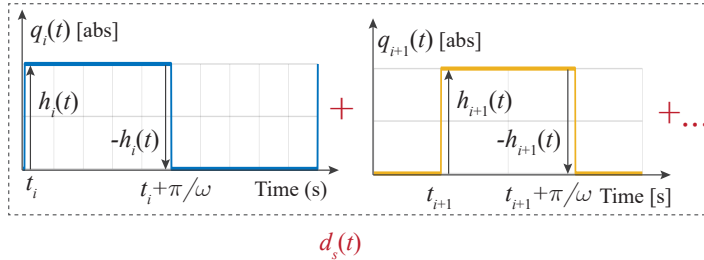


Figure 7.14: Plots of signals $q_i(t)$ in (7.21) and $d_s(t)$ in (7.25).

Step 2: Formulate the Square Waves.

The square wave introduced at the time instants t_i and $t_i + \pi/\omega$ is expressed as

$$q_i(t) = (A_\rho - I)x_c(t_i)q(t - t_i), \quad (7.21)$$

where $q(t)$ is a square wave with an amplitude of 1 and a period of $2\pi/\omega$, defined as:

$$q(t) = \sum_{n=1}^{\infty} 2 \cdot \sin(n\omega t)/n\pi, \quad n = 2k + 1, k \in \mathbb{N}. \quad (7.22)$$

From (7.21) and (7.22), $q_i(t)$ is expressed as

$$q_i(t) = \sum_{n=1}^{\infty} q_i^n(t), \quad (7.23)$$

where

$$q_i^n(t) = 2(A_\rho - I)x_c(t_i) \sin(n\omega(t - t_i))/(n\pi). \quad (7.24)$$

Step 3: Illustrate that Square Waves $q_i(t)$ Combine to Form a Stair-Step Signal $d_s(t)$, Contributing to the Reset-Triggered Signal $z_s(t)$.

At each reset instant t_i within the half-cycle $(0, \pi/\omega]$, a square wave $q_i(t)$ is introduced. Let the number of reset instants within each half-cycle $(0, \pi/\omega]$ be denoted by μ . From (7.23) and (7.24), a stair-step signal $d_s(t)$ is generated within one $2\pi/\omega$ period. This signal is illustrated in Fig. 7.14 and is expressed as:

$$d_s(t) = \sum_{i=1}^{i=\mu} q_i(t) = \sum_{i=1}^{i=\mu} \sum_{n=1}^{\infty} q_i^n(t). \quad (7.25)$$

From (7.25), $d_s(t)$ can be written as

$$d_s(t) = \sum_{n=1}^{\infty} \sum_{i=1}^{i=\mu} q_i^n(t). \quad (7.26)$$

Define $d_s^n(t)$ as the n th harmonic of $d_s(t)$, from (7.24) and (7.26), $d_s(t)$ is expressed as

$$\begin{aligned} d_s(t) &= \sum_{n=1}^{\infty} d_s^n(t), \\ d_s^n(t) &= 2(A_\rho - I)/(n\pi) \cdot \sum_{i=1}^{i=\mu} x_c(t_i) \sin(n\omega(t - t_i)), \end{aligned} \quad (7.27)$$

with their Fourier transforms given by

$$\begin{aligned} D_s(\omega) &= \sum_{n=1}^{\infty} D_s^n(\omega), \\ D_s^n(\omega) &= 2(A_\rho - I)/(n\pi) \cdot \sum_{i=1}^{i=\mu} \mathcal{F}[x_c(t_i) \sin(n\omega(t - t_i))]. \end{aligned} \quad (7.28)$$

Under Assumption 3, the reset-triggered signal $z_s(t)$ follows its base-linear trajectory $z_{bl}(t)$ within the interval $(0, t_1)$, as defined in (7.1). At time t_1 , reset actions introduce a stair-step signal $d_s(t)$ into the system. By replacing the signal $h_i(t)$ (whose Fourier transform is $H_i(\omega) = 1/(j\omega)$) with the stair-step signal $d_s(t)$ (whose Fourier transform is $D_s(\omega)$) in Fig. 3.5, and following the derivation process outlined in 3.A, the nonlinear component $z_{nl}(t)$ is derived. Finally, $z_{bl}(t)$ and $z_{nl}(t)$ combine to form $z_s(t)$, as expressed in (7.1). This concludes the proof. \square

7.B Proof of Theorem 9

Proof. Consider a closed-loop reset control system as illustrated in Fig. 1.8, with a sinusoidal reference input $r(t) = |R| \sin(\omega t)$, satisfying Assumptions 2 and 3. This proof derives the magnitude ratio of the higher-order harmonics (for $n > 1$) relative to the first-order harmonic (for $n = 1$) in the nonlinear component $z_{nl}(t)$ as defined in (7.1).

From (7.1) and (7.3), the signal $z_{nl}^n(t)$, representing the n th harmonic component of $z_{nl}(t)$, is given by:

$$z_{nl}^n(t) = -\mathcal{F}^{-1}[C_s(n\omega)\mathcal{T}_\beta(n\omega)D_s^n(\omega)]. \quad (7.29)$$

From (7.29), the Fourier transform of $z_{nl}^n(t)$ is given by

$$Z_{nl}^n(\omega) = -C_s(n\omega)\mathcal{T}_\beta(n\omega)D_s^n(\omega). \quad (7.30)$$

From (7.28) and (7.30), we obtain:

$$\beta_n(\omega) = \frac{|Z_{nl}^n(\omega)|}{|Z_{nl}^1(\omega)|} = \frac{|C_s(n\omega)\mathcal{T}_\beta(n\omega)|}{n|C_s(\omega)\mathcal{T}_\beta(\omega)|}. \quad (7.31)$$

Here, the proof is concluded. \square

8

A Fixed-Phase Reset Control System

Current reset elements reset based on the zero-crossings of the reset trigger signal, which often shares the same period as the steady-state error. To further explore the potential of reset control, this chapter investigates alternative reset trigger signals. Specifically, it introduces a reset element with a trigger signal whose period differs from the steady-state error. This control element is termed Fixed-Phase Reset Control (FPRC). A Higher-Order Sinusoidal Input Describing Function (HOSIDF) is then developed to analyze the frequency-domain properties of FPRC. The accuracy of this analytical approach is validated through simulations on three systems. The analysis reveals that FPRC provides phase lead compared to previous reset control methods but introduces nonlinearities at low frequencies.

 This chapter is based on the conference paper: Zhang, Xinxin, Hsing-Li Hsu, and S. Hassan HosseinNia. "Frequency-Domain Analysis of the Fixed-Phase Reset Control System." 2024 IEEE Conference on Control Technology and Applications (CCTA). IEEE, 2024.

8.1 Introduction

The mechatronics industry places a substantial emphasis on attaining precise positioning and high-speed performance in its systems, necessitating the optimization of controllers [1]. Linear controllers, such as Proportional-Integral-Derivative (PID) controllers, are extensively employed in industrial settings due to their effectiveness and ease of tuning. However, their performance is constrained by the inherent linear limitations outlined in Bode's phase-gain relationship [2]. In the quest for alternatives, reset control has emerged as a promising approach to surmount these linear limitations.

The pioneering work of Clegg in the 1950s introduced the simplest form of a reset controller, known as the Clegg Integrator (CI) [3]. Notably, the first-order harmonic of the CI exhibits a 52-degree phase lead while maintaining the same slope (-20 dB/decade) as the linear integrator. This characteristic challenges Bode's phase-gain relationship and shows potential for enhancing control system performance. To expand the applicability of reset control, Horowitz introduced the first-order reset element (FORE) [4, 5]. The FORE has demonstrated promising outcomes in mitigating high-frequency noise. Ongoing research in the realm of reset control has yielded various reset controller variants, as exemplified by works such as [6], [7], [8], [9]. Most preceding reset elements operate on the classical "Zero-crossing Law" resetting mechanism, where the reset controller's output resets to zero upon crossing zero by the input signal.

Research efforts have explored the different resetting mechanisms. Studies such as [10, 11] demonstrate that manipulating the timing of reset actions can enhance the performance of systems like PZT positioning stages. Other research indicates that pre-defining reset conditions can optimize a reset adaptive observer [12] and improve tracking capabilities in hard disk drive systems [13]. Despite these efforts, the application of the new resetting mechanism to reset controllers remains unclear. Furthermore, for the effective implementation of the new reset controller, there is a need for a frequency-domain analysis method. To the best of the authors' knowledge, there are currently no available tools for analyzing the frequency responses of reset controllers that utilize non-zero-crossing resetting mechanisms.

This chapter aims to overcome these limitations, and its structure is outlined as follows. The three primary contributions of this research are presented as follows:

1. In Section 8.2, we introduce a novel reset controller termed as Fixed-Phase Reset Control (FPRC). The FPRC incorporates an innovative resetting mechanism that enables the reset controller's output to reset to a predefined value when a specified phase-based signal crosses zero. This mechanism is applied to common reset elements, including the CI [14], the FORE [15], and the Second-Order Single-State Reset Element (SOSRE) [7].
2. Section 8.3 formulates a Higher-Order Sinusoidal Input Describing Function (HOSIDF) for analyzing the frequency response of the Single-Input-Single-Output (SISO) FPRC under sinusoidal inputs. The accuracy of the HOSIDF for FPRC is validated through simulation. This HOSIDF method enables the analysis of the frequency domain properties of the open-loop FPRC.

3. In Section 8.4, The HOSIDF analysis shows the superior phase lead of the FPRC compared to zero-crossing reset control, but it introduces nonlinearities at low frequencies.

Finally, Section 8.5 delivers the conclusions of this chapter and delineates potential avenues for future research.

8.2 New Reset Element: Fixed-Phase Reset Control (FPRC)

8.2.1 The Definition of the Fixed-Phase Reset Control

We introduce a novel reset element termed Fixed-Phase Reset Control (FPRC). This reset mechanism involves multiple resets within a single steady-state period, evenly spaced in terms of phase. Our emphasis in this paper is on the SISO FPRC system, specifically designed for sinusoidal inputs.

Definition 1. The state-space representation for the FPRC, denoted as \mathcal{C} , under a sinusoidal input signal $e(t) = |E| \sin(\omega t)$ is given by:

$$\mathcal{C} = \begin{cases} \dot{x}_r(t) = A_R x_r(t) + B_R e(t), & t \notin U, \\ x_r(t^+) = A_\rho x_r(t), & t \in U, \\ v(t) = C_R x_r(t) + D_R e(t). \end{cases} \quad (8.1)$$

The set of reset instants $U = \{t_i = \frac{2\pi i}{\omega k}, i \in \mathbb{N}\}$ is an unbounded time sequence increasing monotonously with respect to $i \in \mathbb{N}$, i.e., $t_i < t_{i+1}$ for any $i \in \mathbb{N}$ and $\lim_{i \rightarrow \infty} t_i = +\infty$. In traditional reset controller \mathcal{C}_r defined in (1.6), the set of reset instants is defined as $\{t_i\} = \{t_i | e(t_i) = 0, t_i < t_{i+1}\}$. However, in our new proposed reset controller \mathcal{C} , the reset triggered signal is denoted as $e_s = \sin(k\omega t)$, where the variable k denotes the number of reset instants per steady-state cycle, with $k = 2h$, $h \in \mathbb{Z}^+$. When $k = 2$, the FPRC \mathcal{C} is equivalent to the conventional reset controller \mathcal{C} .

The stability of the system and the existence of steady-state solutions are essential for proving the main results in this paper. To establish the necessary conditions, we introduce the following assumption.

Assumption 5. The FPRC defined in (8.1), is assumed to satisfy the condition specified in (1.9). The reset actions are assumed to be finite in any finite time. The initial condition of the reset controller is zero, i.e., $x_r(0) = 0$.

In practice, the base-linear system of \mathcal{C} in (8.1) is usually designed to be stable. In this case, the bounded constraint on $\{\Delta t_i\}$ can be relaxed [10].

8.2.2 Fixed-Phase Reset Control Elements

In this chapter, we integrate the novel Fixed-Phase (FP) resetting mechanism into three reset control structures: the CI, the FORE, and the SOSRE, with their state-space matrices defined in Section 1.4.3. Applying the new reset mechanism defined in

(8.1) to the three control structures, the resulting reset control elements are termed as “Fixed-Phase CI (FP-CI)”, “Fixed-Phase FORE (FP-FORE)”, and “Fixed-Phase SOSRE (FP-SOSRE)”.

8.3 The Frequency-domain Analysis of the FPRC

8.3.1 The Open-loop HOSIDF for FPRC systems

Due to the nonlinearity of the FPRC, the reset output signal $v(t)$ is characterized by an infinite series of harmonics, defined as $v(t) = \sum_{n=1}^{\infty} v_n(t)$. In the Fourier domain, it is expressed as $V(\omega) = \sum_{n=1}^{\infty} V_n(\omega)$. As illustrated in Fig. 8.1, to generate $v_n(t)$, we employ the “Virtual Harmonics Generator” [16] to produce harmonics $e_n(t)$ from the input $e(t) = |E|\sin(\omega t)$, expressed as:

$$e_n(t) = |E|\sin(n\omega t), n \in \mathbb{Z}^+. \quad (8.2)$$

Define $E(\omega)$ and $E_n(\omega)$ as the Fourier transforms of $e(t)$ and $e_n(t)$, respectively.

Theorem 10. The Higher-Order Sinusoidal Input Describing Function (HOSIDF) for the FPRC system in (8.1) with a sinusoidal input $e(t) = |E|\sin(\omega t)$ and a reset triggered signal $e_s(t) = \sin(k\omega t)$ ($k = 2h$, $h \in \mathbb{Z}^+$), under Assumption 5, is denoted as $\mathcal{H}_n(\omega)$. It is defined to describe the transfer function from the input $e_n(t)$ to the output $v_n(t)$. The expression for $\mathcal{H}_n(\omega)$ is as follows:

$$\mathcal{H}_n(\omega) = \frac{V_n(\omega)}{E_n(\omega)} = \begin{cases} \mathcal{C}_{bl}(\omega) + \Phi(\omega), & \text{for } n = 1, \\ \Phi(n\omega), & \text{for odd } n > 1, \\ 0, & \text{for even } n \geq 2, \end{cases} \quad (8.3)$$

with

$$\begin{aligned} \Phi(n\omega) &= \frac{2}{n\pi|E|} \Delta_I(n\omega) \Theta(n\omega), \\ \Delta_I(n\omega) &= C_R(jn\omega I - A_R)^{-1} jn\omega I, \\ \Theta(n\omega) &= (\gamma - 1) \sum_{i=1}^{\frac{k}{2}-1} m_i e^{j \frac{2n\pi i}{k}}, \end{aligned} \quad (8.4)$$

where $m_0 = 0$ and m_i (where $i \in \mathbb{Z}^+$) for \mathcal{C} with different state numbers ζ_c are provided as follows.

1. For the FR-CI and FR-FORE with $\zeta_c = 1$,

$$m_i = m_{i-1} e^{A_R t_i} + [B_R e^{A_R t} * e(t)]|_{t_i}. \quad (8.5)$$

2. For the FR-SOSRE with $\zeta_c = 2$,

$$\begin{aligned} m_i &= \mathcal{L}^{-1}[\Omega_i(s)/s]|_{t_{i-1}}, \\ \Omega_{i+1}(s) &= \frac{E(s) + (s + 2\beta\omega_r)\mathcal{L}^{-1}[\Omega_i(s)]|_{t_i}}{s^2 + 2\beta\omega_r s + \omega_r^2}. \end{aligned} \quad (8.6)$$

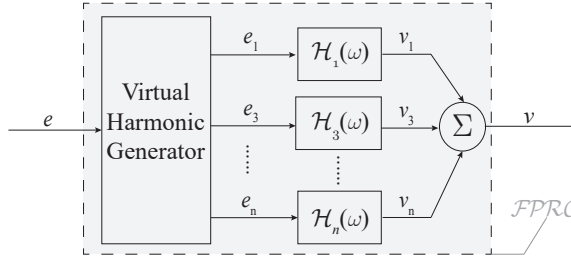


Figure 8.1: The HOSIDF for FPRC systems.

Proof. The proof is divided into scenarios with $\zeta_c = 1$ for the FP-CI and FP-FORE, and with $\zeta_c = 2$ for the FP-SOSRE. Note that the FP-CI is identical to the FP-FORE when $\omega_r = 0$ in (1.12). When $\zeta_c = 1$, m_i is set to $x_r(t_i)$. When $\zeta_c = 2$ for the FP-SOSRE, $x_r(t) = [x_2(t) \ x_1(t)]^T$. In this case, $m_i = x_2(t_i)$. We set $m_0 = 0$ due to the zero-initial condition of the reset controller. Here, we first present the scenario with $\zeta_c = 1$.

Between two reset instants $(t_i, t_{i+1}]$, the FPRC experiences no reset. It can be seen as the base-linear system with an initial condition inherent from the time interval $(t_{i-1}, t_i]$. From (8.1), during $(t_i, t_{i+1}]$, we have

$$\dot{x}_r(t) = A_R x_r(t) + B_R e(t). \quad (8.7)$$

The Laplace transform of (8.7) is given by

$$\begin{aligned} sX_r(s) - x_r(t_{i-1}) &= A_R X_r(s) + B_R E(s) \Leftrightarrow \\ X_r(s) &= (s - A_R)^{-1} (x_r(t_i) + B_R E(s)), \end{aligned} \quad (8.8)$$

where $x_r(t_i)$ is the initial condition of $x_r(t)$ for $t \in (t_i, t_{i+1}]$.

The inverse Laplace transform of (8.8) is given by

$$x_r(t) = x_r(t_i) e^{A_R t} + [B_R e^{A_R t} * e(t)](t). \quad (8.9)$$

From (8.9), the state $x_r(t)$ at the reset instant t_{i+1} can be derived as follows:

$$x_r(t_{i+1}) = x_r(t_i) e^{A_R t_i} + [B_R e^{A_R t} * e(t)]|_{t_{i+1}}. \quad (8.10)$$

From (8.10), for the FPRC with $\zeta_c = 1$ and $m_i = x_r(t_i)$, we have

$$m_i = m_{i-1} e^{A_R t_i} + [B_R e^{A_R t} * e(t)]|_{t_i}. \quad (8.11)$$

This concludes the m_i for the FP-CI and FP-FORE with $\zeta_c = 1$.

From (8.1), at $t_i = 2\pi i / (\omega k)$, the reset action introduces a pulse signal into the $x_r(t)$, given by

$$\Omega_i = x_r(t_i^+) - x_r(t_i) = (A_\rho - I) x_r(t_i). \quad (8.12)$$

When $\zeta_c = 1$, $A_\rho = \gamma$.

Substituting $m_i = x_r(t_i)$ into (8.12), we have

$$\Omega_i = x_r(t_i^+) - x_r(t_i) = (\gamma - 1)m_i. \quad (8.13)$$

Equation (8.13) indicates that the reset action introduces a pulse signal Ω_i to the state $x_r(t)$. Since the periodic property of the base-linear and reset output, the reset actions in the time domain introduce a square wave denoted as $q(t)$ with an amplitude of $(\gamma - 1)m_i/2$, a period of $2\pi/\omega$, and a phase shift of $i2\pi/k$ to $x_1(t)$, which can be seen as a disturbance [17]. Define a normalized square wave with an amplitude of 1 and a period of $2\pi/\omega$, and a phase shift of 0 as $q_0(t)$ given by

$$q_0(t) = \frac{4}{\pi} \sum_{n=1}^{\infty} \frac{\sin(\omega t)}{n}. \quad (8.14)$$

The Fourier transform of $q_0(t)$, denoted as $Q_0(\omega)$, is given by:

$$Q_0(\omega) = \frac{4}{\pi} \sum_{n=1}^{\infty} \frac{E(n\omega)}{n|E|}. \quad (8.15)$$

Thus, $q(t)$ and its Fourier transform are given by

$$\begin{aligned} q(t) &= \mathcal{F}^{-1}[Q(\omega)], \\ Q(\omega) &= \frac{(\gamma - 1)}{2|E|} \sum_{i=1}^{\frac{k}{2}-1} m_i e^{j\frac{2n\pi i}{k}} Q_0(\omega). \end{aligned} \quad (8.16)$$

From (8.15) and (8.16), the n -th harmonic in $Q(\omega)$ defined as $Q_n(\omega)$ is given by

$$\begin{aligned} Q(\omega) &= \sum_{n=1}^{\infty} Q_n(\omega), \\ Q_n(\omega) &= \frac{2(\gamma - 1)}{\pi|E|} \sum_{i=1}^{\frac{k}{2}-1} \frac{m_i e^{j\frac{2n\pi i}{k}} E(n\omega)}{n}. \end{aligned} \quad (8.17)$$

From (8.1), the transfer function from the $x_r(t)$ to $v(t)$ is defined as

$$\Delta_I(\omega) = C_R(j\omega I - A_R)^{-1} j\omega I. \quad (8.18)$$

Taken consider the $q(t)$ as a disturbance adding to the $x_r(t)$, the reset output signal $v(t)$ is given by

$$\begin{aligned} v(t) &= v_{bl}(t) + v_{nl}(t), \\ v_{bl}(t) &= \mathcal{F}^{-1}[C_{bl}(\omega)E(\omega)], \\ v_{nl}(t) &= \mathcal{F}^{-1}[\Delta_I(\omega)Q(\omega)]. \end{aligned} \quad (8.19)$$

From (8.15), (8.17), and (8.19), $V_{nl}(\omega) = \mathcal{F}^{-1}[v_{nl}(t)]$ is given by

$$V_{nl}(\omega) = \sum_{n=1}^{\infty} \frac{2(\gamma - 1)\Delta_I(n\omega)}{n\pi|E|} \sum_{i=1}^{\frac{k}{2}-1} m_i e^{j\frac{2n\pi i}{k}} E(n\omega). \quad (8.20)$$

Define $V_{nl}^n(\omega)$ as the n -th harmonic in $V_{nl}(\omega)$. From (8.20), we have

$$\begin{aligned} V_{nl}(\omega) &= \sum_{n=1}^{\infty} V_{nl}^n(\omega), \\ V_{nl}^n(\omega) &= \frac{2(\gamma-1)\Delta_l(n\omega)}{n\pi|E|} \sum_{i=1}^{\frac{k}{2}-1} m_i e^{j\frac{2n\pi i}{k}} E(n\omega). \end{aligned} \quad (8.21)$$

Based on (8.19) and (8.21), the first-order harmonic in $V(\omega) = \mathcal{F}[v(t)]$ is obtained as

$$V_1(\omega) = V_{bl}(\omega) + V_{nl}^1(\omega). \quad (8.22)$$

From (8.19) and (8.22), the first-order ($n = 1$) transfer function of FPRC is defined as

$$H_1(\omega) = \frac{V_1(\omega)}{E(\omega)} = C_{bl}(\omega) + \frac{2(\gamma-1)\Delta_l(\omega)}{\pi|E|} \sum_{i=1}^{\frac{k}{2}-1} m_i e^{j\frac{2n\pi i}{k}}. \quad (8.23)$$

From (8.19) and (8.21), the n -th ($n > 1$) order harmonic in $V(\omega)$ is given by

$$V_n(\omega) = V_{nl}^n(\omega). \quad (8.24)$$

Then, based on (8.24), the n -th transfer function of FPRC is defined as

$$\mathcal{H}_n(\omega) = \frac{V_n(\omega)}{E(n\omega)} = \frac{2(\gamma-1)\Delta_l(n\omega)}{n\pi|E|} \sum_{i=1}^{\frac{k}{2}-1} m_i e^{j\frac{2n\pi i}{k}}. \quad (8.25)$$

By defining $\Phi(n\omega)$ and $\Theta_n(n\omega)$ in (8.4), equation (8.3) is obtained. Here The proof for the FPRC with $\zeta_c = 1$ is concluded. The following content derives m_i for the FP-SOSRE with $\zeta_c = 2$.

In FP-SOSRE, we have $x_r(t) = [x_2(t) \ x_1(t)]^T$, where $x_2(t)$ and $x_1(t)$ denote the first and the second state of the controller, respectively. From (8.1) and (1.13), during the time interval $(t_i, t_{i+1}]$, the state-space representation of FP-SOSRE can be written as follows:

$$\begin{cases} \dot{x}_1(t) = x_2(t), \\ \dot{x}_2(t) = -2\beta\omega_r x_2(t) - \omega_r^2 x_1(t) + e(t). \end{cases} \quad (8.26)$$

The Laplace transforms of both sides from Equation (8.26) with the initial condition of $x_1(t_i)$ are given by

$$s^2 X_1(s) - s x_1(t_i) = -2\beta\omega_r (s X_1(s) - x_1(t_i)) - \omega_r^2 X_1(s) + E(s). \quad (8.27)$$

From (8.27), $X_1(s)$ is obtained as

$$X_1(s) = \frac{E(s) + (s + 2\beta\omega_r)x_1(t_i)}{s^2 + 2\beta\omega_r s + \omega_r^2}. \quad (8.28)$$

By conducting the inverse Laplace transform of (8.28), we have

$$x_1(t) = \mathcal{L}^{-1} \left\{ \frac{E(s) + (s + 2\beta\omega_r)x_1(t_i)}{s^2 + 2\beta\omega_r s + \omega_r^2} \right\}, \text{ for } t \in (t_i, t_{i+1}]. \quad (8.29)$$

Define

$$\Omega_i(s) = \frac{E(s) + (s + 2\beta\omega_r)x_1(t_i)}{s^2 + 2\beta\omega_r s + \omega_r^2}. \quad (8.30)$$

Substituting $\Omega_i(s)$ into (8.29), $x_1(t)$ is given by

$$x_1(t) = \mathcal{L}^{-1}[\Omega_i(s)], \text{ for } t \in (t_i, t_{i+1}]. \quad (8.31)$$

From (8.29), $x_1(t_{i+1})$ is given by

$$x_1(t_{i+1}) = \mathcal{L}^{-1}[\Omega_i(s)]|_{t_i}. \quad (8.32)$$

Based on (8.30) and (8.32), we have

$$\Omega_{i+1}(s) = \frac{E(s) + (s + 2\beta\omega_r)\mathcal{L}^{-1}[\Omega_i(s)]|_{t_i}}{s^2 + 2\beta\omega_r s + \omega_r^2}. \quad (8.33)$$

From (8.31) and $\dot{x}_1(t) = x_2(t)$, $x_2(t)$ is given by

$$x_2(t) = \mathcal{L}^{-1}[\Omega_i(s)/s], \text{ for } t \in (t_i, t_{i+1}]. \quad (8.34)$$

From (8.34), $x_2(t_{i+1})$ is given by

$$x_2(t_{i+1}) = \mathcal{L}^{-1}[\Omega_i(s)/s]|_{t_i}. \quad (8.35)$$

Since $m_i = x_2(t_i)$, from (8.35), m_i is given by

$$m_i = \mathcal{L}^{-1}[\Omega_i(s)/s]|_{t_{i-1}}. \quad (8.36)$$

This completes the derivation of m_i for the FP-SOSRE with $\zeta_c = 2$. The subsequent steps for deriving $\mathcal{H}_n(\omega)$ for the FP-SOSRE follow the same process as the derivations from (8.14) to (8.25). Here, we conclude the proof. \square

8

In practical scenarios, the system in (8.1) with a sinusoidal input $e(t) = |E|\sin(\omega t)$ and under Assumption 5 will initially undergo a transient response before reaching the steady-state. The frequency response analysis in Theorem 10 is applicable to systems at steady-states. Therefore, we calculate m_i until the cycle has a reset instant t_i meeting the condition of $m_i = m_{i+k}$. This cycle is denoted as the first valid steady-state cycle.

8.4 Results

8.4.1 Validation of the Accuracy of the HOSIDF

We verify the accuracy of the HOSIDF method in Theorem 10 by applying it to analyze three FPRC examples. Figures 8.2(a)-(c) depict the simulated and predicted outputs of three FPRC systems under the input signal $e(t) = \sin(2\pi ft)$, including the FP-CI (with $\gamma = 0$ and $k = 20$) at an input frequency of $f = 1$ Hz, the FP-FORE (with $\omega_r = 1$, $\gamma = 0$, and $k = 4$) at an input frequency of $f = 10$ Hz, and the FP-SOSRE (with $\omega_r = 1$, $\beta = 1$, $\gamma = 0$, and $k = 4$) at an input frequency of $f = 10$ Hz. The results indicate a close alignment between the predicted and simulated outputs, confirming the accuracy of Theorem 10.

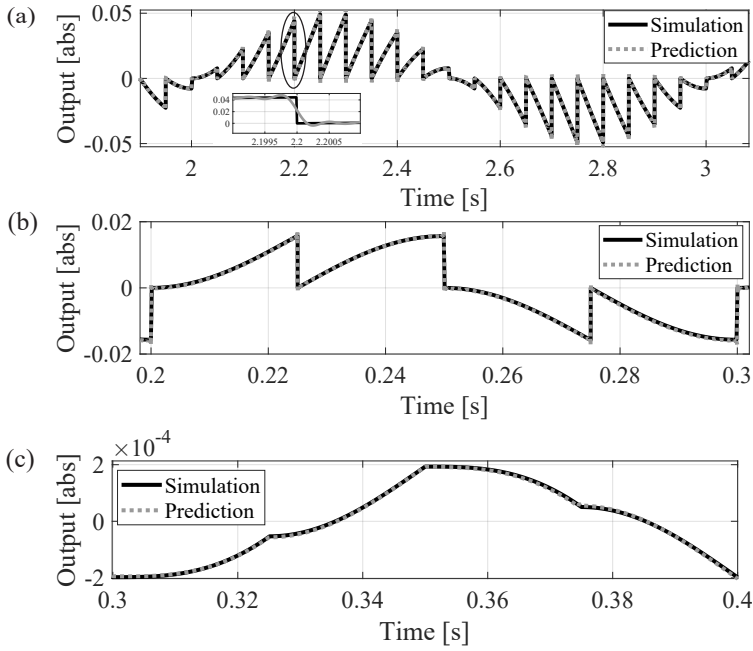


Figure 8.2: The simulated and Theorem 10-predicted outputs for (a) the FP-CI, (b) the FP-FORE, and (c) the FP-SOSRE.

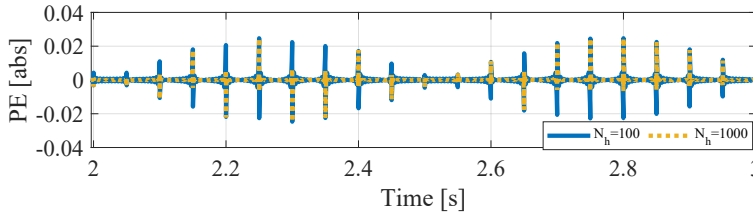


Figure 8.3: The prediction error (PE) of the FP-CI when (a) $N_h = 100$ and (b) $N_h = 1000$.

The small differences between the simulation and prediction results stem from the fact that the output of the reset system includes an infinite number of harmonics, whereas in practice, only a finite number (set to 1000 in Fig. 8.2) of harmonics is considered in the calculation. Figure 8.3 illustrates the prediction error (PE) between the prediction and simulation in the context of the FP-CI shown in Fig. 8.2(a). It shows that as the number of harmonics N_h increases, the PE decreases. Ideally, the PE approaches zero as N_h tends to infinity. Research [18] also demonstrates that the accuracy of the HOSIDF analysis improves as N_h , the number of harmonics considered in the analysis, increases.

8.4.2 Frequency-domain Properties of the FPRC

We employ the HOSIDF analysis to investigate the frequency-domain properties of the FPRC. The reset control system (RCS) employing the FPRC is referred to as FP-RCS and the reset system employing the “Zero-crossing (ZC) law” is denoted as ZC-RCS.

Figure 8.4(a) compares the frequency responses of the FP-CI (with $k = 4$ and $\gamma = 0$) and the traditional ZC-CI (with $k = 2$ and $\gamma = 0$). Their gain-frequency (slope) is the same, but the first-order harmonic in FP-CI provides an 8.4° phase lead compared to that of the CI.

Figure 8.4(b) illustrates the relationship between the number of reset instants k and the phase of the FP-CI (with $\gamma = 0$). As the number of reset instants increases, the phase lead provided by the FP-CI also increases. This characteristic of the FP-CI demonstrates the potential benefits for improved performance achieved by the phase lead of the FPRC.

However, a large number of reset instants k will generate higher-order harmonics. As shown in Fig. 8.4(c), when setting $k = 20$, the three dominant harmonics in the FP-CI are the first, 19th, and 21st harmonics. Although it eliminates the 3rd and 5th harmonics, it introduces higher-order harmonics.

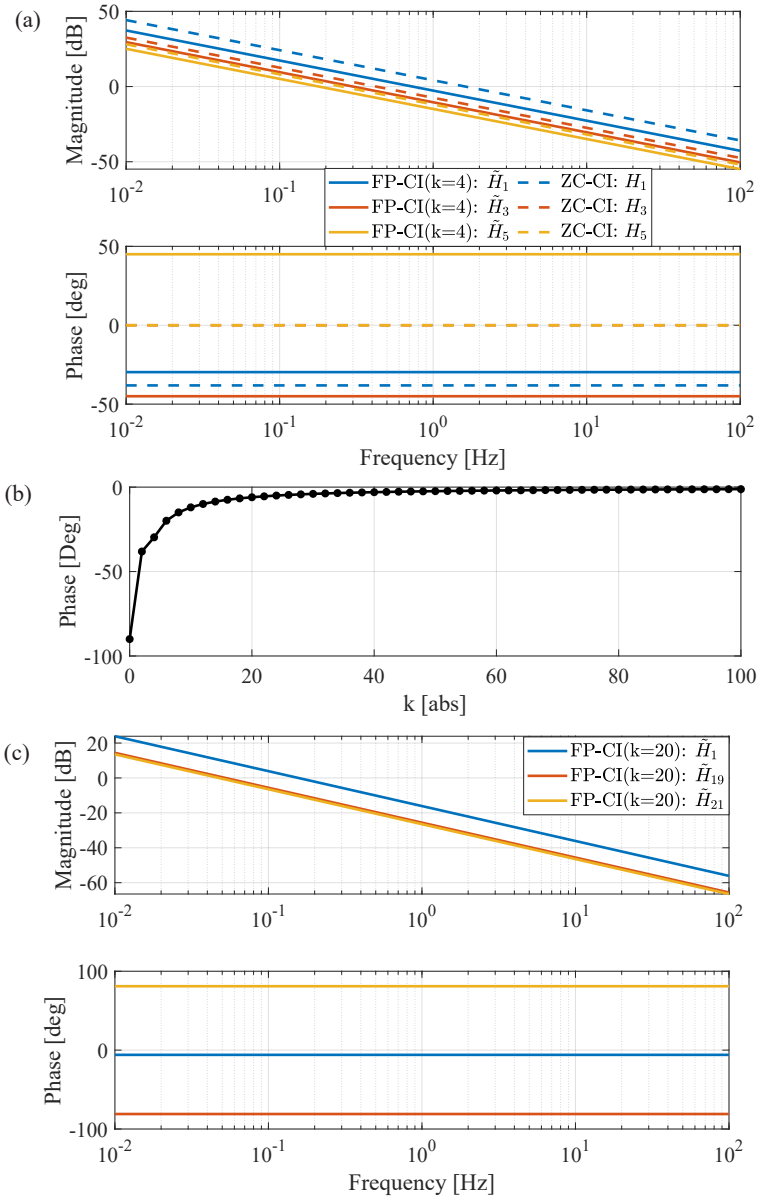


Figure 8.4: (a) The first three dominant harmonics in the FP-CI (with $k = 4$) and the ZC-CI. (b) The relationship between the phase of the first-order harmonic and the number of reset instants k in the FP-CI. (c) The first three dominant harmonics in the FP-CI (with $k = 20$).

8.5 Conclusion

This chapter introduces a reset element termed Fixed-Phase Reset Control (FPRC), designed for Single-Input-Single-Output (SISO) systems with sinusoidal inputs. The FPRC resets based on a signal with a fixed phase, distributing k reset instants per steady-state period. A Higher-Order Sinusoidal Input Describing Function (HOSIDF) is developed to analyze the frequency-domain properties of the FPRC. Simulation results validate the accuracy of the analysis method. The findings indicate that the FPRC provides a phase lead compared to previous reset controllers with the zero-crossing law. Increasing the value of k tends to provide a larger phase benefit; however, higher values of k introduce high-order harmonics into the system. The applicability of the FPRC with the phase benefits to practical closed-loop systems needs further investigation in future studies.

Bibliography

- [1] K. K. Tan, T. H. Lee, and S. Huang. *Precision motion control: design and implementation*. Springer Science & Business Media, 2007.
- [2] K. Åström and R. Murray. *Feedback Systems: An Introduction for Scientists and Engineers*. Princeton University Press, 2010.
- [3] J. C. Clegg. “A nonlinear integrator for servomechanisms”. In: *Transactions of the American Institute of Electrical Engineers, Part II: Applications and Industry* 77 (1958), pp. 41–42.
- [4] I. Horowitz and P. Rosenbaum. “Non-linear design for cost of feedback reduction in systems with large parameter uncertainty”. In: *International Journal of Control* 21.6 (1975), pp. 977–1001.
- [5] K. R. Krishnan and I. M. Horowitz. “Synthesis of a non-linear feedback system with significant plant-ignorance for prescribed system tolerances”. In: *International Journal of Control* 19.4 (1974), pp. 689–706.
- [6] A. Banos and A. Vidal. “Definition and tuning of a pi+ ci reset controller”. In: *2007 European Control Conference (ECC)*. IEEE, 2007, pp. 4792–4798.
- [7] L. Hazeleger, M. Heertjes, and H. Nijmeijer. “Second-order reset elements for stage control design”. In: *2016 American Control Conference (ACC)*. IEEE, 2016, pp. 2643–2648.
- [8] N. Saikumar and H. HosseinNia. “Generalized fractional order reset element (GFrORE)”. In: *9th European Nonlinear Dynamics Conference (ENOC)*. 2017.
- [9] N. Saikumar, R. K. Sinha, and S. H. HosseinNia. “constant in gain lead in phase element–application in precision motion control”. In: *IEEE/ASME Transactions on Mechatronics* 24 (2019), pp. 1176–1185.
- [10] M. F. Y. W. J. Zheng, Y. Guo, and L. Xie. “Improved Reset Control Design for a PZT Positioning Stage”. In: *2007 IEEE International Conference on Control Applications*. 2007.
- [11] D. Paesa, J. Carrasco, O. Lucia, and C. Sagues. “On the design of reset systems with unstable base: A fixed reset-time approach”. In: *IECON 2011 - 37th Annual Conference of the IEEE Industrial Electronics Society*. 2011, pp. 646–651.
- [12] D. Paesa, A. Baños, and C. Sagues. “Optimal reset adaptive observer design”. In: *Systems and Control Letters* 60.10 (2011), pp. 877–883.
- [13] Y. Guo, Y. Wang, L. Xie, H. Li, and W. Gui. “Optimal reset law design of reset control systems with application to HDD systems”. In: *Proceedings of the 48th IEEE Conference on Decision and Control (CDC) held jointly with 2009 28th Chinese Control Conference*. 2009, pp. 5287–5292.

- [14] J. C. Clegg. “A nonlinear integrator for servomechanisms”. In: *Transactions of the American Institute of Electrical Engineers, Part II: Applications and Industry* 77.1 (1958), pp. 41–42.
- [15] I. Horowitz and P. Rosenbaum. “Non-linear design for cost of feedback reduction in systems with large parameter uncertainty”. In: *International Journal of Control* 21.6 (1975), pp. 977–1001.
- [16] N. Saikumar, K. Heinen, and S. H. HosseinNia. “Loop-shaping for reset control systems: A higher-order sinusoidal-input describing functions approach”. In: *Control Engineering Practice* 111 (2021), p. 104808.
- [17] M. B. Kaczmarek, X. Zhang, and S. H. HosseinNia. “Steady-state nonlinearity of open-loop reset systems”. In: *2022 IEEE Conference on Control Technology and Applications (CCTA)*. IEEE, 2022, pp. 1056–1060.
- [18] X. Zhang, M. B. Kaczmarek, and S. H. HosseinNia. “Frequency-domain analysis for reset systems using pulse-based model”. In: *arXiv preprint arXiv:2206.00523* (2022).

9

Conclusions and Recommendations

This chapter summarizes the contributions of this thesis and, based on the insights gained from these contributions and their associated limitations, provides recommendations for future research directions.

9.1 Conclusions

In this dissertation, we have addressed two main research problems: frequency-domain analysis for SISO LTI reset feedback control systems and frequency-domain design of reset control for improving the performance of precision motion systems.

Frequency Response Analysis of Reset Control Systems

Frequency response includes both gain and phase information for open-loop and closed-loop systems. In Chapter 2, we began by developing Higher-Order Sinusoidal Input Describing Functions (HOSIDFs) for reset controllers and open-loop generalized reset control systems in Fig. 2.1. We then compared the simulation results with the predictions made by the HOSIDFs in case studies, and the results confirmed their accuracy.

The proposed open-loop HOSIDFs provide crucial frequency-domain gain and phase information for each harmonic of reset control, serving as an essential reference for control system design. Additionally, we have analytically decomposed the HOSIDFs of reset controllers into their base-linear transfer functions and nonlinear components. This decomposition offers new insights into the behavior of reset controllers in the frequency domain and lays the foundation for subsequent closed-loop HOSIDF analysis.

Since Sinusoidal-Input Describing Function (SIDF) analysis exhibits deviations in closed-loop multiple-reset control systems, we have proposed a method in Chapter 3 to differentiate between two-reset and multiple-reset control systems. This method helps assess the reliability of SIDF analysis. Additionally, by comparing the time consumption between the proposed method and the point-to-point time-domain simulation method, we have found that the proposed method demonstrated approximately 300 times greater efficiency in case studies.

Then, building on the method introduced in Chapter 3, we have developed the HOSIDFs for closed-loop reset systems with two reset instants per steady-state cycle in Chapter 4. The accuracy of the HOSIDFs was validated through simulations and experiments. Together, the open-loop and closed-loop HOSIDFs address the gap in frequency-domain analysis for generalized reset systems, as shown in Fig. 1.8. Additionally, the closed-loop HOSIDFs establishes a frequency-domain relationship between open-loop and closed-loop reset control systems, enabling the application of loop-shaping techniques in reset systems.

Finally, in Chapter 5, we have developed a MATLAB application that consolidated the tools introduced in Chapters 2–4. This application provides an intuitive platform for control engineers to analyze reset control systems in the frequency domain, aiding in the design of high-performance systems. We then showcased the use of the app through a case study. The case study achieved a 21.4% reduction in maximum steady-state error while requiring 85.6% less maximum actuation force on a precision motion stage, compared to the previous reset control. These results highlight the effectiveness of the app in designing reset control for enhanced performance.

Frequency-Domain Design of Reset Control Systems for Improved Precision Motion Performance

Reset control systems introduce both first-order and high-order harmonics in the frequency domain. While the first-order harmonic provides gain-phase advantages over linear control systems, high-order harmonics, when their magnitudes are large, may degrade overall system performance. Using the frequency response analysis tools, we have proposed new reset control strategies to shape these harmonics, thereby achieving enhanced system performance compared to both previous reset and linear control systems.

To achieve this, in Chapter 6, we have introduced a phase-lead shaped reset control element designed to modify the phase of reset instants. This design offers two key advantages. First, it provides phase lead for the first-order harmonic while preserving the gain properties. Leveraging this benefit, a case study has demonstrated improved transient system performance, achieving zero overshoot compared to the previous reset control with 36.0% overshoot and linear control with 64.0% overshoot. Second, it can be configured to enhance the gain benefits of the first-order harmonic while maintaining both the phase of the first-order harmonic and the gain properties of high-order harmonics, contributing to better steady-state precision. Benefiting from this gain enhancement, a case study demonstrated a 37.5% reduction in maximum steady-state error compared to previous reset control, in the presence of reference tracking and disturbances.

Instead of tuning the first-order harmonic, in Chapter 7, we retained the benefits of the first-order harmonic while reducing problematic high-order harmonics by introducing a PID-shaped reset control element. This design has resulted in improved steady-state precision. Two representative case studies conducted on a precision motion stage demonstrated that the PID-shaped reset design resulted in a 75.8% and 51.8% reduction in maximum steady-state errors compared to the previous reset control, under reference, disturbance, and noise inputs. Additionally, we have proved that this design effectively eliminated limit cycle issues in the step responses of the reset control systems.

Up to this point, the reset elements discussed in this thesis trigger reset actions at the zero-crossings of filtered feedback errors. To further explore the potential of reset control systems, we have introduced a reset element called Fixed-Phase Reset Control (FPRC) in Chapter 8, specifically designed for sinusoidal inputs. This element triggers reset actions at the zero-crossings of a signal with predefined frequency. Then, we have developed its open-loop HOSIDF analysis method with validation of its accuracy. Through the HOSIDF analysis, we have founded that by increasing the frequency of the predefined reset-triggered signal within the FPRC, greater phase lead was achieved compared to previous reset elements. However, this improvement came at the cost of introducing high-magnitude high-order harmonics, presenting a trade-off. The practical application of FPRC in closed-loop systems remains a promising direction for future research.

9.2 Concluding Remarks

These contributions not only advanced the theoretical framework of frequency-domain analysis for reset control but also demonstrated practical value in precision motion control applications. We have summarized the main concluding remarks from the thesis as follows:

- In this thesis, we have established a reliable frequency-domain connection between open-loop and closed-loop HOSIDFs. Worth noting is that in the closed-loop HOSIDFs, we introduced a factor $\Gamma(\omega)$ in (4.9), which modulates cross-effects between the first-order and high-order harmonics. Prior literature often assumed that $\Gamma(\omega) = 1$, implying that the closed-loop Describing Function (DF) in reset control can be derived by closing the loop of the open-loop DF, similar to the linear system relationship illustrated in (1.3), where the closed-loop DF represents the first-order harmonic in the closed loop. However, this assumption holds true only in the absence of high-order harmonics. As $|\Gamma(\omega) - 1|$ increases, the closed-loop DF deviates further from the linear closed-loop relationship of the open-loop DF, emphasizing the increasing impact of high-order harmonics, as analytically demonstrated in Remark 3. This observation suggests that $\Gamma(\omega)$ can serve as a robustness factor in future research.
- For closed-loop frequency response analysis of reset control systems, the SIDF analysis assumes two resets per cycle. However, this assumption becomes invalid for many reset controllers, such as the Clegg Integrator (CI)-based reset systems, when operating at low frequencies. In these multiple-reset frequency ranges, the reliability of the SIDF analysis is compromised. In Chapters 3 and 7, we have demonstrated that by identifying the frequency ranges where multiple reset actions occur and incorporating appropriate shaping filter designs, this limitation was effectively addressed, and the reliability of SIDF analysis was ensured. Furthermore, in reset systems where multiple-reset actions occur and high-order harmonics become large, such as CI-based reset systems operating at low frequencies, several issues arise. These include compromised steady-state precision, excessively sharp control inputs, and the occurrence of limit cycle problems. Such challenges may lead to the perception in some previous literature that reset control is unsuitable for achieving desired low-frequency steady-state precision. However, in Chapter 7, we demonstrated that the designed shaping filter effectively reduced problematic high-order harmonics, addressing these issues. Hence, the potential of reset control to achieve high-performance steady-state behavior, when properly designed, is preserved.
- We have explored the application of linear filters to improve the nonlinearity of reset controllers. One such design is the PID shaping filter, where the integral element reduces high-order harmonics, while the derivative element enhances the phase lead of the controller. Specifically, through appropriate design, the shaping filter can achieve improved phase margin of the first-order harmonic while maintaining similar gain properties across harmonics, or enhanced gain of the first-order harmonic while preserving its phase margin and the gain of high-order harmonics, or preserved first-order harmonic properties while reducing high-order harmonics. These frequency-domain properties allow the shaping filter to enhance system performance based on specific system requirements. While linear shaping filter designs push the boundaries of gain-phase trade-offs, there is a limit to tuning the nonlinearity. Moreover, the extent to which this benefit can be leveraged depends on the specific demands of the systems.

9.3 Discussions and Future Recommendations

The proposed frequency response analysis methods for generalized reset control systems provide greater tuning flexibility for improved system performance. Building on this contribution, we have identified a promising direction for future research: integrating loop-shaping techniques with reset control.

Loop-shaping is an effective method for relating time-domain closed-loop performance to frequency-domain properties through SIDF analysis. However, the nonlinear nature of reset control generates both first-order and high-order harmonics, complicating the application of loop-shaping techniques. The proposed HOSIDFs describe the frequency-domain properties (gain and phase) of reset control systems. We expect that this information will facilitate the application of loop-shaping techniques to reset control. For instance, the information from the HOSIDF can be used to explore the trade-off between bandwidth and robustness. Furthermore, practical applications of reset feedback control in advanced engineering fields include Multiple-Input Multiple-Output (MIMO) systems. The proposed HOSIDFs can be utilized to design reset controllers that effectively suppress high-order harmonics to negligible levels while preserving the advantages of first-order harmonics. Achieving this balance will finally enhance the reliability of the superposition principle and enables the effective implementation of loop-shaping techniques in closed-loop MIMO reset control systems.

One note is that while high-order harmonics can degrade system performance by increasing sensitivity to high-frequency noise, they are not always detrimental. This raises the question: what are the thresholds or margins within which high-order harmonics contribute positively or negatively to system performance? Answering this question may deepen our understanding of their role in reset control and provide further insights into the interplay between first-order and high-order harmonics, ultimately guiding the refinement of loop-shaping techniques for reset feedback control.

Though the proposed frequency response analysis method effectively analyzes reset control systems, we have encountered one main limitation: the closed-loop HOSIDFs operate under the assumption that there are two reset instants per steady-state cycle in sinusoidal-input closed-loop reset control systems. This assumption does not hold true for multiple-reset systems. While multiple-reset systems are typically avoided in practice due to their association with high-magnitude high-order harmonics, such harmonics are not always problematic, as discussed in the previous paragraph. Future work is encouraged to extend the frequency response analysis method to accommodate multiple-reset systems, including the derivation of the magnitude and phase for each harmonic. Integrating these advancements with the findings of this dissertation would provide a more complete understanding of the relationship between open-loop and closed-loop reset systems, offering deeper insights that can enhance the design of loop-shaping techniques for reset control systems.

In the second major contribution of this dissertation, we have developed reset control strategies with enhanced gain-phase margin of reset control systems. Though these strategies have enhanced the overall performance of reset systems, we expect future research to push the performance margin further by leveraging the proposed frequency response analysis methods. This can be achieved through two primary approaches: one is tuning the reset elements, which involves optimizing the reset controller structure and designing

the shaping filter to refine and enhance reset actions. The other approach is tuning the linear elements, including adjusting linear components placed in parallel, in series (before or after the reset controller), or within the feedback loop to improve overall system performance. These tuning strategies aim to achieve an optimal trade-off between the gain and phase of the first-order harmonics and high-order harmonics, ultimately resulting in enhanced system performance.

Acknowledgments

During my PhD journey, I chose Delft in the Netherlands—a completely new place to begin this chapter of my life. Here, I broadened my horizons and added another piece to my puzzle of the world. Living and studying in Delft has been truly transformative. I had the privilege of meeting many brilliant and kind individuals whose conversations, shared experiences, and collaborative efforts greatly enriched my academic and personal life. These inspiring and genuine connections have left me with memories I will cherish forever. Of course, life is not always smooth and happy. The challenges I faced have made me rethink myself and the world, encouraging and shaping me into a more self-consistent person, finding peace and balance in life.

First and foremost, I want to express my gratitude to my promotors for their guidance throughout my PhD journey. **Hassan**, I sincerely appreciate your mentorship during our collaboration. Your critical thinking and creative ideas have played a key role in shaping my academic growth. You have always been generous in sharing your experiences and offering advice, providing support when I faced uncertainties. Your suggestions have been invaluable—both in academia and in shaping my outlook on life. And I must say, the delicious beef you prepared during the group gatherings remains the best I've had in the Netherlands. It has been a pleasure to work with you and learn from you throughout my PhD. **Just**, thank you for your insightful guidance. Your extensive academic experience has provided me with advice on both research and career development. I deeply admire your presentation style, which, as we say in Chinese, is “profound yet easy to understand.” Beyond academia, you have shown genuine care for the personal growth and well-being of PhD students, and I truly appreciate you in offering thoughtful suggestions.

Thanks to my committee members: **Prof. De Schutter, Prof. Ionescu, Dr. Jafarian, Prof. Reger, Prof. Vinagre, and Prof. Steeneken** for attending my defense.

Thanks to my colleagues in G-1-120: Jelle, Ali Amoozandeh, Francesco, Mingkai, Malte, Gerben, Nima, Marcin, AD, Dave, Joep, and Ali. Your presence in the office and during coffee breaks made my research life much more enjoyable and far less monotonous. **Jelle**, you are an excellent tennis player, and I've truly enjoyed playing and engaging in fun activities with you. Thank you for your composed and engaging conversations, as well as your encouragement and advice on PhD life and careers. **Ali Amoozandeh**, a great ping-pong player, it has been a pleasure sharing so many fun activities with you. I sincerely appreciate your thoughtful Chinese New Year wishes every year and all the valuable advice you've given me. **Francesco**, it has been a pleasure having you in the office—you are always a gentleman. Thank you for the fun and sincere conversations. And of course, **Mingkai**, it was great having you in G-1-120 at MSD, sharing conversations and suggestions throughout our time together. **Malte**, thanks for your energetic and insightful perspectives and for always inviting me to lunch and drinks.

Thanks to the Chinese community I met in PME: Sifeng, Yuheng, Minxing, Xianfeng, Hanqing, Mingkai, Yujiang, Ze, Yang, Binbin, Ruibo, Xuerong, Xueying, Yong, and Kai.

The delicious food from our gatherings, skiing trips, hiking adventures, and game nights were incredibly relaxing and enjoyable. **Sifeng**, the one who always brings people together, organizing PME Chinese parties and creating a lively atmosphere. It was great to have you as a lab buddy in MSD and thank you for the many fun conversations and your support. **Yuheng**, I truly enjoyed your piano performances. Thank you for your thoughtful conversations and encouragement. I am also grateful for the help and support from **Minxing**, **Xianfeng**, **Hanqing**, and **Yujiang**. **Xuerong** and **Jingyi**, thank you for the delicious Dongbei dishes that brought warmth to our gatherings.

Thanks to other members of PME: Andres, Ron, Luke, Davood, Inge, Ata, and Endre, for the fun and engaging lunch gatherings that made my days more lively. Thanks to Marli, Marianne, and Mascha from the PME secretary and ME graduate school for your assistance.

I had the pleasure of working with my master's students, **Hsing-Li** and **Yixuan**. Collaborating with you has been a wonderful experience, and our discussions have helped me grow and refine my critical thinking. I am truly proud of your work.

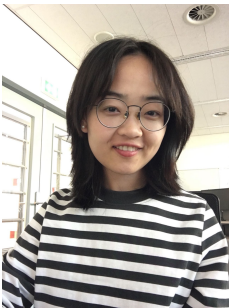
Thank you, **Zhaochong**, from CoR, for the engaging conversations, support, and fun discussions on scientific topics and PhD life. Thanks to **Ze Chang** for your valuable suggestions. Thanks to **Xiaoyu**, **Yun** from DCSC, and **Yifei** from AE for gatherings and making conferences like CCTA, ECC, and Benelux meetings enjoyable.

Thanks to all the sincere friends I've met during this PhD journey. Special thanks to **Yueer** and **Sulian** for your bravery, support, and companionship when I faced a frightening and dangerous moment. **Xinling**, we have known each other since high school, and it has been wonderful to share this PhD experience at TUD with you. Our travels, outings, and mutual support have been invaluable. To **Tingting**, **Yifan**, **Keer**, **Jingjing**, **Ziying**, **Xueqing**, and **Qingru**, our outings and girls' nights filled with delicious food and laughter have brought me so much joy and comfort.

A heartfelt thanks to my boyfriend, **Jinwei**, for your support. Lastly, I am deeply grateful to my mom (**Ms. Ai**) and dad (**Mr. Zhang**), my grandma (**Ms. Lu**) and grandpa (another **Mr. Zhang**)—for your unconditional love, generosity, and support. I also want to extend my thanks to my brother, uncle, aunt, and all my family members for their constant love and encouragement.

*Xinxin Zhang
Delft, March 2025*

Curriculum Vitæ



Xinxin Zhang (x.zhang-15@tudelft.nl, x.zhang.tud@gmail.com) was born on January 1, 1996, in Dezhou, Shandong, China.

She received her B.S. degree in Mechatronics Engineering from Qingdao University, China, in 2017, with a graduate project titled “The Modal Analysis and Optimized Design of Piezoelectric Fan for Enhanced Cooling Abilities.” She then obtained her M.S. degree in Precision Instruments Engineering from Tianjin University, China, in 2020, with research projects on “Terahertz Time-Domain Spectroscopy and Radiation.”

In October 2020, she began her Ph.D. studies in the Department of Precision and Microsystems Engineering at Delft University of Technology in the Netherlands, under the supervision of Dr. S.H. (Hassan) Hossein Nia Kani and Prof.dr.ir. J.L. (Just) Herder.

Her Ph.D. research focuses on developing frequency response analysis tools for reset feedback control systems and designing reset controllers for precision motion systems. The goal is to enhance steady-state performance (tracking precision, disturbance, and noise rejection) and transient-state performance (reducing overshoot and settling time).

List of Publications

Journal Papers

4. **Xinxin Zhang** and S. Hassan HosseinNia, Enhancing Reset Control Phase with Lead Shaping Filters: Applications to Precision Motion Systems, *Control Engineering Practice*, 2025, Under Revision.
3. **Xinxin Zhang** and S. Hassan HosseinNia, Higher-Order Sinusoidal Input Describing Functions for Open-Loop and Closed-Loop Reset Control with Application to Mechatronics Systems, *Mechanical Systems and Signal Processing*, 2025, Under Revision.
2. **Xinxin Zhang** and S. Hassan HosseinNia, Enhancing the reliability of closed-loop describing function analysis for reset control applied to precision motion systems, *IEEE Transactions on Control Systems Technology*, 2025, Conditionally Accepted.
1. **Xinxin Zhang**, Marcin B. Kaczmarek, and S. Hassan HosseinNia. "Frequency response analysis for reset control systems: Application to predict precision of motion systems." *Control Engineering Practice* 152 (2024): 106063.

Peer-Reviewed Conference Papers

7. **Xinxin Zhang**, Hsing-Li Hsu, and S. Hassan HosseinNia. "Frequency-Domain Analysis of the Fixed-Phase Reset Control System." 2024 IEEE Conference on Control Technology and Applications (CCTA). IEEE, 2024.
6. **Xinxin Zhang** and S. Hassan HosseinNia. "Transient Response Analysis of Reset PID Control Systems." The 4th IFAC Conference on Advances in Proportional-Integral-Derivative Control, 2024.
5. **Xinxin Zhang** and S. Hassan HosseinNia. "The Analysis and the Performance of the Parallel-Partial Reset Control System." The 22nd European Control Conference (ECC), 2024.
4. **Xinxin Zhang** and S. Hassan HosseinNia. "Identifying Two-Reset Conditions for Closed-Loop Sinusoidal Input Reset Control Systems." 2024 IEEE/ASME International Conference on Mechatronic and Embedded Systems and Applications. 2024.
3. Luke F. van Eijk, Yixuan Liu, **Xinxin Zhang**, Dragan Kostic, S. Hassan HosseinNia. "A Non-linear Integrator Based on the First-Order Reset Element." The 4th IFAC Conference on Advances in Proportional-Integral-Derivative Control, 2024.
2. **Xinxin Zhang** and S. Hassan HosseinNia. "Frequency-domain Analysis for Infinite Resets Systems." 2023 IEEE International Conference on Mechatronics (ICM). IEEE, 2023.
1. Marcin B. Kaczmarek, **Xinxin Zhang**, and S. Hassan HosseinNia. "Steady-state nonlinearity of open-loop reset systems." 2022 IEEE Conference on Control Technology and Applications (CCTA). IEEE, 2022.